

ABSTRACT

Wei, Shuzhen. Structural Design of Soft Actuators for Smart Textiles. (Under the direction of Dr. Tushar K. Ghosh).

Soft actuators are a new generation of actuators that hold great potential in the emerging areas of smart textiles, human-machine interface devices and soft robotics, primarily for their mechanical compliance. Many other features of soft actuators are also valued including the diversity of input energy and stimuli-sensitive materials, intimate structure-motion relationships, compact, and lightweight. Among various features, structures of the soft actuators are crucial to their actuation behaviors and influence other properties. Here we designed and studied the structures of three types of soft actuators, including the dielectric elastomer actuator (DEA), cellulose film actuator, and cellulose fiber actuator, with the objective of designing soft actuators for smart textiles. Thin dielectric layer is desirable for DEAs to lower the actuation voltage, but it is difficult to form uniformly thin layer, the defects in the thin layer lead to premature dielectric breakdown under high voltage, and the assistive parts needed to constrain the thin film add weight and volume to the actuator. Inspired by the rapid closure of the bistable Venus Flytrap (VFT), we designed bistable laminated DEAs that snap between two stable shapes under a short-period application of voltage. Due to the potential hazard of using high voltage for wearable actuators, we then studied the moisture-driven soft actuators for the abundant moisture near the human skin. Moisture-driven soft actuators are typically constructed into slender structures (i.e., film, fiber) for faster moisture diffusion and thus higher actuation speed. These structures are also fundamental structures in textiles. We choose commercially available regenerated cellulose films (cellophane) and yarns (viscose rayon) as the basic structures. The instantaneous bending behavior of cellophane under moisture change is designed into various other actuation motions through the structure design. The radial expansion of the viscose rayon due to moisture absorption is converted into torsional and linear motions by inserting large twist into the fiber to

form twisted and coiled polymer actuator (TCPA). The hierarchically twisted TCPAs are designed, and their moisture-driven torsional and linear actuation performances are studied. We also enabled electro-thermal actuation through plying TCPAs with CNT yarns.

© Copyright 2021 by Shuzhen Wei

All Rights Reserved

Structural Design of Soft Actuators for Smart Textiles

by
Shuzhen Wei

A dissertation submitted to the Graduate Faculty of
North Carolina State University
in partial fulfillment of the
requirements for the degree of
Doctor of Philosophy

Fiber and Polymer Science

Raleigh, North Carolina
2021

APPROVED BY:

Dr. Tushar Ghosh
Committee Chair

Dr. Ericka Ford

Dr. Yong Zhu

Dr. Michael Daniele

DEDICATION

This is dedicated to my parents, Chunfu Wei, and Lijiao Zhou, whose support and love made this possible.

BIOGRAPHY

Shuzhen Wei was born in a small village in Zhejiang, China. She received her Bachelor's degree in 2016 in Textile Chemistry from Jiangnan University and Master's degree in Textile Engineering in 2018 from NCSU. Her research interests are soft robotics and smart textiles.

ACKNOWLEDGMENTS

I would like to thank my advisor Dr. Tushar K. Ghosh for his motivation and support during my Ph.D. study. This research is an extension of my M.S. work and is still the beginning of my research journey. Prof. Ghosh motivated me to think broader and deeper, and always supported me during the difficulties in research and in daily life.

I am grateful for the great opportunity NCSU gave me. This diverse community provided such brilliant research and living environment for students and brought great people together. I appreciate the support from my fellow colleagues, Ashish Kapoor, Kony Chatterjee, Jordan Tabor, Xiaomeng Fang, and Huiqi Shao. I also appreciate Dr. Michael Daniele (and his Post Doc, Parthiban Rijan), Dr. Yong Zhu (and his Ph.D. student, Yuxuan Liu), Dr. Jess Jur (and his Ph.D. student, Beomjun Ju) for their help with conductive printing.

Lastly, I want to thank my parents, Chunfu Wei, Lijiao Zhou, my young brother, Hongbin Wei, and my love, Bill Zhou, for their endless support and love.

TABLE OF CONTENTS

LIST OF FIGURES	vii-xiii
Chapter 1 Introduction	1
Chapter 2 Bioinspired Structures for Soft Actuators	8
2.1 Introduction.....	8
2.2 Biological Actuators.....	11
2.2.1 How Structures Impact the Actuation Behavior	11
2.2.2 Hierarchical Structures of Biological Actuators.....	14
2.3 Manmade Soft Actuators	26
2.3.1 The Design Process for Soft Actuators.....	26
2.3.2 Structural Design of Soft Actuators.....	30
2.4 Fabrication Techniques for Soft Actuators	57
2.4.1 Molding.....	60
2.4.2 3D Printing.....	61
2.4.3 Thin-film Fabrication.....	63
2.4.4 Self-assembly.....	65
2.4.5 Textile-based Methods: A Conventional but Renewed Approach	66
2.4.6 Soft Actuator Fabrication: Opportunities and Challenges.....	69
2.5 Conclusion	72
Chapter 3 Bioinspired Actuation and Morphing in Textiles.....	81
3.1 Introduction.....	81
3.2 Film-based textile actuators.....	82
3.3 Fiber-based Textile Actuators	89
3.4 Textiles for pneumatic (and fluidic) actuation.....	94
Chapter 4 Twisted and Coiled Polymer Actuators (TCPAs)	101
4.1 Introduction.....	101
4.1 Development of TCPAs	102
4.2 Structural diversity of TCPAs	108
4.3 Structure mechanics and actuation analysis of TCPAs	115
4.3.1 Structure mechanics and actuation analysis of torsional TCPAs	115
4.3.2 Structure mechanics and actuation characterization of linear TCPAs.....	121
4.3.3 Parameter analysis	125
Chapter 5 Bioinspired Bistable Dielectric Elastomer Actuators.....	132
5.1 Introduction.....	132
5.2 Materials and methods	137
5.3 Bistable structure design	138
5.3.1 Prestrain-induced bending and bistability	138

5.3.2 Characteristics of helical structures	139
5.4 Results and discussion	140
5.4.1 Shape characterization	140
5.4.2 Electric field-induced actuation of the helical BiDEA	142
5.4.3 Binary valve for curved surfaces	144
5.5 Conclusion	146
<i>Chapter 6 Moisture-Driven Cellulose Actuators with directional motion and programmable shapes</i>	<i>151</i>
<i>1. Introduction.....</i>	<i>151</i>
<i>2. Materials and methods.....</i>	<i>154</i>
<i>3. Results and Discussion</i>	<i>155</i>
Moisture-induced bending	155
Self-walking Actuators	162
Programmable actuators by heat laminating.....	166
<i>4. Conclusion.....</i>	<i>169</i>
<i>Chapter 7 Multi-Stimuli-Driven Viscose Rayon TCPAs</i>	<i>173</i>
7.1 Introduction.....	173
7.2 Results and discussion	175
7.2.1 Fiber properties.....	175
7.2.2 TCPA properties	178
7.2.3 Torsional actuation of HT.....	182
7.2.4 Torsional actuation of HTsPly.....	184
7.2.5 Linear actuation of HTCo.....	190
7.2.6 Electrical actuation of torsional TCPAs	191
7.3 Conclusion	194
7.6 Supplementary information.....	197
7.6.1 Experimental method.....	197
<i>Chapter 8 Conclusion</i>	<i>210</i>

LIST OF FIGURES

<p>Figure 2-1. The hierarchical structural design of natural actuators. Two examples of antagonistic actuation of (a-c) an elbow, and, (d-f) plant leaves driven by actuators organized at three hierarchical levels. (e,f) Reproduced with permission.^[23] Copyright 2007, Oxford University Press.</p>	16
<p>Figure 2-2. Actuator’s 1st level structural design. (a) Volume expansion of actuators of different shapes due to increased internal pressure. (b) Extension and contraction of actuators with constant volume. (c-e) Different actuation behaviors due to the orientation of reinforcing fibers. The orange parts are the active bodies, and the blue lines are the mechanical reinforcing elements. The blue arrows are the directions of the generated stress under stimuli, the black arrows are the directions of the actuation deformation.....</p>	18
<p>Figure 2-3. Actuator’s 2nd level structural design. (a-c) Film bending under gradient stimuli exposure. (d-e) Bending and wrinkling of laminates composed of active and passive layers. (f) Bistable laminates composed of active layers and a strain-limiting layer. (g-h) folding of a film due to concentrated stress at the hinge. (i-j) volume expansion and bending of 3D structures due to encapsulated active materials in flexible and passive matrices. (k-m) twisting deformation of structures due to, (k) helically wounded inextensible fiber around an expansive cylindrical body, (l) twisted fiber embedded in an expansive body, and (m) the differential strain developed in a bilayered helical structure. Orange parts are active materials, and blue parts are passive materials. Blue arrows are directions of active stresses, and the dotted black arrows are deformation directions of the actuator.</p>	22
<p>Figure 2-4. Power amplification motion of biological organisms. (a) Frog jumping. (b) The structure of Fern sporangium and the rapid bending of its annulus for pore projection. (c) Tongue projection of chameleon during hunting. (d) Curling of larvae to store elastic energy for jumping. (e) Mantis shrimp and its predating appendage components. (f) Bistable leaves of VFT. (a) Reproduced by permission.^[41] Copyright 2015, COMPANY OF BIOLOGISTS LTD. (b) Reproduced with permission.^[21] Copyright 2012, American Association for the Advancement of Science. (c) Reproduced with permission^[40] under CC-BY license. (d) Reproduced with permission.^[42] Copyright 2019, COMPANY OF BIOLOGISTS LTD. (e) Reproduced with permission.^[43] Copyright 2009, COMPANY OF BIOLOGISTS LTD. (f) Reproduced with permission.^[20] Copyright 2005, Springer Nature.....</p>	25
<p>Figure 2-5. Design processes for soft actuators. (a) Steps in the design process, of (b) a natural actuator (pinecone), and (c) an inspired manmade actuator (moisture-sensitive textile actuator). From the choice of stimulus (from the bottom) to the selection of the stimuli (moisture)-responsive materials followed by arrangement of materials into bilayered structures to the integration of bilayered bending actuators into the higher-level system. (b) Reproduced with permission^[60] under CC-BY license. (c) Reproduced with permission.^[61] Copyright 2017, American Association for the Advancement of Science.</p>	30

- Figure 2-6. Capacitive linear actuators. (a-c) Design of stacked DE actuators for linear actuation using thickness strain. (d-f) Design of tubular DE actuators for linear actuation using areal strain. (g-l) HASEL actuator: (g) schematic of the working principle, (i,k) two actuator design schematics and, (j,l) their actuation performances. (m-o) Electrostatic zipping actuator: (m) schematic of the working principle, (n) actuation performances and, (o) an origami structure design and its actuation performance. (a) Reproduced with permission.^[79] Copyright 2017, Springer Nature. (b) Reproduced with permission.^[69] Copyright 2007, IOP Publishing. (c) Reproduced with permission.^[80] Copyright 2005, IOP Publishing. (d) Reproduced with permission.^[65] Copyright 2007, Elsevier. (e) Reproduced with permission.^[81] Copyright 2018, John Wiley and Sons. (f) Reproduced with permission.^[83] Copyright 2017, Author. (g-l) Reproduced with permission.^[84] Copyright 2018, AAAS. (m-o) Reproduced with permission.^[85] Copyright 2018, AAAS. 34
- Figure 2-7. Pneumatic linear actuators. (a) Schematics of fiber-reinforced pneumatic actuators showing different actuation motion. (b) Directional motion of a pneumatic actuator due to the kirigami skin with various cut patterns. (c) A pneumatic actuator with an origami skeleton. (d) Negative pressure-driven actuation of buckled structures. (a) Reproduced with permission.^[91] Copyright 2017, the Authors. (b) Reproduced with permission.^[93] Copyright 2018, American Association for the Advancement of Science. (c) Reproduced with permission.^[94] Copyright 2012, John Wiley and Sons. (d) Reproduced with permission.^[71] Copyright 2016, John Wiley and Sons. 37
- Figure 2-8. Thermal activated linear actuators. (a) Fabrication and working principle of shape memory PE. (b-d) Bicomponent fiber actuator: (b) extrusion of a bicomponent fiber composed of PE and an elastomer, (c) coil generation in the fiber by stretching and releasing, and (d) thermal-induced linear contraction. (a) Reproduced with permission.^[72] Copyright 2012, Elsevier. (b-d) Reproduced with permission.^[73] Copyright 2019, American Association for the Advancement of Science. 40
- Figure 2-9. TCP linear actuators. (a) Cross-sectional views of a twisted yarn, infiltrated and coated with functional materials. (b-d) CNT-based TCPs: (b) hierarchical structures of twisted CNT yarns, schematic of electrical actuation in (c) liquid, and (d) solid electrolyte. (e) Structure of nylon TCP and their assembly in a fabric. (f) A robotic arm powered by a Nylon/spandex TCP. (a) Reproduced with permission.^[111] Copyright 2019, AAAS. (b, d) Reproduced with permission.^[74] Copyright 2014, ACS. (c) Reproduced with permission.^[110] Copyright 2011, AAAS. (e) Reproduced with permission.^[66] Copyright 2016, National Academy of Sciences. (f) Reproduced with permission.^[114] Copyright 2018, John Wiley and Sons. 46
- Figure 2-10. Bending, twisting, and folding actuators. (a-c) UV-actuated LC twisting actuator: (a) twisting and untwisting deformation of the actuators cut at different angles to the LC orientation, (b) the actuation principle, and (c) a top view of the LC alignment and different cutting angles. (d) A self-folding-based walking robot, and (e) its hinge design. (f-h) Bistable bending actuation of DEA: (f) side view of actuation motion showing the two stable shapes, (g)

schematic of actuator fabrication, and (h) photographs of the two stable shapes. (i-k) Pneumatic bending actuator: (i) two structural designs and (j-k) demonstration of the actuation behavior. (a-c) Reprinted with permission from [121]. Copyright 2014 Springer Nature. (d-e) Reprinted with permission by [98]. Copyright 2014 American Association for the Advancement of Science. (f-h) Reprinted with permission from [31]. Copyright 2018 John Wiley and Sons. (i-k) Reprinted with permission from [55]. Copyright 2014 John Wiley and Sons. 51

Figure 2-11. Crawling and rolling actuators with multiple DOF. (a) Images of a moving caterpillar, and, (b) mechanism of its different locomotion. (c) A caterpillar-inspired soft actuator design and (d) the actuation performance. (e) Two applications of the spring-roll DEA, and (f) the schematics of the spring-roll DEA. (g) Images and (h) schematics of a pneumatic actuator with multiple DOF, and (i) its grasping behavior. (a-b) Reprinted with permission from [33]. Copyright 1997 Springer Nature. (c-d) Reprinted with permission from [128]. Copyright 2011 IOP Publishing. (e-f) Reprinted with permission from [82]. Copyright 2004 IOP Publishing. (g-i) Reprinted with permission from [127]. Copyright 2012 John Wiley and Sons. 54

Figure 2-12. Soft actuators with power amplification structures. (a-b) Prestressed DE-based soft gripper and fabrication process. (c-e) Prestressed bistable pneumatic actuators for high speed: (c) fast actuation of the biomimetic tongue, (d) fabrication schematics of the bistable structure, and (e) rapid closure of the biomimetic VFT. (a-b) Reprinted with permission from [132]. Copyright 2007 AIP Publishing. (c-e) Reprinted with permission from [130]. Copyright 2019 John Wiley and Sons. 57

Figure 2-13. Fabrication techniques for soft actuators. (a) Molding processes and (b) a soft pneumatic actuator fabricated by molding. (c) A multi-material printing machine (d) the tunable mechanical properties of the printed object. (e) Schematic of spin coating and blade coating processes to make bilayer structures. (f) Fabrication of mechanically self-assembled structures, and (g) the self-assembled helical structures. (h-j) Schematic of textile processes from fiber spinning, yarn twisting, to fabric assembly. (a-b) Reprinted with permission from [56] under CC-BY license. (c-d) Reprinted with permission from [142]. Copyright 2018 John Wiley and Sons. (e) Reprinted under CC BY license [150]. (f-g) Reprinted with permission by [162]. Copyright 2011, American Association for the Advancement of Science. 69

Figure 3-1. A tendril-like soft robot driven by electrically-controlled osmotic pressure. (a) Schematic of opening and closure of pores (stomata) on a leaf due to osmotic pressure change. (b) A plant's tendril reaching and anchoring on a support. (c) Schematic and (d) a photograph of the soft robot with design and components. (e) Reversible actuation of the tendril under voltage supply of 1.3V. Reproduced under the terms of the Creative Commons CC BY license[16]. Copyright 2019, Springer Nature..... 86

Figure 3-2. Laminate-based thermo-driven textile actuators. (a) Schematic of lamination process of the fabric actuator. (b) Cross-sectional view of the laminated fabric. (c) Photograph of the laminated fabric. (d) Schematic of actuation principle

under different stimuli. Reproduced with permissions.[19] Copyright 2020 WILEY-VCH Verlag GmbH & Co. KGaA, Weinheim.	88
Figure 3-3. Silk-based TCP yarns for length changing fabric. (a) Schematic of TCP fabrication and moisture activation. (b) Photographs showing the movement of a “caterpillar” made of coiled TCP, driven by the moisture from an approaching finger. (c) Length change of smart fabric made with coiled silk yarn, and application schematic of sweat-induced shrinkable sleeve. Reproduced with permission. Copyright 2019[30], John Wiley and Sons.....	93
Figure 3-4. Fiber-reinforced fluidic soft actuators for assistive gloves. (a) Four types of deformation of fluidic elastomeric tubes resulted from fiber arrangement and the strain-limiting layer, including bending, cylindrical twisting, linear extension, and pure twisting. (b) Actuation demonstration of the soft assistive glove. Reproduced with permission[37]. Copyright 2015, Elsevier.....	96
Figure 4-1. Development of CNT-based TCPAs. (a-c) First CNT-TCPA: (a) SEM image of CNTs drawn and twisted from the forest, (b) SEM image of highly twisted CNT yarn, and (c) schematics of electrochemical actuation setup.[7] (d-h) Solid-state CNT-TCPA by infiltrating gel electrolyte: SEM images of (d) four TCPA structures, © twisted CNT yarn showing high porosity, (f) electrolyte- infiltrated coiled CNT yarn,[23] (g) actuation schematics of the TCPA composed of two coiled-plyed CNT yarns, and (h) photographs of linear actuation of (g).[19] (i-k) Multistimuli-sensitive CNT-TCPA by infiltrating guest polymers: (i) different yarn structures and tethering conditions for actuation, (j) SEM images of the cross-sectional view of twisted CNT yarn before and after guest polymer infiltration, and (k) torsional actuation speed as a result of electrical power and applied tensile stress (inset: torsional actuation as a function of time).[13] (l-n) Polymer-coated CNT-TCPA: (l) schematic of surface-coated CNT yarn, (m) SEM images of differently coiled CNT yarns and sharp interface shown in the cracked yarn, (n) electrothermal actuation of three CNT-TCPAs (SRAM: surface-coated; HYAM: infiltrated; pristine yarn).[22]	105
Figure 4-2. Polymer fiber-based TCPAs. (a-d) Nylon fiber-based TCPA: (a) a photograph of coiled TCPA[13], (b) hydrothermal actuation of the TCPA lifting a weight by 12% by alternative application of cold (25°C, blue) and hot (95°C, red) water[7], (c) the tensile stroke and modulus change of the TCPA as a function of temperature[7], and (d) the drastically amplified stroke by coil design[13]. (e-g) Silk fiber-based TCPA[3]: (a) SEM images of untwisted and twisted the dual-filament silk fiber, (f) tensile stroke of two types of coiled TCPAs (ZS: z- twist and s-coil, and ZZ: z-twist and z-coil) with different twist density as a function of relative humidity, (g) two demonstrations of silk fiber-based TCPAs, including the biomimetic “caterpillar” and the contracting sleeves.....	108
Figure 4-3. Textile yarn types. Examples of different types of yarns from left to the right: single PLA fiber[25], multifilament PLA yarn[25], cotton staple yarn[26], two-and three-ply cotton yarn[17], cabled cotton yarn[27]......	109
Figure 4-4. Hierarchical structures of yarns.	110

Figure 4-5. Hierarchical yarn structures and different yarn types used in TCPAs. (a-d) Hierarchical structures evolvment of CNT-based staple yarn TCPAs: (a) CNT sheet with aligned fibers, (b) twisted single yarn with different twist directions, (c) ply yarn with further twist insertion to coil, and (d) cabled yarn by bundling ply yarns and twisting[9]. (e-g) Natural fiber-based single staple yarn TCPAs: I development of torque-balanced two-ply structure, (f) development of coiled single yarn, and (g) photograph of fully coiled, single staple yarn made by cotton, wool, and flax[15]. (h) Photographs of monofilament nylon yarn TCPAs with different structure hierarchy, with the first image as the precursor monofilament[7]. (i-j) Photographs of the evolvment of coiled, multifilament yarn TCPAs from a bundle of filaments: (i) Spandex[31] and (j) viscose rayon[32] multifilament yarn TCPAs. (k-l) Heterogeneous multifilament yarn TCPA: (k) schematic and SEM image of the yarn structure made by, (l), twisting and coiling a bundle of filaments of nylon and spandex[1]...... 114

Figure 4-6. Structure mechanics of single yarn-based torsional TCPAs. (a) Zoom-on view of one pitch of a twisted single yarn. (b) Single helix model of a twisted yarn. (c) Radial expansion-induced untwist actuation. The yellow line on the surface of the yarns represents the helical trace on the surface due to twisting. The red arrow represents the rotation direction during actuation. 116

Figure 4-7. Tethering conditions for single yarn-based torsional TCPAs. The black line on the surface of the yarns represents the helical trace on the surface due to twisting. The red arrow represents the rotation direction during actuation. 119

Figure 4-8. Structural evolvment and actuation of self-ply yarn-based TCPAs. The yellow line on the surface of the yarns represents the helical trace on the surface due to twisting. Blue arrows represent the untwist tendency of a single yarn and the resultant plying direction of the self-ply yarn. The red arrow represents the rotation directions of the single yarn and the resultant further twisting of the self-ply yarn during actuation. Character Z and S are the yarn twist type. 121

Figure 4-9. Structure mechanics of linear TCPAs and their structural design. (a) Twisted single yarn. (b) Self-coiled yarn and its actuation behavior. (c) Mandrel-coiled, homochiral yarn and its actuation behavior. (d) Mandrel-coiled, heterochiral yarn, and its actuation behavior. (e) Mandrel-coiled, homochiral yarn with gradient coil diameter and its actuation behavior. The yellow line on the surface of the yarns represents the helical trace on the surface due to twisting. The red arrow represents the rotation directions of the single yarn and the resultant further twisting of the self-ply yarn during actuation..... 123

Figure 5-1. Bistable structures derived from prestrained laminates. (a-b) Fabrication parameters and mechanics of bistable bending. (c-e) Bistable shapes after trimming. Two states of the bistable structure are denoted with numbers 1 and 2. (c) Four bistable shapes: rectangular plate, disk, tape-spring, and helix. (d-e) Bistable helices with inverted handedness, with (d) structural symmetry, and (e) structural asymmetry of the two-handed helices. 136

Figure 5-2. Structural parameters for the bistable helix from 2D to 3D. 140

Figure 5-3. Effect of fabrication parameters on the bistable shape. (a) Effect of prestrains on the curvature of the bistable disk and bistable helix, and theoretical results, with PI as the support layer. (b) Effect of elastic modulus of the support layer on the curvature, with $\varepsilon A = 40\%$ and constant εB . (c) Experimental samples of (b). (d) Effect of cutting angle on the curvature and experimental samples showing the bistable shapes with cutting angles of 30° , 60° , and 90° . Star dots represent monostable samples.....	142
Figure 5-4. Actuation mechanism and experimental setup. (a) Actuation mechanism of DE. (b) Schematic of reversible actuation of the BiDEA. (c) Laminate components and layout. (d) Actuation setup.....	144
Figure 5-5. Bistable valve design and actuation. Bistable valves with (a) two-ends tethered and (b) one end tethered outside valve boundary, and (c) one-end tethered at the valve boundary. (d) A wavy substrate with open holes. (e) Actuation of bistable valve for pore open and close. The red triangle dots represent the tethering points.	146
Figure 6-1. Material properties of cellophane films. (a) Semicrystalline information by WXR. (b) Water-induced dimensional swelling of uncoated cellophane, and (c) anisotropic swelling in three dimensions. (d) SEM images of the cross-section of the one-side coated cellophane. (e) Anisotropic tensile properties at ambient and wet conditions.	157
Figure 6-2. Actuation of cellophane under natural moisture gradient. (a) Schematic of moisture-induced bending of the pure and coated cellophane. (b) Photographs of moisture-induced bending of cellophane films cut along MD, TD, and 45° to the MD. (c-d) Curvature change of cellophane films and the change of RH and T when (c) water bath and (d) palm of hand approached and removed from beneath.	159
Figure 6-3. Actuation of the one-side coated cellophane in an RH-controlled chamber. (a) Schematic of the customized RH control unit. (b) A photograph of the chamber. (c) Curvature measurement of a bent film. (d) Actuation results under maximum RH capacity of the chamber. (e) One actuation cycle from (f) cyclic actuation within the selected RH range. (g) One actuation cycle from (h) cyclic actuation plotted as a function of RH.	161
Figure 6-4. Schematic of self-walking actuator design. (a) Locomotion steps of pure cellophane on a moist surface. (b) Modifying locomotion by attaching masses. From left to right: pure cellophane, identical masses attached to top ends to decrease the chance of oscillation (symmetric), identical masses attached to top and bottom ends for directional locomotion (asymmetric). (c) Effect of bending angle on the chance of flipping of the symmetric sample. From left to right: $\theta < 180^\circ$, $\theta = 180^\circ$, $\theta > 180^\circ$	163
Figure 6-5. Directional self-walking actuators. (a) Schematic and (b) experimental photographs of the directional motion of asymmetric design. (c) Actuation results of the three self-walking designs.....	166

Figure 6-6. Design and actuation of programmable actuators. (a) Strip trimming angles. (b) The rotational actuator. (c) The lifting actuator. (d) The snake-like actuator. (d) The thickness-changing fabric.....	168
Figure 7-1. Fiber properties. (a) Anisotropy of the fiber under polarized light microscope. (b, c) Water-induced radial expansion of the fiber at the cross-sectional and projected length view under the microscope. (d) Anisotropic swelling of diameter and length of the fiber under water exposure. (e) Moisture-induced fiber diameter change. (f) Tensile property of the fiber under ambient and wet conditions. (g) Reversible stress relief of the prestressed fiber under cyclic moisture change.	176
Figure 7-2. Hierarchical structures of the TCPAs. (a) Schematic of a hierarchical yarn structures constructed from a fiber. Microscope images of (b) a precursor viscose rayon fiber, and (c) its cross-sectional shape, (d) highly twisted monofilament yarn, (e) self-coiled yarn, (f) self-plyed yarn, (g) manually-plyed yarn, (h) cabled yarn (twisting a number of plyed yarns).....	179
Figure 7-3. Fabrication and properties of TCPAs. (a) Maximum twist density of HT1 inserted in air and water, as a function of applied tensile stress. (b) Young's modulus of HT1 varying twist density (turns/cm). (c) Twist density (onset and complete of self-coiling) and spring index of (HTn)Co as a function of $\#nf$. (d) Tensile property of the (HT5)Co. The inset is a comparison of tensile property of the precursor fiber, HT1, and (HT5)Co. (e) Ply density and length of the n(HT1)mPly as a function of $\#nt$. (f) A comparison of the tensile property of the self-coiled yarn and the manually plyed yarn.	180
Figure 7-4. Torsional actuation of HT. (a) Cyclic change of RH (with minor variation of temperature, T) in the chamber for actuation. (b) Number of rotation ($\Delta N'$, reset) during untwisting and retwisting in each cycle. (c) Number of rotation ($\Delta N'$, accumulated) and rotational speed (ω) as a function of time. (d) $\Delta N'$ as a function of RH showing the actuation hysteresis and gradual untwist. The parameters of HT in this experiment is: $df = 21.7\mu\text{m}$, $Tt = 100\text{turn/cm}$, $\#nf = 1$, $lt = 10\text{cm}$	182
Figure 7-5. Torsional actuation of HT and HTsPly. (a, b) $\Delta N'$ of HT and HTsPly in a cyclic moisture actuation as a function of (a) time and (b) RH. (c) ΔN of untwist and retwist. (d) Comparison of torsional actuation performance with other moisture/water driven TCPAs. Triangle symbol (\blacktriangle) represents water actuation, and rectangle symbol (\blacksquare) represents moisture actuation. Unfilled symbol (\square) represents 2-ply yarn, solid-filled symbol (\blacksquare) represents single yarn, and pattern-filled symbol represents 10-ply yarn. The parameters of HT in this experiment is: $df = 21.7\mu\text{m}$, $Tt = 100\text{turn/cm}$, $\#nf = 1$, $lt = 10\text{cm}$. Two of such HTs are self-plyed to form the HTsPly studied here.....	185
Figure 7-6. Effect of fiber diameter and twist density on the torsional results of HTsPly. (a) Cross-sectional images of fibers with diameters of 14, 21.7, 25.1 μm . (b-d) Torsional actuation results of the HTsPly fabricated from fibers of three diameters with same twist density of 100 turn/cm. (e) Microscope images of HTsPlys fabricated from 21.7 μm fiber with different twist density, and (f-h) their torsional actuation results.	187

Figure 7-7. Effect of the number fibers ($\#nf$) and single yarns ($\#nt$) on the torsional results of HTsPly. (a) Microscope images of HTsPlys, and (b-d) their torsional actuation results. (e) Microscope images of HTsPly, and (f-h) their torsional actuation results. 189

Figure 7-8. Linear actuation results of (HTn)Co. (a) Microscope images of the (HTn)Co. (b) Linear strains of (HTn)Co made with different number of precursor fibers as a result of water and moisture. (c) Full (equilibrated) blocking force of selected (HTn)Co by continuous spray of water mist. (d) Blocking force of selected (HTn)Co by one-time spray of water mist. 191

Figure 7-9. (a) Drawing and twisting of CNT yarn from forest. (b) Microscope images of a CNT yarn plied with one and four HT1. (c) Schematic of electrothermal actuation setup. (d) IV curve of the CNT yarn. (e-f) Moisture actuation and (g-h) electrothermal actuation results of the CNT-plied yarn. (i) Microscope images of burned region of the yarn due to overheating. (j) Electrothermal actuation results of the burned yarn shown in (i). 193

Chapter 1 Introduction

Actuators are capable of converting physical or chemical forms of energy into motion. The conventional actuators, such as electrical motors and pneumatic actuators, produces tunable and accurate forces to power the movements of almost all the automatic devices. However, the bulkiness and rigidity of these actuators originating from the metallic parts and their complex assembly restrict their application in some of the emerging technology areas [1], [2], such as wearable devices including smart textiles [3]–[7], and electronic devices for human-machine interface [7], [8], and soft robotics [9]–[11]. To meet the needs in these and other similar applications, actuators made of lightweight soft materials (or soft actuators) with promising features including mechanical flexibility, wide range of contact compliance, and various choice of actuation stimuli are being developed.

Soft actuators are typically made of stimuli-responsive soft polymeric materials or their composites that can continuously and controllably deform to produce large strain and relatively small force (compare to conventional actuators). So far, most of the forms of energy such as electrical, thermal, chemical, pneumatic, and electromagnetic have been used to drive the soft actuators [12]. According to the type of input energy, these actuators can be categorized into electroactive (e.g., piezoelectric [13], dielectric [14], electrochemical [15]) polymer actuators, thermally (e.g., photothermal [16], electrothermal [17]) driven actuators, chemically (e.g., electrochemical [15], moisture [6], solvent [18]) driven actuators, pressurized (e.g., pneumatic [10], hydraulic [19]) soft actuators, and electromagnetic (e.g., magnetoelastic [11], light [20]) soft actuators. The diverse input energy types and availability of corresponding responsive materials for soft actuators demonstrate their future potential. Various fabrication techniques such as 3D printing [21] and thin film fabrication [22] have been used to effectively construct the soft actuators and integrate them into systems for different applications.

Soft actuators have the potential to revolutionize robotics, healthcare, human-assist devices, and many others. However, like most developing technologies, the opportunities come with many challenges. In addition to the materials related issues such as slower response and recovery, lack of precision, and fatigue, the structural integration of materials, controls, and power supply for soft actuators can be uniquely challenging. A diverse actuation behavior can be achieved by soft actuators using many structural form factors including fibers [23], films [14], and other arbitrary shapes [17]. Often multiple materials need to be fabricated into different functional components of the actuators and assembled at scales ranging from nanometers to meters. Challenges come from fabricating and assembling these structures with precision, mechanical integrity and repeatability. While these issues, primarily originating in handling and assembly of multiple unconventional materials with multistep process and DIY-style fabrication methods, novel scalable fabrication methods are needed. The development of additive manufacturing is promising to realize diverse and complex structures using multiple materials [24].

Many of the lessons learnt from the traditional human approach in designing most conventional actuators to meet the needs of producing strong, repetitive movement with precise position control using rigid materials cannot obviously be applied in designing soft actuators. In contrast valuable pertinent lessons could be learnt from studying the countless examples of actuation using mostly soft materials in the biological world [25], [26]. For example, animals use soft materials often supported by stiffer exoskeletons to produce exemplary fast and complex movements. In particular, muscle fibers as the natural actuator, are bundled together to produce tunable linear force that is then converted into the joint movement. It provides insightful lessons for the design of soft manmade actuators, from the structure design of slender muscle fiber with

linear contractile motion, muscle fiber assembly with mechanical integrity and scalable forces, to the muscle-bone connection with strong and reliable interfaces.

While one of the primary motivations to develop the soft actuators is the numerous current and future applications for the “human environment,” textiles, provide other valuable perspectives and potential solutions in the development of soft actuators. Textiles offer many soft and lightweight compatible materials, structural and topological optimization know-how, and processing technologies. From the materials point of view, many soft polymeric and non-polymeric materials can be processed by textile methods and fabricated into the products necessary in our daily life (i.e., ropes, clothes, carpets). From structural point of view, textile materials from fibers and films (typically coatings) to fabrics incorporate a wide range of structures and resultant mechanical features from micro to macro scales maybe useful for soft actuators. These textile elements are readily scalable and reliable under thousands of years of development and refinement. From integration point of view, textile products (i.e., fabrics and higher level) are indeed a hierarchical and functional assembly from fibers and yarns. Stimuli-responsive materials can be directly applied on or integrated into textile products [27]. Soft actuators can be incorporated into textiles at different hierarchical levels [4], [28]. From application point of view, many emerging areas such as human-machine interfaces [8], rehabilitation robotics [3], surgical and medical devices [29], and active thermo-regulative clothes [6], can be regarded as functional extensions of the conventional textile products.

The research described here focuses on the structural design of soft actuators for wearables, by exploring a variety type of soft actuators including the dielectric elastomer actuators (DEAs), moisture-driven film-based actuators, and multi-stimuli-driven twisted and coiled polymer actuators (TCPA). The rational of studying DEAs is primarily due to the fast actuation speed, large actuation strain, and relatively high control precision (compare to other

soft actuators). The film-based bistable DEAs investigated here are inspired by the bistable Venus flytrap (VFT) that is able to snap rapidly and maintain the deformed shape at no energetic cost. The compact bistable DEAs reversibly snaps between two stable shapes under applied high voltage and are proposed as an unconventional valve to control the openings on curved substrates. For wearable application, the high electric field poses potential health risks to the users, therefore, moisture-driven soft actuators are also investigated.

Moisture was selected as an appropriate stimulus due to the wide availability in the ambient environment, especially in the near-body environment, and regenerated cellulose was selected as the responsive material for its large swelling capacity and speed [30]. The commercially available regenerated cellulose film (i.e., cellophane) and yarn (i.e., viscose rayon) were selected for different structures. The cellophane actuators bend instantaneously and reversibly under the change of relative humidity (RH). They are structured into shape-programmable actuators and self-walking robots driven by moisture. The viscose rayon, on the other hand, were highly twisted into TCPAs that generate torsional and linear actuation motions under RH change. The TCPAs were fabricated into hierarchical structures, and their actuation performances were studied at different hierarchical levels. In addition to the moisture actuation, electrical actuation was enabled by twisting conductive carbon nanotube (CNT) yarns with the viscose rayon yarns, through the electrothermal-induced moisture desorption.

This dissertation is a collection of a number of research and review papers at various stages of publication. Each chapter represents one complete research paper. In particular, chapters 2 (under review), 3 (under review), and 4 (unpublished) are three review papers summarizing the diverse background of this research. Chapter 5 (accepted manuscript) is a research paper on the bioinspired bistable DEAs. Chapter 6 (unpublished) is a research paper of the moisture-driven cellophane actuators. Lastly, Chapter 7 (unpublished) is a research paper of

the multi-stimuli-driven viscose rayon TCPAs. The dissertation is appropriately bookended by two chapters, the Introduction and Conclusion.

References

- [1] “Soft Robotics Market | 2021 - 26 | Industry Share, Size, Growth - Mordor Intelligence.” <https://www.mordorintelligence.com/industry-reports/soft-robotics-market> (accessed Oct. 04, 2021).
- [2] G. Bao *et al.*, “Soft Robotics: Academic Insights and Perspectives Through Bibliometric Analysis,” *Soft Robot.*, vol. 5, no. 3, pp. 229–241, Jun. 2018, doi: 10.1089/soro.2017.0135.
- [3] H. K. Yap *et al.*, “A Fully Fabric-Based Bidirectional Soft Robotic Glove for Assistance and Rehabilitation of Hand Impaired Patients,” *IEEE Robot. Autom. Lett.*, vol. 2, no. 3, pp. 1383–1390, Jul. 2017, doi: 10.1109/LRA.2017.2669366.
- [4] T. L. Buckner, R. A. Bilodeau, S. Y. Kim, and R. Kramer-Bottiglio, “Robotizing fabric by integrating functional fibers,” *Proc. Natl. Acad. Sci.*, vol. 117, no. 41, pp. 25360–25369, Oct. 2020, doi: 10.1073/pnas.2006211117.
- [5] C. S. Haines, N. Li, G. M. Spinks, A. E. Aliev, J. Di, and R. H. Baughman, “New twist on artificial muscles,” *Proc. Natl. Acad. Sci.*, vol. 113, no. 42, pp. 11709–11716, Oct. 2016, doi: 10.1073/pnas.1605273113.
- [6] W. Wang *et al.*, “Harnessing the hygroscopic and biofluorescent behaviors of genetically tractable microbial cells to design biohybrid wearables,” *Sci. Adv.*, vol. 3, no. 5, p. e1601984, May 2017, doi: 10.1126/sciadv.1601984.
- [7] Y. Ding, M. Kim, S. Kuindersma, and C. J. Walsh, “Human-in-the-loop optimization of hip assistance with a soft exosuit during walking,” *Sci. Robot.*, vol. 3, no. 15, Feb. 2018, doi: 10.1126/scirobotics.aar5438.
- [8] J. Yin, R. Hinchet, H. Shea, and C. Majidi, “Wearable Soft Technologies for Haptic Sensing and Feedback,” *Adv. Funct. Mater.*, vol. n/a, no. n/a, p. 2007428, doi: <https://doi.org/10.1002/adfm.202007428>.
- [9] J. Hughes, U. Culha, F. Giardina, F. Guenther, A. Rosendo, and F. Iida, “Soft Manipulators and Grippers: A Review,” *Front. Robot. AI*, vol. 3, 2016, doi: 10.3389/frobt.2016.00069.
- [10] R. F. Shepherd *et al.*, “Multigait soft robot,” *Proc. Natl. Acad. Sci.*, vol. 108, no. 51, pp. 20400–20403, Dec. 2011, doi: 10.1073/pnas.1116564108.
- [11] W. Hu, G. Z. Lum, M. Mastrangeli, and M. Sitti, “Small-scale soft-bodied robot with multimodal locomotion,” *Nature*, vol. 554, no. 7690, pp. 81–85, Feb. 2018, doi: 10.1038/nature25443.
- [12] S. M. Mirvakili and I. W. Hunter, “Artificial Muscles: Mechanisms, Applications, and Challenges,” *Adv. Mater.*, vol. 30, no. 6, p. 1704407, 2018, doi: 10.1002/adma.201704407.
- [13] Y. Fu, E. C. Harvey, M. K. Ghantasala, and G. M. Spinks, “Design, fabrication and testing of piezoelectric polymer PVDF microactuators,” *Smart Mater. Struct.*, vol. 15, no. 1, pp. S141–S146, Dec. 2005, doi: 10.1088/0964-1726/15/1/023.
- [14] H. Shao, S. Wei, X. Jiang, D. P. Holmes, and T. K. Ghosh, “Bioinspired Electrically Activated Soft Bistable Actuators,” *Adv. Funct. Mater.*, vol. 28, no. 35, p. 1802999, Aug. 2018, doi: 10.1002/adfm.201802999.
- [15] J. Foroughi *et al.*, “Torsional Carbon Nanotube Artificial Muscles,” *Science*, p. 1211220, Oct. 2011, doi: 10.1126/science.1211220.
- [16] X. Zhang *et al.*, “Photoactuators and motors based on carbon nanotubes with selective chirality distributions,” *Nat. Commun.*, vol. 5, p. 2983, Jan. 2014, doi: 10.1038/ncomms3983.
- [17] A. Miriyev, K. Stack, and H. Lipson, “Soft material for soft actuators,” *Nat. Commun.*, vol. 8, no. 1, p. 596, Sep. 2017, doi: 10.1038/s41467-017-00685-3.

- [18] Q. Zhao, J. Heyda, J. Dzubiella, K. Täuber, J. W. C. Dunlop, and J. Yuan, “Sensing Solvents with Ultrasensitive Porous Poly(ionic liquid) Actuators,” *Adv. Mater.*, vol. 27, no. 18, pp. 2913–2917, May 2015, doi: 10.1002/adma.201500533.
- [19] S. Li, D. M. Vogt, D. Rus, and R. J. Wood, “Fluid-driven origami-inspired artificial muscles,” *Proc. Natl. Acad. Sci.*, vol. 114, no. 50, pp. 13132–13137, Dec. 2017, doi: 10.1073/pnas.1713450114.
- [20] K. Kumar *et al.*, “A chaotic self-oscillating sunlight-driven polymer actuator,” *Nat. Commun.*, vol. 7, p. 11975, Jul. 2016, doi: 10.1038/ncomms11975.
- [21] A. Zolfagharian, A. Z. Kouzani, S. Y. Khoo, A. A. A. Moghadam, I. Gibson, and A. Kaynak, “Evolution of 3D printed soft actuators,” *Sens. Actuators Phys.*, vol. 250, pp. 258–272, Oct. 2016, doi: 10.1016/j.sna.2016.09.028.
- [22] L. Ricotti and T. Fujie, “Thin polymeric films for building biohybrid microrobots,” *Bioinspir. Biomim.*, vol. 12, no. 2, p. 021001, Mar. 2017, doi: 10.1088/1748-3190/aa5e5f.
- [23] M. Kanik *et al.*, “Strain-programmable fiber-based artificial muscle,” *Science*, vol. 365, no. 6449, pp. 145–150, Jul. 2019, doi: 10.1126/science.aaw2502.
- [24] G. Stano and G. Percoco, “Additive manufacturing aimed to soft robots fabrication: A review,” *Extreme Mech. Lett.*, vol. 42, p. 101079, Jan. 2021, doi: 10.1016/j.eml.2020.101079.
- [25] M. H. Dickinson, C. T. Farley, R. J. Full, M. a. R. Koehl, R. Kram, and S. Lehman, “How Animals Move: An Integrative View,” *Science*, vol. 288, no. 5463, pp. 100–106, Apr. 2000, doi: 10.1126/science.288.5463.100.
- [26] K. Oliver, A. Seddon, and R. S. Trask, “Morphing in nature and beyond: a review of natural and synthetic shape-changing materials and mechanisms,” *J. Mater. Sci.*, vol. 51, no. 24, pp. 10663–10689, Dec. 2016, doi: 10.1007/s10853-016-0295-8.
- [27] A. Maziz, A. Concas, A. Khaldi, J. Stålhand, N.-K. Persson, and E. W. H. Jager, “Knitting and weaving artificial muscles,” *Sci. Adv.*, vol. 3, no. 1, p. e1600327, Jan. 2017, doi: 10.1126/sciadv.1600327.
- [28] J. Mu *et al.*, “Sheath-run artificial muscles,” p. 7, 2019.
- [29] M. Cianchetti *et al.*, “Soft Robotics Technologies to Address Shortcomings in Today’s Minimally Invasive Surgery: The STIFF-FLOP Approach,” *Soft Robot.*, vol. 1, no. 2, pp. 122–131, Jun. 2014, doi: 10.1089/soro.2014.0001.
- [30] A. J. Stamm, “Diffusion of Water into Uncoated Cellophane. I. From Rates of Water Vapor Adsorption, and Liquid Water Absorption,” *J. Phys. Chem.*, vol. 60, no. 1, pp. 76–82, Jan. 1956, doi: 10.1021/j150535a019.

Chapter 2 Bioinspired Structures for Soft Actuators

Biological organisms present marvelous morphing behaviors from the quiescent blooming of flowers to the energetic wing-flapping of birds that have always inspired humans to design better-engineered products. The diversity of natural motion is attributed primarily to the intricate and hierarchical structure of actuators that are self-assembled from nanoscale structures to superstructures with only a handful of materials. Compared to the biological actuators, their manmade counterparts, often with significantly limited capabilities, are fabricated from a wide variety of materials with relatively simple structures using limited fabrication techniques. With the rapid developments in various technologies that require soft robotics and human-machine interfaces, there is increasing demand for reliable soft actuators with improved capabilities such as larger output force, repeatability, and a more comprehensive range of motion diversity. Biological actuators provide critical insights into the structure-function relationship and offer exciting concepts to advance the science and technology of artificial soft actuators. Here, we discuss the design approaches found in natural actuation systems from the nanoscale to the highest levels in the structural hierarchy and the physical principles involved in their diverse actuation capabilities. In that context, finally, we review the fabrication techniques that have been utilized for manmade soft actuators, with a focus on the advantages, challenges, and concepts for potential future developments.

2.1 Introduction

The ability to move and morph is fundamental to the survival of animals and plants. The diversity of motion produced by biological actuators is key to the daily existence of natural organisms, from the autonomous beating of the heart for blood circulation to voluntary movement for hunting and escaping. Both plants and animals possess complex actuation systems

powered primarily by two types of elemental actuators, muscle cells for animals[1] and turgor-driven cells for plants[2], that convert biological energy into mechanical output. In addition to the actively controlled actuation behavior, plants also produce passive motions driven by the swelling and drying of cellulose materials on the cell walls under the ambient moisture change.[3] These cell-level actuators are shaped, assembled, and structured with other components in a hierarchical fashion, determining their macroscopic actuation performance. From the mechanical point of view, the actuation behaviors are governed by the stress and strain distribution at various levels of the structure composed of well-arranged active components and supportive matrices. The opening of a pinecone best manifests this principle to release seeds at low humidity conditions.[4] Composed of two macroscopic layers of tissues with different coefficients of hygroscopic swelling, the scales of pinecone bend outward as the outer layer shrinks more significantly under decreasing humidity. Interestingly, the swelling ability of the two layers is governed at the cellular level, as the distinct cellulose fibril arrangements on the cell walls effectively modify the stiffness of the cells.

While bioinspiration aims to reproduce a functional outcome by drawing on ideas from nature or through understanding the principles that underline natural processes, biomimicry aims to directly replicate the mechanism underlying the specific functional behavior found in nature. Notwithstanding the subtle distinction, understanding the fundamentals of biological functions allows us to appreciate why cells and organisms have the structures they do and provides clues to create synthetic systems. Natural structure design solutions have always been a source of inspiration for scientists and engineers to advance their fields, such as robust yet resilient mechanical structures^[5], biomimetic functional textiles^[6], dry adhesives^[7], drag reduction surfaces^[8], etc. Given that actuation is essential for almost all manmade machines to accomplish their designed functions, scientists are continually looking at every natural environment to find

inspiration and ideas to create the new generation of automaton soft robots that can stretch, flex, and morph with high degrees of freedom. Compared to the conventional rigid actuators such as electric motors, the soft actuators have mechanical properties and actuation behaviors closer to the natural actuators. Therefore, the lessons from nature, particularly the intimate relationship between the structures of natural actuators and their behaviors from cellular processes to whole organism functions, provide tremendous insights into designing soft actuators.

Soft actuators are key to emerging technologies and applications such as healthcare and wearable electronics that require a compliant human-machine interface for safety and robust adaptability. The inherent advantages of the often lightweight and compact soft actuators include being able to deform when necessary, safety in interaction with human and other delicate objects, availability of a wide range of materials and mechanical properties, quiescent operation, and use of various stimuli and thus energy inputs. With a variety of materials being employed to build soft actuators^[9], their structural design has been recognized as an essential determinant of performance. As the actuator converts a form of input energy into mechanical energy or motion, its structural mechanics is paramount for mechanical outcomes. For example, linear motors convert rotation with variable torque to linear motion with variable force through a series of structural components, whereas twisted and coiled polymer (TCP) yarns convert their radial expansion to rotation and linear motion depending primarily on their helical structure.^[10] The structure should be even more important in the soft actuators than conventional rigid actuators because of the large and diverse deformation of the soft materials. However, some inherent properties of soft materials such as nonlinear stress-strain relations, hysteresis, and large deformation impose challenges in developing reliable actuators with complex structures. For these and other reasons, the current forms of soft actuators remain relatively simple, and the

output forces and strokes are limited. Another constraint is the limited fabrication techniques. While materials grow and self-assemble into delicate and effective actuators under natural processes, the fabrication steps in engineering are either tedious or lack the ability to process soft materials. Recent developments in additive manufacturing and other techniques have facilitated the fabrication of more complex structures^[11], but issues remain. In this review, we discuss natural and human-engineered structural design approaches for soft actuators from low to high levels in the hierarchy with increasing complexity. We examine shared principles of structural mechanics and discuss their structure-function relationship. Subsequently, we review the fabrication techniques employed for soft actuators, albeit briefly, with a focused discussion on the advantages, challenges, and potential concepts for future development.

2.2 Biological Actuators

2.2.1 How Structures Impact the Actuation Behavior

Living organisms' movement and morphing ability rely on the actively deformable tissues, known as biological actuators. Two primary actuators of animals and plants are muscle cells and turgor-driven cells that aggregate to form structured actuators at higher levels.^[12] The fundamental actuation mode of these two cellular actuators is different, whereas the muscle cells contract or stiffen when activated, and turgor cells undergo volume expansion or shrinkage by autonomous or voluntary excitation. While these actuators are controlled actively by the nervous systems or signaling molecules and convert biochemical energy to mechanical output^[13], there are some instances in plants where the motion is entirely dependent on the passive deformation of hygroscopic materials at changing humidity.^[3] The active cell morphing and passive material deformation generate simple and microscopic mechanical output. Still, the delicate shape differentiation, directed material assembly, and architectural design of higher-level actuators are

ultimately responsible for a wide range of output forces and remarkably diversified motion within and across organisms.^[14] Therefore, understanding the structure-function relationship of biological actuators is essential for studying the diversity of motion.

Muscle tissues, as the motor for animal locomotion, are categorized into three types according to their functionalities: skeletal muscles, cardiac muscles, and smooth muscles.^[15] The structural differences at the cellular to the organ levels determine the actuation behavior and functionalities at different anatomical locations of the muscles. For example, at the cellular level, skeletal muscles and cardiac muscles have striated microscopic appearance due to overlapping of myofilaments that run parallel along the cell length. These repeating, overlapping parts, known as sarcomeres, are the structural and functional units that determine the mechanical output of these muscle cells. However, smooth muscle cells do not have a striate appearance due to different myofilaments arrangements. The loose myofilament arrangement results in slower smooth muscle contraction than the striated muscles.^[16]

The difference in cellular shape and cell aggregation patterns significantly affect the actuation performance, synchronization, and control. Skeletal muscle cells are long fibers that are bundled together with the two ends connected to tendon tissues. Each fiber runs through the whole length of the muscle and is controlled individually by a motor neuron. Therefore, the output force of a muscle can be increased by activating more muscle fibers. Cardiac muscle cells, on the other hand, are branched and connected with gap junctions providing pathways among cells for shared electrical signaling. These unique structures and assembly enable coordinated contraction of the cardiac muscles to power the heart efficiently.^[15] Smooth muscle cells are relatively short and spindle-shaped and have a wide degree of electrical coupling between cells via gap junctions.^[16]

At the organ level, the structural design determines the ultimate macroscopic motion. Skeletal muscles are attached to bones that convert muscle contraction to joint movement. To achieve both high output stress and strain, the attachment point at the fixed bone is away from the rotational joint, while the one at the rotating bone is close to the joint. Cardiac muscles form the contractile wall of the heart, which contracts synchronously to pump the blood from the cardiac chambers. Smooth muscles line the wall of hollow organs such as blood vessels and provide involuntary actuation for activities such as persistent contraction of blood vessels and peristaltic movements of intestines.^[16]

Many animals and plants utilize the structure-function relationship uniquely and display extreme performances. For example, caterpillars can perform flexible motions such as curling, rolling, and even jumping for normal and enhanced locomotion. The muscles arranged peripherally around the cylindrical body of the caterpillar enable deformation with multiple degrees of freedom by coordinated actuation of muscles.^[17] Another interesting example is the potent strike of Mantis shrimp amplified by a bistable element in its smashing appendage. This extensible bistable disk-like element made of stiff materials acts as a power amplifier to boost the striking force and speed beyond the capability of the muscle. In particular, the bistable disk stores the elastic energy from muscle contraction in its bent shape and suddenly snaps to release the energy in a short time for a burst power output.^[18] The power amplification strategies through the elastic energy storage and recoil that allow animals to generate motions beyond their physiological limits are also utilized in plants to produce fast motion.^[19] For example, the bistable leaf of the Venus flytrap (VFT) has the fastest morphing speed in the botanical world, which closes within 0.1 seconds to capture the prey.^[20] Another similar example can be found in the dispersal of

spores in plants for successful reproduction. Fern spores disperse seeds extremely fast and far by coupling hydrodynamic cavitation and elastic energy relaxation.^[21]

2.2.2 Hierarchical Structures of Biological Actuators

The hierarchical assembly of active and passive materials into well-arranged structures is fundamental to the diversified motions in nature. To better understand the relationship between their structure and actuation behavior, we herein classify the biological actuators into three hierarchical levels, i.e., cellular level (1st), tissue level (2nd), and organ level (3rd). We intend to offer a comprehensive picture of the biological actuators' hierarchical design and their performance by discussing the structure-function relationship at different levels. As a result, we derive essential design guidance for the manmade soft actuators.

To begin with, we present two examples of the macroscopic actuation behavior, illustrating the common structural design principles in animals and plants. The first example is the human elbow, where the elbow-arm system (**Figure 2-1c**) can be regarded as the ultimate actuator that interacts with the external world. In this design hierarchy, the 1st order actuator is the skeletal muscle cells. As is shown in Figure 2-1a, three types of muscle cells provide fundamental functionality for all the movements of animals. Briefly, the skeletal muscles exert forces on the skeleton system that interacts with the external world.^[22] The cardiac muscles actuate rhythmically to generate the heartbeats, and smooth muscles contract slowly and involuntarily to transport food in the intestines. The 2nd level actuator (Figure 2-1b) is the bundled skeletal muscle that aggregates the micro-level forces for useful mechanical output. The skeletal muscles are connected to bones (end effector) with tendon linkages (damper). Each skeletal muscle is composed of grouped muscle fibers (cellular actuators), nerve cells (signal transmitter), blood

vessels (energy transmitter), and intracellular matrix (support, tethering). To produce the required macroscopic motion – rotation of the elbow in this case – in the 3rd order of the hierarchy, the actuator design utilizes a pair of antagonistic muscles to control the elbow's directional rotation and force output. A basic lever arm principle is employed in the design of the 3rd order actuator for work and space efficiency and for avoiding injury due to over-straining of the muscles.^[22] Skeletal muscle is connected to the two bones of the elbow-arms system in a particular manner, where one end of the muscle is linked to the far end of the stationary bone, and the other end of the muscle is connected to the near end of the dynamic bone. This design ensures both adequate rotational angle and torque with the limited contractile strain of the muscles.

The second relevant example is a nyctinastic plant that opens and closes leaves with circadian rhythm (Figure 2-1f). The turgor-driven cells in these plants are the 1st level actuator that changes volume under osmotic pressure, known as turgor pressure. The turgor pressure is controlled by modulating the cell membrane permeability of certain solutes to create a difference between the concentration inside and outside of the cell, thereby driving the water flow. Their arrangement boosts the microscopic actuation of turgor cells into tissue-level actuators. To further functionalize the actuation to bend the leaves, antagonistically aggregated turgor cells are concentrated near the hinge of the leaf, similar to the antagonistic muscle arrangement for the rotation of elbow. The extensor and flexor cell aggregates at the inner and outer side of the hinge at the base of a nyctinastic leaf, as seen in the cross-sectional view in Figure 2-1e, are responsible for the bending and unbending of the leaf. Driven by this hierarchically designed structure, the double-leaf pair of nyctinastic plants opens in the daytime and closes at night^[23]

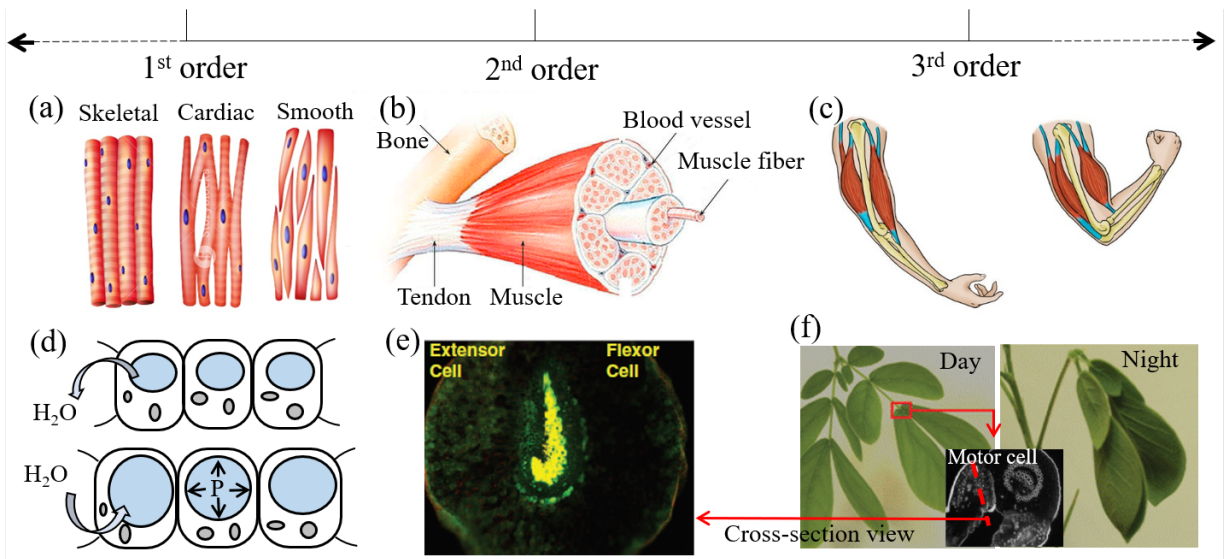


Figure 2-1. The hierarchical structural design of natural actuators. Two examples of antagonistic actuation of (a-c) an elbow, and, (d-f) plant leaves driven by actuators organized at three hierarchical levels. (e,f) Reproduced with permission.^[23] Copyright 2007, Oxford University Press.

The following section uses simplified actuator models to illustrate the 1st and 2nd level structural designs and resultant deformations. The 3rd level actuator is presented with examples of the final actuation performance of various biological organisms.

First level structure

Muscle cells and turgor-driven cells are primary actuators fundamental to the motion of animals and plants, and we define them here as the first (1st) level actuators. Under electric pulses, muscle cells either contract in length or stiffen to resist deformation. In contrast, turgor cells expand in volume due to the osmotic influx of water due to higher concentrations of certain solutes inside them than in the extracellular environment. Besides active actuation, passive actuation is commonly observed in plants as dead cells de-swell in a low-humidity environment.

The difference among the 1st level actuator can be 1) whether the cell volume changes upon actuation, 2) in the shape of the actuator, and 3) in the presence of mechanical reinforcement in

cell walls for anisotropic properties. The schematics presented in **Figure 2-2a, b** show the expansive and constant volume actuators' shape differences. The internal pressure increase of turgor-driven cells results in a significant volume expansion (Figure 2-2a)^[24], while the contraction of muscles cells causes negligible volume change (Figure 2-2b).^[25] In conifer plants, the horizontal and upright growth of the branch is a result of compressional stresses developed in the tracheids (a type of cell with a thickened cell wall) near the stems.^[26] These compressional tracheids are cylindrical in shape compared to the rectangular normal wood tracheids. In addition to that, another key difference of these two tracheids is the orientation of cellulose fibrils on their cell walls. Cellulose fibrils improve the mechanical strength of the cell, and the directional alignment of these fibrils creates mechanical anisotropy that leads to diverse actuation behaviors (Figure 2-2i, ii, iii).^[27] On the other hand, the skeletal muscle cells always take slender shapes for optimized longitudinal contraction and bundle organization, and the subcellular myofilaments are aligned along the cell length direction to generate cell contraction by filament sliding.^[1]

The presence of mechanical anisotropy by utilizing reinforcing elements, the cellulose fibrils on the cell wall, to produce directional actuation is common in plants. For example, conifers exploit the helically wound cellulose fibrils on the cell wall to generate tensile and compressive stresses to guide its organ's growing direction.^[26] The wheat awns utilize the periodic humidity change to propel the seeds after detaching from the wheat plants. The locomotion originates from the bending of the awns through the differential swelling of the cells in the inner and outer parts due to the distinct microfibril arrangement on the cell walls. Elbaum et al analyzed the microscopic structure and material composition of wheat awns. They found no compositional or structural difference of the inner and outer parts of the awns above the cellular level. However, the mechanical analysis suggested significant mechanical difference between the cap and the ridge

(two parts that run parallel along the length of the awn). Using x-ray scattering they found that the cellulose fibril angle in the cell wall, along the cell length determines the mechanical difference and the overall actuation behavior. While the cells on one side of the awn are mechanically strengthened with aligned cellulose fibrils at a small angle, the cells on the other side are less stiff due to the randomly arranged fibrils that tend to absorb moisture and swell; as a consequence, the awn bends periodically at changing humidity.^[28]

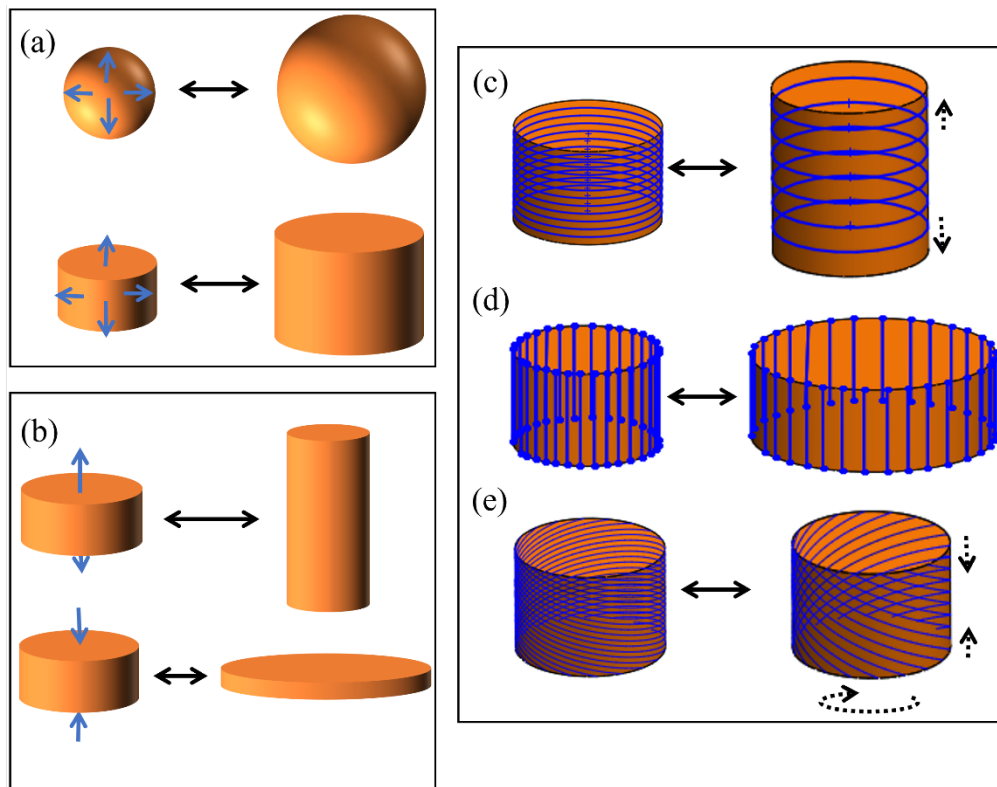


Figure 2-2. Actuator's 1st level structural design. (a) Volume expansion of actuators of different shapes due to increased internal pressure. (b) Extension and contraction of actuators with constant volume. (c-e) Different actuation behaviors due to the orientation of reinforcing fibers. The orange parts are the active bodies, and the blue lines are the mechanical reinforcing elements. The blue arrows are the directions of the generated stress under stimuli, the black arrows are the directions of the actuation deformation.

Second level structure

The cell actuators are organized into tissue-level actuators with the help of other elements such as the extracellular matrix, nerves, and blood vessels. These elements serve multiple purposes,

including structural support, force integration, functionalization, and pathways of control and energy supply. The tissue actuators produce scalable forces by bundling and selective activation of constituent cell actuators. Their functionalities can be differentiated by various factors, such as the arrangement of cellular actuators, properties of connective materials, and arrangement of signal emitters, etc.

Despite the complexity of the architecture and signal transduction in tissue actuators, we can simplify the structural models to fit the general morphing types, such as bending, twisting, wrinkling, folding, etc. The mechanism of the variety of motions originates from the varying strain field in the structure produced by altering the amplitude of stimuli and differential mechanical properties, with the latter resulting from the assembly of active and passive components. Some of the deformation patterns of the second (2nd) level actuators are illustrated in **Figure 2-3**, with the orange and blue parts representing active (1st level actuator) and passive elements, respectively.

Figure 2-3a-c illustrate three out-of-plane deformation types (cylindrical bend, twist, and saddle) of a homogeneous and isotropic film under various stimuli gradients. When the stimulus is imposed from the top in a manner such as to induce in-plane expansion of the top surface of the film, and the expansion direction coincides with one of the principal geometrical axes, the film bends downward (Figure 2-3a). Here, the direction of expansion is determined by the geometrical parameters and the anisotropic mechanical properties of the material. When the direction of expansion is not aligned with one of the principal geometrical axes, the film twists into a helix (Figure 2-3b). When the in-plane expansion of the film occurs on both top and bottom surfaces in different directions, the film tends to deform into a saddle shape (Figure

2-3c). This model may explain the bending and wrinkling of leaves at changing humidity. In contrast, the veins and other microscopic structures in the leaves complicate the mechanical properties and influence the shape.

The out-of-plane deformations more commonly result from mechanical anisotropy, often by means of fiber reinforcement and mechanical gradients in laminated structures. Figure 2-3d-f show the laminate structures with various potential out-of-plane deformations including bending and wrinkling. By laminating two layers (active and passive), the in-plane strain in the active layer exerts a bending moment in the laminate, producing the bending or wrinkling. In trilayer laminates, on the other hand, the combination of directional strains in the top and bottom layers can produce bistable structures, as shown in Figure 2-3f.^[29] One approach is to introduce predetermined directional strains to the laminates by prestretching before laminating, which have been used to fabricate bistable cylindrical structures.^[29] By changing the strain field of the laminate mechanically^[30] or electrically^[31], the bistable structures snap from one stable state to the other.

Examples of further control of the deformed shape of films by limiting the spatial range of the active layer for strain localization can be seen in Figure 2-3g-h. Here, the width of the active part is significantly reduced to that of a hinge that works to fold the laminates. Meanwhile, the self-folding is facilitated by increasing the mechanical flexibility of the hinge on the supportive layer. This model is commonly used in wing structures such as the active deployment of earwigs^[32] and leaf folding^[23].

While the uniform distribution of the volume expansive elements in a passive matrix results in the overall volume expansion, the arrangement and shaping of the active elements give rise to the diversity of morphing. Figure 2-3i-j present typical arrangements of active elements in a passive structure. For example, in plants, the turgor-driven cells are embedded in the supportive matrix to change the volume of the whole structure, and the muscle fibers in animals are concentrically distributed in the matrix that selectively contracts to bend a larger structure in multiple directions. An example of multidirectional bending is the movement of caterpillars that use their peripherally distributed muscles to bend their bodies with multiple degrees of freedom (DOF). Besides, their longitudinally sectioned muscles generate contraction and relaxation waves along the body to push the body to move forward and backward.^[33,34]

Structuring the supportive and active elements to produce different motions is an interesting topic. Here we see another simple but powerful example – twisting actuation, using several compelling structural features. Figure 2-3k illustrates a typical design for torsional deformation of plant cells through winding cellulose fibrils around the isotropic volume-changing cell body. The cellulose fibrils restrain the deformation along its winding direction, converting the volume expansion of the cells to torsional deformation. Another method to produce twisting motion is shown in Figure 2-3l. Here, instead of winding the stiff fibers about an active body, the fibers are twisted about their own axis and then embedded in an isotropic active body. While the stimuli-responsive matrix expand in volume, the twisted fiber-active matrix complex tends to rotate if only fixed at one end, or change in length if rotation is restricted. The third method to generate twisting actuation is a differential strain in a slender object (Figure 2-3m). In a slender structure such as fibers, the differential strain can produce spring-like structures with reverse handedness, while the fibers are allowed for linear contraction but not rotation.^[35] Such spring-like structure

can be further actuated for linear or torsional deformation by differential expansion or contraction of the inner and outer part of the spring. One such example in nature is the helical growth of tendrils of cucumbers and their motion with changing humidity. The asymmetric swelling and asymmetric mechanical properties of the tendrils of cucumbers were found to be the driving forces for the helical coiling and over-winding under stretch.^[36]

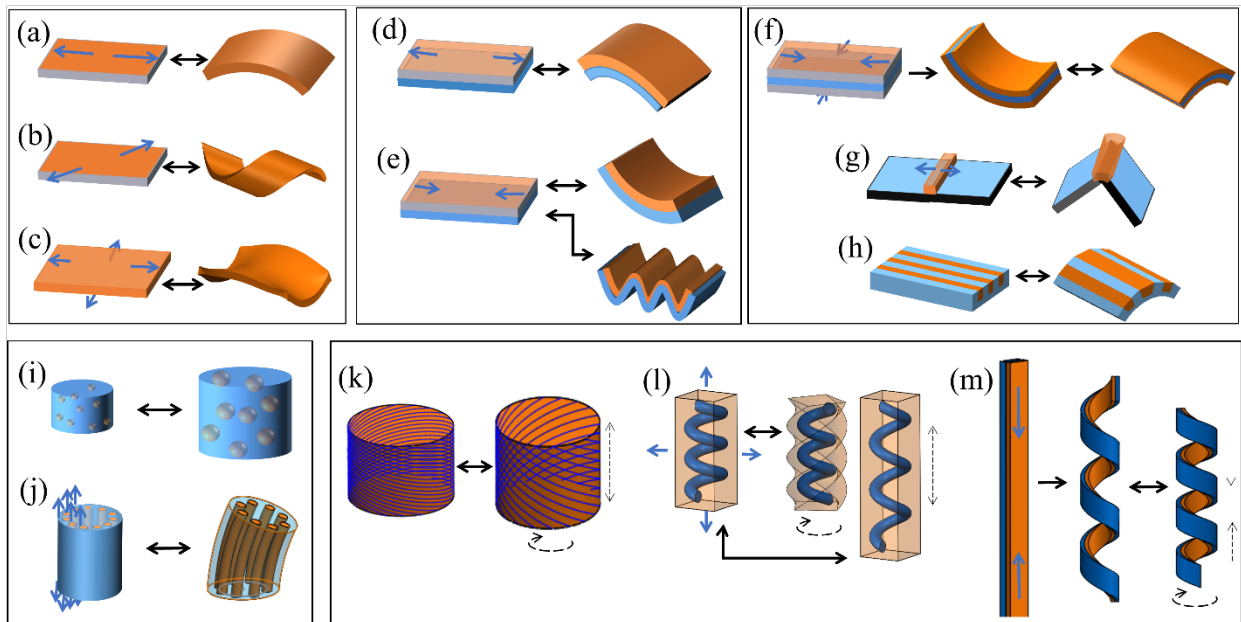


Figure 2-3. Actuator's 2nd level structural design. (a-c) Film bending under gradient stimuli exposure. (d-e) Bending and wrinkling of laminates composed of active and passive layers. (f) Bistable laminates composed of active layers and a strain-limiting layer. (g-h) folding of a film due to concentrated stress at the hinge. (i-j) volume expansion and bending of 3D structures due to encapsulated active materials in flexible and passive matrices. (k-m) twisting deformation of structures due to, (k) helically wound inextensible fiber around an expansive cylindrical body, (l) twisted fiber embedded in an expansive body, and (m) the differential strain developed in a bilayered helical structure. Orange parts are active materials, and blue parts are passive materials. Blue arrows are directions of active stresses, and the dotted black arrows are deformation directions of the actuator.

Third level structure

While in general, the cells combine to make tissues, at even higher levels of hierarchy, the tissues form organs. Therefore, the ultimate macroscopic motions to achieve specific functionalities require higher-level structural design and synergistic activation of lower-level

actuators. Here we classify the organ (e.g., heart, etc.) as the actuator responsible for the final movement as the 3rd level actuator. Regarding structural design, the third (3rd) level actuators share many similarities with the 2nd level actuators if we consider the basic motions such as contraction, bending, twisting, etc. Interestingly, these basic motions combine to yield vastly diversified complex motions, including locomotion of natural species.

The contraction and relaxation of muscles, for example, are responsible for all the complex motions and postures of animals through the 3rd level of structural design. The smooth muscles shorten to decrease the diameter of the arteries, or isometrically contract to maintain the shape of the arteries under blood pressure by adhering circumferentially to their wall.^[37,38] In small intestines, two layers of smooth muscles aligned longitudinally and circumferentially produce length and diameter changes of intestines for peristaltic transport of food.^[39] For walking, jumping, and lifting, antagonistic muscle pairs are connected to the bones with elastic tendons for acceleration, deceleration, and stabilization.

The power amplification to produce extremely large forces or speed for a burst performance needed by animals and even plants during escaping and hunting is achieved using the fundamental principle of storage and rapid release of elastic strain energy. Elastic energy is stored in soft tissues, such as the chameleon's tongue before projection (**Figure 2-4c**)^[40], frog's ankle tendons before jumping (Figure 2-4a)^[41], larvae's roll-up body before jumping (Figure 2-4d)^[42], and suddenly released to produce large power beyond the capability of muscles. For example, the Fern sporangia generate elastic energy by bending the annulus (row of cells) under decreasing humidity. The energy is rapidly released by cavitation that leads to a catapult of spores (Figure 2-4b).^[21] Increasing the spring constant of a biological spring while maintaining

the elastic flexibility further promotes the power output. A superb example is the deadly strike of the Mantis shrimp, whose elastic tissues for strike assistance are partially mineralized that help deliver a time-averaged power density of 2700W kg^{-1} muscle.^[43] In comparison, the power output of the frog during jumping (800W kg^{-1})^[44] and the chameleon's tongue during projection (2000W kg^{-1})^[45] are relatively lower due to the energy storage in soft tissues. Bistable structures provide another energy storage approach featuring an intrinsic energy barrier and release of elastic energy upon appropriate stimulation. The mantis shrimp and VFT utilize bistable elements to amplify the power output (Figure 2-4e).^[46] VFT, known as one of the fastest among plants with a leaf closure time of 100 milliseconds, configures its leaves in a bistable-curved shape. Once mechanically triggered, the water influx in the motor cells drives the snap-bucking instability followed by rapid leaf closure.^[20]

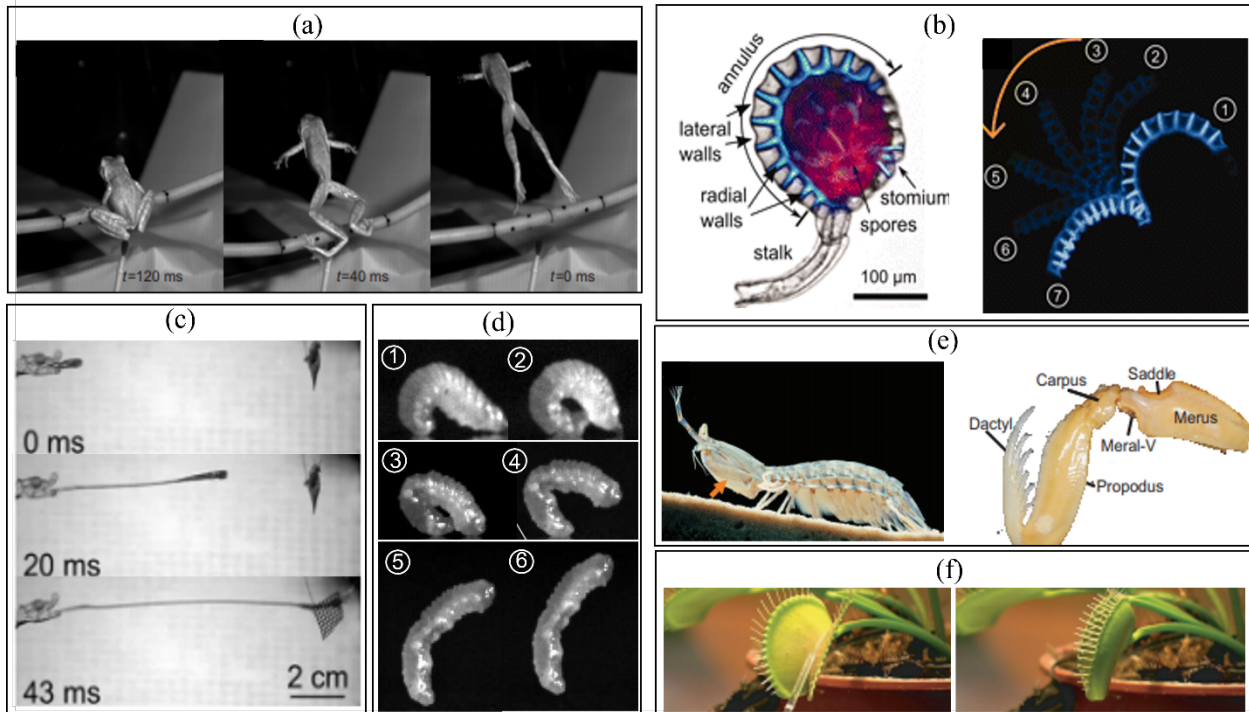


Figure 2-4. Power amplification motion of biological organisms. (a) Frog jumping. (b) The structure of Fern sporangium and the rapid bending of its annulus for pore projection. (c) Tongue projection of chameleon during hunting. (d) Curling of larvae to store elastic energy for jumping. (e) Mantis shrimp and its predating appendage components. (f) Bistable leaves of VFT. (a) Reproduced by permission.^[41] Copyright 2015, COMPANY OF BIOLOGISTS LTD. (b) Reproduced with permission.^[21] Copyright 2012, American Association for the Advancement of Science. (c) Reproduced with permission^[40] under CC-BY license. (d) Reproduced with permission.^[42] Copyright 2019, COMPANY OF BIOLOGISTS LTD. (e) Reproduced with permission.^[43] Copyright 2009, COMPANY OF BIOLOGISTS LTD. (f) Reproduced with permission.^[20] Copyright 2005, Springer Nature.

In summary, it is important to learn how the natural actuators generate a wide range of force, power, and strain with limited capability of elemental actuators through the hierarchical structural design and material assembly. The remarkable examples elucidating this phenomenon have been discussed in this section by grouping the actuators in three hierarchical categories. The natural muscles clearly illustrate the diversified motions through their hierarchical structural design. Animal muscles can produce stresses (isometric) up to 30 Ncm^{-2} , determined intrinsically by the volume density of myofilaments and muscle size^[47], and strains up to 20%^[48] that may help avoid damage. Muscle cells are grouped and arranged in a supportive matrix to transform a

small mechanical output into a large force. More flexibility is introduced by selective activation of actuator groups, organization, and alignment of lower-level actuators, mechanical assistance, and confinement of supportive elements. Secondary to the ordinary movements, nature also uses various methods to amplify the output forces and speeds by storing elastic energy in the muscles, tendons, or by using bistability. The structure-function relationship in the actuation to produce biological motion can provide remarkable insight and inspiration for the design and improvement of soft manmade actuators.

2.3 Manmade Soft Actuators

2.3.1 The Design Process for Soft Actuators

In general, the design steps for soft actuators include choices of the stimulus/energy input and responsive material followed by structural design and, in the end, system integration, as illustrated in **Figure 2-5a**. The stimulus/energy is the driving force to power the actuators. Almost all forms of stimuli (e.g., electrical, magnetic, electromagnetic, thermal, chemical, etc.), as well as materials (polymers, papers, carbon, etc.), have been explored for soft actuators. The choices are often driven by the material's sensitivity to the stimulus and other system constraints (and/or application requirements). Besides the material and stimuli, the distinguishing characteristics of the soft actuators can be in their structural design and/or geometrical configurations.

In terms of the input energy, its amplitude, gradient, and power (speed) are important for the actuation performance. For example, in the case of the dielectric elastomers (DE), the energy amplitude is the applied electrical potential (voltage) that produces Maxwell stress (σ) to compress the DE film, but the energy gradient, electric field (E), determines the amplitude of

stress acting on the film ($\sigma = \frac{1}{2} \epsilon_0 \epsilon_r E^2$). Therefore, one approach to increase the actuation strain of the DE actuator (DEA) is to increase the electric field by reducing the thickness of the DE. Other important aspects in the input energy selection are the precision, reliability, and flexibility of the input control. For example, the electrical and pneumatic energy types are relatively easily controlled, modulated, and implemented compared to the thermal energy that is slow and less accurate in application. Moreover, some stimuli can be applied remotely, while others need to be connected to bulky hardware.

While the selections of input energy and material are interdependent, the intrinsic properties of the materials define their response. These properties include thermal (phase change, etc.), sorptive (moisture response, etc.), electrical (conductivity, etc.), electro-magnetic (polarizability, etc.), photosensitivity (photothermal, etc.), and mechanical properties (Young's modulus, etc.). Some of these properties can be tuned by introducing functional groups that react to different stimuli^[49], by formulating composites to enhance performance^[50-52], and by tuning the mechanical properties to vary the output strain^[53].

Once the material and stimulant are chosen, the next step is to assemble the materials into functional structures to scale, direct, and distribute the force and displacement. Additional considerations are stability, integrity, reliability, and repeatability of the actuator performance. Structures from nanoscales to macroscales are created by using fabrication techniques such as self-assembly and 3D printing in order to achieve the desired performance. Soft actuators based on LCEs^[54] and pneumatic channels^[55] are exemplars of nanoscale and microscale structures, respectively. There is a tremendous variety of structures used for soft actuators, such as layered structures for out-of-plane deformation, stacked structures for higher force output, anisotropic structures for directional deformation, tubular structures for multiple bending directions, origami

structures for folding and deployment, and structures with snap-through instability for a burst of power output. Simulation tools (i.e., ANSYS, ABAQUS, COMSOL) are useful to build virtual actuators with necessary parameters to help provide insight into the relationship between material as well as structural parameters and performance.

The fabrication methods used for soft actuators include processes such as molding^[56], 3D printing^[57], self-assembly^[54], and inkjet printing^[58]. These offer varying levels of spatial resolution, the capability of multiple material assemblies, alignment, and optimization^[59].

Finally, the integration of multiple components of the actuator system is performed for trigger and control. Among many considerations at this stage are energy input, control, deployment environment, interconnects, sensing and feedback, signal processing, and communication.

To illustrate the four design steps of soft actuators, as well as the opportunities and challenges of the bioinspiration in soft actuators, here we examine a natural^[4,60], and a manmade^[61] actuator with a similar working principle (Figure 2-5b, c). Constructed from hygroscopic materials, these two actuators are responsive to the environmental moisture gradient. They form bilayer structures with different swelling characteristics of each layer that leads to the bending motions. The resultant bending actuators are incorporated into higher-level systems for different applications, i.e., plant seed dispersal and textile thermal management. In particular, the natural actuator in the form of the scales of pinecone (Figure 2-5b) are composed of two layers of assembly of mature cells differentiated by the winding angle (angle between the length of fibril and cell directions) of the cellulose fibrils in the cell walls^[4]. These reinforcing fibrils restrict cell elongation when winding at a small angle and allow cell elongation when winding at a large angle. As a result, the differential expansion of the cells in two layers leads to the bending of the scales upon humidity change. As a result, the decrease in environmental humidity induces the

opening of the pinecone scales and thus releasing the seeds. The manmade moisture-driven bilayered actuator is designed to perform similarly (Figure 2-5c)^[61]. Moisture-responsive materials (biological cells or extracellular matrix materials) are printed on a moisture-insensitive layer to form the bilayer bending structure. The differential swelling of the two layers results the bending motion. By integrating them into apparels, the moisture-induced bending motion results in opening of the pores on the clothing and thus increasing the air flow. A thermo-regulative smart apparel with autonomous tuning of air flow can be produced.

Bioinspiration can potentially play an important role in the design of soft actuators. In a way, they can be described as the manmade counterparts of the biological actuators. Soft actuators built from compliant materials are “designed” for mechanical resilience and active deformation to generate stresses and strains to power the movements necessary for locomotion, grasping, and lifting. Functionally, the performance characteristics of biological actuators that power the plants and animals are also desired in manmade actuators for the same reasons, that is, to do mechanical work while providing the needed movements. Therefore, the actuation mechanisms found in nature are excellent exemplars of designing soft artificial actuators^[12,62]. So far, the structural features of the pinecone, wheat awn, VFT, and others and their morphing behavior have inspired the design of manmade soft actuators capable of producing various motions^[3,12]. With simplified structures, the manmade soft actuators can potentially perform similarly or even better than the natural actuators in some of the essential characteristics. However, due to the limited fabrication techniques, there are still challenges in mimicking some natural structural features. Fabrication of structures with mechanical gradient and hierarchy might enable artificial soft actuators with an all-around performance, including the mechanical (e.g., strength and flexibility) and actuation performance (e.g., stress and strain).

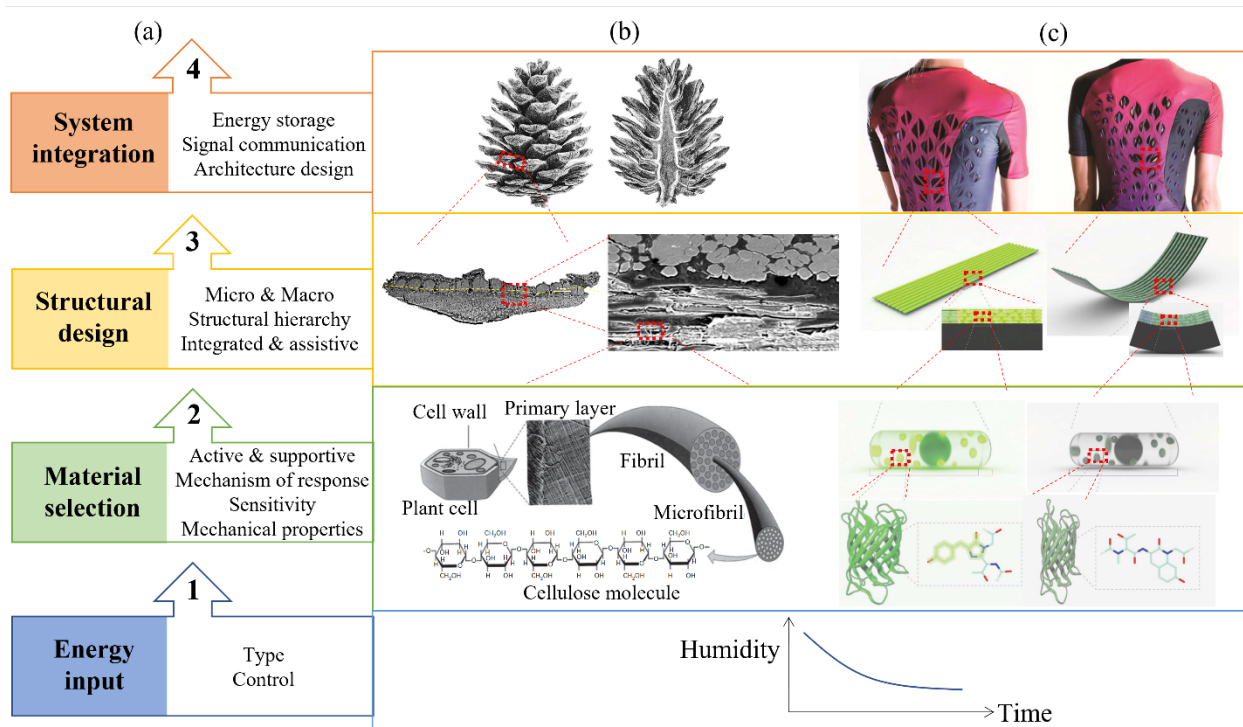


Figure 2-5. Design processes for soft actuators. (a) Steps in the design process, of (b) a natural actuator (pinecone), and (c) an inspired manmade actuator (moisture-sensitive textile actuator). From the choice of stimulus (from the bottom) to the selection of the stimuli (moisture)-responsive materials followed by arrangement of materials into bilayered structures to the integration of bilayered bending actuators into the higher-level system. (b) Reproduced with permission^[60] under CC-BY license. (c) Reproduced with permission.^[61] Copyright 2017, American Association for the Advancement of Science.

2.3.2 Structural Design of Soft Actuators

2.3.2.1 Linear motion

Linear motion (contraction and extension) is fundamental to the morphing ability of almost any actuator and is commonly employed by lower-level biological actuators (e.g., muscle cells) and manmade actuators (e.g., linear motors and McKibben muscles) to produce directional force-displacement. The linear motion can be used, for example in, robotic arms^[63], and the tubular/fiber-shaped linear actuators^[64,65] can be assembled in smart textiles^[66] as well as healthcare devices^[67]. Linear actuation parameters, including but not limited to the tensile strain (%) (also known as tensile stroke), tensile stress (MPa), strain rate (%/s), bandwidth (Hz),

specific work output (kJ/kg), and energy efficiency (%) are relatively easy to quantify. Mirvakili et al. have provided a detailed discussion on the performance parameters of a wide range of these actuators.^[9]

While the development of smart materials such as shape memory polymers and dielectric elastomers have demonstrated superior actuation performance by some measures compared to that of biological muscles^[68], the optimal structural design of these actuators can further improve their performance. Here we discuss the structural design principles of soft linear actuators together with the challenges and opportunities. The examples of linear actuators discussed here include capacitive actuators with a particular focus on stacked DEAs^[69], pneumatic/hydraulic tubular actuators with fiber reinforcement^[70] and buckling structures^[71], thermo-responsive polymer fibers^[72,73], and TCP actuators^[66,74].

Capacitive linear actuators

Linear actuators are designed to produce linear displacement resulting in unidirectional stress or strain. Electrostatic stress in a parallel capacitor is unidirectional, instantaneous, precisely controlled, and if large enough, it is able to compress an elastomeric film. Since the discovery of the deformation of rubber in an electric field in 1880^[75], the dielectric elastomer (DE) actuators have been investigated and have attracted tremendous attention due to their large actuation strain under a high electric field^[76]. In brief, when a DE film is sandwiched between a pair of compliant electrodes and a sufficiently large electric field is applied, the film experiences thickness compression and area expansion as a result of Maxwell stress and electrostrictive stress.^[77] Depending on the elastic nature of DE almost full and fast shape recovery after electrical discharge is possible.

Both thickness and areal strains in DEs have been utilized to design linear actuators. The displacement in the thickness direction is typically amplified by stacking multiple DE actuator layers connected electrically in parallel to respond in unison. The resulting total linear displacement is the sum of each DE layer's thickness strain (**Figure 2-6a**). Various fabrication methods have been proposed (Figure 2-6a, b, c) for the stack actuators. The first generation of stack actuators was fabricated by spin-coating individual DE film layer by layer with mask printed electrodes.^[78,79] However, this method requires great laminating precision for appropriate electrode placement. In a subsequent improvement, the folded DE actuators were fabricated by folding only one DE layer with a pair of electrodes placed on its two surfaces (Figure 2-6b).^[69] Yet another method of stacking a linear DE actuator was proposed by cutting thin helices from an elastic tube and placing the electrodes on either side of the helical film (Figure 2-6c).^[80]

The areal expansion of DE is utilized to make linear actuators by configuring the DE into tubular structures. A hollow elastomeric fiber fabricated like a cylindrical capacitor in Figure 2-6d shows the elongation as well as radial expansion when actuated with an electric field. By applying prestrains, uniaxially or uniformly (through inflation), the actuation strains in length and radial directions were tuned due to the prestrain-induced mechanical anisotropy.^[65] Figure 2-6e presents the rolled DE actuator that converts the biaxial actuation strain to uniaxial force output, as the radial strain is further restricted by the adhesion and friction between layers.^[81] In other approaches to direct the uniform areal strain in the length direction, a biaxially pre-stretched DE film is wrapped around a compressed helical spring to form a spring roll configuration. Once the film is secured at the ends, the areal expansion due to activation of the film results in linear expansion of the roll, see Figure 2-6f.^[82,83]

While efforts have been underway to improve the actuation performance of DEs, along several directions, including increasing the permittivity, tuning the elastic modulus for higher strain or stress, and reducing the thickness, a new type of electrostatic actuators, called hydraulically amplified self-healing electrostatic (HASEL) actuators, shows great promise.^[84] In a HASEL actuator, a liquid dielectric medium is enveloped by a thin elastomeric shell replacing the traditional monolithic DE, to provide much higher output forces, see Figure 2-6g, i. When a voltage is applied, the active area is compressed in the thickness direction, driving the liquid dielectric to the inactive area and forming, in this instance, a donut shape (Figure 2-6i). The pull-in instability, which is fatal to traditional DE films is utilized here to greatly enhance the actuation strain and speed (Figure 2-6h). Further, by stacking the HASEL units, the thickness increase of each unit leads to a linear strain of 37% and a high actuation frequency up to 20Hz (Figure 2-6i). Even a higher linear strain of 79% can be achieved by uniaxially prestretching the actuator in the planar direction with a constant load (Figure 2-6l).

While the HASEL actuators require an encapsulation of liquid dielectrics for the hydraulic pressure, the electrostatic zipping actuators utilize the electrostatic stresses by using several droplets of liquid dielectric without any encapsulation.^[85] Electrostatic zipping actuators are simple in design but are capable of producing extremely large actuation strokes and forces, as is shown in Figure 2-6k, l, m. Although they all utilize electrostatic forces, one of the most significant differences is that the traditional DE and HASAL actuators maintain a uniform distance between electrodes before and during actuation, while that in the electrostatic zipping actuators decreases from the center to the hinge, allowing the stresses to first build-up at the hinge and gradually extending to the whole strip as it zips to close (Figure 2-6k). By applying a

small droplet of, for example, silicone oil to the hinge, both permittivity and dielectric strength of the interface increase, while the former enhances the Maxwell stress and the latter permits application of higher voltage. Various origami structures have been proposed to provide lift forces utilizing zipping actuators; see Figure 2-6l and m.^[85]

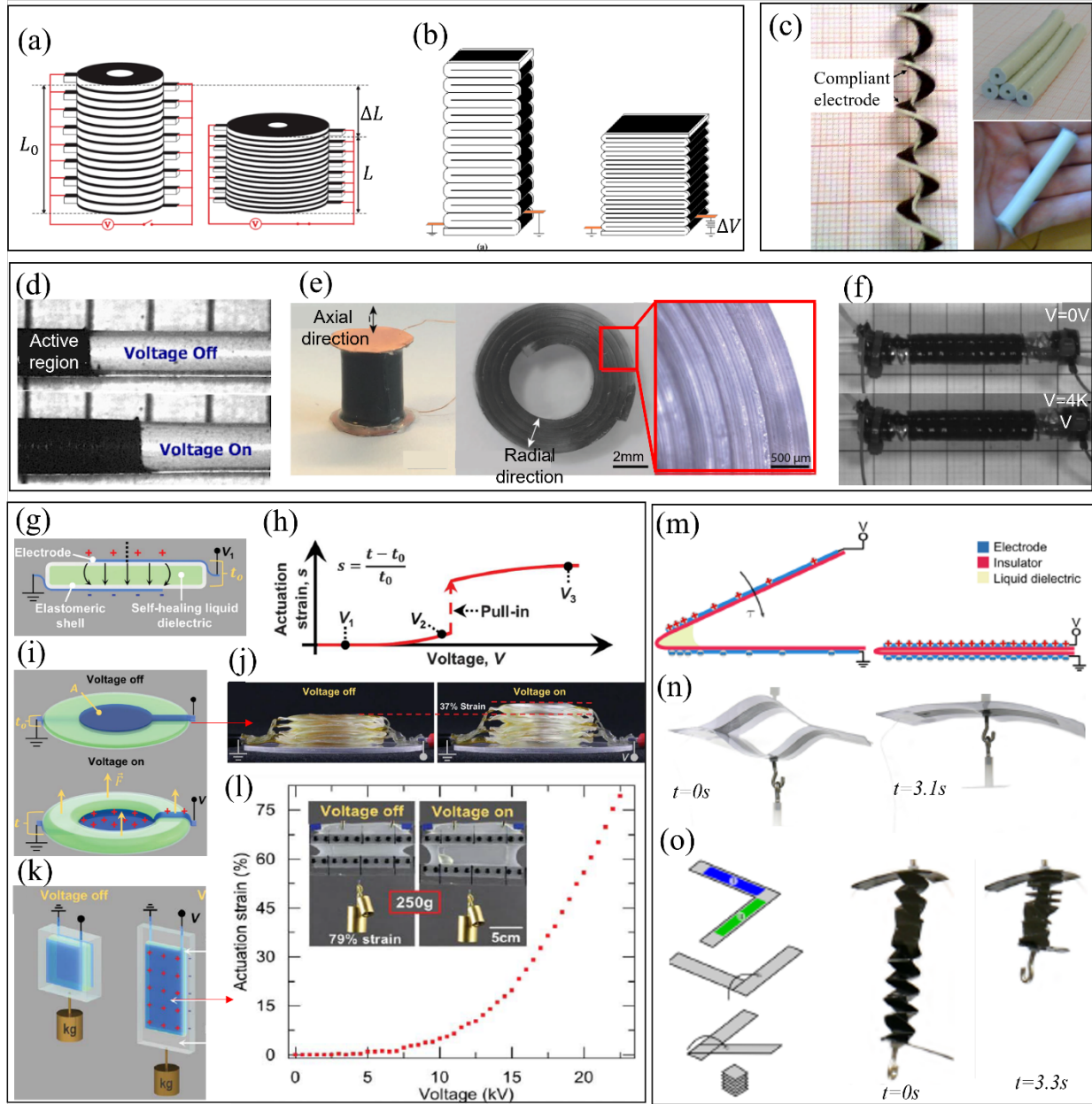


Figure 2-6. Capacitive linear actuators. (a-c) Design of stacked DE actuators for linear actuation using thickness strain. (d-f) Design of tubular DE actuators for linear actuation using areal strain. (g-l) HASEL actuator: (g) schematic of the working principle, (i,k) two actuator

design schematics and, (j,l) their actuation performances. (m-o) Electrostatic zipping actuator: (m) schematic of the working principle, (n) actuation performances and, (o) an origami structure design and its actuation performance. (a) Reproduced with permission.^[79] Copyright 2017, Springer Nature. (b) Reproduced with permission.^[69] Copyright 2007, IOP Publishing. (c) Reproduced with permission.^[80] Copyright 2005, IOP Publishing. (d) Reproduced with permission.^[65] Copyright 2007, Elsevier. (e) Reproduced with permission.^[81] Copyright 2018, John Wiley and Sons. (f) Reproduced with permission.^[83] Copyright 2017, Author. (g-l) Reproduced with permission.^[84] Copyright 2018, AAAS. (m-o) Reproduced with permission.^[85] Copyright 2018, AAAS.

Pneumatic/hydraulic linear actuator

The pneumatic/hydraulic actuation has been widely explored to build soft robots primarily because of their advantages such as large force output, ease of prototyping and control, actuation reliability, and available bench-top fabrication techniques. Among the diverse soft actuators, pneumatic/hydraulic actuators seem to have the most commercial successes.^[86-90] In fabricating these actuators, silicone elastomers are the most commonly employed material because of their commercial availability in a broad range of tunable mechanical and time-dependent properties as well as facile fabrication. By creating air channels in layers of elastomer films, the pneumatic pressure created by external pumps can be readily controlled and directed to inflate and deflate the soft actuator to produce various motions and forces.

Although the pneumatic (or hydraulic) pressure is isotropic in the channels, the directional deformation of the elastomer matrix can be accomplished by creating appropriate structures (e.g., corrugated)^[71] or by introducing mechanical anisotropy with oriented reinforcing fibers^{[70] [91]}.

For example, in an elastomeric tube with radially wound inextensible fibers, the radial deformation of the tube is constrained, and therefore the increase of inner pressure results in the axial extension, radial expansion, or twisting of the tube (**Figure 2-7a**).^[91] In particular, by aligning the fiber at an angle to the longitudinal direction of the tube, the volume expansion tends to rotate the tube together with limited length and radial changes. To deliver linear extension or contraction motion, the rotational deformation can be canceled by winding two sets

of fibers symmetrically about the tube for torque balancing.^[70] A well-known critical angle of 54.7° defines the boundary between linear contraction and expansion.^[92] Additionally, by covering the fiber-reinforced pneumatic-driven-elastomeric tubular linear actuator with a kirigami skin, the extension and contraction of the tube can generate crawling locomotion (Figure 2-7b). The crawling of the tube upon inflation and deflation is due to the buckling pattern of the kirigami skin that introduces directional friction.^[93]

Another type of linear actuator driven by pneumatic pressure relies on the buckling of its structure. Figure 2-7d shows two buckling beam actuators contracting in length when the vacuum is applied. Negative pressure is utilized for safer implementation and large contraction (actuation strain and stress up to 45% and 65kPa).^[71] Another pressure-driven actuator shown in Figure 2-7c can extend several times of its own length while lifting up a heavy weight. The large output strain and force originate from the origami skeleton, where the pressure change acts to unfold and extend the origami structure. Such actuators are easy to prototype at low cost, and different design and integration are demonstrated to produce multiple DOF at different scales.^[94]

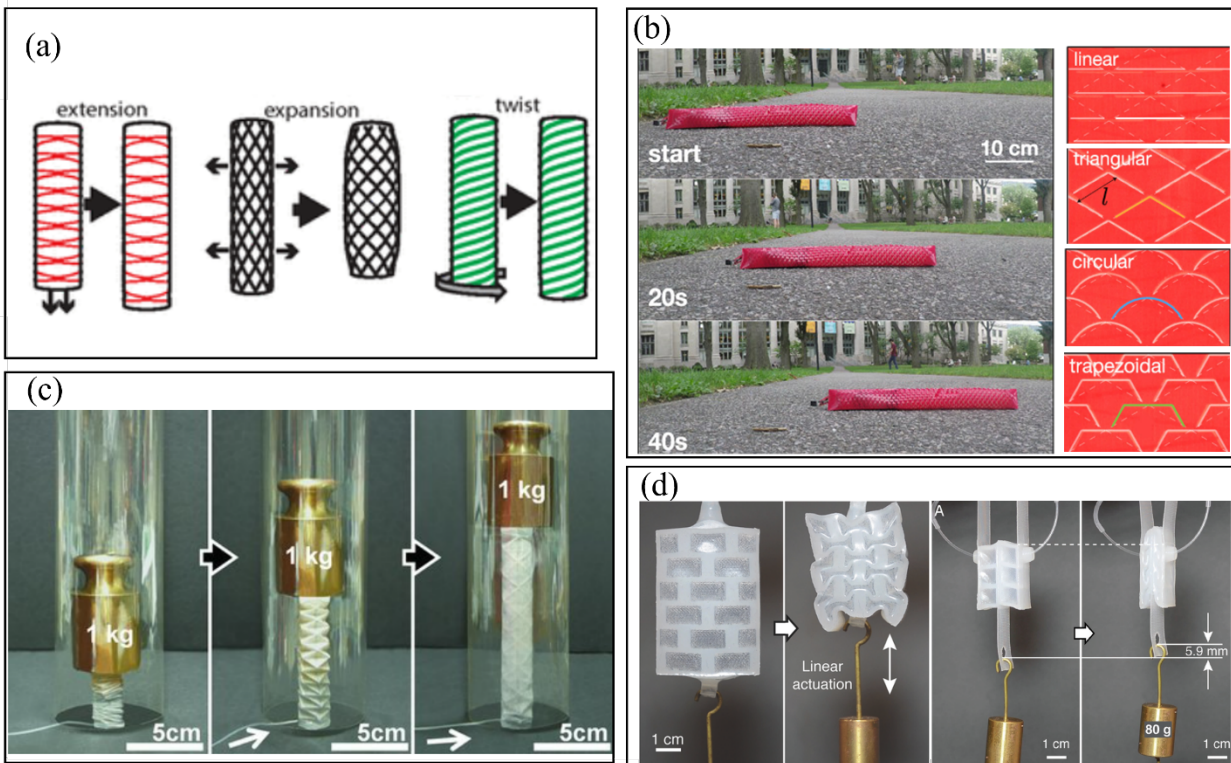


Figure 2-7. Pneumatic linear actuators. (a) Schematics of fiber-reinforced pneumatic actuators showing different actuation motion. (b) Directional motion of a pneumatic actuator due to the kirigami skin with various cut patterns. (c) A pneumatic actuator with an origami skeleton. (d) Negative pressure-driven actuation of buckled structures. (a) Reproduced with permission.^[91] Copyright 2017, the Authors. (b) Reproduced with permission.^[93] Copyright 2018, American Association for the Advancement of Science. (c) Reproduced with permission.^[94] Copyright 2012, John Wiley and Sons. (d) Reproduced with permission.^[71] Copyright 2016, John Wiley and Sons.

Thermal-activated linear actuators

Thermal-driven soft actuators convert the heat to mechanical output, typically through the phase-change of the materials.^[95–97] The two effects of phase-transition, mechanical property and volume change, have been used to build soft actuators with stiffness-tuning features^[97] and thermal-induced motions^[96]. Compared with the electrostatic and pneumatic actuators that utilized “external” forces (i.e., electrostatic attraction compresses the dielectric elastomer, and the pneumatic/hydraulic pressure expands elastomeric channels), the thermal soft actuators deform due to the “internal” stress developed within the responsive materials. These “internal”

stresses can result from the change in the mobility of molecular chains near the phase transition point or the breakage of intermolecular bonds. The “internal” stresses utilized for the shape change of soft actuators include thermal expansion^[98] and shrinkage^[99], solvent-induced swelling^[100], photo-induced isomerization^[101], potential-induced ion redistribution^[102], shape memory effect (SME), etc.

A well-known example of internal stress-induced deformation is the thermal-responsive SMP, which upon thermal activation, deforms to most commonly an irreversible shape from a predefined temporary shape. **Figure 2-8a** is a typical process for structuring and activation of shape memory polyethylene (PE).^[72] To develop the shape memory properties, the thermoplastic PE is cross-linked to provide fixation points for processing (A→B). After being heated above its melting temperature (T_m) (B→C), the PE is stretched to a temporary shape (C→D) and held until the temperature is down below its T_m where crystalline structures are formed to sustain this temporary shape (D→E). When the temperature is elevated again above the T_m , the crystalline structures are melted, and the internal retractile stresses due to prestretch is released, leading to shape recovery (E→C).

One of the shortcomings of the SMPs as a soft actuator is that it requires manual shape reset after the thermally induced change in shape. Therefore, reversible SMPs have been developed by mechanically loading the SMP^[103,104] or by using mechanical coupling with an elastic component^[105]. The reversible deformation through mechanical loading is based on the crystallization-induced elongation of the SMP under constant tensile stress and melting-induced contraction.^[103] For example, a shape memory PE film under constant tensile stress of 0.855 MPa has been reported to exert 40% reversible strain under cooling and heating cycles.^[104]

Another method uses a bias spring as the elastic component to reset the deformation of the SMP. Along this line, Chen et al. laminated a prestretched shape memory polyurethane (SMPU) and a passive PU to construct a reversible bending actuator, where the heat-induced contraction of SMPU generates bending, and the elastic recovery force of passive PU leads to unbending.^[105]

While bilayer structures are common in bending actuators (*cf.* section 0), specially configured bilayers can also be used for linear actuators. Mehmet et al. proposed a large stroke linear actuator by configuring a bicomponent fiber into a helical structure that can be actuated by the thermally induced differential expansion of the two components.^[73] The bicomponent fiber composed of an elastomer and PE is drawn from a precursor, see Figure 2-8b. The periodic helical shape is generated upon release of the fiber from a high stretch (Figure 2-8c). While the applied stretch elastically deforms the elastic component, rubber (fully recoverable deformation) it plastically deforms the PE (partially recoverable). Therefore, when the stretch is removed, the contraction mismatch results in the helical deformation of the fiber, where the PE component moves to the outer portion of the helical fiber. Interestingly, the coiled fiber is generated with two ends fixed from rotation. This phenomenon of reverse handedness is observed in nature, in particular, in the tendril of cucumbers^[36], and was also reported in early textile literature^[35]. The actuation behavior of the helical bicomponent fiber is shown in Figure 2-8d. Upon moderate heating (up to 10°C) from ambient temperature, it can generate a reversible linear strain up to 50%. The bilayered structure in the coil is the key to the large deformation of the structure from a small strain in one layer, and the helical configuration converts the bending of the bilayer into a linear deformation.

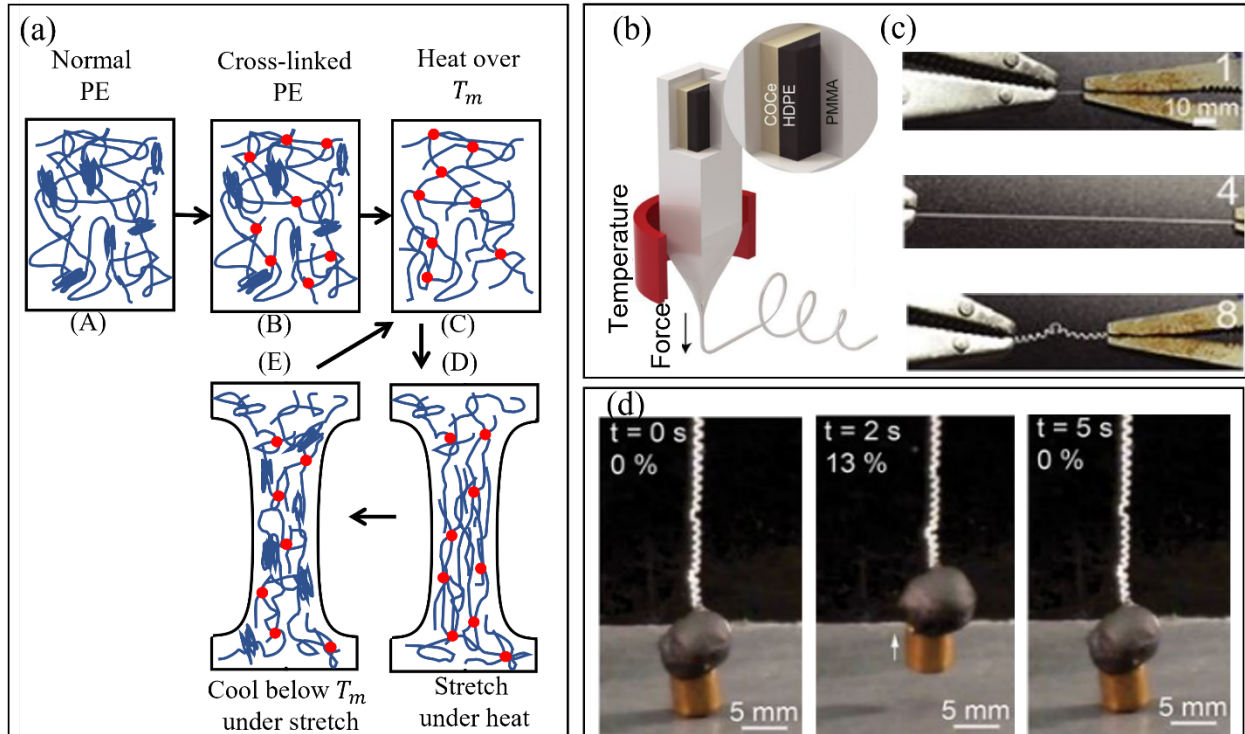


Figure 2-8. Thermal activated linear actuators. (a) Fabrication and working principle of shape memory PE. (b-d) Bicomponent fiber actuator: (b) extrusion of a bicomponent fiber composed of PE and an elastomer, (c) coil generation in the fiber by stretching and releasing, and (d) thermal-induced linear contraction. (a) Reproduced with permission.^[72] Copyright 2012, Elsevier. (b-d) Reproduced with permission.^[73] Copyright 2019, American Association for the Advancement of Science.

Twisted and coiled polymer linear actuators

Twisting is an ancient and essential technique to assemble fibers into textile structures such as yarns and ropes. In recent years, twisted fibrous structures have been explored as a new type of soft actuator, labeled as twisted and coiled polymer (TCP) artificial muscle. The TCPs can be designed to exhibit two types of actuation behavior, torsional and linear, while the former actuation is generated by highly twisted fibers, the latter is caused by the twisted and then coiled fibers. The TCPs can not only be fabricated relatively easily using a wide range of materials, but they also stand out among the many soft actuators because of their fast rotational speeds in torsion and remarkable linear stroke and force output in linear modes. The working principle of

TCPs is based on the radial expansion-induced torsion of the highly twisted structures and the torsion-induced linear motion of the coiled shapes. The radial expansion of constituent fibers can originate from the thermal expansion, ionic charge influx, or solvent diffusion. Therefore, the responsive materials used for the TCP yarn actuators include thermally responsive polymers such as nylon and PE^[106], conducting fiber-forming materials such as carbon nanotubes^[74] and graphene^[107], solvent swelling polymers such as silicone rubber^[108] and hygroscopic swelling fibers^[109].

There are two general categories of TCP yarn actuators based on the material arrangement in the TCP structures. In one case, the TCP is composed of only one fiber material, where the fibers serve both as the responsive material for radial expansion and as the smart structure that converts the diameter change into the intended actuation strain. Thermo-responsive TCPs such as those made of nylon and PE and hygroscopic fiber-based TCPs are in this category. In the other case, the twisted fiber is coated or infiltrated with guest materials, where the fibers serve as the structural skeleton that transforms the volume expansion into torque. One example is the electrical charge injection-based carbon nanotube (CNT) TCP. When electrically charged, it produces a large tensile contraction in an electrolyte environment, which can be liquid^[110] or solid electrolyte that is infiltrated into the structure during fabrication^[74]. The applied electrical potential induces a large amount of ion injection into CNT bundles to neutralize the charges and result in the volume expansion of the CNT yarn. Another example utilizes the volume expansion (e.g., hygroscopic expansion, thermal expansion) of the guest materials for actuation. In this, the twisted fiber serves as a structural element that converts the volume expansion of the guest material into torsional motions. Mu et al. compared the actuation performance of pristine CNT yarn, CNT yarn coated or infiltrated with functional polymers (**Figure 2-9a**).^[111] A larger

actuation stroke has been reported for the coated TCPs than the infiltrated ones, while the pristine CNT yarn produced the minimum response. The advantages of coating over infiltration were reported as, 1) improved actuation performance (higher stroke, actuation speed, and work density), as the deformation on the yarn surface is more effective than near the core of the yarn; 2) higher actuation performance at same conditions lead to higher energy efficiency; 3) lower cost of materials and less energy consumption.

The mechanical principle of TCP actuation is akin to the fiber-reinforced pneumatic actuators, where the pressure-driven volume expansion is directed into linear motion and/or rotation, depending on the orientation of the reinforced fibers (Figure 2-7b). However, the twisted yarn actuators have significantly more complex geometries in which; 1) the structures can be composed of a monofilament, filament yarns, as well as staple yarns, and different composition results in different microstructure parameters, 2) the helix angle (angle between the length direction of the constituent fibers and that of the yarn) decreases from the surface to the center of the yarn, 3) the yarn geometry and properties are very sensitive to the fabrication processes, such as twist density and mechanical conditions during and after twisting, 4) a variety of hierarchical structures from nanoscales to macroscales can be formed, including the twist-distorted molecular rearrangement in the fiber, fiber migration in the highly twisted yarn, and coils formed due to over-twisting or mandrel winding. The structural and mechanical parameters at different levels, coupled with the nature of material responses, lead to the ultimate actuation behavior of the TCP.

The importance of understanding the mechanics of the twisted structures to design better products (e.g., yarns, cords, ropes, etc.) has been recognized long ago by many engaged in textile research.^[112] The renewed interest in the analysis of twisted structures stems from the recent

need to understand the physical origin of the actuation performance and the intimate structure-function relationship of the TCP actuators. The single helix model and elastic spring mechanics are often used to analyze the geometries and actuation response of TCPs.^[106,113] Aziz et al. used the single helix model to quantitatively link the volume expansion of the twisted fiber to the resulting torsional/linear actuation.^[113] For the twisted yarns (or fibers), the ratio of twist change due to yarn volume expansion is expressed as,

$$\frac{n}{n_0} = \left(\frac{V_0 \lambda l_0 l_s^2 - \lambda^3 l_0^3}{V l_s^2 - l_0^3} \right)^{\frac{1}{2}} \quad \text{Equation 1}$$

where the structural parameters with and without the subscript 0 represent their values before and after actuation, respectively. V , l , d , n are the volume, length, diameter, and number of twists of the yarn. The parameter l_s is the precursor fiber length before twisting, which is assumed to be constant throughout the experiment, and λ is the ratio of yarn length after and before actuation (l/l_0). By assuming negligible length change of the yarn during actuation ($\lambda=1$), the free torsional stroke (ΔT , untwisting per unit length of the yarn), can be written as,

$$\Delta T = \frac{n_0}{l_0} \left(\frac{d_0}{d} - 1 \right) \quad \text{Equation 2}$$

The resulting blocking torque (τ_{block}) is calculated based on the well-known elastic rod theory as,

$$\tau_{block} = \Delta T J G \quad \text{Equation 3}$$

where, J is the polar moment of inertia, G is the shear modulus, and the product JG is the torsional stiffness of the yarn. For the twisted and coiled yarn, the change in the coil length (ΔL) due to yarn untwisting can be calculated using the mechanics of elastic springs, and is expressed as,

$$\Delta L = \frac{\Delta T l^2}{N} \quad \text{Equation 4}$$

where, N is the number of turns of the coil, and l is the length of the yarn forming the coil.

A large body of research on TCPs has been published after the early discovery of the remarkable actuation of CNT yarn^[110] and nylon filaments^[106]. Ongoing investigations on TCPs explore a variety of materials, twist geometries, processing types, theoretical modeling, stimuli type, performance improvement, and application areas. Some of the examples of TCP actuators are shown in Figure 2-9. Highly twisted, two-ply, twisted, and coiled (due to overtwist), and two-ply of coiled yarns are shown in Figure 2-9b.^[74] When the CNT-based TCP is immersed in an electrolyte bath and electrically charged, the opposite charges migrate from the electrolyte into the CNT yarn due to electrical potential gradient, resulting in fast reversible rotation of the yarn or immediate yarn length contraction.^[110] In the actuation setup for the CNT-TCP in a liquid electrolyte shown in Figure 2-9c, half of the TCP is active, and the other half serves as the reversing mechanism. DC voltage is applied to the TCP and a counter-electrode, while a reference electrode is used for voltage recording. Lee et al. improved upon this pioneering work by replacing the liquid electrolytes with solid electrolytes and by avoiding the unwanted untwisting of the inactive part of the yarn via torque balanced plied structure, see Figure 2-9b. In this work, two S-twisted yarns are plied in the Z direction to achieve the torque balance of the structure. The solid electrolyte is infiltrated into the yarn after twisting for both torsional and tensile TCPs.^[74] Mu et al. improved the actuation performance of CNT-TCP by coating the solid electrolyte on the surface of the yarn where the response is maximum due to the highest helical angle, instead of infiltrating the entire yarn (Figure 2-9a).^[111]

Low-cost, low-weight polymer fibers have also shown great potential in the field of twisted yarn artificial muscles, and the most popular means of actuation are heat and solvent. A fabric structure made from nylon TCPs, with integrated heating elements for electrothermal actuation,

is shown in Figure 2-9e. The coiled nylon yarn is annealed just below its melting temperature to set the shape. The electrothermal actuation is enabled by wrapping a thin copper wire for resistive heating. The coiled nylon TCPs can be further assembled into fabrics to produce smart fabrics with the potential application of thermo-regulative clothing and smart curtain by changing fabric porosity and/or permeability.^[66] Figure 2-9f demonstrates one of the applications of coiled polymer yarn as the antagonistic contractile muscles for the robotic arm. The double helix yarn composed of spandex and nylon is capable of producing 48% tensile stroke and lifting much larger weight than those yarns composed only of nylon.^[114]

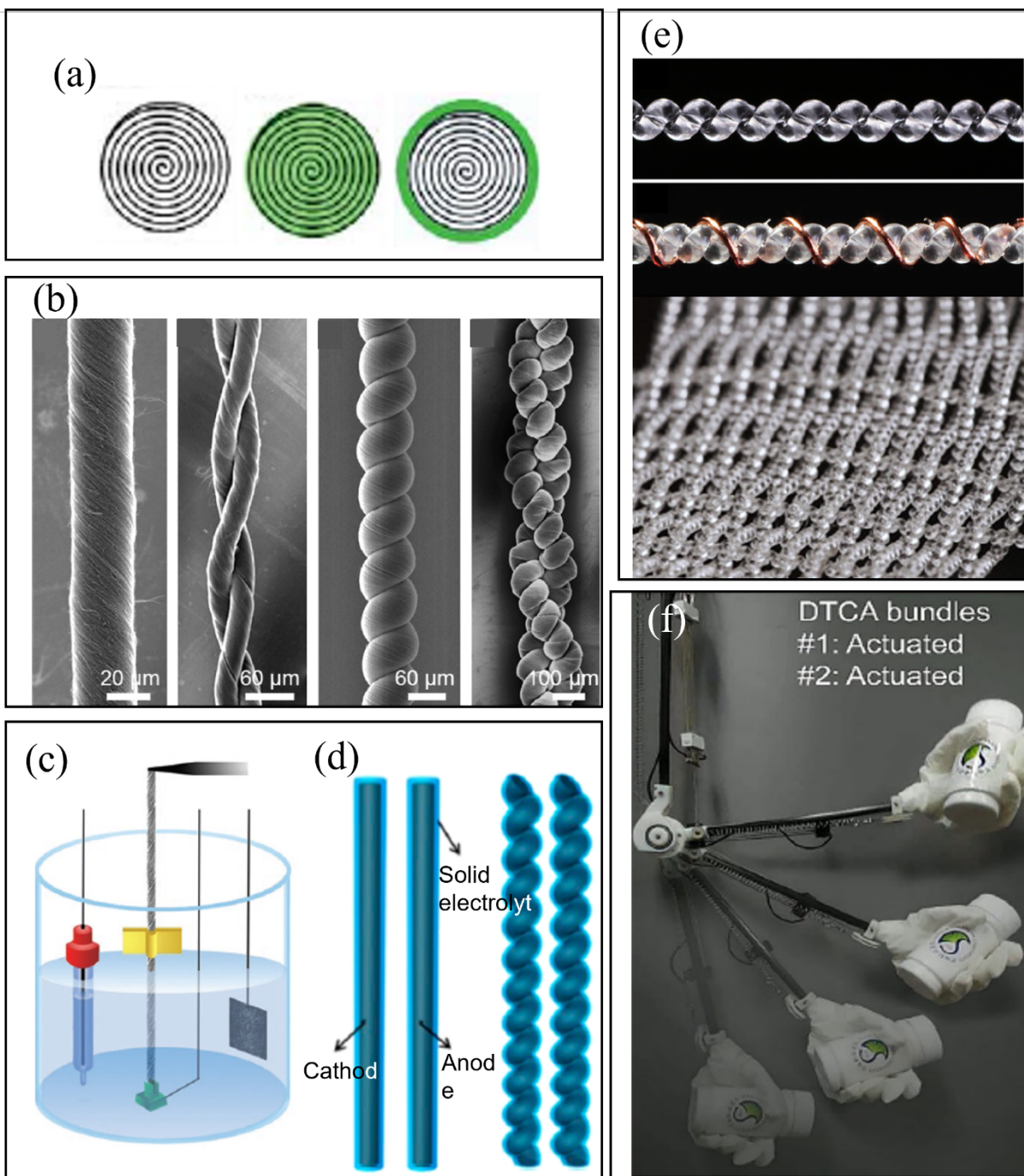


Figure 2-9. TCP linear actuators. (a) Cross-sectional views of a twisted yarn, infiltrated and coated with functional materials. (b-d) CNT-based TCPs: (b) hierarchical structures of twisted CNT yarns, schematic of electrical actuation in (c) liquid, and (d) solid electrolyte. (e) Structure of nylon TCP and their assembly in a fabric. (f) A robotic arm powered by a Nylon/spandex TCP. (a) Reproduced with permission.^[111] Copyright 2019, AAAS. (b, d) Reproduced with permission.^[74] Copyright 2014, ACS. (c) Reproduced with permission.^[110] Copyright 2011, AAAS. (e) Reproduced with permission.^[66] Copyright 2016, National Academy of Sciences. (f) Reproduced with permission.^[114] Copyright 2018, John Wiley and Sons.

2.3.2.2 Bending, wrinkling, and folding

When an isotropic and homogeneous plate is mechanically bent, there is a continuous strain distribution along the thickness of the paper, where the maximum compressional and maximum tensile strains locate at the outside of the concave and convex surfaces, respectively, and the zero strain resides at the middle, known as the neutral plane. Conversely, when tensile or compressive strain is actively induced away from the neutral bending plane of a 2D structure, it bends. Based on this principle, out-of-plane deformations, such as bending, wrinkling, and folding in soft actuators, are achieved.

Natural examples of this mechanism of bending, wrinkling, and folding, to derive different morphing structures are abundant. For example, the scales of pine cone bend to release seeds at decreasing environmental humidity, mimosa leaflets spontaneously fold upon touch^[23], the inner surface of the porcine airway develops wrinkled morphology due to volumetric growth of lining tissues^[115], and the extremely large area ratio of earwig wings between folding and unfolding enables it to navigate efficiently both in air and at the ground^[32]. The engineering analogs of these natural morphing structures are active bending, wrinkling, and self-folding soft actuators. They have been used in the locomotion of soft robots^[116], smart textiles for active moisture management^[61], wings of drones with better aerodynamic performance^[117], etc.

The underlying mechanism of these deformations is the strain localization driven by the tunable anisotropic mechanical behavior, residual stresses, and mechanical mismatch between layers of laminates. The basic design principles to produce localized strains utilizes gradients in either of stimuli/energy input, degree of response of the materials to the stimuli, stiffness of the material, and the flexibility of structures, for bending, twisting, and wrinkling actuation, see **Figure 2-10**. The first method of gradient stimuli input-induced bending can be simply demonstrated by

placing a thin cellulose film on the palm of your hand. It bends upward due to exposure to higher humidity at the near-hand side.^[118] A steep gradient in material response is achieved by coating a thin layer of moisture-insensitive material to the same cellulosic film that can bend unidirectionally under a homogeneous environment (e.g., humidity chamber). A more typical strategy to generate bending, twisting, or wrinkling is introducing differential mechanical stiffness in the composite, typically using laminates. For instance, DE films can be laminated onto a stiffer elastic film to produce bending DEAs, and a variety of actuation performances are achieved with additional fabrication steps, such as fiber reinforcement for directional bending^[119,120] and anisotropic surface stress mismatch for bistable bent structures and binary actuation^[31].

Figure 2-10a-c illustrate the light-induced reversible winding and unwinding of a thin liquid crystal elastomer (LCE) film.^[121] The cylindrically twisted film, when exposed to UV, reversibly winds or unwinds, depending on the directional anisotropy of the film Figure 2-10a. Here, the shape change originates from the anisotropic deformation of the nematic LC doped with azobenzene molecules that undergo photoisomerization (Figure 2-10b). The orientation of nematic LC is specially designed with a gradual change from 0° to 90°, from the top to the bottom surfaces of the film, which converts the microscopic deformation to anisotropic macroscopic bending (Figure 2-10c).

Compared to the delicate microstructural design that always involves sophisticated chemical synthesis and modification, layered structures are more predominant in the manmade bending actuators for the ease of fabrication and multifunctionality of the different layers. They can serve as the structural support layer, stimuli-responsive layer, mechanical tuning layer, protective

layer, etc. Ionic polymer-metal composites (IPMC) actuator for example, is typically composed of two electrically conductive layers and a middle ionically conductive layer soaked with an electrolyte. Upon activation with a low voltage, the ion migration within the middle layer causes swelling near one electrode and shrinkage near the other, causing bending. The film unbends as the voltage is removed.^[122]

Folding is a special case of bending often due to an abrupt local drop in mechanical stiffness due to a minimum in-plane width or thickness or a highly localized bending moment. A self-folding robot made from shape memory polymer - prestretched polystyrene (PSPS) - is shown in Figure 2-10d.^[98] The robot can self-fold from a flat sheet into a pre-defined structure and then walks by cyclic folding of certain hinges. As shown in Figure 2-10e, two types of hinges for unidirectional and bidirectional folding are designed for the purpose of shaping and movement. To form these hinges, the laminates, initially composed of two contractive surface layers of PSPS, two passive paper substrates as inner layers, and a middle polymer-backed electrical circuit, were selectively laser trimmed to remove materials from the surfaces. The resultant hinge structures are shown in Figure 2-10e, where the structuring hinge bends unidirectionally, and the walking hinge bends bilaterally, under the activation of the contractile shape memory layer.

Multistable bent structures can also be fabricated by laminating films with stress mismatch. Natural organisms such as Mantis shrimp and VFT employ bistable structures for high power output (force and speed) and structural stability for morphing. The bioinspired structural design of a bistable DEA is shown in Figure 2-10f-h.^[31] It has two predefined bent shapes (Figure 2-10h) and can rapidly roll up under a short duration of voltage input (Figure 2-10f). The bistable laminate comprises two prestrained elastomer layers and a strain-limiting film in the middle,

with the former serving as both an elastic energy reservoir and an active element under the electric field, and the latter serving as the neutral bending plane (Figure 2-10g). The electric field-induced strain of the DE layer activates rapid snap-through of the laminated actuator.^[31]

While we consider the film and the laminate as 2D structures, most pneumatically or hydraulically driven actuators can be regarded as 3D structures. There are macroscopic channels for the fluid flow and consequent production of force. Although there are various investigations into the structural design for larger bending angles, faster actuation speed, and higher force output, the fundamental principle remains the same as the 2D bending, i.e., stress or stiffness gradient in the thickness direction. Therefore, pneumatic bending actuators are generally composed of asymmetric air channels in an inflatable body, with the bending motion enhanced by corrugated structures and strain-limiting layers.^[55,123] While the air/fluid flow induces the volume expansion of the channels, the corrugated structure and the strain-limiting layer improve and limit the deformation, respectively. Mosadegh et al. reported a pneumatic bending actuator design with improved actuation speed and output force (Figure 2-10j-k).^[55] Two structural designs are shown in Figure 2-10j. While both pneumatic actuators are composed of an extensible top layer and an inextensible bottom layer, the second design (Figure 2-10j, right) has disconnected top layers for higher bending flexibility and smaller channel size near the bottom layer for faster inflation.

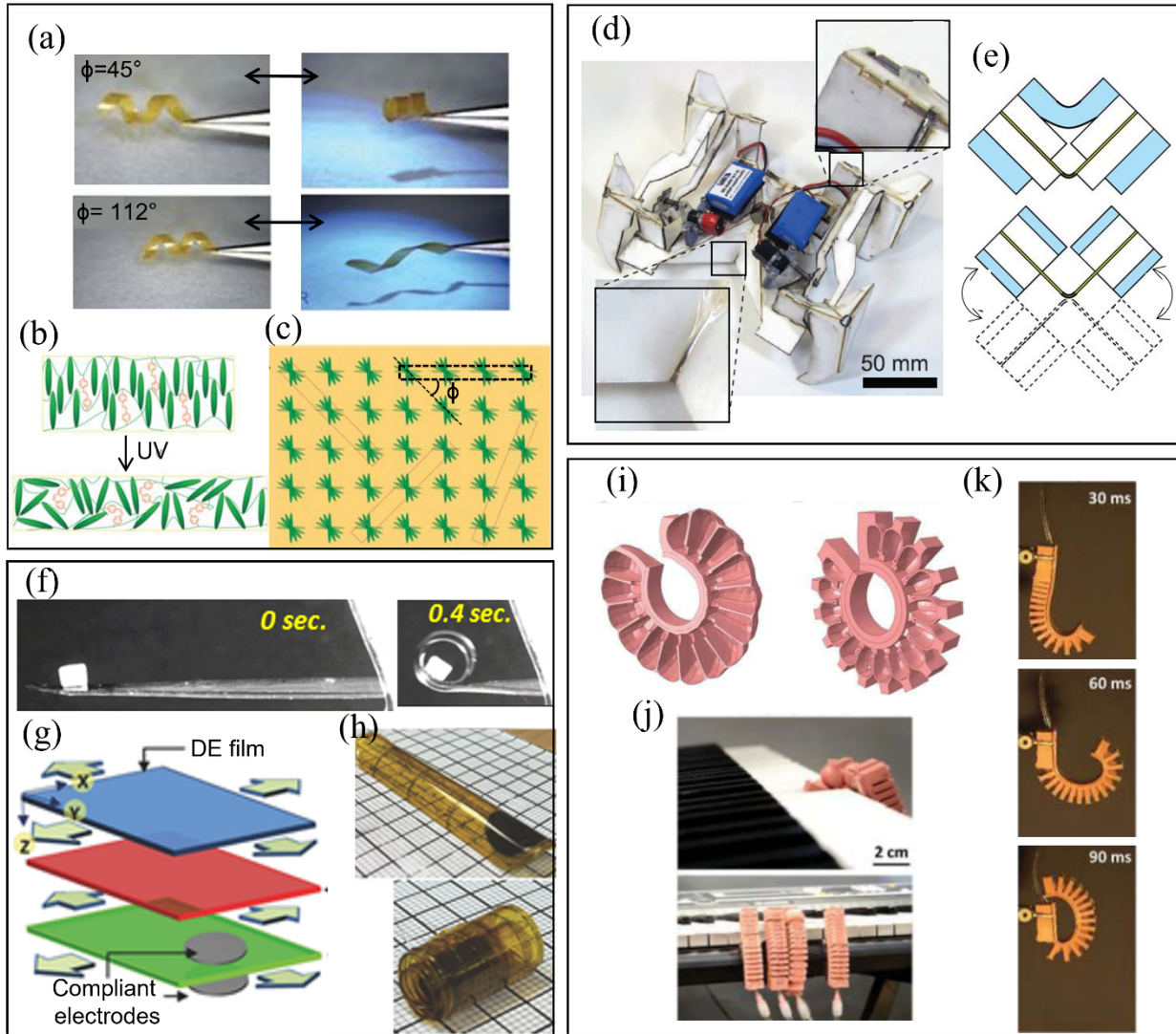


Figure 2-10. Bending, twisting, and folding actuators. (a-c) UV-actuated LC twisting actuator: (a) twisting and untwisting deformation of the actuators cut at different angles to the LC orientation, (b) the actuation principle, and (c) a top view of the LC alignment and different cutting angles. (d) A self-folding-based walking robot, and (e) its hinge design. (f-h) Bistable bending actuation of DEA: (f) side view of actuation motion showing the two stable shapes, (g) schematic of actuator fabrication, and (h) photographs of the two stable shapes. (i-k) Pneumatic bending actuator: (i) two structural designs and (j-k) demonstration of the actuation behavior. (a-c) Reprinted with permission from ^[121]. Copyright 2014 Springer Nature. (d-e) Reprinted with permission by ^[98]. Copyright 2014 American Association for the Advancement of Science. (f-h) Reprinted with permission from ^[31]. Copyright 2018 John Wiley and Sons. (i-k) Reprinted with permission from ^[55]. Copyright 2014 John Wiley and Sons.

2.3.2.3 Crawling and rolling

Crawling and rolling are common types of motion in mollusks such as worms, slugs, and octopuses. For example, caterpillars propel their body by generating a wave of contraction and

relaxation of their body segments.^[33] Octopus moves and captures prey through its eight flexible arms.^[124] Compared to rigid skeletons and joints, these soft-bodied animals have increased DOF that enables multi-directional bending, extension, and contraction. Although there seem to be issues and challenges, such as low speed and force, lack of stability under turbulence, the complexity of position control of end effectors associated with the soft body actuation, animals have their unique methods to overcome them. For example, the slow locomotion of caterpillars is enhanced by generating larger peristaltic waves, or even by curling up into a wheel and roll with the momentum (**Figure 2-11a-b**).^[33] The octopus arm presents a very complex motion and unique fetching ability.^[125] It has infinite DOF, originating from the three-dimensional (3D) arrangement of muscle fibers that are oriented along the longitudinal, transverse, and helical directions.^[126] Instead of sending commands from the central nervous system, many motor neurons are distributed in the arms to control the complex motions of the flexible arms in a more efficient but simple manner.^[124]

Interestingly, during fetching, the octopus arm can move like the vertebrate arm to precisely control the position of the end effector by creating joints with stiffened muscles.^[125]

The mollusks capable of crawling and rolling with infinite DOF can be described as having a cylindrical body composed of lengthwise actuation modules with muscle fibers arranged in 3D like the octopus' arm. The activation of differently aligned muscles generates contraction, extension, bending, and twisting of the modules, and the integrated actuation of the modules results in the complex motion with multiple DOF.

This concept of design with multiple DOF provides insights for fabricating soft actuators with diverse motions and locomotion. For example, the pneumatic channels^[127], shape-memory fibers^[128], and DEs^[82] have been incorporated into cylindrical bodies to produce the multiple-

DOF actuation. Inspired by the rolling locomotion of the caterpillar, Lin et al. designed a soft worm-like robot that can rapidly roll up into a wheel to increase the speed of motion over 20-fold.^[128] The robot is composed of a cylindrical body made of silicone elastomer and two SMA muscles connected to the body in series to induce the rolling motion see Figure 2-11c. In particular, the SMA muscles are coordinated appropriately to generate enough angular momentum to initiate the free-wheel rotation (Figure 2-11d). In another report, Pei et al. presented a self-walking robot whose legs were composed of cylindrical DE units.^[82] As shown in Figure 2-11e, the robot is composed of six legs that bend sequentially to move the body. Each leg can bend in multiple directions due to the arrangement of four sets of independently controlled electrodes (Figure 2-11f) to enable multidirectional locomotion of the robot. While the multiple DOF tubular actuators assembled in parallel control the walking direction of the robot, they can be assembled in series to increase the DOF (Figure 2-11e). Martinez et al. proposed a soft pneumatic gripper that is able to deform according to the shape of the target object and thus grab objects of different shapes (Figure 2-11i).^[127] Such grasping capability is due to the sectioning of the gripper, arrangement of the pneumatic channels, and their individual control (Figure 2-11g, h). In each section of the gripper, three peripherally arranged channels lead to three bending directions, and three body sections generate a total of 27 combinations of motion, in addition to the tunable actuation amplitude of each pneumatic channel.

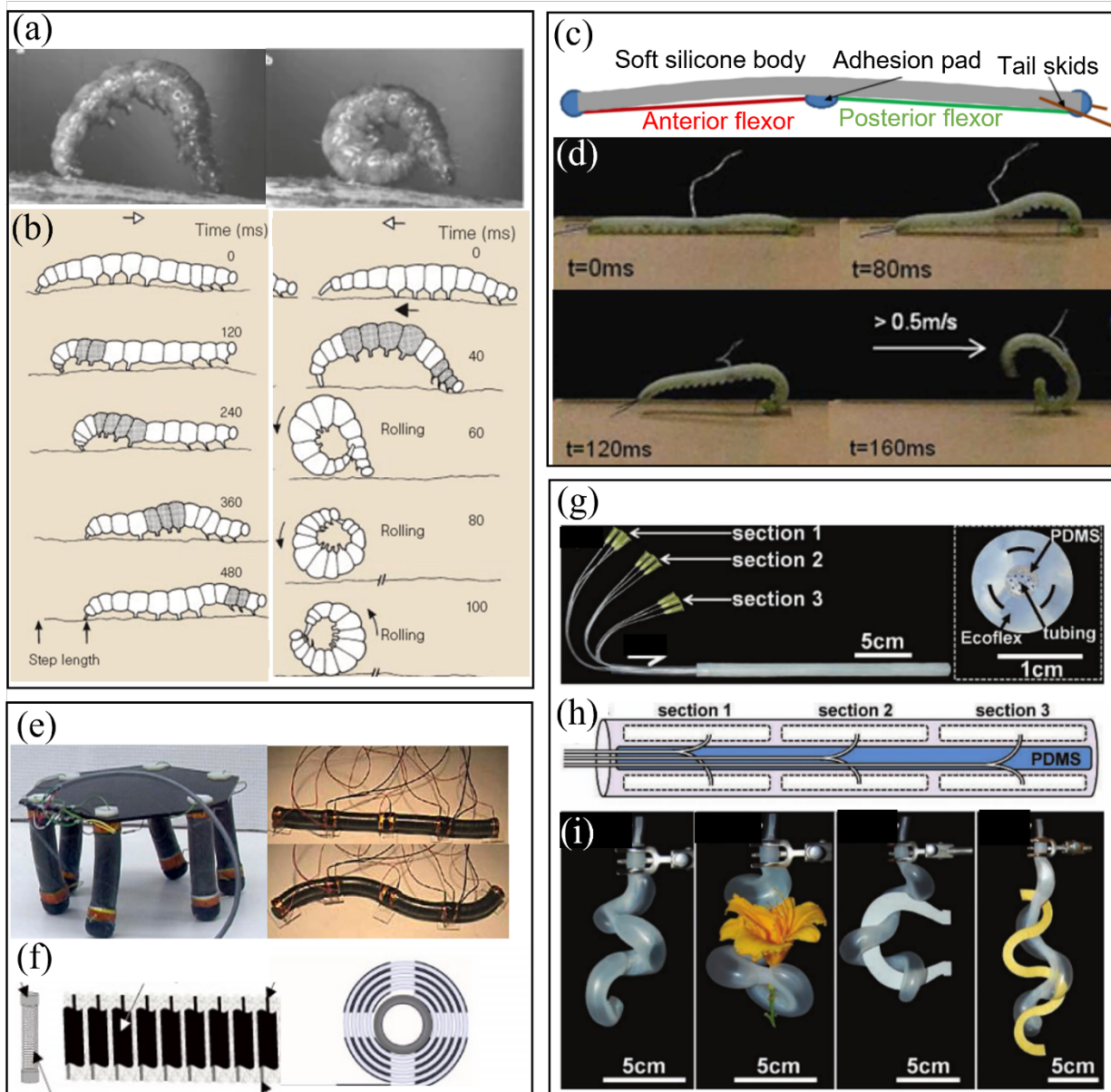


Figure 2-11. Crawling and rolling actuators with multiple DOF. (a) Images of a moving caterpillar, and, (b) mechanism of its different locomotion. (c) A caterpillar-inspired soft actuator design and (d) the actuation performance. (e) Two applications of the spring-roll DEA, and (f) the schematics of the spring-roll DEA. (g) Images and (h) schematics of a pneumatic actuator with multiple DOF, and (i) its grasping behavior. (a-b) Reprinted with permission from [33]. Copyright 1997 Springer Nature. (c-d) Reprinted with permission from [128]. Copyright 2011 IOP Publishing. (e-f) Reprinted with permission from [82]. Copyright 2004 IOP Publishing. (g-i) Reprinted with permission from [127]. Copyright 2012 John Wiley and Sons.

2.3.2.4 Power amplification

Soft actuators are generally limited by their power output. The low morphing speeds and small mechanical forces of soft materials are two primary reasons for the low power output. As the soft actuators, in general, work by deforming their own bodies instead of through displacement of the discrete elements, the morphing speed becomes restrained by the intrinsic response time of the material in relation to the stimuli. For example, electrostatic and pneumatic actuators respond typically faster than electrochemical, thermal, and moisture-driven actuators. When the electrostatic force or the pneumatic pressure difference is applied, the elastic materials deform almost instantaneously and relatively fast to reach the mechanical equilibrium where the external and elastic forces are counterbalanced. On the other hand, in the case of the thermally driven soft actuators, the actuation speed is restricted by both the generation of temperature gradient (depends on thermal diffusion) and the material response.

To generate a high power output and speed seemingly beyond their physiological limits, animals and plants utilize power amplification strategies, avoiding the necessity of large energy consumption. Such a burst of power output is a necessary approach to generate extreme motion (high speed, force, or displacement) instantaneously or in a short period of time by a sudden release of stored energy. For example, the Fern sporangium effectively ejects the spore by rapid elastic energy release through a catapult-like motion of a bent annulus.^[21] Chameleon projects its tongue at the target via direct mechanical energy transformation from the prestressed elastic tissues, with a peak power of 3000W/kg, which is about 10-fold of its muscle's normal power output.^[129] Nematodes can jump an average nine times their body length to reach a host insect. The nematode, while standing on its tail, bends its body to store elastic energy, which is suddenly released when the surface tension of water that helps hold the body in bent shape is overwhelmed by the recovery force of the bent body, leading to the jumping motion.^[17] Mantis shrimp is well-known for its deadly strike that can cause water cavitation and can smash hard

shells. Its raptorial appendage has a stiff saddle-shaped spring that is compressed to store a high amount of elastic energy prior to the smashing.^[18] The leaf closure speed of VFT, recognized as the fastest in the botanic world, results from the snap-through instability of its bistable shell structure.^[20]

The structural design of the soft actuators for power amplification requires energy storage and coordination between two key elements: the elastic element that deforms to preserve elastic energy and the latching mechanism that can help store and instantaneously release the elastic energy. The natural organisms mentioned earlier offer three potential strategies to meet the requirements; (1) Using muscle (or other internal elastic elements) for energy storage and external forces for energy release (e.g., jumping off of the nematode^[17]). (2) Using muscle for energy storage and a structured element for energy release (e.g., chameleon's tongue projection^[129]). (3) Using a bistable structure both for energy storage and release (e.g., rapid opening of VFT^[20]).

Power amplification through energy storage and release is also used in soft manmade actuators for superior actuation capabilities to produce fast grasping and weightlifting of robotic hands^[130] as well as rapid locomotion of soft robots^[131]. For example, rapid and powerful soft grippers with self-holding capability are fabricated by prestressing an elastomeric layer and laminating it to a strain limiting layer, see **Figure 2-12 a, b**.^[132] External energy input, such as pressurized air^[130] or electric field^[132], is applied to open the structure, which rapidly closes by itself upon removal of the external force due to the stored elastic energy. In this way, the gripper not only responds faster but also grasps objects with a larger force regardless of external energy input. Also, the strategy obviates the need for continuous application of the external energy that might lead to

dielectric breakdown.^[132] Multistable structures with multiple routes for energy minimization offer another means of amplification. With this approach, it is possible to create soft grippers with self-sustainable open and closed states. For example, the pneumatic tentacle, shown in Figure 2-12c-d, opens under pressure and rapidly curls and captures the insect when the pressure is removed, while the bistability enables the pneumatic actuator to rapidly and reversibly transform between the open and closed state with short blast of pressure supply.^[130]

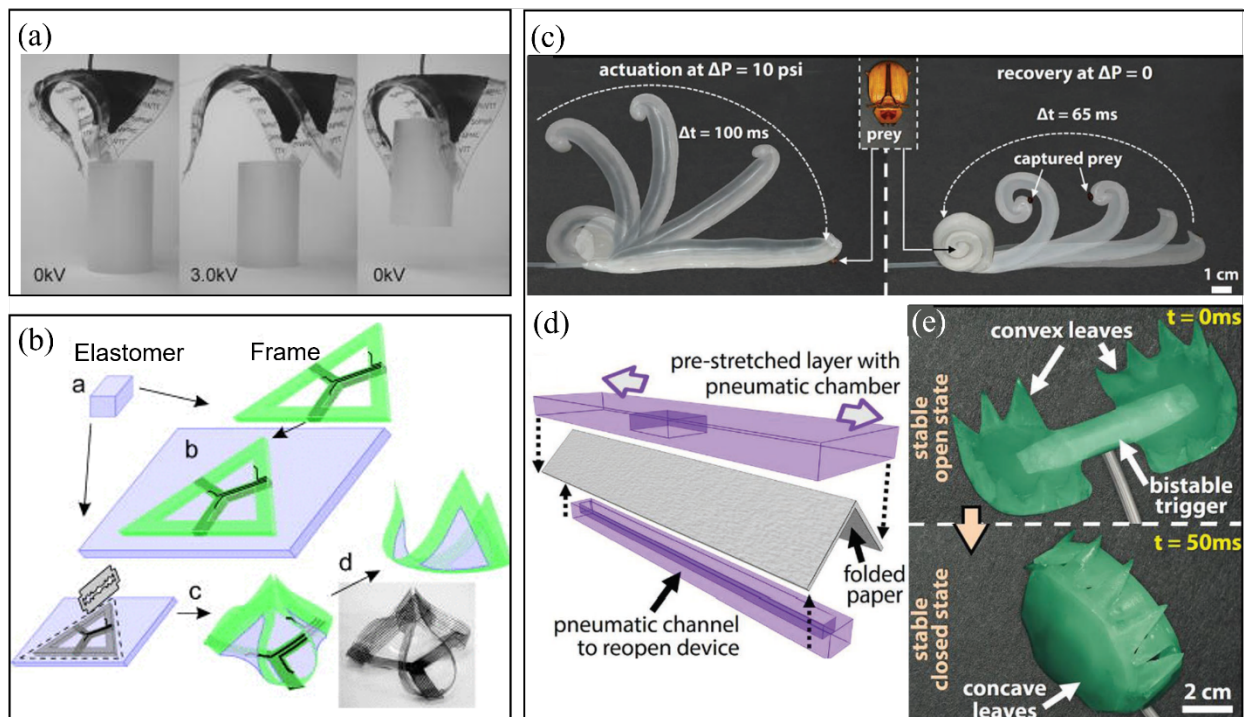


Figure 2-12. Soft actuators with power amplification structures. (a-b) Prestressed DE-based soft gripper and fabrication process. (c-e) Prestressed bistable pneumatic actuators for high speed: (c) fast actuation of the biomimetic tongue, (d) fabrication schematics of the bistable structure, and (e) rapid closure of the biomimetic VFT. (a-b) Reprinted with permission from ^[132]. Copyright 2007 AIP Publishing. (c-e) Reprinted with permission from ^[130]. Copyright 2019 John Wiley and Sons.

2.4 Fabrication Techniques for Soft Actuators

One of the advantages of using soft materials is their facile processing that offers opportunities for shaping materials in a wide range of length scales. Synthetic polymers constitute the majority

of the materials used for soft actuators and are classified into thermoplastic and thermoset types. The fabrication processes for both types usually start from the liquefied form such as melts or solutions, followed by solidification through cooling, solvent evaporation, and/or curing (crosslinking), during which the designed structure is formed. Three basic forms of structures, i.e., 1D structure (i.e., fiber), 2D structure (i.e., film), and 3D structure, are fabricated by extrusion, casting, and various molding techniques, with a variety of structural characteristics and features from nano to macro levels introduced by small modifications of or combinations of these three techniques. Lately, 3D printing has become a popular method for bench-top fabrication for soft actuators. Complex shapes and features such as hollow inner structures, overhangs, curves, and others that are unachievable or difficult with conventional manufacturing methods, can be fabricated in one single step by 3D printing. 3D printing is somewhat limited in material diversity and spatial resolution required for soft actuators despite its potential. In fabricating soft actuators, the active material is often packed with other components with distinctly different properties made of different materials and requires different fabrication methods. While designing and assembling these independently fabricated components, issues such as mechanical compatibility and functional continuity should be considered. The advantage of the availability of polymers in a wide range of properties and their ease of processing as well as modification provide solutions to some of these issues. For example, the interfacial mechanical failures can be addressed by improving interfacial strength via plasma treatment on the surface of different parts to promote bonding.^[133] Another issue is the necessary electrical interconnects within and around the soft actuators. The lack of integrity of the electrical connections due to repetitive and/or large deformation caused by mechanical property mismatch of soft body and metallic wires can be resolved by using flexible conducting materials such as conducting polymers or polymer-metal composites.^[134] Polymer composites offer another

versatile route of processing for soft actuators. Composites incorporating a variety of materials at different structural levels are widely used in natural and manmade products because of their ability to produce outstanding complementary and sometimes synergistic functional properties. For soft actuators, composites can provide additional functionalities to create multi-stimuli active actuators, help introduce mechanical anisotropy for directional deformation, or improve the properties such as conductivity and mechanical strength. For example, conductive nano-/micro-particles are mixed with elastomers to fabricate soft electrodes for DEAs.^[135] Although these conductive rubber electrodes are limited by the mechanical modulus due to the conductive fillers, they have good adhesion, better compliance to produce large and uniform deformation than shaped (e.g., serpentine) metallic traces.

Soft actuators can be fabricated using either a bottom-up and top-down approach. Similar to nature's approach of "growing" elementary constituents into functional muscles, bottom-up fabrication arranges active and supportive materials into functional structures.^{[54] [136]} Among a variety of bottom-up fabrication methods, while coating and laminating are used for 2D film structures, molding and 3D printing are popular techniques for 3D structures. Besides these commonly used fabrication methods, other methods, albeit less utilized, include self-assembly and fiber extrusion. Unlike the bottom-up approach, top-down fabrication techniques are subtractive in that the desired structures are generated by removing materials from the bulk through selective dissolving (chemical etching), burning (laser etching), cutting, or etching. The top-down methods are not stand-alone methods for soft actuator fabrication but are typically used as assistive tools for shaping. A representative example of the bottom-up fabricated soft actuator is the kirigami-based actuators, where patterns created by cutting blade or laser are critical to the response.^[93]

A brief overview of the various current and potential fabrication techniques for soft actuators focusing on their capabilities, considerations, and limitations is presented in the following. Finally, an in-depth discussion of opportunities and challenges in soft actuator fabrication is also included.

2.4.1 Molding

Molding is a conventional manufacturing and prototyping method to create structures, by filling a structured mold with liquid precursor materials followed by solidification and demolding. Most pneumatic actuators are fabricated by molding, where liquid silicone - the most popular elastomeric material for soft actuators - is cured in a mold with appropriate channel structures and additional strain limiting components.^[137]

Molding can be classified into laminate casting (also known as soft lithography), retractable-pin casting, lost-wax casting, and rotational molding.^[56] Among these, laminate casting is often used in fabricating pneumatic and fluidic actuators, as it enables more versatile internal hollow structures.^[56] Using this method, the main structure of the actuator is fabricated in two or more parts with the open channel, which is then bonded together by adhesives to form the inner microfluidic channels (**Figure 2-13a**). However, the structures tend to fail at the interface. Retractable-pin casting is an alternative method that produces a more mechanically robust structure without the part-bonding steps that enable the fabrication of relatively simple internal structures. To generate complex internal structures while maintaining mechanical integrity, a potential solution is lost-wax casting by utilizing wax as the mold that melts upon heating. Rotational molding, usually used in manufacturing large size plastic tubes and containers, has the

advantage of producing uniformly thick walls but lacks the capability to produce complex structures.^[138] Marchese et al. designed a variety of structures of hydraulic actuators and proposed different molding recipes for rapid prototyping, according to their structural complexity and desired actuation performances.^[56] Notably, three structures were fabricated, including cylindrical (retractable pin), ribbed (lamine casting and lost wax), and pleated shapes (lost wax). Upon comparing performances such as actuator stiffness, output forces, and required input pressure of the three actuator morphologies, a suitable and reliable fabrication method was suggested for the desired performance.

2.4.2 3D Printing

With the development of additive manufacturing, also known as 3D printing, many complex structures can be fabricated with ease without human handling. With a variety of deposition and solidifying methods, structural components with a wide range of resolution and structural complexities can be fabricated. Compared to molding, 3D printing has more flexibility in shaping materials, facilitated by digital design, more material selection from metals, polymers, gels, to composites, more flexibility in material blending, and coextrusion for composites, higher precision due to automatic control, and higher fabrication efficiency. Yirmibesoglu et al. compared molding and 3D printing by fabricating pneumatic actuator structures with different levels of complexity. He found that fabricating the same structures with the same material, 3D printed actuators perform better or match the performance of the molded counterparts, in addition to the better fabrication reliability and simpler fabrication processes.^[136]

A variety of 3D printing techniques have been developed to meet specific application and material requirements, with a wide range of resolutions from several to hundreds of microns.^[57]

Fused deposition modeling (FDM) is the most commonly used technique for prototyping

structures with thermoplastic materials such as acrylonitrile butadiene styrene (ABS) and polylactic acid (PLA). In FDM, the 3D shapes, previously designed in software, are generated with a heated nozzle extruding and depositing molten polymers in layers on a heated stage moving in the third dimension. The FDM process can help produce complex inner structures using multiple materials, but the current lack of process compatible soft materials limits its application in fabricating soft actuators.

In order to print soft materials for stretchable and compliant devices, direct ink writing (DIW) with a variety of elastic polymers such as silicones^[139], hydrogels^[140], and liquid crystal elastomers^[141] has been reported. The DIW printing process starts with the preparation of viscoelastic ink with appropriate viscosity that is pumped out through the nozzle controllably at programmed positions, followed by the solidification treatment. Multiple inks can be mixed before the extrusion process to tune the mechanical properties of the printed materials^[142], or extruded from several nozzles to form different functional part of the object^[143]. For example, a multi-material DIW platform, shown in Figure 2-13c, was used to fabricate objects mimicking the biological, mechanical gradient. A 3D printed hand that resembles the shape and the mechanical gradient of a human's hand is shown in Figure 2-13d, with local modulus values spanning three orders of magnitude.^[142] Another multi-material 3D printing approach is extruding different materials from different nozzles. Zhang et al. reported a stiffness-tunable pneumatic actuator, with different components printed in one process via a commercial multi-material 3D printer. A variable-stiffness pneumatic actuator is fabricated with incorporated shape memory polymers and heating elements via 3D printing.^[143] Other examples of 3D printed actuators include dielectric elastomer actuators^[144], hydrogel actuators that respond to multiple stimuli^[145], magnetically activated actuators^[59], liquid crystal polymer actuators^[146], etc.

2.4.3 Thin-film Fabrication

Maybe the most common and essential shape in soft actuators are films. In some cases, films are considered as the main body of the actuator that is responsible for the designed function.^[147] In other cases, films in soft actuators can serve as the strain limiting layers in bending actuators^[31], as flexible electrodes that help generate the electric field in DEAs, as a functional outer layer to facilitate unique interactions with the environment.^[93,148,149] and as the active layer in the laminates that generate the unique motions such as bending and twisting^[31,150]. For example, the DEA is a typical film-based soft actuator, which is basically composed of a thin DE film sandwiched by two even thinner compliant electrode layers.^[120] Depending on the material properties and morphological parameters, a variety of fabrication techniques such as dip coating, spin coating, spray coating, blade casting, screen printing, inkjet printing, etc., can be used to form films, see Figure 2-13c. These techniques apply viscous polymer fluids to a substrate and form uniform films with thicknesses ranging from nanometers to millimeter-scale^[151] followed by appropriate solidification. Fabricating a free-standing film usually requires a flat and rigid substrate with low surface energy, while applying a functional layer in the form of a film on a substrate to make layered structures needs to consider the substrate surface roughness and the interfacial strength. Considering the material and structural diversity of soft actuators, current thin-film fabrication processes still require improvement for better uniformity, handling, control of residual stresses, precise deposition, and lamination.

Among the various film fabrication techniques, dip coating^[152], spin coating^[153], and drop-casting^[154] are the most common and convenient bench-top techniques for rapid prototyping of soft actuators, with the film thickness ranging from several microns to submillimeter and size of several square centimeters. The processes are relatively simple and are compatible with polymer

fluids with a range of viscosities. Drop-casting is the simplest method in which a predetermined amount of fluid is added onto a substrate to form a uniform layer. However, it is limited to low viscosity fluids and a small coating area. Spin coating is a fast process, where droplets of polymer applied at the center of a substrate are evenly spread by rapid substrate rotation. Dip coating is a slow process where a substrate with the necessary shape is immersed into a liquefied polymer and removed at a specified speed. Here the film thickness is tunable by solution viscosity, speed of withdrawal, and the number of dipping steps.

Conductive films are often required to be patterned on soft actuators for electrical actuation and sensing, such as compliant electrodes for DEAs, electrothermal coating for bilayer actuators, interdigitated electrodes for electro-adhesive devices and resistive sensors for strain detection. Precision patterning of conductive films is important for both mechanical compliance and specific functions such as electro-adhesion. To create patterned films, a variety of techniques including screen printing, soft lithography, and inkjet printing, are employed. In screen printing, the ink is pushed through a screen with a patterned mask and selectively penetrates through the screen mesh, leaving a patterned thin layer on the substrate that is later solidified by solvent evaporation, heat, or UV exposure.^[155] Soft lithography is typically used in microfluidic devices to pattern the internal channels and is also useful to fabricate thin films with nanoscale surface topologies.^[156] In comparison, inkjet printing is mask-less and contact-less and has the advantage of larger-scale production and fewer human errors.^[58] Inkjet printing is similar to FDM in a way that they both extrude the fluidic material out of the nozzle onto a substrate that subsequently solidifies it. While inkjet printing is designed for 2D fabrication, the FDM is meant for 3D shapes. Therefore, the parameters crucial in the FDM process, including the material viscosity, nozzle size, drop height, curing speed, are also crucial in inkjet printing for pattern resolution and

precision. Additionally, the interface compatibility and strength between the printed material and substrate also needs to be taken into account for inkjet printing.

2.4.4 Self-assembly

With the increasing trend of device miniaturization, nanofabrication for functional structures with sub-micron features is becoming more important. Self-assembly of structures is fundamental in nature and it provides an attractive route for fabricating miniaturized structures in engineering synthesis. It is an autonomous process to aggregate components into stable and functionalized structures due to specific local interactions under certain physical or chemical conditions.^[157] Self-assembly takes place at the molecular level or higher, where the components and the surrounding environment have mutual recognition properties. These properties can lead to non-covalent or weak covalent interactions between molecules or higher-level interactions due to external influences such as electromagnetic field and surface tension.^[158] These interactions responsible for building nano- or mesostructures can be initiated and tuned by chemical and physical stimuli to direct the self-assembly processes and increase the structural complexity.^[159]

The published literature in employing self-assembly techniques in soft actuator fabrication are few. Liquid crystal elastomer (LCE) is one type of material that undergoes self-assembly during fabrication. LCEs have been utilized as stimuli-responsive materials for soft actuators that are able to change shape based on the arrangement of the self-assembled liquid crystal (LC) molecules.^[54,160] Ware et al reported LCE-based actuators with programmable shape changes by creating complex profiles of self-assembled LCs using an optical patterning method.^[54] Another example of self-assembly is in the nanostructured block copolymer. The linear block copolymer, styrene-ethylene-butylene-styrene (SEBS), self-assembles into micellar structures surrounded by

rubbery matrix, as a result of incompatibility between two polymer segments in the supramolecule. Such physically cross-linked copolymer elastomer has been investigated as DEA with tunable electromechanical behavior via modification of mechanical stiffness and polarizability.^[53]

Mechanical self-assembly is from a totally different perspective, and it is often utilized to structure soft actuators. Mechanical self-assembly refers to the spontaneous shape deformation due to strain-induced mechanical instability.^[161] Strain in soft materials is relatively easily developed by stretching, swelling, thermal expansion, etc., and therefore provides a powerful yet simple solution to soft actuator structuring. For example, using a simple stretch-attach-release process, a variety of 3D structures can be obtained.^[161] Typical structures such as helical ribbons, rolled tubes, multistable multilayers are generated by stretching and mechanically restraining the strain with certain boundary conditions. Amon et al. investigated the chiral-forming mechanism of seed pod and experimentally mimicked the structure via the stretch-attach-release route. By cutting a strip from a laminate at various angles to the stretch direction, different helical configurations were obtained (Figure 2-13d).^[162] Shao et al. reported bistable DEAs based on this principle.^[31] Particularly, the bilateral stretch on two DE films is supported by a stiff middle layer. The release of external forces results in self-shaping into two bent shapes. Structural diversity of the bistable DEAs is achieved by tuning the internal (mechanical properties of the material) and external (stretch, the direction of stretch) parameters.

2.4.5 Textile-based Methods: A Conventional but Renewed Approach

The conventional textile processes have been recently used to fabricate soft actuators. Textile processes are designed to transform various polymers into fine fibrous structures such as fibers,

yarns, and fabrics and assemble them into products in our daily life, providing potential solutions to multiple challenges in the fabrication and integration of soft actuators. First of all, the two basic textile structures, i.e., fibers and films, have unique structural features such as huge surface area and anisotropic mechanical properties that are important to the actuation performance of soft actuators. Second, textile processes from fiber spinning to fabric assembly can produce a variety of structures from elementary level (fiber) to higher levels (e.g., fabrics), providing potential approaches to actuator structuring and integration. Third, the large-scale fabrication of textiles can accelerate the production speed of soft actuators from current bench-top techniques. Lastly, with the increasing need of intelligent human interfaces such as haptic devices, smart wearables, and rehabilitation devices, textile products can serve as ideal substrates that provide structural integrity, flexibility, comfort, and desired mechanical properties to integrate soft actuators to the near-human environment.

Figure 2-13h-j presents schematics of three major textile manufacturing steps, including fiber extrusion (or, spinning), yarn twisting (also known as spinning), and fabric assembly. Similar to extrusion-based 3D printing, fiber extrusion is a fast process to produce continuous 1D structures. The unique macro- and microstructures of fibers formed during extrusion bring about excellent properties for soft actuators. For example, the extremely large aspect (length/diameter) ratio of fibers leads to low bending stiffness and large surface area that can improve the mechanical flexibility and stimuli-responsiveness of the fiber-shaped actuators. Stimuli-induced radial expansion of some fibers due to the anisotropic response originating from the molecular alignment during the spinning process has been utilized for actuation.^[106] Extrusion of fibers with multiple polymeric components and different cross-section shapes can be used for structural designs of soft actuators. For example, Arora et al. proposed fiber-shaped DEAs with a trilayered

core-sheath structure, where the inner core and outer layer are conductive, and the middle layer is a dielectric.^[65] Kanik et al. reported a bicomponent fiber actuator by coextrusion.^[73] Here two materials with different thermal expansion coefficients were parallelly extruded to form a bicomponent fiber that actuates due to differential thermal expansion.

Highly twisted fibers and yarns have been used to fabricate TCP actuators that exhibit remarkable actuation behavior and largely outperform other soft actuators.^[106,111] More details of this type of actuator are provided in section 0. The TCPs reported thus far, however, are typically limited in length due to the currently used two-end-tethered twisting process. As an old technique in the textile industry, twisting is a large-scale continuous process that can produce yarns of thousands of meters (Figure 2-13e). Adapting such a continuous twisting method for TCP fabrication can open up new applications and markets.

In textiles, yarns are assembled into fabrics in almost infinite varieties of periodic patterns (or designs) by weaving, knitting, braiding, etc. They have distinct mechanical properties due to their structural features and can potentially open up new approaches to design soft actuators.^[163] Fabrics can be used as actuator structures or substrates to provide reliable mechanical integrity and a means of system integration. For example, electroactive polymers were coated onto passive fabrics with different structures (knitted and woven) to construct textile actuators that can produce tunable forces.^[164] Shape memory fibers were woven into a fabric to generate bending and twisting motions.^[165] Moisture-sensitive yarns were knitted into a fabric that contracts under increasing humidity.^[166]

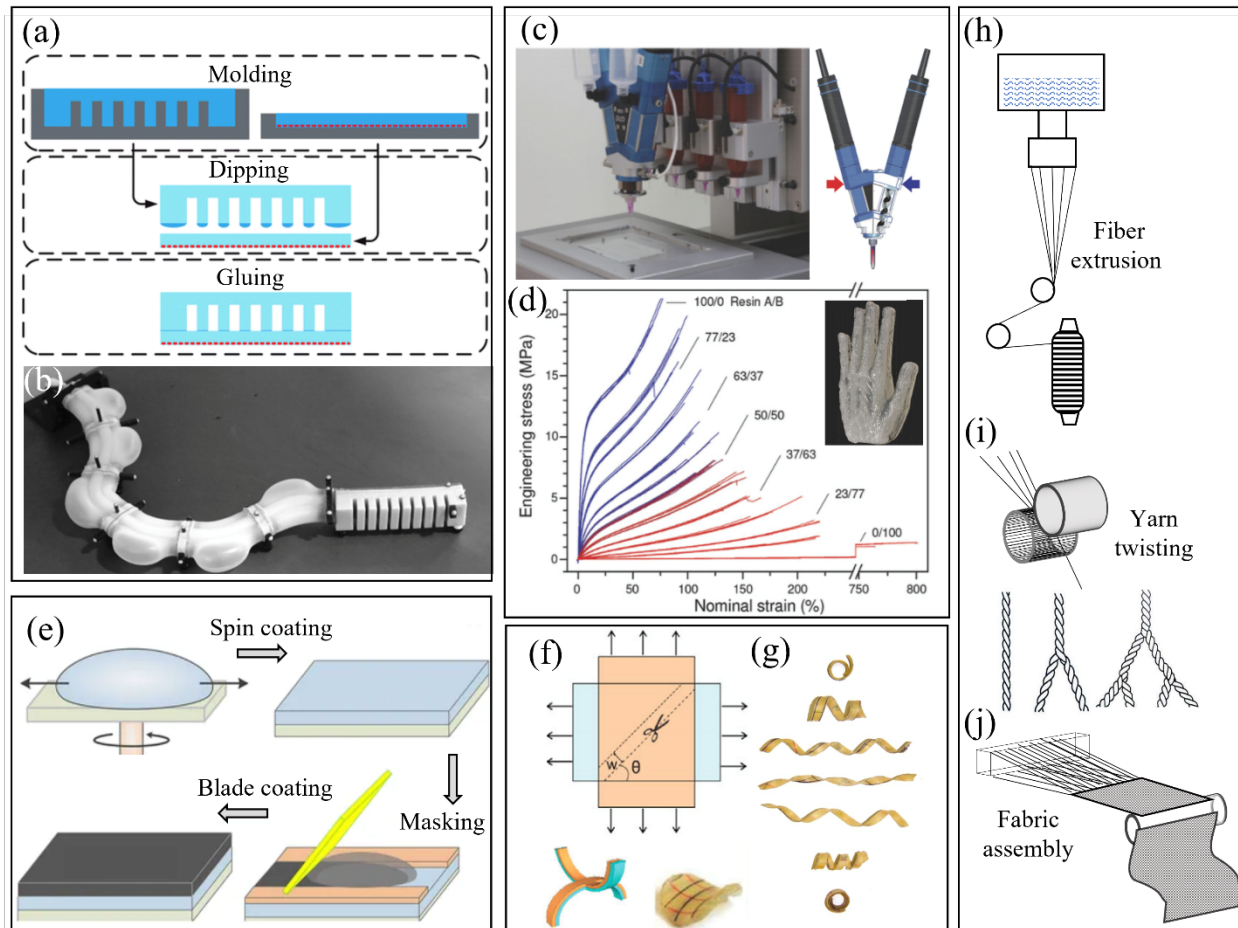


Figure 2-13. Fabrication techniques for soft actuators. (a) Molding processes and (b) a soft pneumatic actuator fabricated by molding. (c) A multi-material printing machine (d) the tunable mechanical properties of the printed object. (e) Schematic of spin coating and blade coating processes to make bilayer structures. (f) Fabrication of mechanically self-assembled structures, and (g) the self-assembled helical structures. (h-j) Schematic of textile processes from fiber spinning, yarn twisting, to fabric assembly. (a-b) Reprinted with permission from [156] under CC-BY license. (c-d) Reprinted with permission from [142]. Copyright 2018 John Wiley and Sons. (e) Reprinted under CC BY license [150]. (f-g) Reprinted with permission by [162]. Copyright 2011, American Association for the Advancement of Science.

2.4.6 Soft Actuator Fabrication: Opportunities and Challenges

The biggest advantages of soft actuator fabrication are the diversity of soft materials and their ease of processing. In general, thermoplastic (e.g., nylon, polypropylene, polyethylene) and thermoset (e.g., silicone, polyurethane) polymers constitute two major types of soft materials for actuators. The property of phase change between bulk solid and viscous liquid near the melting

point (T_m) enables the flexibility in shaping thermoplastic polymers. The characteristics associated with melting, melt-flow, and subsequent solidification are well-understood for the fiber-forming polymers in the textile industry and are recently adopted by polymer inkjet printing in 2D and extrusion-based 3D printing for structuring soft actuators. On the contrary, thermoset polymers transform from liquid or soft solid to harder solid under heat, during which non-reversible chemical reactions take place to interlock individual molecules in a chemical network through the process of crosslinking. Other crosslinking methods include ultraviolet (UV) radiation, mixing with catalyst, and even adding water (for hydrogel). Two-part silicone products are the most common thermoset polymers in prototyping soft actuators, primarily due to their great variety of crosslinking methods, reaction time, liquid viscosity, and the mechanical properties of the cured elastomer.

A variety of fabrication methods cover the soft actuator size ranging from micrometers to meters with complex shapes. While molding and 3D printing are widely used to create 3D shapes, spin coating and blade coating are commonly used for uniform and thin 2D films. Soft lithography and self-assembly are able to create nanoscale and microscale features, and the resultant ultrathin films are ideal for electronic device miniaturization. Textile processes, although not yet widely utilized in soft actuator fabrication, have recently gained attention due to their potential to produce unique functionalities, promising structural hierarchies, and scaled-up manufacturing. Intensive interest in wearables research has also drawn attention to textiles.

Despite the advantage in soft material processing and the rapid advancement of fabrication techniques, there are still ongoing issues that remain to be addressed. These issues include delamination between individually fabricated parts as a result of poor interfacial strength, precision during multi-process fabrication, undesired internal stresses due to thermal expansion

or solvent evaporation, interconnects for conductive pathway, etc. Unlike conventional rigid actuators that are composed of individually manufactured parts and discretely joined components with fasteners, soft actuators typically have their functional components seamlessly merged together without additional “screws”. Therefore, creating complex architectures using multiple materials with strong interfacial bonding is challenging. For example, the fabrication of silicone-based pneumatic/hydraulic actuators are convenient with molding technology. However, the sophisticated macro to micro internal channel fabrication is difficult. Solutions to this issue can be molding several subparts and then glue parts together or removing the supportive inner core by dissolving or other means. When it comes to sticking parts together, the bonding strength and alignment of parts are two major concerns. The bonding strength between different parts, generally speaking, is determined by the various interfaces from relatively flat surfaces to fibrous surfaces and to dispersed-particle laden surfaces. It also involves various materials with similar or dissimilar mechanical and chemical properties. Approaches to enhance interfacial strength include surface treatment (e.g., plasma activation) and the development of stronger adhesives. Another issue is introducing or eliminating internal stresses in the soft actuators. When internal stress is necessary for energy storage (e.g. prestressed elastomer film), it is important to employ techniques to stretch uniformly, uniaxially, or biaxially, and subsequently maintain the stress for subsequent processes. In many cases, the internal stress built up during fabrication is unwanted and may lead to structural deformation and instability. This problem is more predominant in fabricating thin laminates with soft materials, where the internal stresses are induced from solvent evaporation, temperature variation, and handling that results in undesirable film bending and wrinkling.

In general, improved and diverse fabrication techniques that are scalable instead of benchtop manual assembly are needed to achieve multiple functionalities such as flexibility with structural integrity, ease of energy/stimuli input, and control.

2.5 Conclusion

The need for reliable actuators that are soft, compact, powerful, fast, and lightweight is increasing and is currently mostly unmet. As more actuation principles and materials are explored for greater performance, the structural complexities of the devices are increasing. In this review, we discuss the relationship between actuator structure and the resulting motions. We begin with a review of how natural actuators produce diverse performance by utilizing hierarchical structures and discuss how manmade actuators can benefit through the understanding of natural designs. We then review the variety of motions generated by manmade soft actuators and the related structural designs. Finally, we present a discussion of current and potential fabrication methods for soft actuators.

The biological organisms produce remarkable actuation motions by assembling lower-level actuators into larger structures in a hierarchical manner. While the 1st level actuators (motor cells) only exhibit monotonic motions and microscale forces, the 2nd level actuators (tissues) constructed by bundling, layering, and other forms produce diverse motions and enhanced output forces. The 3rd level actuators (organs) generate visible actuation motions of the biological organisms to physically interact with the external world. The 3rd level actuators are assembled from the 2nd level actuators and other supportive elements, sharing similar structural design principles as the 2nd level actuator. Simplified models have been proposed to effectively explain the diversity of natural actuation phenomena and provide guidance for the design of soft

actuators. Compared to the well-evolved biological actuators, soft manmade actuators are still in its infancy, with relatively simple structures and limited motions. The most common motions produced by manmade soft actuators, including linear extension and contraction, bending, twisting, and folding, have been achieved by constructing responsive materials into mostly rudimentary structures, such as laminated layers of DEs for linear displacement and placing reinforcing fibers in pneumatic actuators for tunable and anisotropic actuation. Some deviation from this to more complex designs for multiple DOF motion and rapid motion have been reported.

Exploring and adopting the key elements of biological actuators/motors to produce controlled artificial motion is challenging but potentially rewarding. This rapidly advancing research area is at the confluence of some of the primary disciplines of science and engineering and is deeply interdisciplinary. The mimicry of biological structures has opened up limited but significant pathways for improvements in soft manmade actuators. One of the reasons for the little success is the deficiency of current fabrication techniques. Currently, fabrication methods such as molding, 3D printing, as well as many thin-film fabrication and deposition techniques are employed to make various structures for soft actuators. However, such problems as structural scalability (nano- and micro-actuators), precision, multi-material fabrication, complex inner structures (hollow structure), and large-scale manufacturing remain challenging. Additional challenges arise from the seamless integration of often mechanically incompatible components such as sensors, power supplies, and processors into a functional system. Elegant but simple and practical ideas to solve these and other problems in designing soft actuators may just be there in the natural mechanisms around us. Nature produces useful functions at the least energetic and materials cost using hierarchical structures. In living systems, motions to perform complex tasks

originate in muscles. Successful artificial systems can just be based on mimicking the motions using available mechanisms rather than trying to copy the mechanism of muscles; biomimicry and bioinspiration should not be seen as bio-replication. Abstracting good ideas from living systems to stimulate the invention of new processes or functional solutions may open up unlimited opportunities, now and in the future.

References

- [1] A. W. Feinberg, *Annual Review of Biomedical Engineering*. **2015**, *17*, 243.
- [2] R. J. Morris, M. Blyth, *J Exp Bot*. **2019**, *70*, 14.
- [3] I. Burgert, P. Fratzl, *Philosophical Transactions of the Royal Society of London A: Mathematical, Physical and Engineering Sciences*. **2009**, *367*, 1541.
- [4] C. Dawson, J. F. V. Vincent, A.-M. Rocca, *Nature*. **1997**, *390*, 668.
- [5] U. G. K. Wegst, H. Bai, E. Saiz, A. P. Tomsia, R. O. Ritchie, *Nature Materials*. **2015**, *14*, 23.
- [6] L. Eadie, T. K. Ghosh, *Journal of The Royal Society Interface*. **2011**, *8*, 761.
- [7] H. Lee, B. P. Lee, P. B. Messersmith, *Nature*. **2007**, *448*, 338.
- [8] K. B. Golovin, J. W. Gose, M. Perlin, S. L. Ceccio, A. Tuteja, *Philosophical Transactions of the Royal Society A: Mathematical, Physical and Engineering Sciences*. **2016**, *374*, 20160189.
- [9] S. M. Mirvakili, I. W. Hunter, *Advanced Materials*. **2018**, *30*, 1704407.
- [10] S. Aziz, G. M. Spinks, *Mater. Horiz*. **2020**, *7*, 667.
- [11] F. Schmitt, O. Piccin, L. Barbé, B. Bayle, *Front. Robot. AI*. **2018**, *5*, 84.
- [12] M. Bengisu, M. Ferrara, in *Materials That Move: Smart Materials, Intelligent Design*. Springer International Publishing, Cham, **2018**, pp. 39–48.
- [13] J. Braam, *New Phytologist*. **2005**, *165*, 373.
- [14] B. Bar-On, X. Sui, K. Livanov, B. Achrai, E. Kalfon-Cohen, E. Wiesel, H. Daniel Wagner, *Appl. Phys. Lett*. **2014**, *105*, 033703.
- [15] J. A. Hill, E. N. Olson, in *Muscle*, Elsevier, **2012**, pp. 3–9.
- [16] J. Feher, in *Quantitative Human Physiology*, Elsevier, **2017**, pp. 351–361.
- [17] J. F. Campbell, H. K. Kaya, *Nature*. **1999**, *397*, 485.
- [18] S. N. Patek, W. L. Korff, R. L. Caldwell, *Nature*. **2004**, *428*, 819.
- [19] Q. Guo, E. Dai, X. Han, S. Xie, E. Chao, Z. Chen, *Journal of The Royal Society Interface*. **2015**, *12*, 20150598.
- [20] Y. Forterre, J. M. Skotheim, J. Dumais, L. Mahadevan, *Nature*. **2005**, *433*, 421.
- [21] X. Noblin, N. O. Rojas, J. Westbrook, C. Llorens, M. Argentina, J. Dumais, *Science*. **2012**, *335*, 1322.
- [22] R. L. Lieber, J. Friden, *Journal of Applied Physiology*. **1993**, *74*, 520.
- [23] M. Ueda, Y. Nakamura, *Plant & cell physiology*. **2007**, *48*, 900.
- [24] N. Kamiya, M. Tazawa, T. Takata, *Protoplasma*. **1963**, *57*, 501.
- [25] R. J. Baskin, P. J. Paolini, *Journal of General Physiology*. **1966**, *49*, 387.
- [26] P. Fratzl, R. Elbaum, I. Burgert, *Faraday Discuss*. **2008**, *139*, 275.
- [27] I. Burgert, M. Eder, N. Gierlinger, P. Fratzl, *Planta*. **2007**, *226*, 981.
- [28] R. Elbaum, L. Zaltzman, I. Burgert, P. Fratzl, *Science*. **2007**, *316*, 884.
- [29] Z. Chen, Q. Guo, C. Majidi, W. Chen, D. J. Srolovitz, M. P. Haataja, *Phys. Rev. Lett*. **2012**, *109*, 114302.
- [30] J. Lin, Q. Guo, S. Dou, N. Hua, C. Zheng, Y. Pan, Y. Huang, Z. Chen, W. Chen, *Extreme Mechanics Letters*. **2020**, *36*, 100653.
- [31] H. Shao, S. Wei, X. Jiang, D. P. Holmes, T. K. Ghosh, *Advanced Functional Materials*. **2018**, *28*, 1802999.
- [32] J. A. Faber, A. F. Arrieta, A. R. Studart, *Science*. **2018**, *359*, 1386.
- [33] J. Brackenbury, *Nature*. **1997**, *390*, 453.
- [34] H.-T. Lin, D. J. Slate, C. R. Paetsch, A. L. Dorfmann, B. A. Trimmer, *Journal of Experimental Biology*. **2011**, *214*, 1194.

- [35] S. L. Cunningham, *Ph.D. Thesis*, Massachusetts Institute of Technology, **1963**.
- [36] S. J. Gerbode, J. R. Puzey, A. G. McCormick, L. Mahadevan, *Science*. **2012**, 337, 1087.
- [37] P. B. Dobrin, *Physiological reviews*. **1978**, 58, 2.
- [38] R. C. Webb, *Advances in Physiology Education*. **2003**, 27, 201.
- [39] J. Wood, W. Perkins, *American Journal of Physiology-Legacy Content*. **1970**, 218, 762.
- [40] C. V. Anderson, *Sci Rep*. **2016**, 6, DOI 10.1038/srep18625.
- [41] H. C. Astley, A. Haruta, T. J. Roberts, *Journal of Experimental Biology*. **2015**, 218, 3360.
- [42] G. M. Farley, M. J. Wise, J. S. Harrison, G. P. Sutton, C. Kuo, S. N. Patek, *Journal of Experimental Biology*. **2019**, 222, DOI 10.1242/jeb.201129.
- [43] T. I. Zack, T. Claverie, S. N. Patek, *Journal of Experimental Biology*. **2009**, 212, 4002.
- [44] M. M. Peplowski, R. L. Marsh, *Journal of Experimental Biology*. **1997**, 200, 2861.
- [45] C. V. Anderson, S. M. Deban, *PNAS*. **2010**, 107, 5495.
- [46] S. N. Patek, M. V. Rosario, J. R. A. Taylor, *Journal of Experimental Biology*. **2012**, 1317.
- [47] P. J. Schaeffer, S. L. Lindstedt, in *Comprehensive Physiology*, American Cancer Society, **2013**, pp. 289–314.
- [48] G. M. Spinks, *Advanced Materials*. **2019**, 1904093.
- [49] L. Zhang, H. Liang, J. Jacob, P. Naumov, *Nature Communications*. **2015**, 6, 7429.
- [50] Q. M. Zhang, H. Li, M. Poh, F. Xia, Z.-Y. Cheng, H. Xu, C. Huang, *Nature*. **2002**, 419, 284.
- [51] K. B. Subramani, E. Cakmak, R. J. Spontak, T. K. Ghosh, *Advanced Materials*. **2014**, 26, 2949.
- [52] X. Fang, A. Li, O. Yildiz, H. Shao, P. D. Bradford, T. K. Ghosh, *Carbon*. **2017**, 120, 366.
- [53] R. Shankar, T. K. Ghosh, R. J. Spontak, *Adv. Mater.* **2007**, 19, 2218.
- [54] T. H. Ware, M. E. McConney, J. J. Wie, V. P. Tondiglia, T. J. White, *Science*. **2015**, 347, 982.
- [55] B. Mosadegh, P. Polygerinos, C. Keplinger, S. Wennstedt, R. F. Shepherd, U. Gupta, J. Shim, K. Bertoldi, C. J. Walsh, G. M. Whitesides, *Advanced Functional Materials*. **2014**, 24, 2163.
- [56] A. D. Marchese, R. K. Katzschmann, D. Rus, *Soft Robotics*. **2015**, 2, 7.
- [57] T. D. Ngo, A. Kashani, G. Imbalzano, K. T. Q. Nguyen, D. Hui, *Composites Part B: Engineering*. **2018**, 143, 172.
- [58] N. Berdozzi, Y. Chen, L. Luzi, M. Fontana, I. Fassi, L. Molinari Tosatti, R. Vertechy, *IEEE Robotics and Automation Letters*. **2020**, 5, 2770.
- [59] S. Sundaram, M. Skouras, D. S. Kim, *Science Advances*. **2019**, 15.
- [60] A. L. Duigou, M. Castro, *Scientific Reports*. **2016**, 6, 18105.
- [61] W. Wang, L. Yao, C.-Y. Cheng, T. Zhang, H. Atsumi, L. Wang, G. Wang, O. Anilonyte, H. Steiner, J. Ou, K. Zhou, C. Wawrousek, K. Petrecca, A. M. Belcher, R. Karnik, X. Zhao, D. I. C. Wang, H. Ishii, *Science Advances*. **2017**, 3, e1601984.
- [62] S. Coyle, C. Majidi, P. LeDuc, K. J. Hsia, *Extreme Mechanics Letters*. **2018**, 22, 51.
- [63] Ohta, P., Valle, L., King, J., Low, K., Yi, J., Atkeson, C. G., Park, Y. L, *Soft robotics*, **2018**, 5, 2.
- [64] P. Chakraborti, H. A. K. Toprakci, P. Yang, N. Di Spigna, P. Franzon, T. Ghosh, *Sensors and Actuators A: Physical*. **2012**, 179, 151.
- [65] S. Arora, T. Ghosh, J. Muth, *Sensors and Actuators A: Physical*. **2007**, 136, 321.
- [66] C. S. Haines, N. Li, G. M. Spinks, A. E. Aliev, J. Di, R. H. Baughman, *PNAS*. **2016**, 113, 11709.

- [67] E. T. Roche, M. A. Horvath, I. Wamala, A. Alazmani, S.-E. Song, W. Whyte, Z. Machaidze, C. J. Payne, J. C. Weaver, G. Fishbein, J. Kuebler, N. V. Vasilyev, D. J. Mooney, F. A. Pigula, C. J. Walsh, *Science Translational Medicine*. **2017**, *9*, 373.
- [68] J. D. W. Madden, N. A. Vandesteeg, P. A. Anquetil, P. G. A. Madden, A. Takshi, R. Z. Pytel, S. R. Lafontaine, P. A. Wieringa, I. W. Hunter, *IEEE Journal of Oceanic Engineering*. **2004**, *29*, 706.
- [69] F. Carpi, C. Salaris, D. D. Rossi, *Smart Mater. Struct.* **2007**, *16*, S300.
- [70] F. Connolly, P. Polygerinos, C. J. Walsh, K. Bertoldi, *Soft Robotics*. **2015**, *2*, 26.
- [71] D. Yang, M. S. Verma, J.-H. So, B. Mosadegh, C. Keplinger, B. Lee, F. Khashai, E. Lossner, Z. Suo, G. M. Whitesides, *Advanced Materials Technologies*. **2016**, *1*, 1600055.
- [72] J. Hu, Y. Zhu, H. Huang, J. Lu, *Progress in Polymer Science*. **2012**, *37*, 1720.
- [73] M. Kanik, S. Orguc, G. Varnavides, J. Kim, T. Benavides, D. Gonzalez, T. Akintilo, C. C. Tasan, A. P. Chandrakasan, Y. Fink, P. Anikeeva, *Science*. **2019**, *365*, 145.
- [74] J. A. Lee, Y. T. Kim, G. M. Spinks, D. Suh, X. Lepró, M. D. Lima, R. H. Baughman, S. J. Kim, *Nano Lett.* **2014**, *14*, 2664.
- [75] W. C. Röntgen, *Ann. Phys.* **1880**, *247*, 771.
- [76] A. O'Halloran, F. O'Malley, P. McHugh, *Journal of Applied Physics*. **2008**, *104*, 071101.
- [77] T. Yamwong, A. M. Voice, G. R. Davies, *Journal of Applied Physics* **2002**, *91*, 1472.
- [78] H. F. Schlaak, M. Jungmann, M. Matysek, P. Lotz, in *Smart Structures and Materials 2005: Electroactive Polymer Actuators and Devices (EAPAD)*. **2005**, pp. 121–133.
- [79] H. S. Jung, S. Y. Yang, K. H. Cho, M. G. Song, C. T. Nguyen, H. Phung, U. Kim, H. Moon, J. C. Koo, J.-D. Nam, H. R. Choi, *International Journal of Control, Automation and Systems*. **2017**, *15*, 25.
- [80] F. Carpi, A. Migliore, G. Serra, D. D. Rossi, *Smart Mater. Struct.* **2005**, *14*, 1210.
- [81] H. Zhao, A. M. Hussain, M. Duduta, D. M. Vogt, R. J. Wood, D. R. Clarke, *Advanced Functional Materials*. **2018**, *28*, 1804328.
- [82] Q. Pei, M. Rosenthal, S. Stanford, H. Prahlad, R. Pelrine, *Smart Mater. Struct.* **2004**, *13*, N86.
- [83] X. Fang, *Ph.D. Thesis*, North Carolina State University, **2017**.
- [84] E. Acome, S. K. Mitchell, T. G. Morrissey, M. B. Emmett, C. Benjamin, M. King, M. Radakovitz, C. Keplinger, *Science*. **2018**, *359*, 61.
- [85] M. Taghavi, T. Helps, J. Rossiter, *Sci. Robot.* **2018**, *3*, 25.
- [86] SynTouch, <https://syntouchinc.com/>, accessed: April, **2021**.
- [87] Soft Robotics - Enabling Machine Builders to do More, <https://www.softroboticsinc.com/>, accessed: April, **2021**.
- [88] ReWalk Robotics - More Than Walking, <https://rewalk.com/>, accessed: April, **2021**.
- [89] Qbrobotics: robotics and automation, <https://qbrobotics.com/>, accessed: April, **2021**.
- [90] Empire Robotics – Agile Robotics Grippers, <http://www.empirerobotics.com/>, accessed: April, **2021**.
- [91] F. Connolly, C. J. Walsh, K. Bertoldi, *PNAS*. **2016**, DOI 10.1073/pnas.1615140114.
- [92] Ching-Ping Chou, B. Hannaford, *IEEE Transactions on Robotics and Automation*. **1996**, *12*, 90.
- [93] A. Rafsanjani, Y. Zhang, B. Liu, S. M. Rubinstein, K. Bertoldi, *Science Robotics*. **2018**, *3*, 15.
- [94] R. V. Martinez, C. R. Fish, X. Chen, G. M. Whitesides, *Advanced Functional Materials*. **2012**, *22*, 1376.

- [95] J. Han, W. Jiang, D. Niu, Y. Li, Y. Zhang, B. Lei, H. Liu, Y. Shi, B. Chen, L. Yin, X. Liu, D. Peng, B. Lu, *Advanced Intelligent Systems*. **2019**, *1*, 1900109.
- [96] A. Miriyev, K. Stack, H. Lipson, *Nature Communications*. **2017**, *8*, 596.
- [97] E. Piskarev, J. Shintake, V. Ramachandran, N. Baugh, M. D. Dickey, D. Floreano, *Advanced Intelligent Systems*. **2020**, *2*, 2000069.
- [98] S. Felton, M. Tolley, E. Demaine, D. Rus, R. Wood, *Science*. **2014**, *345*, 644.
- [99] C. L. Choy, F. C. Chen, K. Young, *Journal of Polymer Science: Polymer Physics Edition*. **1981**, *19*, 335.
- [100] A. Sydney Gladman, E. A. Matsumoto, R. G. Nuzzo, L. Mahadevan, J. A. Lewis, *Nat Mater*. **2016**, *15*, 413.
- [101] K. Kumar, C. Knie, D. Bléger, M. A. Peletier, H. Friedrich, S. Hecht, D. J. Broer, M. G. Debije, A. P. H. J. Schenning, *Nature Communications*. **2016**, *7*, 11975.
- [102] B. Kim, D.-H. Kim, J. Jung, J.-O. Park, *Smart Mater. Struct.* **2005**, *14*, 1579.
- [103] T. Chung, A. Romo-Uribe, P. T. Mather, *Macromolecules*. **2008**, *41*, 184.
- [104] L. Ma, J. Zhao, X. Wang, M. Chen, Y. Liang, Z. Wang, Z. Yu, R. C. Hedden, *Polymer*. **2015**, *56*, 490.
- [105] S. Chen, J. Hu, H. Zhuo, *Composites Science and Technology*. **2010**, *70*, 1437.
- [106] C. S. Haines, M. D. Lima, N. Li, G. M. Spinks, J. Foroughi, J. D. W. Madden, S. H. Kim, S. Fang, M. J. de Andrade, F. Göktepe, Ö. Göktepe, S. M. Mirvakili, S. Naficy, X. Lepró, J. Oh, M. E. Kozlov, S. J. Kim, X. Xu, B. J. Swedlove, G. G. Wallace, R. H. Baughman, *Science*. **2014**, *343*, 868.
- [107] H. Cheng, Y. Hu, F. Zhao, Z. Dong, Y. Wang, N. Chen, Z. Zhang, L. Qu, *Advanced Materials*. **2014**, *26*, 2909.
- [108] M. D. Lima, M. W. Hussain, G. M. Spinks, S. Naficy, D. Hagenasr, J. S. Bykova, D. Tolly, R. H. Baughman, *Small*. **2015**, *11*, 3113.
- [109] A. Mirabedini, S. Aziz, G. M. Spinks, J. Foroughi, *Soft Robotics*. **2017**, *4*, 421.
- [110] J. Foroughi, G. M. Spinks, G. G. Wallace, J. Oh, M. E. Kozlov, S. Fang, T. Mirfakhrai, J. D. W. Madden, M. K. Shin, S. J. Kim, R. H. Baughman, *Science*. **2011**, 1211220.
- [111] Mu J, De Andrade MJ, Fang S, Wang X, Gao E, Li N, Kim SH, Wang H, Hou C, Zhang Q, Zhu M, *Science*. **2019**, *365*, 6449.
- [112] J. W. S. Hearle, P. Grosberg, S. Backer, *Wiley*, **1969**, *1*.
- [113] S. Aziz, *Ph.D Thesis*, University of Wollongong, August, **2017**.
- [114] K. Kim, K. H. Cho, H. S. Jung, S. Y. Yang, Y. Kim, J. H. Park, H. Jang, J.-D. Nam, J. C. Koo, H. Moon, J. W. Suk, H. Rodrigue, H. R. Choi, *Advanced Engineering Materials*. **2018**, *20*, 1800536.
- [115] B. Li, Y.-P. Cao, X.-Q. Feng, H. Gao, *Journal of the Mechanics and Physics of Solids*. **2011**, *59*, 758.
- [116] W. Hu, G. Z. Lum, M. Mastrangeli, M. Sitti, *Nature*. **2018**, *554*, 81.
- [117] M. Di Luca, S. Mintchev, G. Heitz, F. Noca, D. Floreano, *Interface Focus*. **2017**, *7*, 20160092.
- [118] M. Wang, X. Tian, R. H. A. Ras, O. Ikkala, *Advanced Materials Interfaces*. **2015**, *2*, 1500080.
- [119] S. Shian, K. Bertoldi, D. R. Clarke, *Adv. Mater.* **2015**, *27*, 6814.
- [120] M. Duduta, D. R. Clarke, R. J. Wood, in *2017 IEEE International Conference on Robotics and Automation (ICRA)*. **2017**, pp. 4346–4351.
- [121] S. Iamsaard, S. J. Aßhoff, B. Matt, T. Kudernac, J. J. L. M. Cornelissen, S. P. Fletcher, N. Katsonis, *Nature Chemistry*. **2014**, *6*, 229.
- [122] K. Jung, J. Nam, H. Choi, *Sensors and Actuators A: Physical*. **2003**, *107*, 183.

- [123] R. F. Shepherd, F. Ilievski, W. Choi, S. A. Morin, A. A. Stokes, A. D. Mazzeo, X. Chen, M. Wang, G. M. Whitesides, *PNAS*. **2011**, *108*, 20400.
- [124] G. Sumbre, Y. Gutfreund, G. Fiorito, T. Flash, B. Hochner, *Science* **2001**, *293*, 1845.
- [125] G. Sumbre, G. Fiorito, T. Flash, B. Hochner, *Nature*. **2005**, *433*, 595.
- [126] W. M. Kier, M. P. Stella, *Journal of Morphology* **2007**, *268*, 831.
- [127] R. V. Martinez, J. L. Branch, C. R. Fish, L. Jin, R. F. Shepherd, R. M. D. Nunes, Z. Suo, G. M. Whitesides, *Advanced Materials*. **2013**, *25*, 205.
- [128] H.-T. Lin, G. G. Leisk, B. Trimmer, *Bioinspir. Biomim.* **2011**, *6*, 026007.
- [129] J. H. de Groot, van L. Johan L, *Proceedings of the Royal Society of London B: Biological Sciences*. **2004**, *271*, 761.
- [130] A. Pal, D. Goswami, R. V. Martinez, *Advanced Functional Materials*. **2019**, 1906603.
- [131] Y. Tang, Y. Chi, J. Sun, T.-H. Huang, O. H. Maghsoudi, A. Spence, J. Zhao, H. Su, J. Yin, *Science Advances*. **2020**.
- [132] G. Kofod, W. Wirges, M. Paajanen, S. Bauer, *Appl. Phys. Lett.* **2007**, *90*, 081916.
- [133] Y. Yang, Y. Liu, Y. Shen, *Advanced Functional Materials*. **2020**, *30*, 1910172.
- [134] T. Agcayazi, K. Chatterjee, A. Bozkurt, T. K. Ghosh, *Advanced Materials Technologies*. **2018**, *3*, 1700277.
- [135] S. Rosset, H. R. Shea, *Applied Physics A*. **2013**, *110*, 281.
- [136] O. D. Yirmibesoglu, J. Morrow, S. Walker, W. Gosrich, R. Cañizares, H. Kim, U. Daalkhajjav, C. Fleming, C. Branyan, Y. Menguc, in *2018 IEEE International Conference on Soft Robotics (RoboSoft)*. **2018**, pp. 295–302.
- [137] B. Gorissen, D. Reynaerts, S. Konishi, K. Yoshida, J.-W. Kim, M. De Volder, *Adv. Mater.* **2017**, *29*.
- [138] H. Zhao, Y. Li, A. Elsamadisi, R. Shepherd, *Extreme Mechanics Letters*. **2015**, *3*, 89.
- [139] M. Schaffner, J. A. Faber, L. Pianegonda, P. A. Rühs, F. Coulter, A. R. Studart, *Nature Communications*. **2018**, *9*, DOI 10.1038/s41467-018-03216-w.
- [140] A. Zolfagharian, A. Z. Kouzani, S. Y. Khoo, I. Gibson, A. Kaynak, in *2016 IEEE Region 10 Conference (TENCON)*. **2016**, pp. 2272–2277.
- [141] C. Yuan, D. J. Roach, C. K. Dunn, Q. Mu, X. Kuang, C. M. Yakacki, T. J. Wang, K. Yu, H. Jerry Qi, *Soft Matter*. **2017**, *13*, 5558.
- [142] D. Kokkinis, F. Bouville, A. R. Studart, *Advanced Materials*. **2018**, *30*, 1705808.
- [143] Y.-F. Zhang, N. Zhang, H. Hingorani, N. Ding, D. Wang, C. Yuan, B. Zhang, G. Gu, Q. Ge, *Advanced Functional Materials*. **2019**, *29*, 1806698.
- [144] A. Chortos, E. Hajiesmaili, J. Morales, D. R. Clarke, J. A. Lewis, *Advanced Functional Materials*. **2020**, *30*, 1907375.
- [145] J. Odent, S. Vanderstappen, A. Toncheva, E. Pichon, T. Wallin, K. Wang, R. F. Shepherd, P. Dubois, J.-M. Raquez, *Journal of Materials Chemistry A*. **2019**, DOI 10.1039/C9TA03547H.
- [146] S. Gantenbein, K. Masania, W. Woigk, J. P. W. Sesseg, T. A. Tervoort, A. R. Studart, *Nature*. **2018**, *561*, 226.
- [147] H. Arazoe, D. Miyajima, K. Akaike, F. Araoka, E. Sato, T. Hikima, M. Kawamoto, T. Aida, *Nature Materials*. **2016**, *15*, 1084.
- [148] Y. Tokudome, H. Kuniwaki, K. Suzuki, D. Carboni, G. Poologasundarampillai, M. Takahashi, *Advanced Materials Interfaces*. **2016**, *3*, 1500802.
- [149] S. Song, M. Sitti, *Advanced Materials*. **2014**, *26*, 4901.
- [150] D. Niu, W. Jiang, H. Liu, T. Zhao, B. Lei, Y. Li, L. Yin, Y. Shi, B. Chen, B. Lu, *Scientific Reports*. **2016**, *6*, 27366.

- [151] F. M. Weiss, T. Töpfer, B. Osmani, S. Peters, G. Kovacs, B. Müller, *Advanced Electronic Materials*. **2016**, 2, 1500476.
- [152] K. P. Becker, Y. Chen, R. J. Wood, *Advanced Functional Materials* **2020**, 30, 1908919.
- [153] Y. Fang, Y. Li, Y. Li, M. Ding, J. Xie, B. Hu, *ACS Appl. Mater. Interfaces*. **2020**, 12, 23689.
- [154] Y. Li, R. Tanigawa, H. Okuzaki, *Smart Mater. Struct.* **2014**, 23, 074010.
- [155] A. Koivikko, E. Sadeghian Raei, M. Mosallaei, M. Mäntysalo, V. Sariola, *IEEE Sensors Journal*. **2018**, 18, 223.
- [156] Y. Chen, Z. Wang, M. M. Kulkarni, X. Wang, A. M. Al-Enizi, A. A. Elzatahry, J. F. Douglas, A. V. Dobrynin, A. Karim, *ACS Omega*. **2018**, 3, 15426.
- [157] D. Philp, J. F. Stoddart, *Angewandte Chemie International Edition in English*. **1996**, 35, 1154.
- [158] G. M. Whitesides, B. Grzybowski, *Science*. **2002**, 295, 2418.
- [159] M. Grzelczak, L. M. Liz-Marzán, R. Klajn, *Chemical Society Reviews* **2019**, 48, 1342.
- [160] M. Camacho-Lopez, H. Finkelmann, P. Palffy-Muhoray, M. Shelley, *Nature Materials*. **2004**, 3, 307.
- [161] Z. Chen, G. Huang, I. Trase, X. Han, Y. Mei, *Phys. Rev. Applied* **2016**, 5, 017001.
- [162] S. Armon, E. Efrati, R. Kupferman, E. Sharon, *Science*. **2011**, 333, 1726.
- [163] N.-K. Persson, J. G. Martinez, Y. Zhong, A. Maziz, E. W. H. Jager, *Advanced Materials Technologies*. **2018**, 3, 1700397.
- [164] A. Maziz, A. Concas, A. Khaldi, J. Stålhand, N.-K. Persson, E. W. H. Jager, *Science Advances*. **2017**, 3, e1600327.
- [165] M.-W. Han, M.-S. Kim, S.-H. Ahn, *Composites Part B: Engineering*. **2020**, 108170.
- [166] T. Jia, Y. Wang, Y. Dou, Y. Li, M. J. de Andrade, R. Wang, S. Fang, J. Li, Z. Yu, R. Qiao, Z. Liu, Y. Cheng, Y. Su, M. Minary-Jolandan, R. H. Baughman, D. Qian, Z. Liu, *Advanced Functional Materials*. **2019**, 29, 1808241.

Chapter 3 Bioinspired Actuation and Morphing in Textiles

3.1 Introduction

While conventional textiles serve as passive covers (clothing, carpet, etc.) and tools (rope, fishing net, etc.) in every aspect of human life, new functionalities such as sensing and actuation are being incorporated into textiles to achieve “smartness” akin to living organisms. Textiles-based actuators have potential applications in many emerging areas of smart wearables, as textiles have evolved as human-environment interfaces (e.g., clothes, gloves) and human factors such as biomechanics and comfort, durability, as well as aesthetics have already been part of the development.

The ability to controllably actuate fiber or fabric elements in textiles for active movement and generating force could be an important innovation in smart textiles. These actuation elements have been integrated for various end-use applications including shape-morphing apparels for thermoregulation[1], smart gloves for rehabilitation[2] and augmented realities[3], exoskeletal suits for motion assistance[4], artificial muscles for robotics[5], etc. Many of these developments are based on movements in plants and other natural organisms, whose marvelous actuation behavior have evolved over many thousands of years for optimal efficiency, functionality, as well as survival and adaptation. For example, fibers have been utilized as the unique shape for skeletal muscle cells to best exploit their contractile actuation[6], and as the mechanically anisotropic fillers on the plants’ cell wall to tune their swelling response[7].

For the following discussion, we consider textile actuators as those having textile constituents (fibers, yarns, fabrics) as active or supportive parts in an active-morphing system. For example, shape memory fiber (SMF) is a fiber-level textile actuator that changes shape at elevated temperature. SMFs integrated into a fabric produces a fabric-level actuator that can bend, twist, or contract[8], [9]. In another instance, textile fibers and fabrics are used in

conjunction with soft pneumatic actuators as mechanical modifiers to guide the pressure-induced deformation pattern[2]. Textile-based actuators can be potentially fabricated in a variety of structures ranging from micro- to meter-scales based on the use of shape-responsive fibers, in the form of yarns or fabrics. These structures provide a wide range of mechanical properties, including the robustness and compliance of textiles; characteristics that are desirable for soft actuators. The compact textile structures and their methods of assembly can be of help in system integration.

The following sections focus on the recent development of applications of textile-based actuators and are organized as film-based textile actuators, fiber-based textile actuators, and textiles as supportive elements for pneumatic/fluidic actuation.

3.2 Film-based textile actuators

From a mechanical point of view, a large deflection of a thin film corresponds to only a small deformation in in-plane strain. Therefore, films are often used as simple yet effective shape for actuators. Typical mode of actuation of film-based actuators involves out-of-plane deformation including bending, twisting, and wrinkling. These deformation patterns are generally created by inducing differential in-plane strain response in the film, via a number of methods such as laminating, anisotropic reinforcement, and localized application of stimuli. A variety of film-based morphing behavior with these mechanical design principles are observed in plants, such as the quiescent blooming of lily flowers[10], the opening of pine cones[11], and rapid closure of Venus Flytrap[12]. For example, pinecones open during low humidity to release seeds and close up if the humidity increases and microscopic examination unveiled the structural and mechanical origin of such reversible behavior. The scales of pinecone, composed of two macroscopic layers of tissues with different coefficient of hygroscopic swelling, bend outward as the outer layer shrinks more significantly under decreasing humidity. Further analysis found that

the swelling ability of two layers is governed at the cellular level, where distinct cellulose fibril arrangement on the cell wall effectively modifies the stiffness of the cells. Overall, the cellulose fibrils tune the mechanical properties of the cells, which aggregates to form layers in the laminated scales that bend upon change in humidity[11]. The exquisite use of moisture variation for actuation and layered structure design in plants has been an inspiring source to create film-based soft actuators[13].

Films are somewhat similar to textiles in many ways. Fabrics can be regarded as films when we zoom out and consider their protective and decorative functionalities as a layer covering various surfaces such as human bodies, floors, the interior of buildings and cars. Yet, they are much more than a typical two-dimensional (2D) film. The unique hierarchical structure of fabrics via periodic interlacement/interlooping of fibers or yarns in a 2D manner (except for nonwoven fabrics) significantly differentiates them from typical films, providing versatile mechanical properties and high breathability. The unique combination of mechanical properties of fabrics such as, strength and flexibility, originate primarily from the relative movement of constituent fibers and yarns under small strain. These and other characteristics of fabrics such as, the ability to tune their structures to produce various levels of mechanical response, including compliance, without significant change in constituent material properties, excellent conformity to various surface morphologies, and water and moisture vapor permeability should be of value in designing actuators for wearables.

Coatings and laminating are usually used on fabric surfaces for additional functionalities, serving as another common film structure in textiles. For example, various coatings on high-strength fiberglass fabrics such as those of silicone and PTFE are applied for thermal insulation and chemical and temperature resistance, respectively[14]. For actuation purposes, thin coated layers can potentially serve as barriers for directional stimuli responses and active material

carriers, while the patterned conductive coatings can be electrical heating elements for thermally-activated actuators. Due to these and other possibilities of incorporating stimuli sensitive agents through coating and lamination on fabrics, there is a growing interest in film-based textile actuator design and application. Wang et al[1] proposed moisture activated actuators for dynamic ventilation of wearable textiles that respond to the environmental humidity gradient. It is similar to the pinecone that opens as a result of differential swelling in its laminated scale structure, in that the morphing part of the fabric is composed of laminated layers with different moisture sensitivity. The moisture active layer (living cells) is printed onto passive apparel pre-trimmed based on heat and sweat map of the back of a human, a self-modulated ventilation clothes are fabricated.

Although the environmental humidity gradient is green energy for actuators, it is a passive actuation method, having no active control. While active control of humidity for hygroscopic actuation is tedious and inefficient, electrohydrodynamic swelling offers an alternative as an efficient actuation principle with ability to convenient electrical control and localized stimulation. In electrohydrodynamic swelling, the electrical potential between two electrodes induces the mobility of ionic liquids, and the asymmetric migration of cations and anions due to their size and interaction with solvents and electrode matrix creates asymmetric swelling around the electrodes. Uduste et al[15] employed this mechanism to fabricate laminated fabric actuators that can bend cyclically at an alternating voltage of $\pm 3V$. The fabric actuator is composed of two activated carbon fabric layers as flexible electrodes and a middle silk layer for mechanical support, both components infiltrated with ionic liquids as the electrically mobile agent. The activated carbon cloth layers converted from viscose rayon via pyrolysis and activation, provide meter-size conductive pathways, a large surface area for ionic interaction, meso- and micro-porous structures for liquid imbibition, and mechanical flexibility for swelling

and bending. They also used this trilayered fabric design as flexible electrodes to control the motion of a tendril-like soft robot[16]. **Figure 3-1a, b** show two natural phenomenon that inspired this work, including the osmotic pressure-driven opening and closure of pores (stomata) on leaves, and the coiling of plant's tendrils to anchor on a support. The soft robotic design is illustrated in Figure 3-1c, d, where the tendril-shaped end-effector coils and uncoils (Figure 3-1e) according to the osmotic pressure controlled by the electrical control unit (ECU). The osmotic pressure difference in the end-effector and the ECU is controlled by charging and discharging the cloth electrodes in the ECU. When it is charged, the ions migrate to and immobilized on the electrode surface, inducing a drop of the ion concentration inside the ECU, which leads to water influx to the end effector and uncoiling of the artificial tendril. By cyclic charging and discharging, reversible coiling and uncoiling of the artificial tendril is achieved.

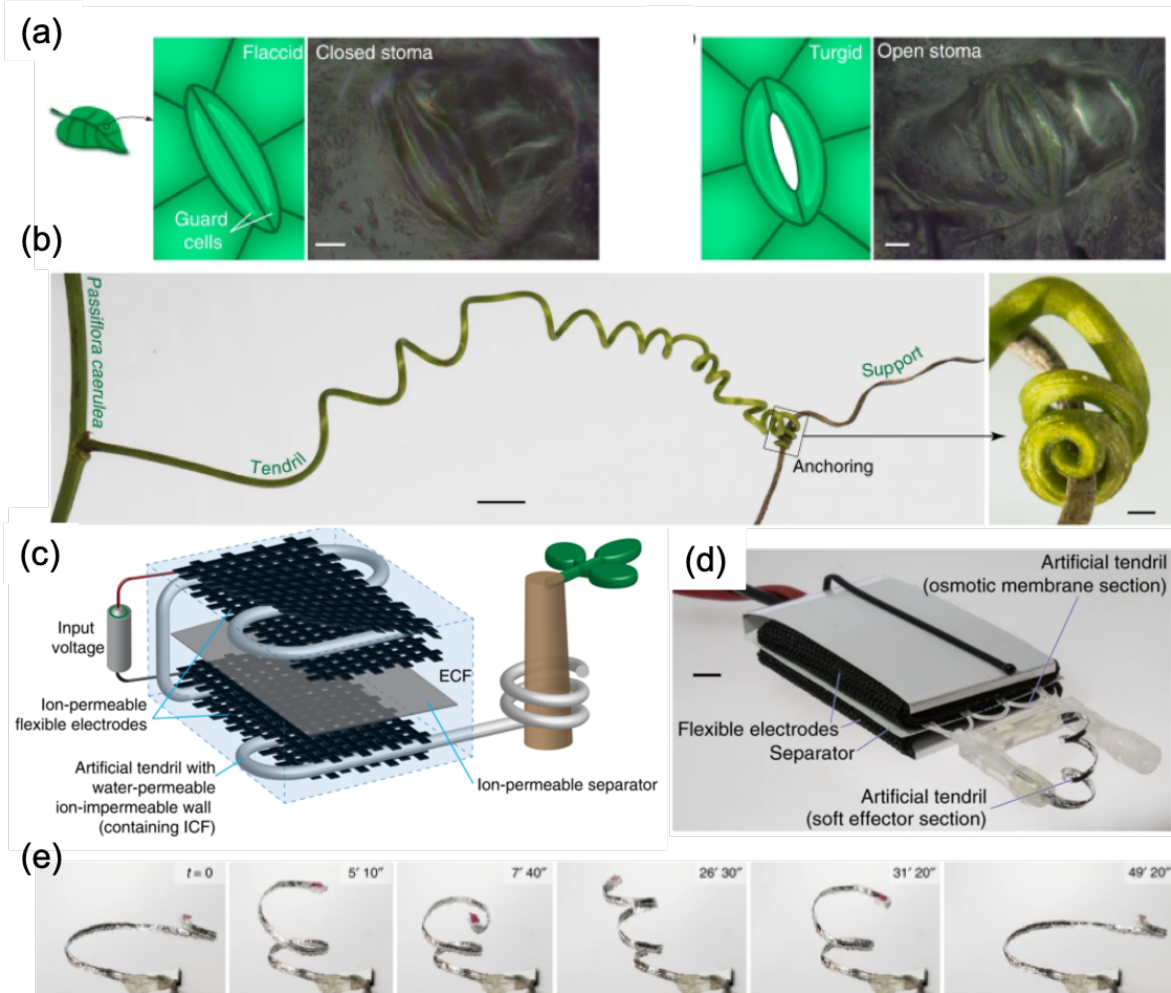


Figure 3-1. A tendril-like soft robot driven by electrically-controlled osmotic pressure. (a) Schematic of opening and closure of pores (stomata) on a leaf due to osmotic pressure change. (b) A plant's tendril reaching and anchoring on a support. (c) Schematic and (d) a photograph of the soft robot with design and components. (e) Reversible actuation of the tendril under voltage supply of 1.3V. Reproduced under the terms of the Creative Commons CC BY license[16]. Copyright 2019, Springer Nature.

Conductive fabrics are used as flexible electrodes not only for the ionic actuators but also for the electronic actuators. The ionic actuators operate by ion migration, and the electronic actuators work by electron interaction. Dielectric elastomer actuators (DEA) constitute one type of electronic actuators that feature large actuation strain as well as fast actuation speed, and compliant electrodes are of paramount importance for its performances. Guo et al[17] explored the feasibility of the fabric electrode for the DEA. Three typical DEA designs including a planar

actuator, bending actuator, and electro-adhesive actuator were tested for the actuation strain and electro-adhesive force. Although the fabric electrode is low-cost and suitable for wearable applications, the actuation strain is moderate (7~9% linear strain at 9kV) due to electrode stiffness, and the electro-adhesive force is limited (2N shear force at 5kV over around 120mm*120mm area) by the electrode geometry. In another work, the authors further compared five types of fabric electrodes varying in material content and structure and identified the knit fabric electrode as suitable for unidirectional actuation and woven fabric electrode for bidirectional actuation. However, the actuation strain is still small (6.8%, compared to 89% of DEA with carbon grease electrode) due to the strain-stiffening of fabric electrode[18].

Another use of conductive fabric is in electrical heating for thermo-responsive actuators. Yin et al[19] reported a wirelessly controlled, multiple stimuli-driven bimorph fabric actuator that is composed of a conductive fabric and a polypropylene film with different coefficient of thermal expansion. By laminating the two layers with a simple roll laminator (**Figure 3-2a**), a flexible fabric actuator (Figure 3-2c) is fabricated, with a cross-section shown in Figure 3-2b. Figure 3-2d illustrates the basic bending behaviors of a flat fabric under a variety of stimuli (light, heat, magnetic field, electrical current), as a result of differential thermal expansion. The fabric actuator bends in response to heat generated by electrical or photothermal heating the conducting fabric. By simple mounting and patterning, the bimorph fabric actuator was demonstrated as grippers and artificial blooming flowers.

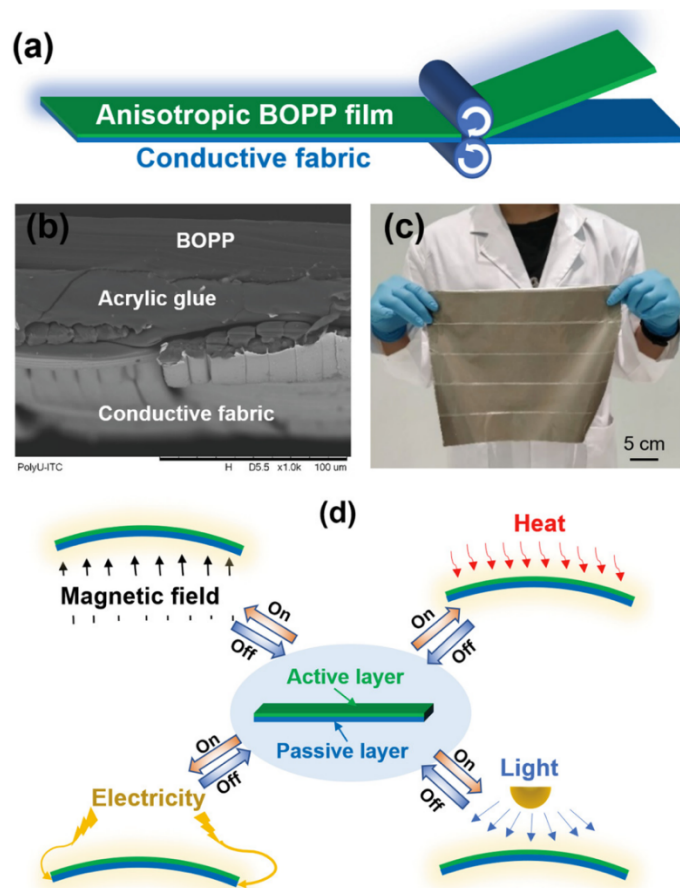


Figure 3-2. Laminate-based thermo-driven textile actuators. (a) Schematic of lamination process of the fabric actuator. (b) Cross-sectional view of the laminated fabric. (c) Photograph of the laminated fabric. (d) Schematic of actuation principle under different stimuli. Reproduced with permissions.[19] Copyright 2020 WILEY-VCH Verlag GmbH & Co. KGaA, Weinheim.

In addition to laminating, coating is convenient method to apply a thin layer of material on textiles and fabricate film-based textile actuators. Ali et al[20] reported a polypyrrole (PPy)-coated fabric actuator with tunable actuation strain and force via fabric structure design. PPy is an electroactive polymer that changes volume in an electrolyte environment as a result of electrical potential-induced ion and solvent injection. One contradiction of PPy actuation is the inverse relation of actuation speed and output force, as the force increases with the cross-sectional area while the mass transfer-dependent speed is reduced. To obtain large actuation force without sacrificing the speed, they coated a thin layer of PPy on a woven fabric, and the resultant fabric with 10 parallel yarns could reversibly provide approximately 100 mN force by

alternating input voltage between 0.5 and 1V.[20] The output force can be further increased by integrating more yarns in the fabric (by making a more compact fabric, a larger fabric, or a 3D fabric), and the actuation strain can be amplified by coating PPy on a more easily extensible knitted fabric.

3.3 Fiber-based Textile Actuators

Use of fibers in inducing and controlling actuation is a common strategy in nature. For example, skeletal muscle cells responsible for movement in animals are long fiber-shaped actuators that are bundled together with two ends connected to bones. Each fiber runs through the whole length of the muscle and is individually controlled by a motor neuron. Therefore, the output force of a muscle can be increased by activating more muscle fibers. At the cellular level, skeletal muscle has striated microscopic appearance due to the overlapping of myofilaments that run in parallel along the cell length. The chemical-induced sliding of these filaments is responsible for the cell contraction at the sub-cellular level. These repeating overlapping parts, known as sarcomeres, are the structural and functional units that determine the mechanical output of these muscle cells[6]. Therefore, the fiber-shaped skeletal muscle cells is an effective design for the optimal contractive actuation at the cell level, as well as for the compact hierarchical assembly with compactness and controllable force output at the tissue level.

Developing fiber-based textile actuators has advantages of greater design flexibility for small- and large-scale morphing structures and a broader control on the actuation performance. One can imagine an active fiber that contracts in response to a stimulus and exerts microscale forces. It can be used as micro engines for special applications such as miniaturized devices with structural simplicity and high energy density[21]. Bundling fibers into a yarn results in a mechanically stronger unit with higher contractile forces. Yarn actuators with scalable forces and compact structures can serve as artificial muscles for robotics[5]. Assembling these actuating

fibers and yarns into a fabric produces morphing fabric[8] whose deformation pattern can vary depending on the fiber arrangement, number of active fibers, actuation sequence, etc. The fabric actuator with definite and reversible deformation can be ultimately designed into smart wearables for many current and future applications.

Shape-morphing fibers that can be used for actuation purposes include shape memory alloys and polymers (SMA, SMP), highly twisted and/or coiled polymer fibers (TCPF)[22], multi-component fibers[23], etc. The working principle of SMA and SMP is their phase change-induced shape morphing from a temporarily stabilized shape to a permanent shape, known as the shape memory effect. They have been assembled into fabric structures for stiffness-changing pneumatic radial tire cord[9] and braided for medical stents that can deploy in situ from a collapsed state into a larger diameter tube to mechanically support tubular organs when the temperature is raised within the physiologically tolerable range[24].

TCPF is a relatively new type of fiber-based actuator that rapidly rotate or contract when subject to stimuli such as heat and moisture. The highly twisted structure of TCPF enables efficient conversion of radial expansion of the precursor fiber into torque, which generates fast rotation of the twisted shape and linear deformation of the coiled shape. **Figure 3-3a** shows the fabrication process of twisted and coiled structures, as well as two modes of actuation. Nylon is the most common fiber to make TCPF actuators owing to its low cost and temperature-activated shape change[22]. By winding a metallic fiber or coating with a conductive material, nylon TCPF can be activated via electrical heating, where large output force can be used for robotic manipulation and high linear strain can be used for morphing structures[25].

Multi-component fibers, similar to the laminated films, deform into wavy or coiled shapes as a result of differential response of constituent materials due to different modulus and coefficient of thermal expansion (CTE)[26]. Based on the moisture-induced deformation of

bicomponent cellulose fibers, Nike developed active thermoregulation sportswear[27] that can increase fabric porosity in the presence of sweat for evaporative cooling. The bicomponent cellulose fibers are composed of moisture-sensitive cellulose and moisture-neutral triacetate that are twisted into yarns and then knitted into a fabric. When moisture increases, the fiber straightens due to differential swelling, and the yarn's diameter decreases, leading to a larger distance between yarns. The thermoregulation effect is further improved with radiative cooling by coating the bicomponent cellulose fiber with CNTs[23]. The moisture-induced inter-fiber distance change in a yarn alters the infrared (IR) transmittance within the human IR radiation range, due to the distance-dependent IR emissivity of CNT material. When moisture increases, the inter-fiber distance decreases, and IR radiation increases, resulting in both evaporative and radiative cooling.

To achieve diverse actuation functionalities for different applications, fiber actuators are assembled and integrated into higher-level structures. One of the simplest and effective approaches is incorporating fiber actuators maybe as seamlines into passive substrates such as films[28], fabrics[22] and their composites[8]. Han et al[8] fabricated a multi-mode actuating textile composite by laminating two layers of woven fabrics composed of glass and nylon fibers, and SMA wires into a middle passive fabric. The glass fibers and nylon fibers are the passive weft and warp elements of the fabric and the SMA wires serve as the actively contractile warp element. By varying the lamination angle, the composite fabric can produce bilateral bending and twisting in tens of seconds through current supply to the SMA wires. Chenal et al[29], on the other hand, exploited the large modulus change of SMP fibers near its glass transition temperature to create a variable stiffness fabric.

TCPF yarn actuators are able to exhibit larger strain, faster response, and higher structural flexibilities compared to the small actuation strain of SMA. TCPF yarns made of

different materials are woven into fabric and film substrates to provide bending deformation and linear forces. Chen et al[28] sewn CNT-based TCP yarns (14% linear strain) into a film substrate to fabricate spring-like ribbon actuators with rapid linear contraction of 20% within a second. Higher actuation strain is generated in spandex-based TCP yarns (45% linear strain), which were woven into a passive fabric to provide electroactive contractile forces for robotic arms and wearable actuators. Jia et al[30] used silk-based TCP yarns (active) as the warp element and untwisted silk yarns (passive) as the weft elements to fabricate smart sleeves that contract in length when humidity increases and recovers when humidity decreases (Figure 3-3c). The TCP actuator is fabricated through a series of twisting steps, see Figure 3-3a. Initially, a silk fiber is highly twisted at one end, and then folded at the middle point and applying opposite twist to the ply for self-balancing. Such plied and self-balanced yarn generates torsional actuation when experiencing swelling in the presence of moisture. By further coiling the plied silk on a mandrel and heat setting the shape, the linear TCP is fabricated. A walking caterpillar made with linear TCP that expands as moisture increases from an approaching hand, and contract otherwise is illustrated in Figure 3-3b.

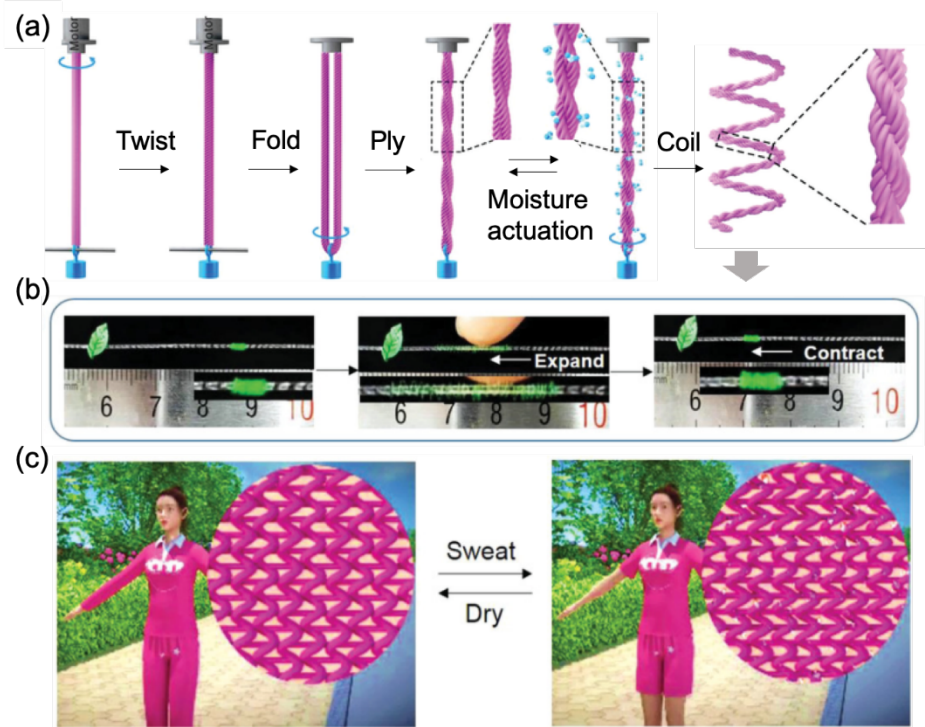


Figure 3-3. Silk-based TCP yarns for length changing fabric. (a) Schematic of TCP fabrication and moisture activation. (b) Photographs showing the movement of a “caterpillar” made of coiled TCP, driven by the moisture from an approaching finger. (c) Length change of smart fabric made with coiled silk yarn, and application schematic of sweat-induced shrinkable sleeve. Reproduced with permission. Copyright 2019[30], John Wiley and Sons.

4D printing has also been used to fabricate morphing structures by extruding smart fibers in a predefined shape. Boley et al[31] printed a planner fiber network that transforms into the desired face shape when the temperature drops. The complex and precision fabrication is enabled by the software-assisted structural design and stress-tensor evaluation, multi-material printing, and precise and continuous material allocation for printing, while the doubly curved shapes are enabled by the flexibility of fiber network.

There is ample evidence in the published literature that fibers can not only be used as active elements to power the actuation but can also be integrated as passive mechanical reinforcement in a deformable body to tune the overall response. In terms of mechanical reinforcement, research is primarily focused on the soft pneumatic and hydraulic actuators,

where the fibers are arranged along certain directions in the soft body to create mechanical anisotropy. The textile fiber-assisted soft actuators will be discussed in the following section.

3.4 Textiles for pneumatic (and fluidic) actuation

Soft pneumatic and fluidic actuators composed of flexible skin with hollow internal channels in which pressure is applied for inflation and deflation have attracted tremendous attention in the soft actuator community due to their reliable actuation performance, simple control, ability to generate large forces, and scalability. McKibben muscle is the early version of soft pneumatic actuators[32] made of cylindrical rubber bladder sheathed with a braided tubular fabric, which upon inflation contract in length and expand in radius. To resemble the actuation behavior of mammalian skeletal muscles, McKibben muscles are paired antagonistically to power the motion of robotic arms[33]. The underlying mechanical principle of McKibben muscle actuation is the directional deformation of the sheath fabric with helically arranged fibers that restrict the expansion in the axial direction. The mechanical anisotropy-induced differential deformation is the key in the development of soft pneumatic actuators, much like the fiber-reinforced architectures of biological actuators such as elephant trunks, mammalian tongues, and plant cells. The resultant deformation such as contraction, twisting, and bending, have been used in applications such as rehabilitation gloves to facilitate the hand function of paralyzed patients[2], haptic feedback, and compressive garments for preventative therapy[34]. Another popular application of soft pneumatic actuators is robotic gripper to handle delicate and complex-structured objects, and the commercialized finger-typed grip that bend to grasp objects[35] and granular jamming-based gripper that change hardness to grip and release objects[36].

Textile fibers such as nylon, Kevlar, and glass fibers are usually used as mechanical reinforce elements on the cylindrical elastomeric tube to achieve a wide range of motions. By

winding fibers helically around the tube at certain angles, the pneumatic actuators upon pressurizing generates particular trajectories such as linear extension, contraction, twisting, and bending. Combination of these motions for specific tasks such as hand motion assistance[37], [38] can be achieved by integrating segments optimized for different trajectories.

Figure 3-4 illustrates the development of a wearable assistive glove by integrating segmented fluidic actuators[37]. To support hand motion comfortably and sufficiently, the soft actuators need to follow the natural finger trajectories, provide enough actuation force without imposing large pressure on fingers. Therefore, the fluidic actuators are fabricated in segments to achieve finger-like multi-degree of freedom that can be actuated with single pressure input. In general, the bending deformation is facilitated by incorporating a strain-limiting layer on one side of the fluidic tube, and the radial expansion is suppressed by symmetrically arranging fibers in the fluidic tube at an appropriate angle. The variation in segmental deformation is determined by the fiber arrangement and the strain limiting layer as shown in

Figure 3-4a. In particular, four types of deformation are presented, with bending resulted from a strain-limiting layer and two sets of symmetrically arranged fibers, cylindrical twisting originated from a strain-limiting layer and one set of helically wound fiber, linear extension and pure twisting due to two sets symmetric and one set helically wound fibers. Finally, the fiber-reinforced fluidic actuators are integrated into a glove structure with two fabric layers that can be adjusted in size by Velcro adhesion (hook and loop) to demonstrate some basic activities such as picking up a phone and a bottle while wearing this assistive device (

Figure 3-4b).[37].

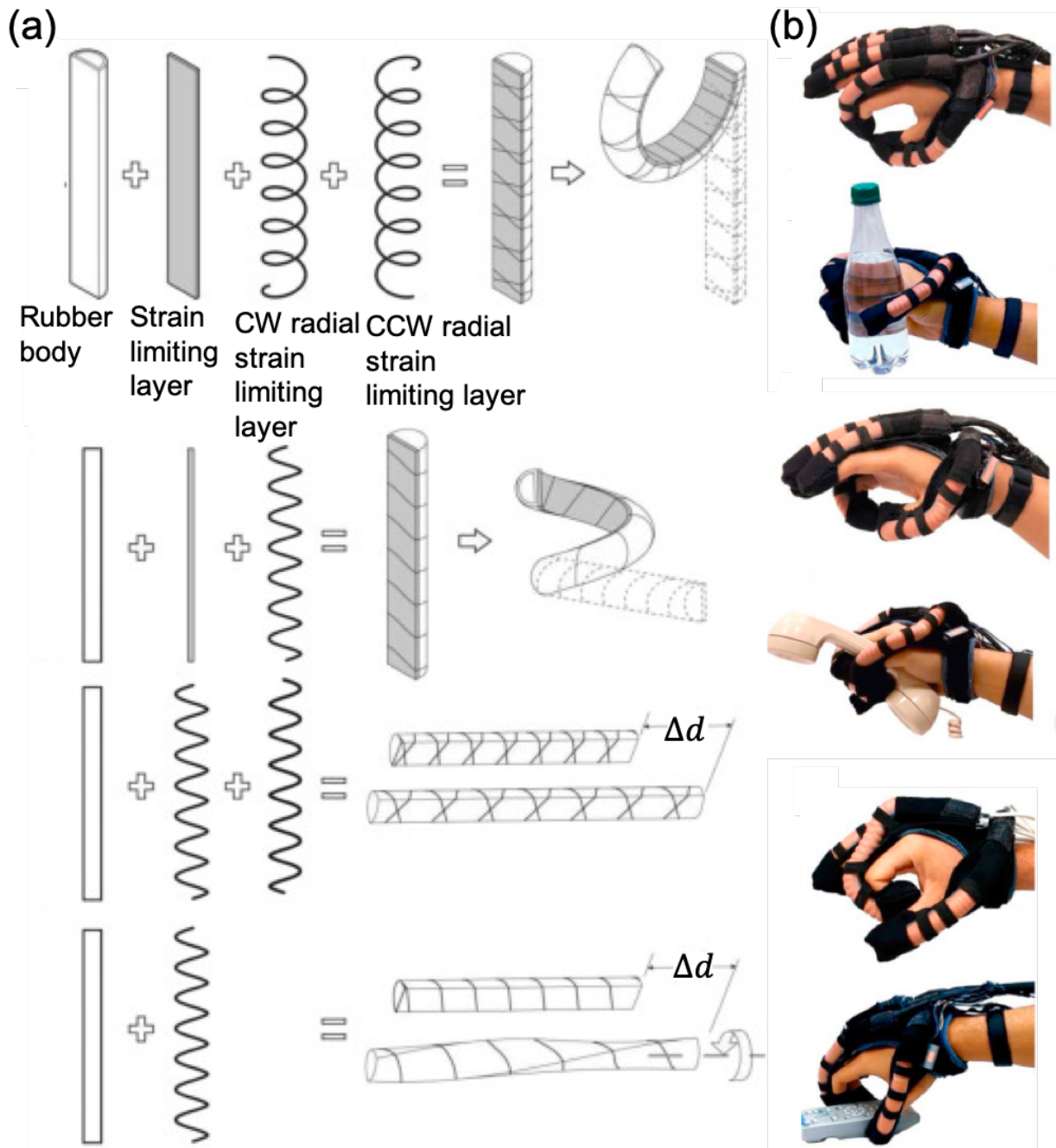


Figure 3-4. Fiber-reinforced fluidic soft actuators for assistive gloves. (a) Four types of deformation of fluidic elastomeric tubes resulted from fiber arrangement and the strain-limiting layer, including bending, cylindrical twisting, linear extension, and pure twisting. (b) Actuation demonstration of the soft assistive glove. Reproduced with permission[37]. Copyright 2015, Elsevier.

A wide range of extensibility of fabrics are also used to tailor the mechanical response of soft pneumatic actuators. Knit and woven fabrics have distinct mechanical properties, which

differs along the two major axes of each type of fabric[2]. In general, woven fabrics have less extensibility and higher stiffness along both warp and weft directions due to the alignment of yarns. Whereas, knit fabrics poses higher extensibility and lower stiffness at initial extension due to interlaced loops, which after being straightened during deformation show significant increase of stiffness. In addition, knit fabrics have large anisotropic mechanical properties along the two orthogonal directions. Cappello et al[2] utilized knit and woven fabrics with such unique mechanical features as sheath for the pneumatic actuators to modulate overall strain distribution, and the resultant actuators were integrated into motion assistance gloves. The fabric-constrained pneumatic actuator is composed of an elastomeric pneumatic tube covered on the top side with a knit fabric and on the bottom side with a woven fabric integrated by sewing. In addition, the course direction (cross direction) of the relatively low stiffness knit fabric is aligned with the longitudinal direction of the tube to allow maximum deformation. When the tube is inflated, the actuator bends toward the woven fabric side due to its strain limiting effect. Additionally, higher bending deformation can be achieved by designing the knit fabric into a pleated structure.

References

- [1] W. Wang *et al.*, “Harnessing the hygroscopic and biofluorescent behaviors of genetically tractable microbial cells to design biohybrid wearables,” *Sci. Adv.*, vol. 3, no. 5, p. e1601984, May 2017, doi: 10.1126/sciadv.1601984.
- [2] L. Cappello *et al.*, “Exploiting Textile Mechanical Anisotropy for Fabric-Based Pneumatic Actuators,” *Soft Robot.*, vol. 5, no. 5, pp. 662–674, Oct. 2018, doi: 10.1089/soro.2017.0076.
- [3] M. Zhu *et al.*, “Haptic-feedback smart glove as a creative human-machine interface (HMI) for virtual/augmented reality applications,” *Sci. Adv.*, vol. 6, no. 19, p. eaaz8693, May 2020, doi: 10.1126/sciadv.aaz8693.
- [4] Y. Ding, M. Kim, S. Kuindersma, and C. J. Walsh, “Human-in-the-loop optimization of hip assistance with a soft exosuit during walking,” *Sci. Robot.*, vol. 3, no. 15, Feb. 2018, doi: 10.1126/scirobotics.aar5438.
- [5] K. Kim *et al.*, “Double Helix Twisted and Coiled Soft Actuator from Spandex and Nylon,” *Adv. Eng. Mater.*, vol. 20, no. 11, p. 1800536, 2018, doi: 10.1002/adem.201800536.
- [6] J. A. Hill and E. N. Olson, “An Introduction to Muscle,” in *Muscle*, Elsevier, 2012, pp. 3–9. doi: 10.1016/B978-0-12-381510-1.00001-6.
- [7] J.-S. Wang *et al.*, “Hierarchical chirality transfer in the growth of Towel Gourd tendrils,” *Sci. Rep.*, vol. 3, p. 3102, Oct. 2013, doi: 10.1038/srep03102.
- [8] M.-W. Han, M.-S. Kim, and S.-H. Ahn, “Shape memory textile composites with multi-mode actuations for soft morphing skins,” *Compos. Part B Eng.*, p. 108170, Jun. 2020, doi: 10.1016/j.compositesb.2020.108170.
- [9] M. Oku, “Pneumatic radial tire with belt cords having at least one shape-memory alloy filament,” US5242002A, Sep. 07, 1993 Accessed: Jul. 10, 2020. [Online]. Available: <https://patents.google.com/patent/US5242002A/en>
- [10] H. Liang and L. Mahadevan, “Growth, geometry, and mechanics of a blooming lily,” *Proc. Natl. Acad. Sci.*, vol. 108, no. 14, pp. 5516–5521, Apr. 2011, doi: 10.1073/pnas.1007808108.
- [11] C. Dawson, J. F. V. Vincent, and A.-M. Rocca, “How pine cones open,” *Nature*, vol. 390, no. 6661, p. 668, Dec. 1997, doi: 10.1038/37745.
- [12] Y. Forterre, J. M. Skotheim, J. Dumais, and L. Mahadevan, “How the Venus flytrap snaps,” *Nature*, vol. 433, no. 7024, pp. 421–425, Jan. 2005, doi: 10.1038/nature03185.
- [13] B. Shin *et al.*, “Hygrobot: A self-locomotive ratcheted actuator powered by environmental humidity,” *Sci. Robot.*, vol. 3, no. 14, p. eaar2629, Jan. 2018, doi: 10.1126/scirobotics.aar2629.
- [14] “Heat Resistant Fabric | Thermal Insulation | Insulation Manufacturer.” <https://mid-mountain.com/> (accessed Jul. 19, 2020).
- [15] I. Uduste, F. Kaasik, U. Johanson, A. Aabloo, and I. Must, “An All-Textile Non-muscular Biomimetic Actuator Based on Electrohydrodynamic Swelling,” *Front. Bioeng. Biotechnol.*, vol. 8, May 2020, doi: 10.3389/fbioe.2020.00408.
- [16] I. Must, E. Sinibaldi, and B. Mazzolai, “A variable-stiffness tendril-like soft robot based on reversible osmotic actuation,” *Nat. Commun.*, vol. 10, no. 1, Art. no. 1, Jan. 2019, doi: 10.1038/s41467-018-08173-y.
- [17] J. Guo, C. Xiang, T. Helps, M. Taghavi, and J. Rossiter, “Electroactive textile actuators for wearable and soft robots,” in *2018 IEEE International Conference on Soft Robotics (RoboSoft)*, Apr. 2018, pp. 339–343. doi: 10.1109/ROBOSOFT.2018.8404942.

- [18] C. Xiang *et al.*, “Electroactive Textile Actuators for Breathability Control and Thermal Regulation Devices,” *Polymers*, vol. 11, no. 7, Art. no. 7, Jul. 2019, doi: 10.3390/polym11071199.
- [19] R. Yin *et al.*, “Wireless Multistimulus-Responsive Fabric-Based Actuators for Soft Robotic, Human–Machine Interactive, and Wearable Applications,” *Adv. Mater. Technol.*, vol. n/a, no. n/a, p. 2000341, doi: 10.1002/admt.202000341.
- [20] A. Maziz, A. Concas, A. Khaldi, J. Stålhand, N.-K. Persson, and E. W. H. Jager, “Knitting and weaving artificial muscles,” *Sci. Adv.*, vol. 3, no. 1, p. e1600327, Jan. 2017, doi: 10.1126/sciadv.1600327.
- [21] J. Yuan *et al.*, “Shape memory nanocomposite fibers for untethered high-energy microengines,” *Science*, vol. 365, no. 6449, pp. 155–158, Jul. 2019, doi: 10.1126/science.aaw3722.
- [22] C. S. Haines *et al.*, “Artificial Muscles from Fishing Line and Sewing Thread,” *Science*, vol. 343, no. 6173, pp. 868–872, Feb. 2014, doi: 10.1126/science.1246906.
- [23] X. A. Zhang *et al.*, “Dynamic gating of infrared radiation in a textile,” *Science*, vol. 363, no. 6427, pp. 619–623, Feb. 2019, doi: 10.1126/science.aau1217.
- [24] J. Flomenblit, N. Budigina, and Y. Bromberg, “Two way shape memory alloy medical stent,” US5562641A, Oct. 08, 1996 Accessed: Jul. 19, 2020. [Online]. Available: <https://patents.google.com/patent/US5562641A/en>
- [25] Y. Almubarak and Y. Tadesse, “Twisted and coiled polymer (TCP) muscles embedded in silicone elastomer for use in soft robot,” *Int. J. Intell. Robot. Appl.*, vol. 1, no. 3, pp. 352–368, Sep. 2017, doi: 10.1007/s41315-017-0022-x.
- [26] M. Kanik *et al.*, “Strain-programmable fiber-based artificial muscle,” *Science*, vol. 365, no. 6449, pp. 145–150, Jul. 2019, doi: 10.1126/science.aaw2502.
- [27] “What is Nike AeroAdapt?,” *Nike News*. <https://news.nike.com/news/nike-aeroadapt-material-innovation> (accessed Mar. 05, 2020).
- [28] P. Chen, S. He, Y. Xu, X. Sun, and H. Peng, “Electromechanical Actuator Ribbons Driven by Electrically Conducting Spring-Like Fibers,” *Adv. Mater.*, vol. 27, no. 34, pp. 4982–4988, 2015, doi: 10.1002/adma.201501731.
- [29] T. P. Chenal, J. C. Case, J. Paik, and R. K. Kramer, “Variable stiffness fabrics with embedded shape memory materials for wearable applications,” in *2014 IEEE/RSJ International Conference on Intelligent Robots and Systems*, Sep. 2014, pp. 2827–2831. doi: 10.1109/IROS.2014.6942950.
- [30] T. Jia *et al.*, “Moisture Sensitive Smart Yarns and Textiles from Self-Balanced Silk Fiber Muscles,” *Adv. Funct. Mater.*, vol. 29, no. 18, p. 1808241, May 2019, doi: 10.1002/adfm.201808241.
- [31] J. W. Boley *et al.*, “Shape-shifting structured lattices via multimaterial 4D printing,” *Proc. Natl. Acad. Sci.*, vol. 116, no. 42, pp. 20856–20862, Oct. 2019, doi: 10.1073/pnas.1908806116.
- [32] F. Daerden and D. Lefeber, “Pneumatic Artificial Muscles: actuators for robotics and automation,” p. 11.
- [33] Z. Zhang, “Pressurized artificial muscles,” *J. Intell. Mater. Syst. Struct.*, 2011.
- [34] M. Zhu, T. N. Do, E. Hawkes, and Y. Visell, “Fluidic Fabric Muscle Sheets for Wearable and Soft Robotics,” *Soft Robot.*, vol. 7, no. 2, pp. 179–197, Jan. 2020, doi: 10.1089/soro.2019.0033.
- [35] D. I. Labs, “Soft Robotics,” *Soft Robotics*. <https://www.softroboticsinc.com/> (accessed Jul. 19, 2020).

- [36] “Empire Robotics – Agile Robotics Grippers.” <http://www.empirerobotics.com/> (accessed Jul. 19, 2020).
- [37] P. Polygerinos, Z. Wang, K. C. Galloway, R. J. Wood, and C. J. Walsh, “Soft robotic glove for combined assistance and at-home rehabilitation,” *Robot. Auton. Syst.*, vol. 73, pp. 135–143, Nov. 2015, doi: 10.1016/j.robot.2014.08.014.
- [38] F. Connolly, C. J. Walsh, and K. Bertoldi, “Automatic design of fiber-reinforced soft actuators for trajectory matching,” *Proc. Natl. Acad. Sci.*, Dec. 2016, doi: 10.1073/pnas.1615140114.

Chapter 4 Twisted and Coiled Polymer Actuators (TCPAs)

4.1 Introduction

Twisted fibrous structures have been associated with humankind from the early days of civilization through the industrial revolution to the modern day. What may have started as a means of assembling fibers into continuous strands to make ornamental headgears, etc. [citation] is still used to produce the chic fashion items of today. The recent discovery of twisted and coiled polymer actuators (TCPA) may have given a new twist to the traditional use of twisted fibers in textiles. The recent discovery of the remarkable torsional and linear actuation behavior of highly twisted fibers of certain kind under appropriate stimuli, has brought renewed interest in the understanding twisting as well as the mechanics of twisted structures. The TCPAs have been recognized for potential applications in robotics[1], [2] and smart wearables[3], [4] due to their extraordinary large actuation stroke and forces[5]. Equally important for their potential commercial applications is the relatively simple, scalable, and available manufacturing processes, structural compactness for ease of handling and efficient assembly. The actuation behavior of the TCPAs originate from the radial expansion of the constituent fibers, and their highly twisted and sometimes hierarchical structure is responsible for their outstanding performances[5], [6]. A variety of fiber types with radial expansion properties have been twisted and coiled to build TCPAs. Modeling and characterization methods of the twisted structures for improved control and reliability of TCP fabrication and actuation have also been reported.

This section aims to introduce the development of TCPAs beginning with the selection of materials. A summary of TCPAs based on different types of yarn structures (single filament, filament yarn, staple yarn, twisted structure, multi-ply structure, and coiled structure) is provided, followed by a brief discussion of their mechanical models and characterization techniques of TCPAs.

4.1 Development of TCPAs

Since Foroughi et al.[6] reported the remarkable torsional actuation of the first TCPA made by inserting a high level of twist into carbon nanotube (CNT) yarns (**Figure 4-1a-c**), there has been intense research interest in the TCPAs. A wide range of TCPA research aims to discover new materials with better responsiveness and lower cost[7], improve actuation performances by structure design[8], [9], establish the relationship between material/structure and ultimate actuation behaviors[10], [11], and integrate TCPAs into higher-level systems for various applications[2], [3], [5]. A variety of fiber-forming materials including metallic fibers[12], carbon-based fibers[13], [14], synthetic fibers[1], [7] and natural fibers[3], [15], [16] have been studied with diverse yarn structures such as highly twisted single yarn with single filament[7], multiple filaments[15] and staple fibers[6], [17], plied yarns[1], [3], coiled yarns[5], and plied coils[7], [8].

The first CNT-based TCPA is illustrated in Figure 4-1a-c. The CNT yarn was fabricated by directly twist an aerogel sheet drawn from the CNT forest. By immersing in an electrolyte bath and applying a low voltage, the yarn generates large and fast rotation (maximum torsional stroke is $250^\circ/\text{mm}$, and maximum torsional speed is 590rpm). Three schematics of the actuation setup shown in Figure 4-1c were proposed. The first and third designs generate the largest torsional stroke but poor in reversibility, and the second one produces reversible actuation but a reduced stroke. The actuation principle is the volume expansion of CNT yarn and the twisted structure. The double-layer charge injection under electrical potential difference generates hydraulic pressure and leads to yarn volume expansion. Radial expansion is preferred due to higher mechanical flexibility in the radial direction than the length direction of the yarn.

However, the use of liquid electrolytes and low working voltage restricts the performance. Lee et al.[18] reported solid-state CNT-based TCPA by replacing the liquid

electrolyte with a gel electrolyte. The electrolyte solution was infiltrated into twisted CNT yarns and solidified upon drying. Figure 4-1e, f presents the porosity of the yarn surface before infiltrating, and the infiltrated coiled yarn. Both torsional and linear actuating structures were proposed (Figure 4-1d). The first and second twist structures in the figure are used for torsional actuation, and the last two coiled structures are used for linear actuation. The second and fourth structures are torque-balanced structures fabricated by plying two yarns in the opposite direction. As a result, the gel electrolyte-infiltrated actuators generate a maximum 2330rpm rotational speed in the twisted form and 1.3% linear strain in the twisted and coiled form[18].

As the electrochemical actuation is driven by double-layer charge injection, the electrolyte ion size and applied voltage are crucial in the actuation performance. Particularly, the ion size affects both volume change per injected charge and mobility and results in complex influence on the actuation strokes. Gel electrolytes have larger electrochemical windows, and therefore, a higher voltage can be applied without degrading the electrolyte. And obviously, higher voltage leads to larger actuation stroke. Lee et al.[19] later investigated the effect of ion size of the electrolyte and manner of voltage supply on the actuation performances. Figure 4-1g, h shows the schematic and real image of actuation. Based on the observation that it takes long (tens of seconds) to reach the potential equilibrium for maximum stroke (11.6%), non-equilibrium actuation was conducted, and the effect of the manner of voltage application and actuation results were analyzed. For the non-equilibrium actuation, a smaller ion size was preferred due to higher mobility. As a result, the actuator produced a 6% linear stroke within a second of 10V voltage application[19].

Another route of improvement of CNT-based TCPA is by infiltrating responsive guest materials, such as paraffin wax[13], silicone[20], PU, and PEDOT:PSS[21]. By infiltrating or coating CNT yarn with these guest materials that undergo volume change under various stimuli

such as heat and solvent, it opens a wide spectrum of possibilities. Figure 4-1i-k shows a multistimuli-responsive TCPA with a very fast rotational speed up to 11500rpm and a linear stroke of 5.6%[13]. The CNT yarns were infiltrated with paraffin wax that undergoes 20% volume expansion when temperature increases from 30°C to 90°C. Figure 4-1j shows the cross-section of CNT yarn before and after wax-infiltration. CNT yarn served both as the structural element and the electrothermal heating element. By applying a voltage to the TCPA, the electrical power generates heat on the CNT and leads to torsional or linear actuation. The actuation result shown in Figure 4-1k is conducted on the TCPA with the structure and condition shown in the second figure in Figure 4-1i, where half of the yarn is actuating, and the other half serves as the returning spring. As a result, it produced nearly 8000rpm rotational speed with input electrical power of 20mW/cm, and the reversible actuation only took 0.1 second[13].

Mu et al.[22] considered the structure of the guest material in the yarn and reported improved actuation performances of CNT-based TCPA by restricting the guest material or the gel electrolyte on the CNT yarn surface (Figure 4-1i,m). Compared to the gel electrolyte-infiltrated TCPAs, the surface-coated TCPAs demonstrate 5 and 9 times higher in linear strokes and work density, respectively. The electrothermal actuation and sorption-induced actuation of responsive guest material-incorporated yarns also show higher performances of surface-coated TCPAs (Figure 4-1n). The origin of such enhanced performance is the helical angle associated with the location of the incorporated materials. The helical angle (angle between the length direction of the CNT fiber and length direction of the yarn) is a crucial parameter to determine the actuation response. Higher the helical angle, higher the torsional and linear stroke from volume expansion. In a twisted yarn structure, the helical angle (Figure 4-1b) is largest on the yarn surface and gradually decreases to zero in the center of the yarn. Therefore, under the same amount of stimuli (voltage or temperature), the volume expansion at the surface is more efficient

than that in the inner of the yarn and therefore produces higher actuation results. Moreover, by restricting the guest material on the surface of the yarn, the passive cooling of electrothermal actuation and adsorption/desorption speed of sorption-based actuation is enhanced, contributing to faster response and higher actuation frequency[22].

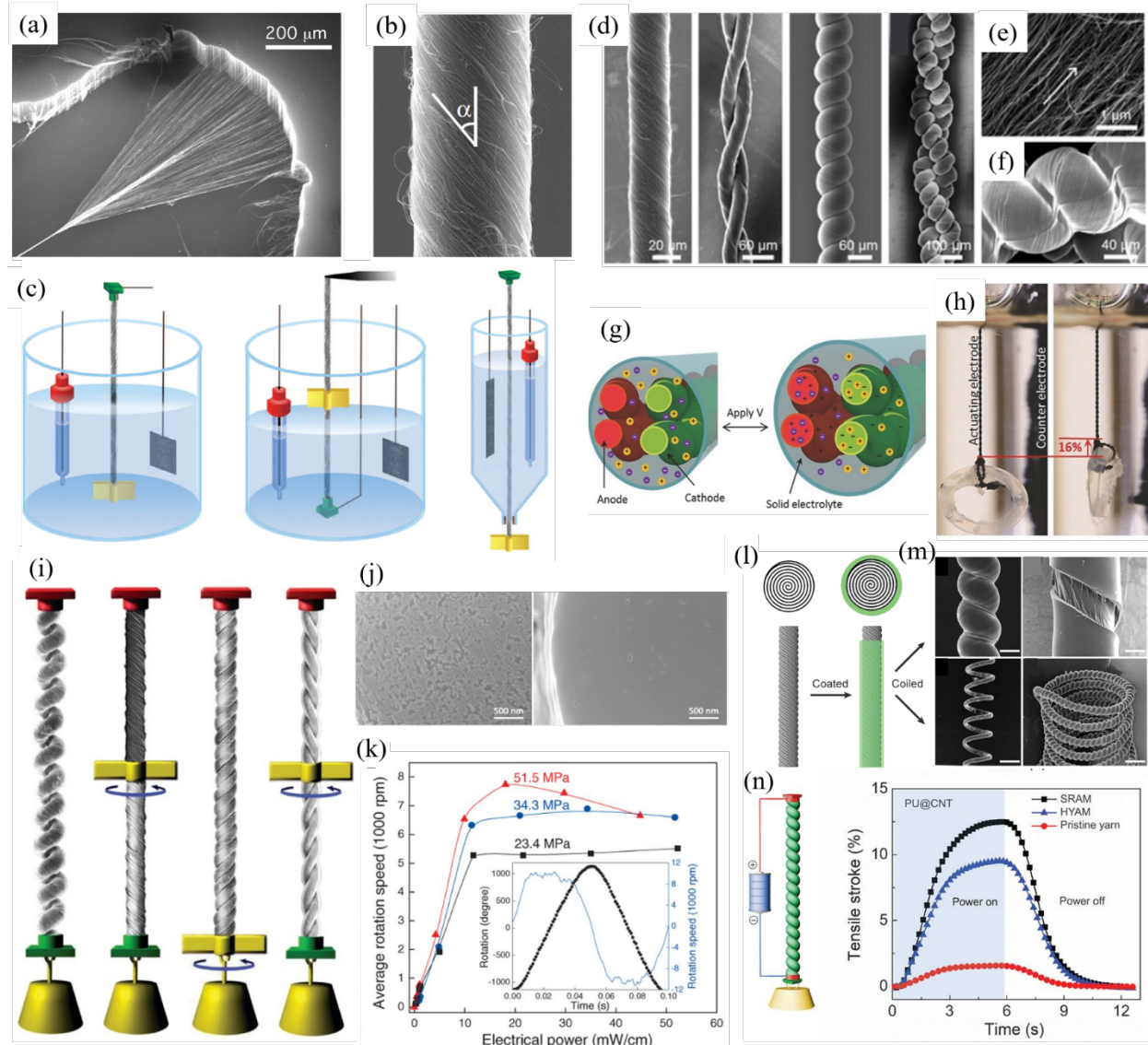


Figure 4-1. Development of CNT-based TCPAs. (a-c) First CNT-TCPA: (a) SEM image of CNTs drawn and twisted from the forest, (b) SEM image of highly twisted CNT yarn, and (c) schematics of electrochemical actuation setup.[7] (d-h) Solid-state CNT-TCPA by infiltrating gel electrolyte: SEM images of (d) four TCPA structures, (e) twisted CNT yarn showing high porosity, (f) electrolyte-infiltrated coiled CNT yarn,[23] (g) actuation schematics of the TCPA composed of two coiled-plied CNT yarns, and (h) photographs of linear actuation of (g).[19] (i-k) Multistimuli-sensitive CNT-TCPA by infiltrating guest polymers: (i) different yarn structures and tethering conditions for actuation, (j) SEM images of the cross-sectional view of twisted

CNT yarn before and after guest polymer infiltration, and (k) torsional actuation speed as a result of electrical power and applied tensile stress (inset: torsional actuation as a function of time).[13] (l-n) Polymer-coated CNT-TCPA: (l) schematic of surface-coated CNT yarn, (m) SEM images of differently coiled CNT yarns and sharp interface shown in the cracked yarn, (n) electrothermal actuation of three CNT-TCPAs (SRAM: surface-coated; HYAM: infiltrated; pristine yarn).[22]

Soon after the first report on CNT-based TCPA in 2011[6], Haines et al. reported the nylon-based TCPAs driven by heat[7]. Nylon-based TCPA produces a high contractile strain of 49%, large contractile stress, low hysteresis, reliable actuation for more than a million cycles, and the maximum output energy density of 2.48J/g (63 times higher than the natural muscle)[7]. As a low-cost and common textile fiber for daily use, it soon became one of the most popular polymer fibers for TCPAs. As is shown in **Figure 4-2b**, the nylon-based TCPA reversibly contracts to 12% strain, lifting a weight of 500g by alternatively applying cold and hot water. When increasing temperature from 20°C to 180°C, the coiled TCPA contracts with a minor decrease of modulus due to thermal softening of the polymer, and followed by a drastically increase of modulus when adjacent coils come in contact with each other (Figure 4-2c). The coil parameters are important for the actuation performance and can be easily tuned during fabrication. The spring index (C , the ratio of the coil diameter and fiber diameter) is used to characterize the coil structure and is inversely related to the spring stiffness (Figure 4-2a). Larger C results in higher tensile stroke but produces lower stress[7]. Figure 4-2d is a coil that is designed in a spiral manner to avoid contact between adjacent coils during contraction, and therefore produces ultrahigh linear strain (200%) at an elevating temperature[5].

Textile fibers such as nylon and polyethylene (PE) with the original thermal-induced linear strain of 4% and 0.3% are amplified to 34% and 16% by twisting and coiling structures. The mechanism of this performance amplification is explained in several papers[5]–[7], [24], and will be discussed in section 0. In brief, the radial expansion of the constituting fiber or the yarn (or the linear contraction) is converted into an untwist deformation in a highly twisted structure

[125]. And in a twisted and coiled structure, it is converted into linear contraction[5]. Based on this mechanism, more fibers with stimuli-induced radial expansion have been exploited to make TCPAs, such as thermal-responsive fibers with high CTE and hygroscopic fibers with high CHE.

Figure 4-2e-g shows the structure and actuation performances of silk-based TCPA[3]. The hygroscopic silk fiber swells under increasing humidity due to moisture absorption with a maximum radial strain of 15%. After twist insertion and further coil formation, the silk-TCPA produces a maximum torsional stroke of $547^\circ/\text{mm}$, and linear contraction of 70% by increasing relative humidity from 20% to 80%. The positive effects of the level of relative humidity and twist density of the structure on the actuation strokes were shown in Figure 4-2f. In addition, the effect of chirality of twist and coil on the actuation results was also presented in this figure, where the homochiral (ZZ) TCPAs contract with 40-70% strain and the heterochiral (ZS) TCPAs expand with 600-1000% strain under RH increase from 20% to 90%. The opposite linear actuation behavior of these two types of TCPAs was previously reported for nylon-based TCPA[7], and the mechanism will be presented in section 0. Here these two types of silk-based TCPAs were exploited as biomimetic “caterpillar” and thermo-regulative clothes (Figure 4-2g). The heterochiral “caterpillar” moves forward on a barbed wire by expanding and contracting when a human finger repeatedly approaches. By woven homochiral TCPAs into a fabric, the actuation of the TCPAs produces overall length contraction of the fabric. The fabric was constructed as a sleeve and integrated onto sample clothes for reversible sweat-induced length change to achieve active moisture and thermal management[3].

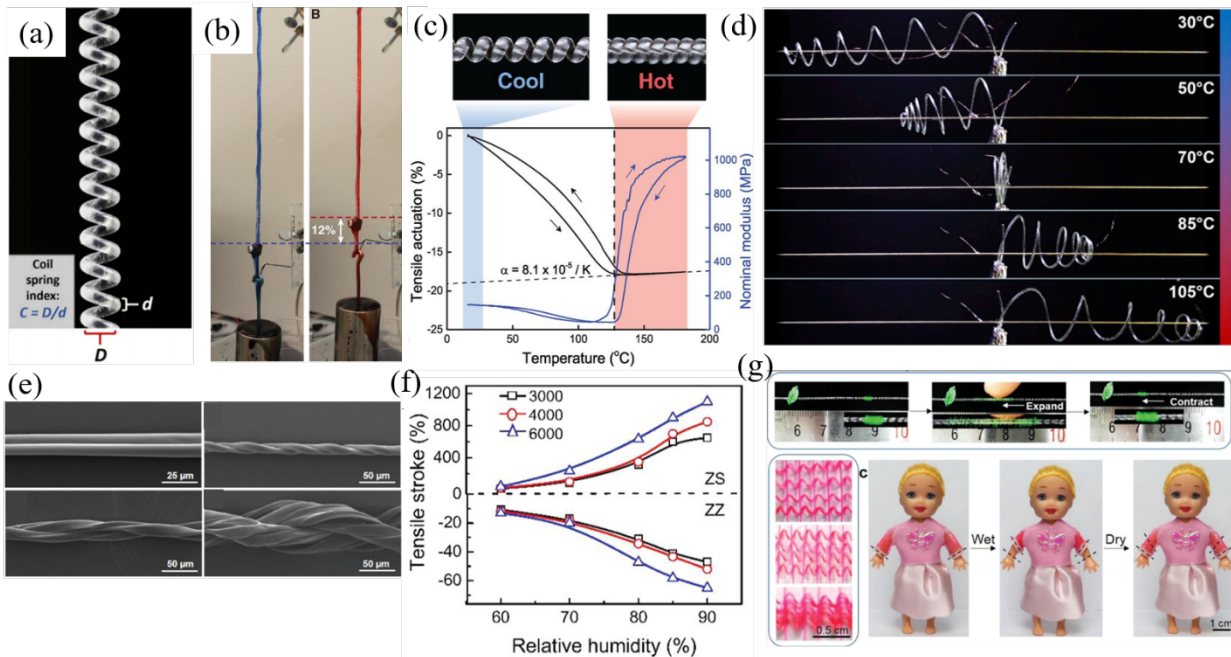


Figure 4-2. Polymer fiber-based TCPAs. (a-d) Nylon fiber-based TCPA: (a) a photograph of coiled TCPA[13], (b) hydrothermal actuation of the TCPA lifting a weight by 12% by alternative application of cold (25°C, blue) and hot (95°C, red) water[7], (c) the tensile stroke and modulus change of the TCPA as a function of temperature[7], and (d) the drastically amplified stroke by coil design[13]. (e-g) Silk fiber-based TCPA[3]: (a) SEM images of untwisted and twisted the dual-filament silk fiber, (f) tensile stroke of two types of coiled TCPAs (ZS: z-twist and s-coil, and ZZ: z-twist and z-coil) with different twist density as a function of relative humidity, (g) two demonstrations of silk fiber-based TCPAs, including the biomimetic “caterpillar” and the contracting sleeves.

4.2 Structural diversity of TCPAs

As is briefly mentioned above about the importance of yarn structures (twisted, twisted and coiled, torque-balanced, twist density, helical angle, spring index, chirality) on the actuation results of TCPAs, it is important to inspect different structures of the yarn carefully, to not only better analyze the actuation results but also to design actuators with higher performances. There is a large content to cover in terms of yarn structures, and here I will focus the discussion of yarn structures based on the yarn type (**Figure 4-3**) and hierarchical structures and limit to those so far investigated for TCPAs. Then an overview of TCPAs-based on these structures will be presented, with an emphasis on the advantages and resultant performances of such structured TCPAs.

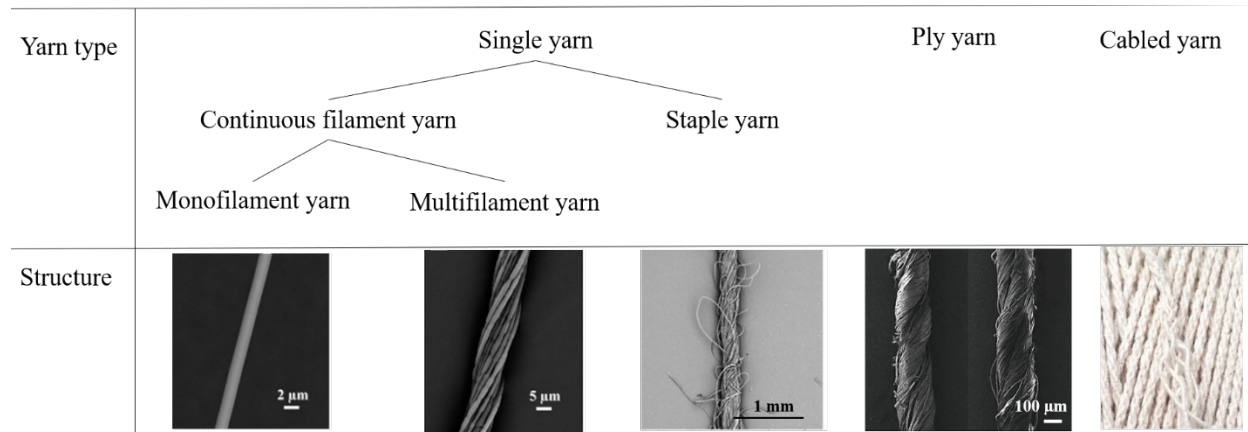


Figure 4-3. Textile yarn types. Examples of different types of yarns from left to the right: single PLA fiber[25], multifilament PLA yarn[25], cotton staple yarn[26], two-and three-ply cotton yarn[17], cabled cotton yarn[27].

Yarns can be made from filaments (long fibers) or staple fibers (short fibers). Based on the constituting elements (single or multiple fibers, long or short fibers, etc.), yarns are categorized into single yarns, ply yarns, cabled yarns, and other more (Figure 4-3). Single yarns are composed of monofilament (twisted or untwisted), multifilament with typically small amount of twist, or twisted staple fibers. Ply yarns are fabricated from twisting two or more single yarns for better uniformity and higher mechanical strength. Cabled yarns are produced by twisting multiple ply yarns for even higher mechanical performance (both higher strength and elongation) to be used in certain applications such as tire cords and sewing threads[28].

The bottom-up assembly of different types of yarns from their constituting elements leads to hierarchical structures that play a crucial role in the yarn mechanics. **Figure 4-4** presents four hierarchical levels of the yarns of interest in this research. When we consider a single fiber (filament or staple fiber) as the 1st level structure in the structure hierarchy of yarns, single yarns can be regarded as the 2nd level structure. Ply yarns made by twisting multiple single yarns and cabled yarns made by twisting multiple ply yarns can be considered as the 3rd and 4th level structures, respectively. Twisting, as a simple and effective textile method, is used in hierarchical yarn fabrication to construct a variety of yarns with diverse geometries and mechanical

properties. It is increasingly realized as a smart assembly approach for multifunctionality, that is especially required in smart textile applications[29].

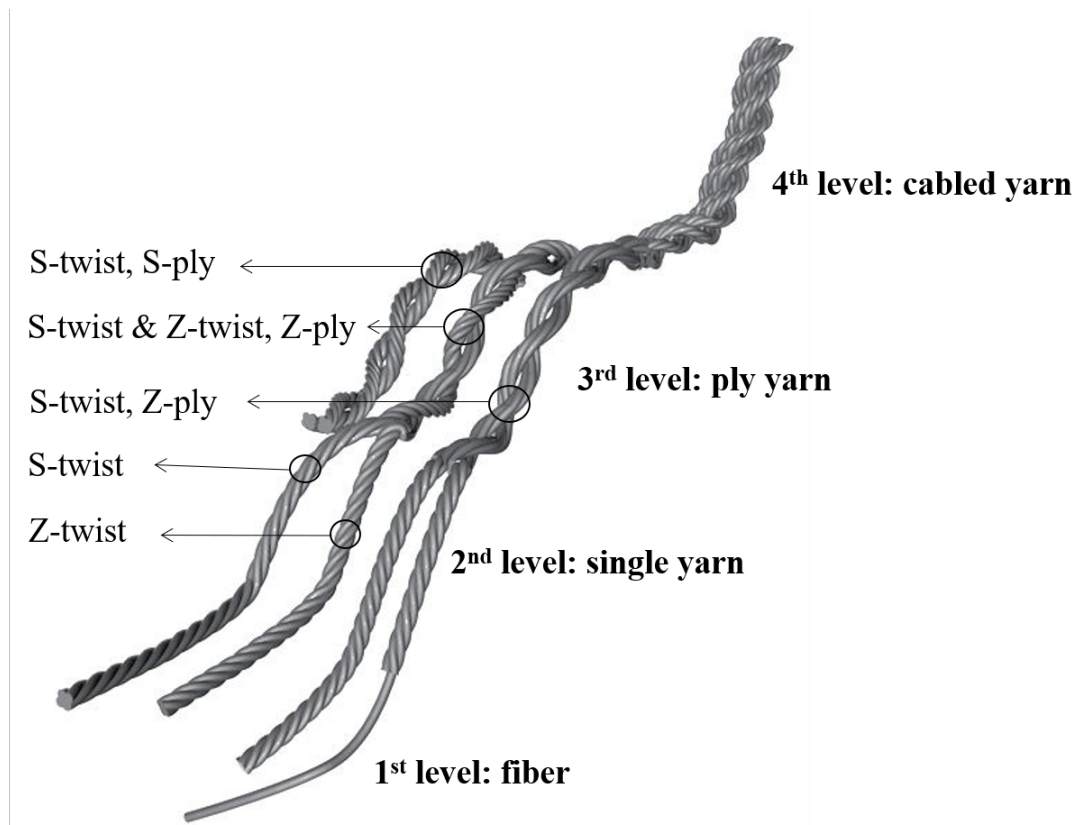


Figure 4-4. Hierarchical structures of yarns.

Several yarn types and hierarchical structures have been employed for TCPAs. For example, the early CNT-based TCPAs took the form of staple yarns, where the nanoscale short CNT fibers are drawn from the forest and then twisted into a helical yarn structure for torsional actuation (Figure 4-1)[6]. More twists were inserted into this staple yarn structure to make a coiled yarn structure for linear motion[13]. These helical or coiled single yarn structures can be regarded as the 2nd level structures in the yarn structure hierarchy, where the constituting CNTs are the 1st level structure.

Higher-level structures of CNT-based TCPAs are explored, including ply yarns (3rd level) and cabled yarn (4th level) (**Figure 4-5a-d**)[9]. To construct a mechanically stable structure is one

of the most common purposes of the two-ply yarn, where the opposite chirality of the ply yarn and constituting single yarns provide balanced torque (Figure 4-5e)[17]. A simple method for making a torque-balanced two-ply yarn is by folding a highly twisted single yarn in the middle and letting it snarl to self-develop an opposite twist (Figure 4-5e). In this way, the strict tethering condition and returning springs required reversible actuation of TCPAs can be eliminated, as the twist of the ply yarn and of constituting single yarns can be converted from each other during actuation.

Plying is also a simple and effective scale-up approach of TCPAs for utilization in real applications such as robotics with higher mechanical strength and work output[9], [30]. Kim et al. reported the multiplied and coiled CNT yarns showing higher mechanical toughness (3.5 times) and contractile work density (1.72 times) than that of single CNT yarns[9]. The evolution of CNT yarn structures from a sheet of CNT fibers to cabled CNT yarns is shown in Figure 4-5a-d, and the final cabled structure is investigated as a torsional and linear actuator. The hierarchical cabled CNT yarn (Figure 4-5d) is composed of multiple ply yarns that are coiled after plying several single yarns (Figure 4-5c), while the single CNT yarns with helically aligned CNTs in Z or S directions (Figure 4-5b) are prepared by directly drawing and twisting from a spinnable CNT forest. By multiplying, the resulting cabled yarn TCPAs with high mechanical strength and actuation stroke was then sewed into a film substrate for higher-level actuation[9].

Another example of staple yarn TCPA is fabricated from natural fibers such as cotton, wool, and flax[15] (Figure 4-5g), as natural fibers are typically short. Compared to the CNT-based TCPAs, they are cheaper, safer, and more conventional in textile products and thereby hold great potential as wearable actuators.

While CNT and most natural fiber-fabricated TCPAs take the form of staple yarn[6], the synthetic polymer fiber-based TCPAs are typically filament yarns and higher structures made out

of them[7]. For example, the first nylon-based TCPA is a monofilament yarn, where a nylon filament with a diameter ranging from 100 to 1000 μ m is twisted and coiled for linear actuation (Figure 4-5h) [7]. Ply yarn with a torque-balanced structure was also fabricated to prevent unwanted end rotation and is assembled into fabrics for higher mechanical work output. While the nylon TCPA generate a repeated linear stroke around 20%[7], the ultra stretchable spandex TCPAs show a higher linear stroke of 45%[31] under lower actuation temperature. As is shown in Figure 4-5i, a bundle of spandex filaments is twisted and coiled into a multifilament single yarn, which is then subjected to heat setting treatment to stabilize the shape for actuation. However, the spandex TCPAs requires an additional heat source for actuation. To overcome this issue, Kim et al. blend spandex with silver-coated nylon and fabricated a coiled multifilament yarn TCPA that can be actuated by joule heating[1]. Figure 4-5k shows the schematic of this yarn structure, and the complete wrapping of the spandex filaments over nylon is visualized in SEM. The evolvement of coiled yarn structure is shown in Figure 4-5l, where a multifilament silver-coated nylon yarn and a multifilament spandex yarn are twisted together. During twisting, the spandex filaments tend to wind on the surface of the structure, while the nylon filaments stay in the center due to the stiffness difference of the two types of filaments. Further twisting increases the compactness of the yarn and leads to fully coiling into a double helix yarn (as is shown in the schematic) at the end of the process. As a result, this double helix yarn-structured TCPA produces a high linear stroke (40%) under joule heating, and in addition, spandex serves as an insulating layer on the surface of the yarn providing electrical safety. Another example of multifilament yarn TCPA is the moisture-drive viscose rayon TCPA. Figure 4-5j shows a multifilament viscose rayon yarn, and 9-ply of the yarns that is twisted and coiled under different tensile loads [32].

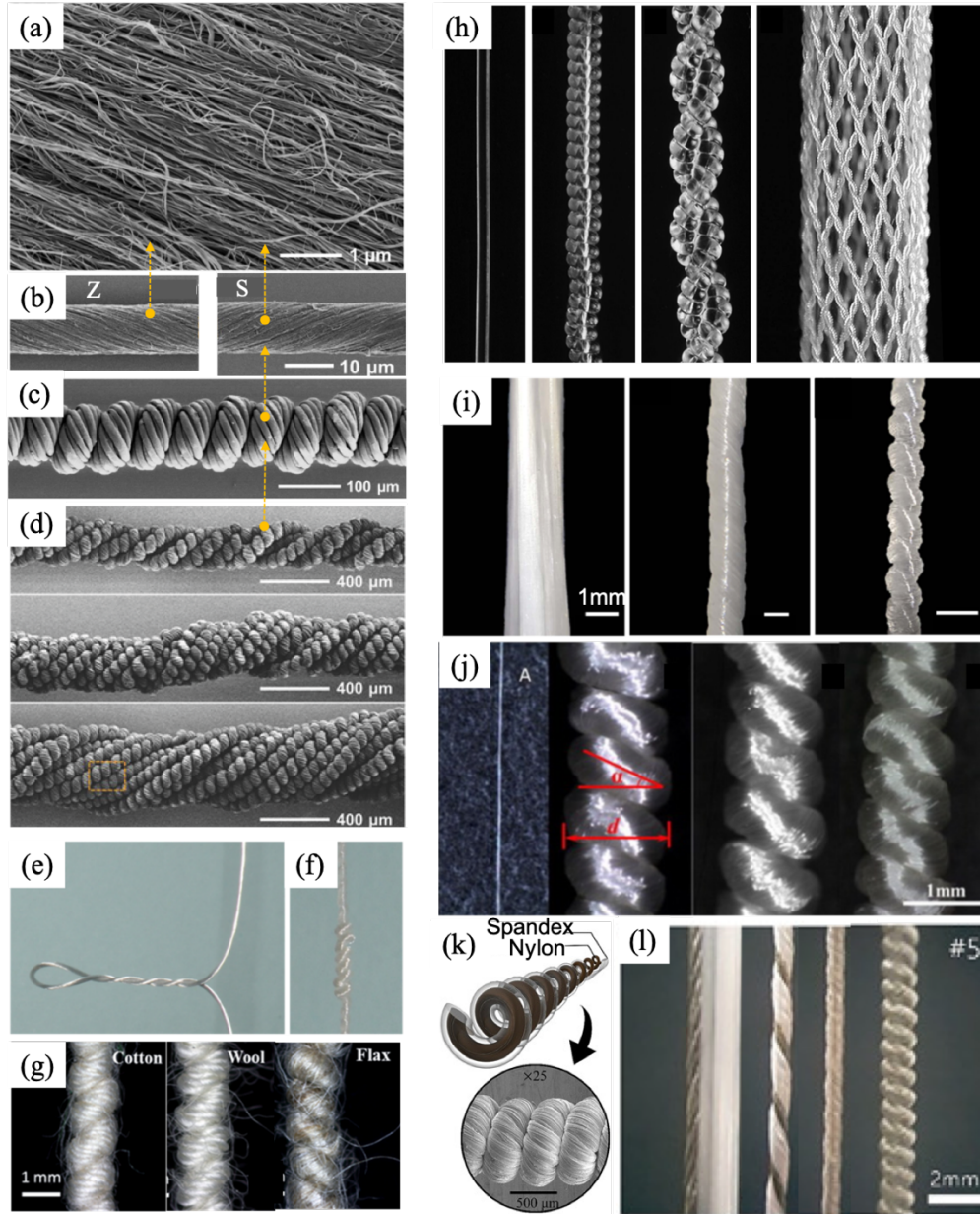


Figure 4-5. Hierarchical yarn structures and different yarn types used in TCPAs. (a-d) Hierarchical structures evolution of CNT-based staple yarn TCPAs: (a) CNT sheet with aligned fibers, (b) twisted single yarn with different twist directions, (c) ply yarn with further twist insertion to coil, and (d) cabled yarn by bundling ply yarns and twisting[9]. (e-g) Natural fiber-based single staple yarn TCPAs: (e) development of torque-balanced two-ply structure, (f) development of coiled single yarn, and (g) photograph of fully coiled, single staple yarn made by cotton, wool, and flax[15]. (h) Photographs of monofilament nylon yarn TCPAs with different structure hierarchy, with the first image as the precursor monofilament[7]. (i-j) Photographs of the evolution of coiled, multifilament yarn TCPAs from a bundle of filaments: (i) Spandex[31] and (j) viscose rayon[32] multifilament yarn TCPAs. (k-l) Heterogeneous multifilament yarn TCPA: (k) schematic and SEM image of the yarn structure made by, (l) twisting and coiling a bundle of filaments of nylon and spandex[1].

In summary, TCPAs have taken a variety of yarn geometries in a hierarchical manner due to the inherent geometrical features of the constituting fibrous materials and the enhancement of actuation behaviors. CNT- and some natural fiber-based TCPAs are staple yarns, while most synthetic fiber-based TCPAs are monofilament and multifilament yarns. To enhance and diversify the actuation performance, these single twisted yarns are further coiled, plied and cabled into higher-level yarn structures. The structure-actuation behavior relationship is highly valued in the research of soft actuators (section 4.3.1). It is especially important in the development of TCPAs, as the radial expansion of the yarn is converted into a variety of rotational and linear motions due to the structural mechanics of the yarn. In the next section, the structural mechanics and modeling techniques of the TCPA actuation will be reviewed, and more insights will be drawn from the theoretical analyses of yarns in the textile community.

4.3 Structure mechanics and actuation analysis of TCPAs

4.3.1 Structure mechanics and actuation analysis of torsional TCPAs

The geometry of a twisted single yarn is shown in **Figure 4-6a**. The ideal helical yarn geometry is utilized to study the structural mechanics of twisted yarns in both the textile community[33] and TCPA research[6]. The precursor fiber (before twisting) is regarded as a slender uniform rod with a length of l_f and a diameter of d_f . After twisting, the geometry of the twisted yarn is characterized by the yarn length (l_t), the yarn diameter (d_t , regarded the same as fiber diameter, $d_t = d_f$), twist density ($T_t = \frac{n_t}{l_t}$), and the surface twist angle (α_t). And the relationship of yarn geometry, fiber geometry, and inserted number of twist (n_t) is given by,

$$l_t^2 = l_f^2 - \pi^2 n_t^2 d_t^2 \quad \text{Eq.1}$$

and,

$$\alpha_t = \tan^{-1} \pi d_t T_t \quad \text{Eq.2}$$

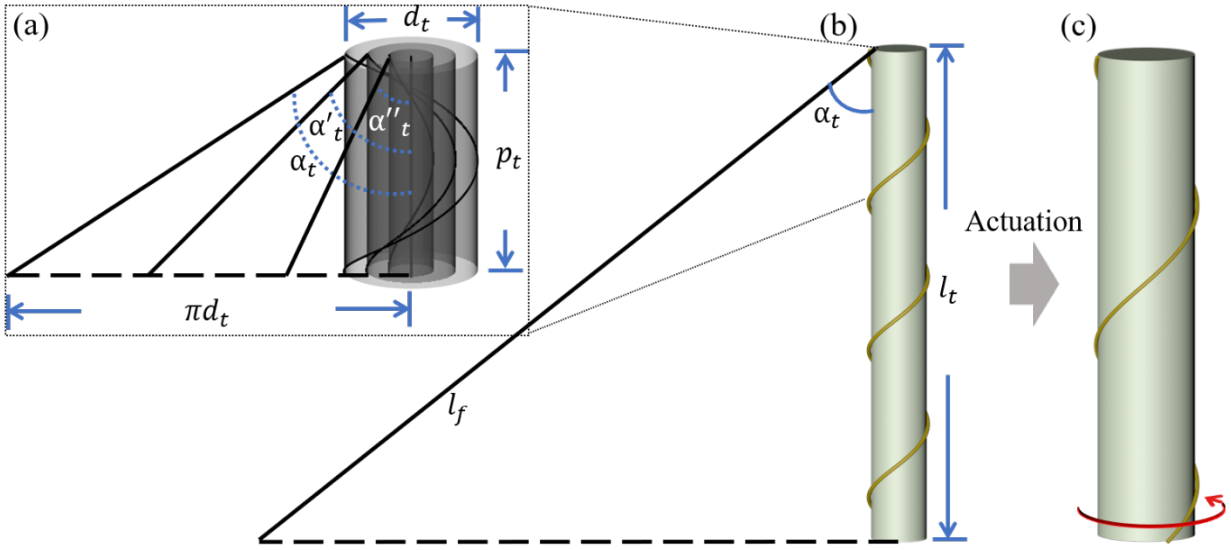


Figure 4-6. Structure mechanics of single yarn-based torsional TCPAs. (a) Zoom-on view of one pitch of a twisted single yarn. (b) Single helix model of a twisted yarn. (c) Radial expansion-induced untwist actuation. The yellow line on the surface of the yarns represents the helical trace on the surface due to twisting. The red arrow represents the rotation direction during actuation.

The physical origin of the torsional actuation of TCPAs is explained by the single helix model[24]. When the yarn length contracts and (or) the diameter increases, the twisted yarns generate torsional motion in the untwisting direction. The torsional actuation can be characterized by the ratio of final ($n_t + \Delta n_t$) and initial (n_t) number of turns, given by[7],

$$\frac{n_t + \Delta n_t}{n_t} = \frac{\Delta l_f}{l_f} \frac{1}{\cos^2 \alpha_t} - \frac{\Delta d_t}{d_t} - \frac{\Delta l_t}{l_t} \tan^2 \alpha_t \quad \text{Eq.3}$$

Assuming the change of fiber and yarn length ($\Delta l_f, \Delta l_t$) is negligible during actuation, and the radial change of the twisted yarn (Δd_t) is the only driven force, the torsional stroke (ΔT_t) in terms of the number of untwists (Δn_t) per yarn length is given by[24],

$$\Delta T = T \left(\frac{d_t}{d_t + \Delta d_t} - 1 \right) \quad \text{Eq.4}$$

The blocking torque ($\tau_{t,blocked}$) due to untwisting is given by[24],

$$\tau_{blocked} = 2\pi\Delta T_{t,free}S_t \quad \text{Eq.5}$$

where $\Delta T_{t,free}$ is the free torsional stroke of the twisted single yarn. S_t , the torsional stiffness of the yarn, is a product of J_t and G_t , where J_t is the second moment of inertia, given by $J_t = \frac{\pi d_t^4}{32}$, and G_t is the shear modulus of the yarn.

Given the coefficient of stimuli-induced expansion, coefficient of thermal expansion (ρ) for instance, the diameter change of the yarn (Δd_t) due to temperature change ($\Delta T'$) follows,

$$\Delta d_t = \rho\Delta T'd_t \quad \text{Eq.6}$$

Plugging Eq.6 into Eq.4, the thermal-induced torsional stroke can be written as,

$$\Delta T_t = \frac{T\rho\Delta T'}{1 + \rho\Delta T'} \quad \text{Eq.7}$$

Plugging Eq.6 into Eq.5 and expanding the expression of $\Delta T_{t,free}$ and S_t , a comprehensive relationship of the blocking torque and the fundamental parameters can be written as,

$$\tau_{t,blocked} = \frac{\pi T_t \rho \Delta T' G_t \pi d_t^4}{16(1 + \rho \Delta T')} \quad \text{Eq.8}$$

The torsional stroke and torque also depend on the tethering conditions. **Figure 4-7** shows three typical tethering methods of single twist yarn-based torsional TCPA for reversible actuation. As is shown in Figure 4-7a, the free end of the yarn actuator is connected to a rotational shaft with a constant torque imposed by a weight hanging with a thread on the shaft. When the yarn over l_A is actuated, it untwists together with the shaft, lifting up the weight. When the stimulus is removed, the twist is recovered due to the constant torque by the weight. Higher

weight leads to larger torque but a lower torsional stroke. The advantage of this setup is the ability to actuate the whole yarn, as the torque is linearly proportional to the length of the active part.

The second method is fixing both ends of the yarn actuator, actuating a portion of the yarn while using the rest as the returning spring (Figure 4-7b). In addition, a weight can be attached to the intersection between active and passive parts. Compared to the first method, it is simple, but the reduced active length leads to a lower number of rotations and actuation torque[6].

A similar method uses an elastic fiber as the returning spring, which is attached to the end of the yarn actuator (Figure 4-7c). Again, a weight can be attached in between for additional external torque[24]. The known and tunable shear stiffness of the returning spring, as well as its passive nature, add convenience and precision in overall experiment and characterization.

A general form of the rotation angle at the end of the active yarn (θ) under the tethering condition in Figure 4-7c can be obtained using the torque balance equation as[24],

$$S'_A \left(2\pi\Delta T_{t,free} l_A - \tau_{ext} \left(\frac{1}{S'_A} - \frac{1}{S_A} \right) - \theta \right) = S_r \theta \quad \text{Eq.9}$$

where S_A , S'_A , and S_r are the torsional stiffness of the un-actuated yarn, actuated yarn, and the returning spring, $\tau_{t,ext}$ is the torque provided by the hanging weight. This equation represents a static model of torsional actuation, where the torque generated by the yarn actuator at this tethering condition (left of the equation) is equal to the torque generated by the returning spring (right of the equation).

By rearranging Eq.9, the θ under tethering condition as Figure 4-6d follows[24],

$$\theta = (2\pi\Delta T_{t,free} l_A - \tau_{ext} \left(\frac{1}{S'_A} - \frac{1}{S_A} \right)) \left(\frac{S'_A}{S'_A + S_r} \right) \quad \text{Eq.10}$$

The θ under the tethering condition shown in Figure 4-7b is calculated in the same way as that in Figure 4-7c, only to change the S_r by S_A . When the yarn is tethered as Figure 4-7a, the θ is obtained by reducing Eq.10 to

$$\theta = 2\pi\Delta T_{t,free}l_A - \tau_{t,ext}\left(\frac{1}{S'_A} - \frac{1}{S_A}\right) \quad \text{Eq.11}$$

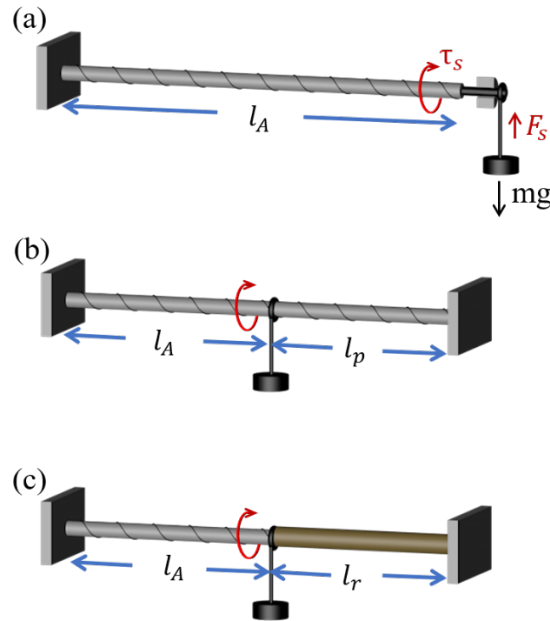


Figure 4-7. Tethering conditions for single yarn-based torsional TCPAs. The black line on the surface of the yarns represents the helical trace on the surface due to twisting. The red arrow represents the rotation direction during actuation.

The reversible actuation of single yarn-based TCPAs usually requires shape-setting to remove the internal stress, or applying external torque to balance the internal torque. A more efficient method is to fabricate self-ply yarn, which is torque balanced by releasing a partial single yarn twist into the ply yarn twist (**Figure 4-8**). The self-ply yarns are always used as torsional TCPAs.

Elkhamy et al.[34] analyzed the evolution of the ply twist from the single yarn twist by calculating the equilibrium strain energy of the single yarn above the convergence point and the ply yarn below the convergence point (Figure 4-8). Isotropic linear elasticity is assumed in the

analysis. The strain energy of the twisted single yarn per unit length (U_t) is composed of tensile strain energy ($U_{t,t}$) and shear strain energy ($U_{t,s}$), each written as,

$$U_{t,t} = \frac{2F_t^2}{E\pi d_t^2} \quad \text{q.12}$$

$$U_{t,s} = 2\pi T_t \quad \text{q.13}$$

where F_t is the tension applied to the single yarn during the twisting process. The strain energy of the self-ply yarn per unit length (U_p) is the sum of the tensile strain energy ($U_{p,t}$), shear strain energy ($U_{p,s}$), and bending strain energy ($U_{p,b}$), each expressed as,

$$U_{p,t} = \frac{4T_t^2}{E\pi d_t^2} \cos \alpha_p \quad \text{q.14}$$

$$U_{p,s} = \frac{E\pi d_t^4}{24} \left(\pi T_t \cos \alpha_p - \frac{\sin \alpha_p \cos \alpha_p}{d_t} \right)^2 \quad \text{q.15}$$

$$U_{p,b} = \frac{E\pi d_t^2}{64} \sin^4 \alpha_p \quad \text{q.16}$$

where α_p is the helical angle of self-ply yarn. Therefore the total strain energy of the ply yarn is,

$$U_p = \frac{4T_t^2}{E\pi d_t^2} \cos \alpha_p + \frac{E\pi d_t^4}{24} \left(\pi T_t \cos \alpha_p - \frac{\sin \alpha_p \cos \alpha_p}{d_t} \right)^2 + \frac{E\pi d_t^2}{64} \sin^4 \alpha_p \quad \text{q.17}$$

Tayebi et al.[35] showed an illustrative plot of the above strain energies of the self-ply monofilament yarn as a function of α_p . As α_p increases during self-plying process (no tension at the yarn ends), the $U_{p,t}$ and $U_{p,b}$ increases and the $U_{p,s}$ decreases, resulting in a reduction of the

total strain energy, U_p . Further increasing of α_p leads to the rising of U_p . Therefore, by solving the Eq.17 and get the U_p minimum, the configuration characteristics of self-ply yarn at equilibrium is obtained.

The actuation principle of the self-ply TCPA is shown in Figure 4-8. The radial change-induced reversible untwisting and twisting of constituting single yarn leads to the further twisting and recovery of the self-ply yarn.

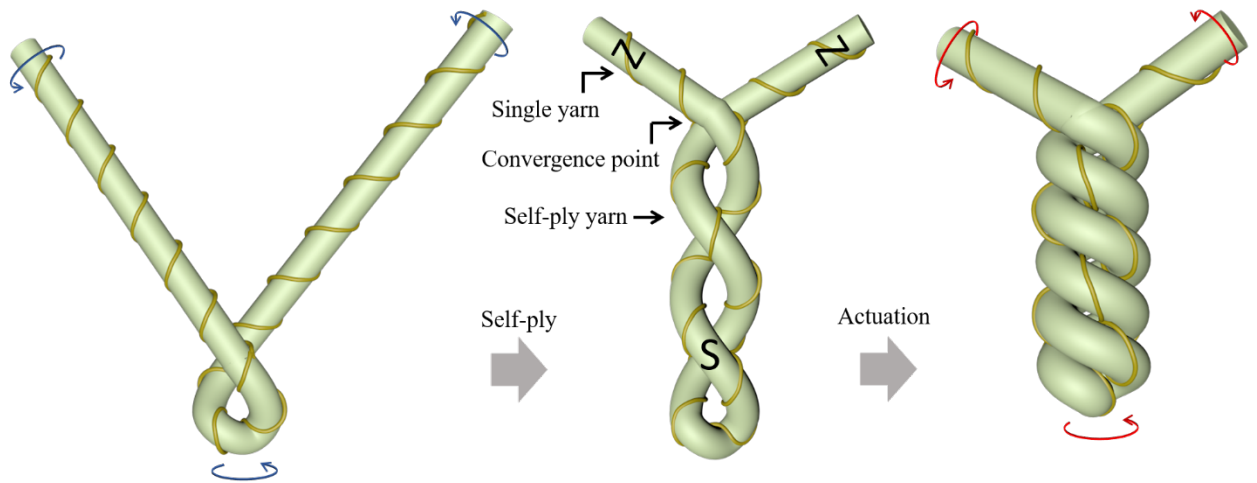


Figure 4-8. Structural evolution and actuation of self-ply yarn-based TCPAs. The yellow line on the surface of the yarns represents the helical trace on the surface due to twisting. Blue arrows represent the untwist tendency of a single yarn and the resultant plying direction of the self-ply yarn. The red arrow represents the rotation directions of the single yarn and the resultant further twisting of the self-ply yarn during actuation. Character Z and S are the yarn twist type.

4.3.2 Structure mechanics and actuation characterization of linear TCPAs

Linear TCPAs are fabricated by coiling the twisted single yarn is on itself (self-coil) or on a mandrel (mandrel-coil) to form a coiled yarn (**Figure 4-9**). The self-coiling of an overtwisted yarn is due to the strain energy minimization. The critical twist density ($T_{critical}$) upon which coil starts to develop is given by[24],

$$T_{critical} = \frac{8\sqrt{2\sigma E_t}}{\pi d_t G_t} \quad \text{Eq.18}$$

where σ is the tensile stress (force normalized to the cross-sectional area of the twisted single yarn, $\frac{4F}{\pi d_t^2}$) applied at yarn ends during coiling, E_t is the Young's modulus of the twisted single yarn.

The $T_{critical}$ can also be written as a function of applied tensile force as[36],

$$T_{critical} = \frac{8(1 + \nu)}{\pi^{\frac{3}{2}} E_t^{\frac{1}{2}} d_t^2} \sqrt{F} \quad \text{Eq.19}$$

where ν is the Poisson's ratio, and assume that the twisted fiber or yarn is a mechanically isotropic material ($2G(1 + \nu) = E$). However, most textile fibers and yarns are highly anisotropic, and thus the Eq.19 need to be modified.

Figure 4-9b shows the actuation behavior of the self-coiled TCPA. The untwisting of the constituting single yarn due to radial expansion leads to the linear contraction of the TCPA. However, the adjacent coils tend to lay on each other during the coiling process, and therefore linear contraction strain is limited.

Mandrel-coiled TCPAs with tunable coil diameter and pitch length have higher actuation stroke (Figure 4-9c). Another merit of mandrel-coiled yarns is the structural diversity and the resultant actuation behavior diversity. The twisted yarn can be wound around a mandrel in various manners, such as winding in the same or an opposite direction to the twist direction to fabricate homochiral or heterochiral coiled TCPAs (Figure 4-9c, d). The opposite structures lead to opposite actuation behaviors, where the homochiral TCPAs contract under the untwisting moment of the single yarn and the heterochiral TCPAs extend. Moreover, by winding the twisted

yarn around a cone-shaped mandrel to avoid adjacent coil contact during contraction, a much higher actuation stroke can be achieved (Figure 4-9e).

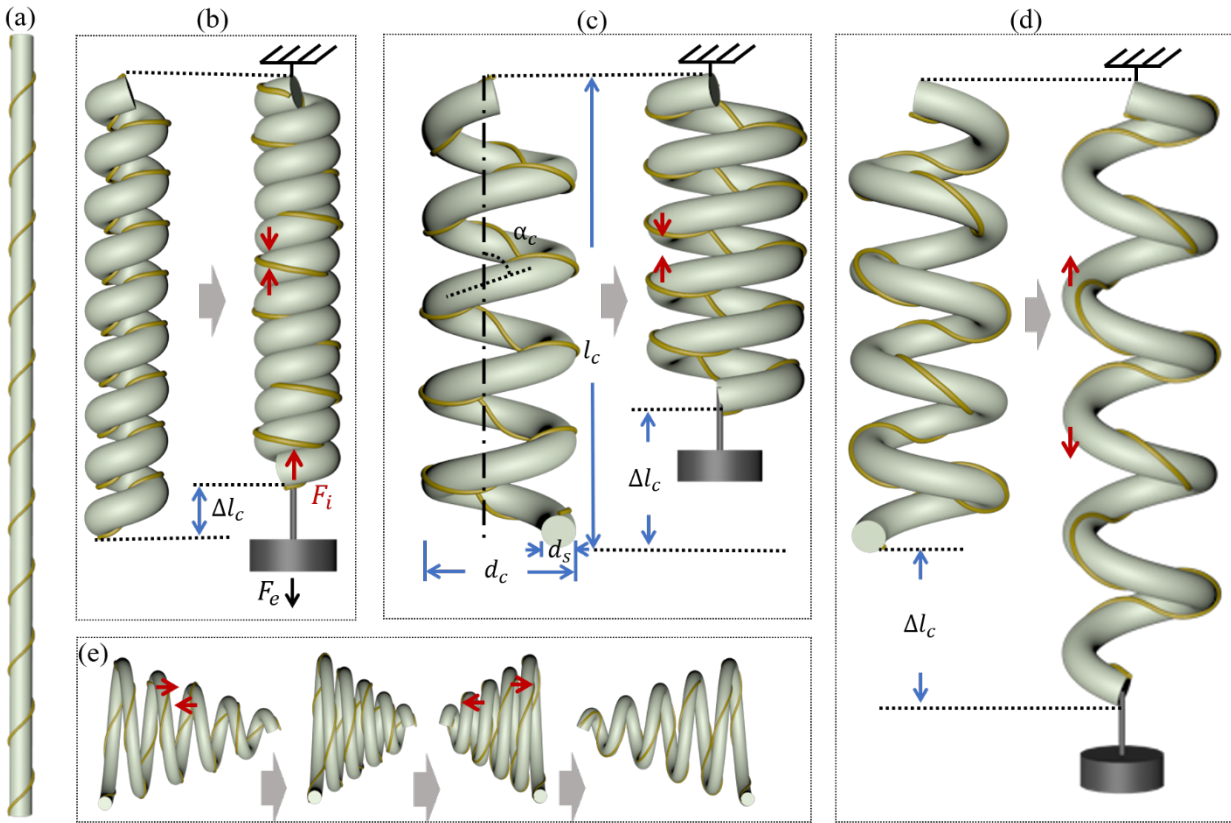


Figure 4-9. Structure mechanics of linear TCPAs and their structural design. (a) Twisted single yarn. (b) Self-coiled yarn and its actuation behavior. (c) Mandrel-coiled, homochiral yarn and its actuation behavior. (d) Mandrel-coiled, heterochiral yarn, and its actuation behavior. (e) Mandrel-coiled, homochiral yarn with gradient coil diameter and its actuation behavior. The yellow line on the surface of the yarns represents the helical trace on the surface due to twisting. The red arrow represents the rotation directions of the single yarn and the resultant further twisting of the self-ply yarn during actuation.

The geometry of the coiled TCPA is characterized by the length (l_c), diameter (d_c), number of coils (n_c), coil angle (α_c) and the spring index ($C = \frac{d_c}{d_t}$) of the coiled yarn. The insights of the mechanism of linear deformation of the coiled yarn were provided by Love with the elastic spring model[37]. According to Love, the linear extension of a coiled spring is originated from the torsional rotation of the constituting fiber. Thus the linear strain of the coiled yarn ($\varepsilon_c = \frac{\Delta l_c}{l_c}$) is given by[24],

$$\varepsilon_c = \frac{l_t^2 \Delta T}{l_c n_c} \quad \text{Eq.20}$$

Considering the tethering condition for linear TCPAs (Figure 4-9d), a load is always attached to the coiled yarns to characterize the mechanical output as well as enhance the actuation behavior[36], [38]. Abbas et al.[38] used Catiglianos Second Theorem[39] to express the elastic elongation of the coiled yarn under both external force and actuation torque as,

$$\Delta l_c = f_{11} F_e - f_{12} \tau_t \quad \text{Eq.21}$$

where f_{11} and f_{12} are the flexibility coefficients of the coil (check the literature[38], [39] for their expression), F_e is the external force acting on the coil. As a result, the linear displacement Δl_c can be calculated by inputting the structural and mechanical parameters of the twisted single yarn to obtain f_{11} and f_{12} , the external tension, F_e , and the actuation torque of the twisted single yarn, τ_t , by solving Eq.8. In a static condition, the $F_e = F_c$. Therefore we can rearrange Eq.22 and get[38],

$$F_c = \frac{\Delta l_c + f_{12} \tau_t}{f_{11}} \quad \text{Eq.22}$$

Abbas et al.[38] also considered the dynamic condition during the linear TCPA actuation,

$$F_e + F_c + F_d = 0 \quad \text{Eq.23}$$

F_e under dynamic condition (upward motion) is given by,

$$F_e = m\ddot{x} - mg \quad \text{Eq.24}$$

where \ddot{x} is the acceleration. F_d is the damping force, written as[38],

$$F_d = b\dot{x} \quad \text{Eq.25}$$

where b is the damping coefficient that can be obtained experimentally, and \dot{x} is the linear velocity. Plugging the Eq.22, Eq.24, Eq.25 into Eq.23, we get an second-order differential equation[38],

$$m\ddot{x} - mg + b\dot{x} + \frac{x - x_0 + f_{12}\tau_t}{f_{11}} = 0 \quad \text{Eq.26}$$

where $x - x_0$ is the linear displacement Δl_c . By solving the time-dependent stimuli change (e.g., temperature-time function[38]) and inputting into Eq.8 to obtain the time-dependent torque, the linear actuation displacement Δl_c as a function of time can be obtained[38].

4.3.3 Parameter analysis

According to the above analysis, the actuation results of the TCPAs are determined by several factors at different hierarchical levels of the yarns, including the mechanical, structural, and stimuli-responsive parameters of the precursor fiber (1st level), the mechanical and structural parameters of the twisted (2nd level) and/or coiled yarns (3rd level). Table 1 gives an overview of these parameters, and how they affect other parameters and the final actuation results. The number of parameters and complexity of these parameters (constant, variable, mutual-dependent) contributes to the final actuation performance. A careful inspection of their relationships can give insight into the TCPA modeling, design, and performance improvement.

Table 1. TCPA parameters and their effects.

	1 st level (fiber)		2 nd level (twisted yarn)		3 rd level (coiled yarn)	
	Parameter	Effect	Parameter	Effect	Parameter	Effect
Structural	d_f	P: d_t, α_t, GJ N: $T, l_t, T_{critical}$	d_t	P: $\alpha_t, \tau_{blocked}$ N: T, l_t, C	d_c	P: C, α_c N: F_c
	l_f	P: l_t	l_t	P: $n_t, \tau_{blocked}$	l_c	
			$T (= \frac{n_t}{l_t})$	P: $\alpha_t, \Delta T, \tau_{blocked}$	$C (= \frac{d_c}{d_t})$	N: k
			α_t	P: d_t	α_c	P: d_c
Mechanical	E_f	P: E_t	E_t	P: $T_{critical}$	k	P: F_c N: ε_c
	G_f	P: G_t	G_t	P: $\tau_{blocked}$ N: $T_{critical}$		
Stimuli-responsive	e.g., CTE, CHE	P: Δd_f	ΔT	P: $\tau_{blocked}, \varepsilon_c$	ε_c	P: F_c
	$E_f \sim$ stimuli	P: E_t	$\tau_{blocked}$		F_c	
	$G_f \sim$ stimuli	P: G_t				
	$\Delta d_f \sim$ stimuli	P: ΔT				

*“Effect” is direct effect from equation (1-6) and related assumptions. “P” is positive effect, “N” is negative effect.

*Red text is actuation result parameters at different hierarchical levels.

*When considering the effect of a parameter, other parameters are regarded constant.

4.3.3.1 Parameters of the precursor fiber

The original fiber (1st level) has three groups of parameters important to the geometry and actuation behavior of the TCPAs. First of all, the diameter of the precursor fiber (d_f) directly influences (1) the d_t , (2) the l_t , (3) the α_t (for the same T), (4) the torsional rigidity (GJ), (5) T (for same α_t), and (6) $T_{critical}$. With same T , larger d_f leads to a shorter l_t , larger α_t , and larger GJ resisting twisting deformation, and small $T_{critical}$. Due to these effects, with same T , the larger d_f ultimately contributes to higher $\tau_{blocked}$ for the twisted yarn and earlier development of coils during the twisting process. However, the ΔT , torsional stroke, is not dependent on d_f when T is constant[40]. Another structural parameter of the fiber is the l_f , which obviously, affects the l_t that is in linear relationship to the number of the total untwist (Δn_t). For easier comparing between experiments, T is always used for torsional actuation by normalizing Δn_t to the l_f .

In terms of mechanical properties of fibers, the shear modulus (G_f) positively affects the shear modulus of the twisted single yarn (G_t) and thus positively contributes to the actuation torque of a twisted yarn (Eq.8). In many cases, G_f is regarded as $\frac{E_f}{2(1+\nu)}$ by assuming the fiber as an isotropic elastic rod[36], [41], and directly used as G_t . However, In polymer fibers are usually mechanically anisotropic due to the directional alignment of molecules during fabrication process[42], therefore careful inspection of G_f is needed. Moreover, the actuation stimuli (e.g., temperature, moisture) always soften the material and thus decreases the E_f and G_f . To better analyze the actuation result, the E_f and G_f at different temperatures need to be considered[40].

Stimuli-responsive parameters comprise another important group of precursor fiber parameters originating the actuation behavior. The coefficient of thermal expansion (CTE) and coefficient of hygroscopic expansion (CHE) are the most common parameters of the stimuli-responsive materials used for TCPAs, expressing the relationship between the volume expansion and temperature/humidity. Although some researchers use a constant coefficient value in the analysis, the CTE and CHE for most polymers changes with the level of stimuli (level of temperature or humidity) and are microstructure-dependent[43].

4.3.3.2 Parameters of the twisted single yarn

The twisted yarn (2nd level) has two groups of parameters that are determined by the fiber parameters and fabrication parameters and are directly responsible for its actuation results (listed in the stimuli-responsive parameter group). The d_t , again, is regarded the same as the d_f , and therefore can be considered to have the same effects as the d_f as mentioned before. The l_t , while always used to normalize the torsional actuation results, if considered, is proportional to the Δn_t and the $\tau_{blocked}$. The twist density, T , is a fabrication parameter, and can also be used to

characterize the structure of the yarn. Equation 4 shows that for a given fiber, the T and Δd_f are directly responsible for the torsional stroke. Higher the T , higher the ΔT of the twisted yarn, and therefore higher $\tau_{blocked}$. However, upon a critical twist value ($T_{critical}$), further twisting leads to self-coiling of the yarn.

The mechanical property of the twisted yarn responsible for the actuation results is the G_t (Equation 8). The G_t can be obtained experimentally[11], or calculated considering the anisotropic properties of the fiber and twisted geometry[38], or briefly regarded the same as G_f [36], [41] in the theoretical analysis. In practical, a large twist far beyond the linear elastic range of the fiber is always used to fabricate TCPAs, and therefore a more precise approach is to measure the G_t . For example, Aziz et al conducted the torsional mechanical test of a nylon fiber at different twist density within the linear elastic range, and obtained the G_t that was later used to calculate the $\tau_{blocked}$ [11].

References

- [1] K. Kim *et al.*, “Double Helix Twisted and Coiled Soft Actuator from Spandex and Nylon,” *Advanced Engineering Materials*, vol. 20, no. 11, p. 1800536, 2018, doi: 10.1002/adem.201800536.
- [2] L. Saharan, M. J. de Andrade, W. Saleem, R. H. Baughman, and Y. Tadesse, “iGrab: hand orthosis powered by twisted and coiled polymer muscles,” *Smart Mater. Struct.*, vol. 26, no. 10, p. 105048, Sep. 2017, doi: 10.1088/1361-665X/aa8929.
- [3] T. Jia *et al.*, “Moisture Sensitive Smart Yarns and Textiles from Self-Balanced Silk Fiber Muscles,” *Adv. Funct. Mater.*, vol. 29, no. 18, p. 1808241, May 2019, doi: 10.1002/adfm.201808241.
- [4] J.-B. Chossat, D. K. Y. Chen, Y.-L. Park, and P. B. Shull, “Soft Wearable Skin-Stretch Device for Haptic Feedback using Twisted and Coiled Polymer Actuators,” *IEEE Transactions on Haptics*, pp. 1–1, 2019, doi: 10.1109/TOH.2019.2943154.
- [5] C. S. Haines, N. Li, G. M. Spinks, A. E. Aliev, J. Di, and R. H. Baughman, “New twist on artificial muscles,” *PNAS*, vol. 113, no. 42, pp. 11709–11716, Oct. 2016, doi: 10.1073/pnas.1605273113.
- [6] J. Foroughi *et al.*, “Torsional Carbon Nanotube Artificial Muscles,” *Science*, p. 1211220, Oct. 2011, doi: 10.1126/science.1211220.
- [7] C. S. Haines *et al.*, “Artificial Muscles from Fishing Line and Sewing Thread,” *Science*, vol. 343, no. 6173, pp. 868–872, Feb. 2014, doi: 10.1126/science.1246906.
- [8] P. Chen, S. He, Y. Xu, X. Sun, and H. Peng, “Electromechanical Actuator Ribbons Driven by Electrically Conducting Spring-Like Fibers,” *Advanced Materials*, vol. 27, no. 34, pp. 4982–4988, 2015, doi: 10.1002/adma.201501731.
- [9] K. J. Kim *et al.*, “Enhancing the Work Capacity of Electrochemical Artificial Muscles by Coiling Plies of Twist-Released Carbon Nanotube Yarns,” *ACS Appl. Mater. Interfaces*, vol. 11, no. 14, pp. 13533–13537, Apr. 2019, doi: 10.1021/acsami.8b21417.
- [10] S. Sharafi and G. Li, “A multiscale approach for modeling actuation response of polymeric artificial muscles,” *Soft Matter*, vol. 11, no. 19, pp. 3833–3843, 2015, doi: 10.1039/C4SM02797C.
- [11] S. Aziz, S. Naficy, J. Foroughi, H. R. Brown, and G. M. Spinks, “Characterisation of torsional actuation in highly twisted yarns and fibres,” *Polymer Testing*, vol. 46, pp. 88–97, Sep. 2015, doi: 10.1016/j.polymertesting.2015.07.003.
- [12] S. M. Mirvakili *et al.*, “Niobium Nanowire Yarns and their Application as Artificial Muscles,” *Advanced Functional Materials*, vol. 23, no. 35, pp. 4311–4316, 2013, doi: 10.1002/adfm.201203808.
- [13] M. D. Lima *et al.*, “Electrically, Chemically, and Photonically Powered Torsional and Tensile Actuation of Hybrid Carbon Nanotube Yarn Muscles,” *Science*, vol. 338, no. 6109, pp. 928–932, Nov. 2012, doi: 10.1126/science.1226762.
- [14] H. Cheng *et al.*, “Moisture-Activated Torsional Graphene-Fiber Motor,” *Advanced Materials*, vol. 26, no. 18, pp. 2909–2913, May 2014, doi: 10.1002/adma.201305708.
- [15] X. Yang, W. Wang, and M. Miao, “Moisture-Responsive Natural Fiber Coil-Structured Artificial Muscles,” *ACS Appl. Mater. Interfaces*, vol. 10, no. 38, pp. 32256–32264, Sep. 2018, doi: 10.1021/acsami.8b12144.
- [16] D. Liu *et al.*, “Spider dragline silk as torsional actuator driven by humidity,” *Science Advances*, vol. 5, no. 3, p. eaau9183, Mar. 2019, doi: 10.1126/sciadv.aau9183.
- [17] Y. Li *et al.*, “Moisture-Sensitive Torsional Cotton Artificial Muscle and Textile,” *Chinese Phys. B*, 2020, doi: 10.1088/1674-1056/ab7745.

- [18] J. A. Lee *et al.*, “All-Solid-State Carbon Nanotube Torsional and Tensile Artificial Muscles,” *Nano Lett.*, vol. 14, no. 5, pp. 2664–2669, May 2014, doi: 10.1021/nl500526r.
- [19] J. A. Lee *et al.*, “Electrochemically Powered, Energy-Conserving Carbon Nanotube Artificial Muscles,” *Advanced Materials*, vol. 29, no. 31, p. 1700870, 2017, doi: 10.1002/adma.201700870.
- [20] M. D. Lima *et al.*, “Efficient, Absorption-Powered Artificial Muscles Based on Carbon Nanotube Hybrid Yarns,” *Small*, vol. 11, no. 26, pp. 3113–3118, Jul. 2015, doi: 10.1002/smll.201500424.
- [21] X. Gu *et al.*, “Hydro-actuation of hybrid carbon nanotube yarn muscles,” *Nanoscale*, vol. 8, no. 41, pp. 17881–17886, 2016, doi: 10.1039/C6NR06185K.
- [22] J. Mu *et al.*, “Sheath-run artificial muscles,” p. 7, 2019.
- [23] J. A. Lee *et al.*, “All-Solid-State Carbon Nanotube Torsional and Tensile Artificial Muscles,” *Nano Lett.*, vol. 14, no. 5, pp. 2664–2669, May 2014, doi: 10.1021/nl500526r.
- [24] S. Aziz, “Polymer Fibre Artificial Muscle,” p. 199.
- [25] H. Yuan *et al.*, “Stable jet electrospinning for easy fabrication of aligned ultrafine fibers,” *Journal of Materials Chemistry*, vol. 22, no. 37, pp. 19634–19638, 2012, doi: 10.1039/C2JM33728B.
- [26] M. Eldessouki, S. Ibrahim, and R. Farag, “Dynamic properties of air-jet yarns compared to rotor spinning,” *Textile Research Journal*, vol. 85, no. 17, pp. 1827–1837, Oct. 2015, doi: 10.1177/0040517514563726.
- [27] “cabled cotton warp 235g: no. 6 hard,” *Handweavers Studio Weaving Supplies*. <https://www.handweavers.co.uk/cabled-cotton-warp-235g-no-6-hard.ir> (accessed Oct. 30, 2020).
- [28] H. M. Behery, “6 - Yarn structural requirements for knitted and woven fabrics,” in *Advances in Yarn Spinning Technology*, C. A. Lawrence, Ed. Woodhead Publishing, 2010, pp. 155–189. doi: 10.1533/9780857090218.1.155.
- [29] “Enabling E-Textile Microinteractions: Gestures and Light through Helical Structures,” *Google AI Blog*. <http://ai.googleblog.com/2020/05/enabling-e-textile-microinteractions.html> (accessed Oct. 30, 2020).
- [30] A. Simeonov *et al.*, “Bundled Super-Coiled Polymer Artificial Muscles: Design, Characterization, and Modeling,” *IEEE Robotics and Automation Letters*, vol. 3, no. 3, pp. 1671–1678, Jul. 2018, doi: 10.1109/LRA.2018.2801469.
- [31] S. Y. Yang *et al.*, “High performance twisted and coiled soft actuator with spandex fiber for artificial muscles,” *Smart Mater. Struct.*, vol. 26, no. 10, p. 105025, Sep. 2017, doi: 10.1088/1361-665X/aa84e4.
- [32] Y. Li and M. Miao, “Water-responsive artificial muscles from commercial viscose fibers without chemical treatment,” *Materials Research Letters*, vol. 8, no. 6, pp. 232–238, Jun. 2020, doi: 10.1080/21663831.2020.1743787.
- [33] J. W. S. Hearle, P. Grosberg, and S. Backer, “Structural mechanics of fibers, yarns, and fabrics,” vol. 1, 19690000, Accessed: Jan. 06, 2021. [Online]. Available: <https://www.bcin.ca/bcin/detail.app?id=81759>
- [34] “Processing mechanics of alternate twist ply (ATP) yarn technology,” p. 267.
- [35] A. Tayebi and S. Backer, “69—THE MECHANICS OF SELF-PLYING STRUCTURES. PART I: MONOFILAMENT STRANDS,” *The Journal of The Textile Institute*, vol. 64, no. 12, pp. 704–710, Dec. 1973, doi: 10.1080/00405007308630327.
- [36] C. Wu and W. Zheng, “A Modeling of Twisted and Coiled Polymer Artificial Muscles Based on Elastic Rod Theory,” *Actuators*, vol. 9, no. 2, Art. no. 2, Jun. 2020, doi: 10.3390/act9020025.

- [37] A. Love, *A treatise on the mathematical theory of elasticity*, vol. 1. 1892. Accessed: Nov. 02, 2020. [Online]. Available: <https://hal.archives-ouvertes.fr/hal-01307751>
- [38] A. Abbas and J. Zhao, "A physics based model for twisted and coiled actuator," in *2017 IEEE International Conference on Robotics and Automation (ICRA)*, May 2017, pp. 6121–6126. doi: 10.1109/ICRA.2017.7989726.
- [39] C. L. Dym, "Consistent Derivations of Spring Rates for Helical Springs," *Journal of Mechanical Design*, vol. 131, no. 7, p. 071004, Jul. 2009, doi: 10.1115/1.3125888.
- [40] S. Aziz, S. Naficy, J. Foroughi, H. R. Brown, and G. M. Spinks, "Controlled and scalable torsional actuation of twisted nylon 6 fiber," *Journal of Polymer Science Part B: Polymer Physics*, vol. 54, no. 13, pp. 1278–1286, 2016, doi: 10.1002/polb.24035.
- [41] F. Karami and Y. Tadesse, "Modeling of twisted and coiled polymer (TCP) muscle based on phenomenological approach," *Smart Mater. Struct.*, vol. 26, no. 12, p. 125010, Dec. 2017, doi: 10.1088/1361-665X/aa8d7d.
- [42] J. W. S. Hearle and W. E. Morton, *Physical Properties of Textile Fibres*. Elsevier, 2008.
- [43] C. L. Choy, F. C. Chen, and K. Young, "Negative thermal expansion in oriented crystalline polymers," *Journal of Polymer Science: Polymer Physics Edition*, vol. 19, no. 2, pp. 335–352, 1981, doi: 10.1002/pol.1981.180190213.

Chapter 5 Bioinspired Bistable Dielectric Elastomer Actuators

Abstract

Nature has plenty of imitable examples of bistable thin structures that can actuate in response to mechanical and environmental stimuli, such as touch, light, moisture, etc. Scientists and engineers have used these as models to develop real-world systems with enhanced shape stability, energy efficiency, and power output. The bistable leaf of the Venus Flytrap (VFT) has a uniquely simple structure that enables exquisite actuation to trap the prey instantly. Here we present a strategy, inspired and derived from the VFT, that incorporates dielectric elastomer (DE) layers in a bistable actuator capable of reversible snapping via electrical stimulation. The trilayered laminated actuator is composed of two prestrained layers and a strain limiting middle layer. The balance between elastic energy and bending energy of the laminates results in the bistable shapes. We explore a broad design space of the bistable architecture through analysis and experiments to validate the fabrication parameters. The rapid snap-through between the two stable configurations is activated by a voltage pulse applied on the DE layers that change the laminate's strain field. While a high electric field is used as the actuation trigger, the self-stabilization characteristic of bistable structure obviates the need for continuous voltage supply. Finally, we recommended a new method of flow control by modulating porosity on curved surfaces via operating BiDEAs as binary valves.

5.1 Introduction

Soft actuators, often made mostly of elastomers having low to moderate elastic moduli, operate through continuous self-deformation to produce shape change under various stimuli. These actuators offer many distinct advantages, including high resistance to mechanical damage, contact compliance independent of shape, noise-free actuation, and better compatibility for human-robot interaction. Compared to the traditional rigid actuators, they are light-weight,

inherently safe even in the absence of precision control, and have facile design and processability at low costs. The inherent softness of these devices is valued in many emerging applications such as soft machines and robotics, human-machine interfaces as in augmented reality [1], healthcare devices [2], compliant grippers [3], and robotics for locomotion in complex terrains [4], etc. While the ability of the elastomeric materials to undergo repeated large deformation and recovery cycles is the key to the performance of these actuators, deformation and recovery of flexible bodies bring about challenges in actuation speed [5], precise position control [6], and repeatability [7]. The challenges come primarily from two aspects, including 1) the mechanical properties of the constituent materials and 2) the characteristics of the stimuli. From a material perspective, the viscoelastic properties may affect the response speed and uncertainty of control [7], [8], and lower modulus may lead to larger viscoelastic loss and low response speed [5]. Stimuli such as temperature and moisture gradients have their problems in generating speed and precision [9], [10], and pneumatic and hydraulic pressure require complex fluidic control systems and external pressurizing devices [11]. Stimuli with better control precision and speed, such as ultraviolet light (UV) [12] and electric field/voltage [13], have their challenges in potentially inducing material degradation and safety issues. Strides have been made to address both of these issues of materials and stimuli. For example, CNT electrode was optimized for dielectric elastomer actuator (DEA) to prevent premature dielectric breakdown at high voltage [14], self-healable elastomer was used to recover its properties after dielectric breakdown [15], and ultrathin electrode and elastomer was fabricated to lower the actuation voltage to hundreds of volts [16]. Although, the necessity of continuous application of high voltage on DEA still poses a potential for damage to the material and device failure.

One approach to overcome these challenges is to design soft actuators with bistable structures. Bistable structures feature in two stable shapes with associated energy minimum and

mechanical instability in between. These characteristics offer the advantage of programmable shape deformation, self-stabilization, tunable power output during shape transformation. With unique functionalities, bistable soft actuators have been investigated for binary robotic systems [17], deployment of load-bearing structures [18], propulsion of swimming robots [19], tactile display [20], and flow control [11], [21]. Typical construction of bistable actuators involves combining a bistable element (buckled beam or plate) and two active elements that antagonistically drive the bistable transformation. Chouinard et al. reported an antagonistic DEA module for binary robotic systems. The bistability is obtained using a rotary hinge to push out-of-plane a stretched DE film, dividing it into two antagonistic actuators [17]. Chen et al. used a shape memory polymer (SMP) coupled with a bistable truss to provide rapid and powerful propelling force for a swimming robot [19]. Other types of bistable actuator design include pressure-induced bistable dome snapping [11] and coupling between tunable material stiffness and applied pressure [20].

Bistable actuators are also found in nature, with compact architectures, high energy density, and high output power compared to the engineered bistable soft actuators. From the standpoint of simple architecture, the bistable leaves of the VFT are the best exemplar [22]. The rapid closure upon sensing of touch has the fastest speed in the botanical world. Turgor cells (elementary actuators for plants, works by controlling cellular volume through turgor pressure) are selectively distributed in the bistable curved leaves to change the local strain field, thereby activating shape transformation. From the aspect of high power output, the striking of the appendage of Mantis shrimp is overwhelmingly powerful [23]. A bistable saddle-shaped film with very high stiffness but still resilient is the key element, which stores mechanical energy from muscle and instantaneously releases it to drive the striking motion.

This study aims to provide a compact and energy-efficient design paradigm for a bistable dielectric elastomer actuator (BiDEA) by mimicking the working principle of Venus Flytrap. In the proposed BiDEA, we use an asymmetrically prestrained trilayered laminated structure to demonstrate the electric field-induced shape transformation by manipulating the local strains and take advantage of its bending-stretching coupling, as conceptualized in our previous work [24], [25]. A variety of cylindrical bistable shapes are derived from a combination of prestrain, film stiffness, and trimming strategy (**Figure 5-1c-e**). Asymmetric tape-spring and symmetric disk shapes were analyzed in our previous works, with theoretical analyses for the curvature of the stable shapes and bistability range. In this context, symmetry refers to the same level of elastic energies stored in the two stable configurations, determined by the levels of prestrains in the DE layers and dictates the shape stability and ease of actuation. Here the symmetric helical shapes with additional features produced from trimming are analyzed. To switch between to stable shapes, a pulse-wise voltage is applied to the DE on the concave, creating stress large enough to overcome the mechanical energy barrier and instantaneously transform it to the other stable shape. Reversible actuation of the helical BiDEA between the two stable shapes is also demonstrated.

Valves are essential (electro-) mechanical devices used in fluidic and pneumatic systems to control the flow, typically by rotating or linearly moving a rigid element in a tubing. Soft valves are critical components in some of the emerging technologies, including soft robotics [11] and microfluidics [26], [27]. The proposed BiDEAs can be used as a soft valve for on/off control of openings on curved surfaces. Wagner et al. reported a bistable electrostatic valve with pneumatic coupling, wherein one of the two buckled silicon membranes can be activated electrically, and the pneumatic coupling induces the snapping of the other membrane to control the opening [21]. Kink-close is used as an effective method to stop flow in a rubber tubing,

where an energy-minimized bending DEA [28] and a pressure-activated snapping dome [11] is used to pinch silicone tubes. A soft-seal valve is also reported as a commercial product that controls flow in a tube by inflating rubber linings to block the flow [29]. Here, we propose a flow control mechanism by opening and closing cavities on curved surfaces that, to our knowledge, have not been achieved elsewhere. The reported BiDEAs can be designed to accommodate the surface and cavity geometry and can be easily implemented as a binary valve.

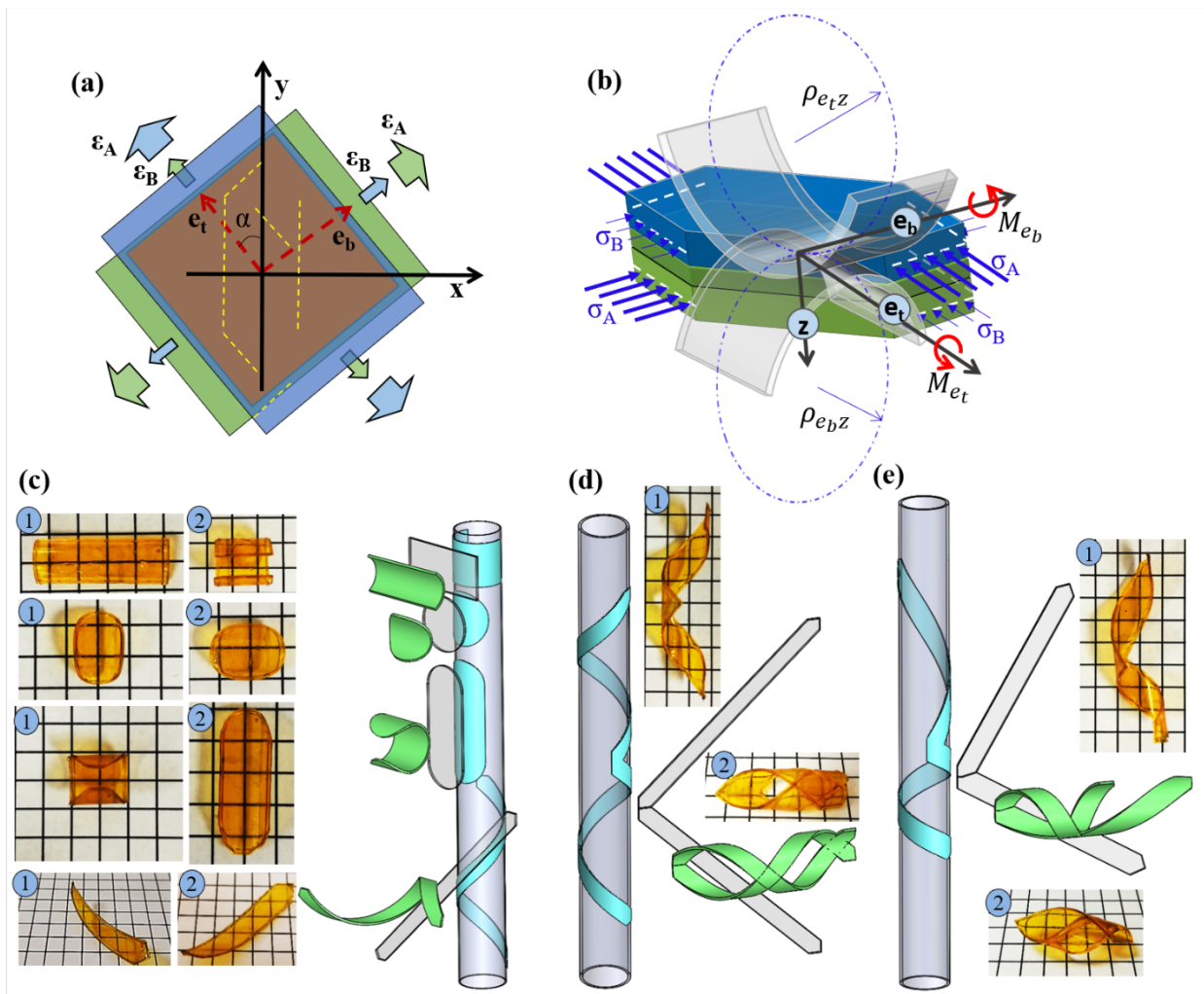


Figure 5-1. Bistable structures derived from prestrained laminates. (a-b) Fabrication parameters and mechanics of bistable bending. (c-e) Bistable shapes after trimming. Two states of the bistable structure are denoted with numbers 1 and 2. (c) Four bistable shapes: rectangular plate, disk, tape-spring, and helix. (d-e) Bistable helices with inverted handedness, with (d) structural symmetry, and (e) structural asymmetry of the two-handed helices.

5.2 Materials and methods

The BiDEAs are fabricated by laminating two orthogonally prestrained elastomeric films (VHB 4905, 3M Corp., MN) onto a middle supporting film of either polyimide (PI, Kapton 100HPP-ST, Dupont, DE) or polyester (PET, RF025, DUNMORE Aerospace, PA), using a procedure describe in our earlier publications [24], [25]. The trilayered laminates are then trimmed with a razor blade to obtain the various shapes. Flexible electrodes are applied to the supporting film and DE films before bonding them together. Poly(3,4-ethylenedioxythiophene) polystyrene sulfonate (PEDOT:PSS, Orgacon™ EL-P5015 Agfa-Gervuert N.V.) is screen printed onto one side of the supporting film as the ground electrode, and carbon nanotube (CNT) sheets are transferred onto the outside of the DE films overlapping the ground electrode. The CNT films were drawn from vertically aligned multiwall carbon nanotube forests synthesized in a tube furnace by the modified chlorine mediated chemical vapor deposition process [30]. The electrodes are subsequently conneted to two computer-controlled high-voltage power supplies (EMCO, model 4120, XP Power) using CNT yarns (Nanocomp Technologies, Inc., NH) and silver epoxy (MG Chemicals, B.C., Canada). Two thin silicone films (Ecoflex™ 00-35, Smooth-On Inc., PA) prepared earlier by spin coating are applied to cover the surface electrodes to eliminate possible electrical leakage.

Initial shape characterization was conducted by capturing still images of the BiDEAs with a camera and measuring the curvature using image analysis software (ImageJ, NIH). Electromechanical response of the BiDEAs were examined by a customized setup consisting of power supplies, a digital video camera and a computerized voltage-trigger. The actuation of the BiDEAs were recorded in real-time using a video camera. The video images were analyzed using ImageJ to determine the shape.

5.3 Bistable structure design

5.3.1 Prestrain-induced bending and bistability

The BiDEAs reported here are based on the principle that laminates with in-plane stresses outside of the neutral plane spontaneously produce out-of-plane deformations such as bending, twisting, and wrinkling. The trilayered laminates, used here, are fabricated with top and bottom DE layers, biaxially prestrained, and attached to the stiffer strain limiting mid-layer to hold the elastic energy in the other layers (Figure 5-1a). The prestrain mismatch of two surface DE layers acts to bend the laminate, while the middle layer serves as the neutral plane. The biaxial bending moments resulting from differential prestrains tend to bend the laminate about orthogonal axes and generate a bistable cylindrical structure (Figure 5-1b).

In the laminate, illustrated in Figure 1a and b, two reference coordinate systems are used to define the principal geometries in 2D (x, y) and 3D (e_t, e_b, z), where the x, y -axes are along with the width and length directions of the trimmed shape during fabrication, and $e_t z$ and $e_b z$ -planes are two planes of curvature in the bent shape. To simplify the analysis, the two DE layers are identically prestrained orthogonally with a larger prestrain (ε_A) and a smaller prestrain (ε_B), and are cross-laminated to the middle layer to get the net asymmetry in prestrains ($\Delta\varepsilon = \varepsilon_A - \varepsilon_B$). Therefore, e_t and e_b can also be interpreted as axes of net asymmetric strains, and the two stable states are energetically symmetric. The relatively high elastic modulus of the middle layer limits its in-plane deformation, and thus the bistable cylindrical shape has zero Gaussian curvature at most regions except for the edges due to the boundary effect [30]. The curvatures in $e_t z$ - ($C_{e_t z}$) and $e_b z$ -planes ($C_{e_b z}$) are opposite in sign and quantitatively identical, due to the same levels of net prestrains and bending stiffnesses (Figure 5-1b). The analysis of the bistable shape follows that in our previous paper [24], capturing the stress distribution along with the laminate thickness and the bending rigidity of different layers, such that,

$$C_{e_{bz}} = C_{e_{tz}} = \frac{2(\sigma_A h_b^2 - \sigma_B h_t^2)}{5E_a(h_t^3 + h_b^3) + E_s h_s^3} \quad \text{Equation 1}$$

Here σ_A and σ_B are contractile stresses induced by strains ε_A and ε_B , h_b and h_t are the thicknesses of the bottom and top DE layers after prestrain, and E_a and E_s are Young's modulus of the DE and strain limiting layers.

5.3.2 Characteristics of helical structures

Now that we have fabricated the bistable laminates, the final shape of the laminate is obtained simply by trimming with a razor blade or laser to yield various shapes, such as rectangular, round, helical, and others. Bistable helical shapes are generated by trimming strips out of the laminate at various angles (α) to the direction of the net prestrain (Figure 1a). After self-equilibration, a bistable helix with two stable shapes having lengths (L_1, L_2), pitches (P_1, P_2), and identical radii of curvature ($\rho_{e_{tz}}, \rho_{e_{bz}}$) for the two stable shapes (Figure 5-2) is obtained. Here the subscripts 1 and 2 denote the two stable states. Angles α and $(\pi - \alpha)$ serve as the helical angles of the two stable states. The geometrical parameters, L_1, L_2, P_1, P_2 , can be expressed in terms of the other geometrical and material parameters as,

$$L_1 = l \cos \alpha, \quad \text{Equation 2}$$

$$L_2 = l \sin \alpha, \quad \text{Equation 3}$$

$$P_1 = \frac{L_1}{N_1} = \frac{L_1}{\frac{l \sin \alpha}{2\pi \rho_{e_{tz}}}} = \frac{2\pi l \cos \alpha}{l \sin \alpha * C_{e_{tz}}}, \quad \text{Equation 4}$$

$$P_2 = \frac{L_2}{N_2} = \frac{L_2}{\frac{l \cos \alpha}{2\pi \rho_{e_{bz}}}} = \frac{2\pi l \sin \alpha}{l \cos \alpha * C_{e_{bz}}}, \quad \text{Equation 5}$$

where l is the length of trimmed strip in 2D, and $C_{e_{tz}}$ and $C_{e_{bz}}$ are calculated curvatures according to Equation 1.

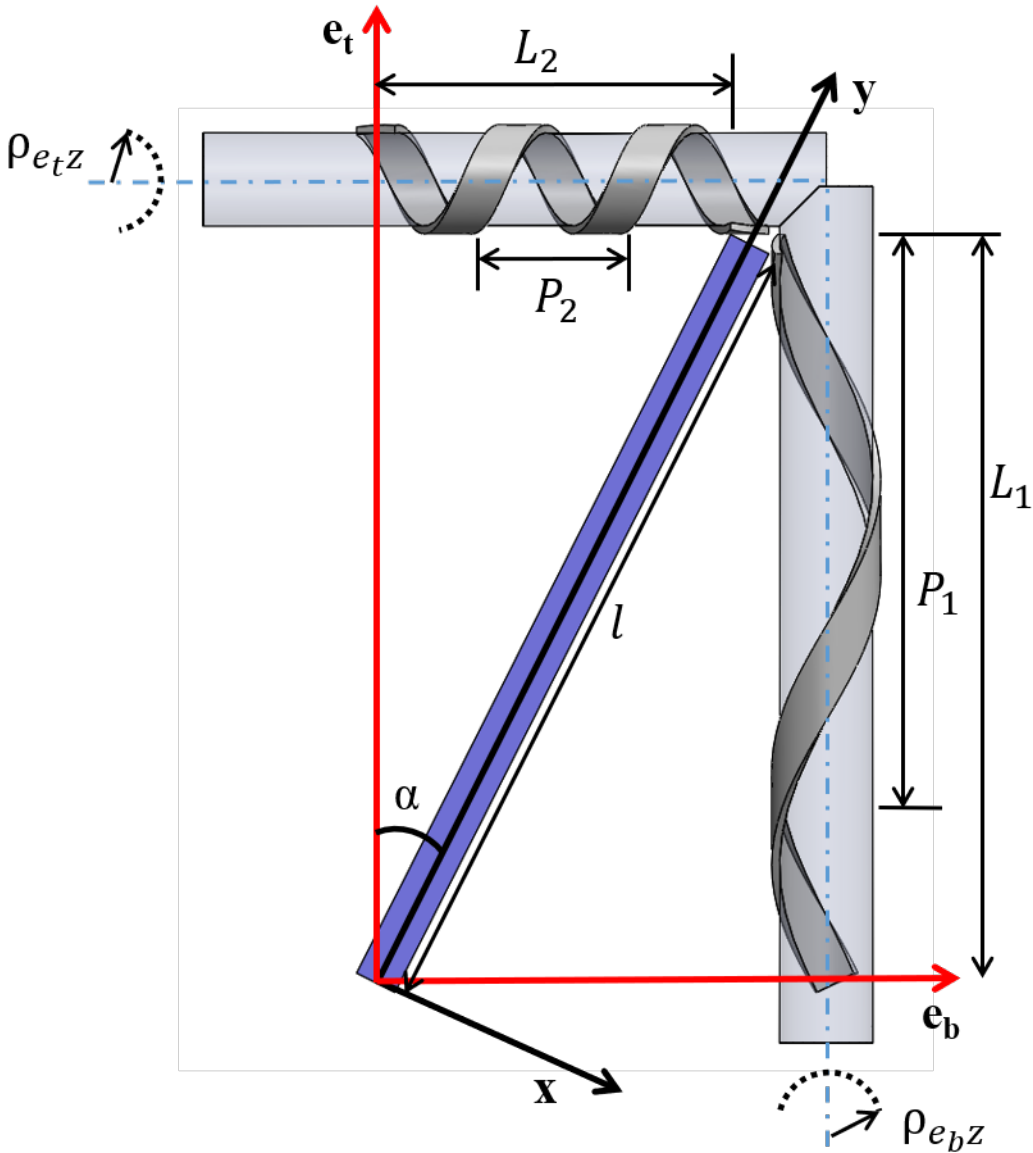


Figure 5-2. Structural parameters for the bistable helix from 2D to 3D.

5.4 Results and discussion

5.4.1 Shape characterization

The effect of prestrains on the bistable shapes of helices and disks is presented in **Figure 5-3a**. It is evident that the curvature increases with the increase in net prestrain, resulting from either reducing ε_B or increasing ε_A . As expected, the curvature values of the helix and the disk

are the same under the same prestrain combinations and match well with the calculated values of curvature. When the net prestrain is lower than a certain level, the resulting curvature cannot hold against its weight, leading to a nearly flat monostable laminate. Figure 5-3b (and d) show the effect of the stiffness of the strain limiting layer on the bistable shape, in terms of both experimental (disk and helix) and theoretical curvatures. PET and PI films with the same thickness but different elastic moduli were chosen as the middle layer. Again, the two trimmed shapes share identical curvatures at given prestrains, as expected. Higher support layer stiffness results in smaller curvature both experimentally and theoretically.

The effect of trimming angle is illustrated in Figure 5-3c. Here the two DE layers are prestrained at $\varepsilon_A = 100\%$, $\varepsilon_B = 40\%$, and attached to the PI film support layer of $25\mu\text{m}$ thick. The angle α ranges from 0 to 90° . As a result, the helical length for the two stable states changes, while the curvature remains constant.

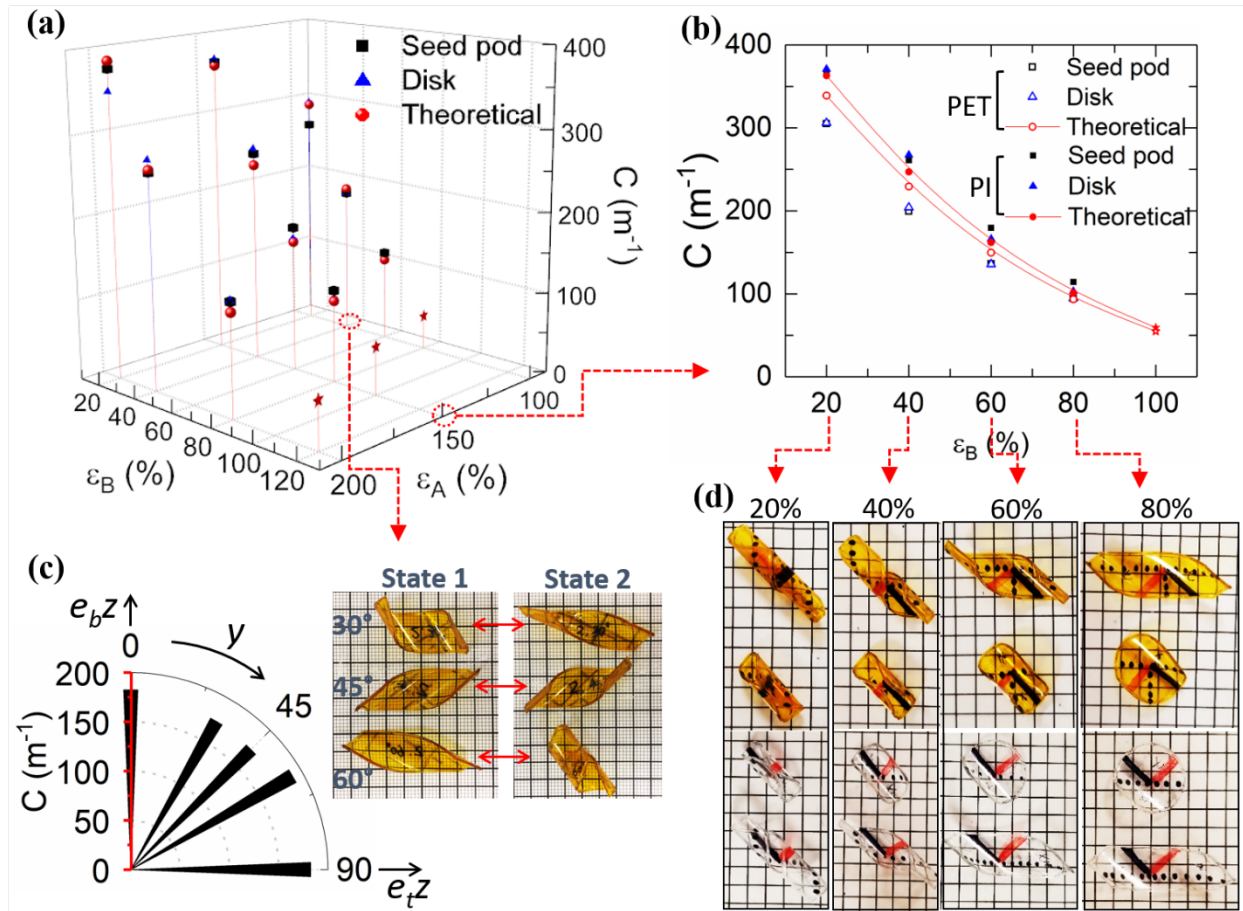


Figure 5-3. Effect of fabrication parameters on the bistable shape. (a) Effect of prestrains on the curvature of the bistable disk and bistable helix, and theoretical results, with PI as the support layer. (b) Effect of elastic modulus of the support layer on the curvature, with $\epsilon_A = 40\%$ and constant ϵ_B . (c) Experimental samples of (b). (d) Effect of cutting angle on the curvature and experimental samples showing the bistable shapes with cutting angles of 30° , 60° , and 90° . Star dots represent monostable samples.

5.4.2 Electric field-induced actuation of the helical BiDEA

To activate the shape transformation of the BiDEA, both top and bottom DE layers are used as active elements by applying a pair of compliant electrodes on each layer. The electric field-induced actuation response in DEs is due to the electrostatic attraction between the oppositely charged compliant electrodes on the surfaces of a thin elastomeric film[31], [32], see **Figure 5-4a**. The resulting deformation of the DE films upon applying an electric field to the electrodes alters the strain field in the laminate and thus activates the shape transformation

(Figure 5-4b, **Video S1**). While the middle electrode (PEDOT:PSS) printed on the strain limiting layer works as the common ground, the two surface electrodes (CNT film) placed on the outside of the DE layers are positively charged and individually controlled for the reversible actuation, see Figure 5-4c.

One of the problems encountered upon application of electric field is the dielectric breakdown of the air at the edges of the DE layers where the electric field is generally higher and exceeds the dielectric strength of the air (3×10^6 V/m [33]) sooner. The electrical breakdown of the air at the sharp electrode edges and corners of a conductor is well documented [33]. Silicone oil and a thin film of silicone were tested as insulating materials around the electrode edges. While silicone oil can be easily brushed onto the surface of the BiDEA without affecting its mechanical properties, the silicone film was more effective as an insulator. To eliminate the air breakdown without significantly affecting the mechanical properties of the laminate, two thin films (10-15 μ m) of low-modulus silicone were formed using spin coating and subsequently laminated to the outer surfaces of the BiDEA.

Figure 4 illustrates the actuation mechanism, the actuator layout, and the experimental setup. The sample shown in Figure 5-4d is a helical BiDEA with a curvature of 110 m^{-1} and is reversibly actuated at 5kV. Cyclic actuation of the helical BiDEA with the alternative voltage supply for V_1 and V_2 is shown in Video S1.

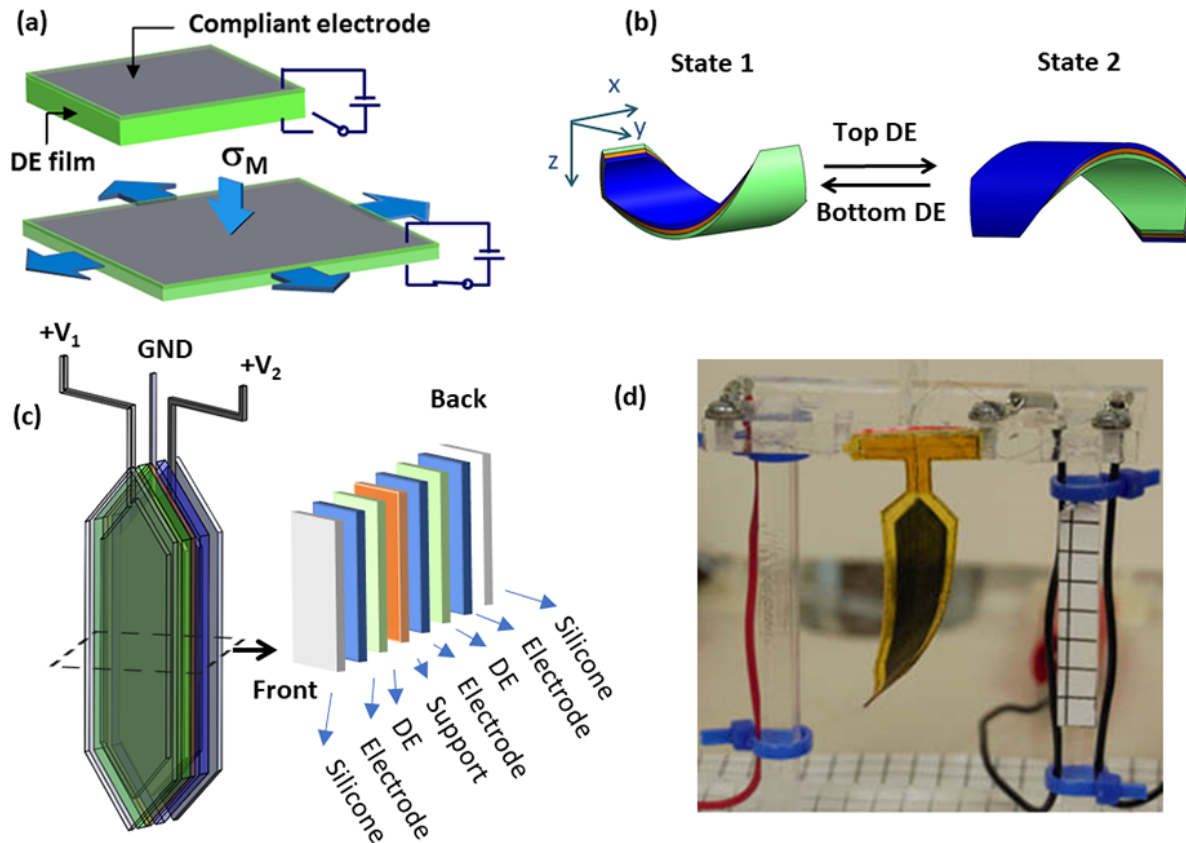


Figure 5-4. Actuation mechanism and experimental setup. (a) Actuation mechanism of DE. (b) Schematic of reversible actuation of the BiDEA. (c) Laminate components and layout. (d) Actuation setup.

5.4.3 Binary valve for curved surfaces

As mentioned earlier, we explored the use of BiDEA as a soft valve. Utilizing the BiDEAs as binary valves for porosity control of openings on curved surfaces has several advantages: 1) Automatic valve control with applied potential is convenient and reliable, 2) The binary mechanism can keep pores open or close (on or off) without continuous application of voltage, 3) The soft BiDEAs can conform to the curvature of the porous substrate for better sealing, 4) The porosity of the surface can be controlled by varying the tethering conditions of the BiDEA, and 5) Individual activation of BiDEA is attainable to control the porosity in a spatially distributed manner.

Three tethering conditions of the disk type BiDEA are proposed for a brief comparison of the efficacy of porosity control and the required operational space. The examples shown in **Figure 5-5a-c** have identical fabrication and material parameters but are trimmed differently for three tethering conditions. The bistable valve in Figure 5-5a is tethered at two ends (marked by red triangles) along the centerline at points further out from the valve boundary to allow for complete flattening of the curved center axis required for zero Gaussian curvature of the other stable state. Therefore for this shape, we included a small extension on both sides of the BiDEA valve. In this case, the degree of pore opening is small, but the advantage is that the BiDEA requires a small space to operate. Figure 5-5b shows another version of the BiDEA valve tethered at one end, with the tether anchored away from the valve boundary. While the valve, in this case, cannot fully close, the extent of the opening is the largest. It is because the thin extended strip is monostable due to its small width [34]. Figure 5-5c shows the BiDEA valve configuration with a single anchor placed at the valve boundary along the center bending axis. In this case, the valve can fully close and open with a large opening.

The electrical control of the binary valve on a curved surface is presented in Figure 5-5e and **Video S2**. The corrugated porous substrate (Figure 5-5d) is 3D printed with a curvature of 110 m^{-1} same as that of the BiDEA discussed earlier for reversible actuation. The fabrication of the BiDEAs is based on the relationship of various parameters represented in Equation 1. Here we adopt the third tethering conditions for the bistable valve considering the full closure state and decent magnitude of opening. By applying a voltage to the top pair of electrodes, the BiDEA snaps down to close the pore, while applying a potential to the bottom pair of electrodes reverses the deformation and opens the pore.

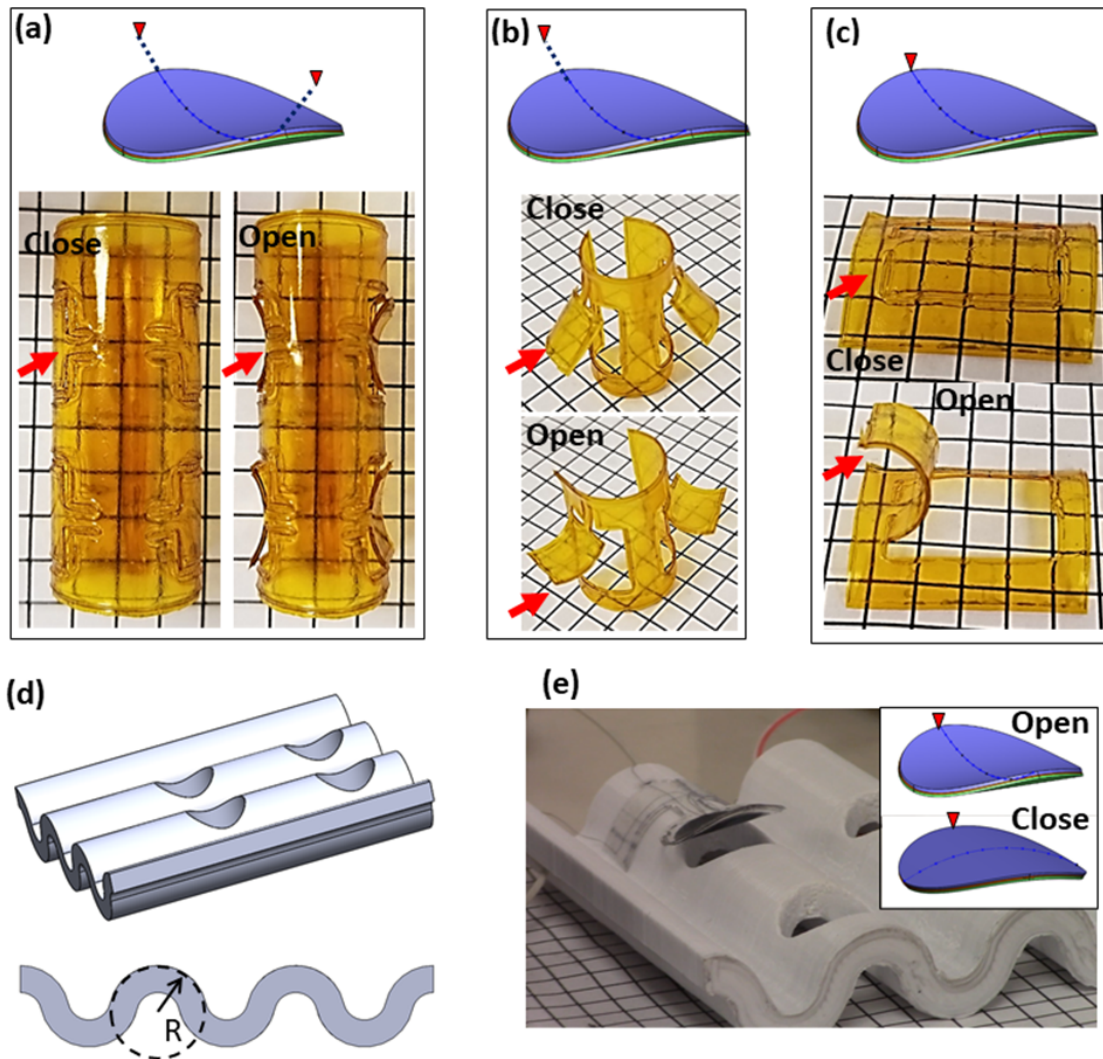


Figure 5-5. Bistable valve design and actuation. Bistable valves with (a) two-ends tethered and (b) one end tethered outside valve boundary, and (c) one-end tethered at the valve boundary. (d) A wavy substrate with open holes. (e) Actuation of bistable valve for pore open and close. The red triangle dots represent the tethering points.

5.5 Conclusion

We have presented a novel design for a DE-based bistable soft actuator and addressed the general design issues and their limitations. The BiDEA is a trilayer laminate that can be reversibly transformed from one stable cylindrical shape to another upon application of an electric field to the constituent DE layers. Diverse BiDEA structures were investigated by manipulating the fabrication parameters, including prestrain combinations, mechanical properties

of the constituent layers, and trimmed shape geometry, all guided by laminate bending analyses. The feasibility of reversible actuation of the BiDEAs was also demonstrated by applying an electric field alternatingly to the appropriate DE layer in the structure. The self-equilibrating feature of the bistable structure enables the programmable deformation and eliminates the necessity of continuous high voltage application. We have also demonstrated that this compact, lightweight, shape-programmable, electrically-activated binary actuator can be used as a soft valve or shutter that can operate on curved surfaces. Finally, the BiDEAs offer promising potential for application in wearable or other soft robotics due to their advantages of facile manufacturing, low cost, and flexibility.

References

- [1] J.-B. Chossat, D. K. Y. Chen, Y.-L. Park, and P. B. Shull, "Soft Wearable Skin-Stretch Device for Haptic Feedback using Twisted and Coiled Polymer Actuators," *IEEE Trans. Haptics*, pp. 1–1, 2019, doi: 10.1109/TOH.2019.2943154.
- [2] M. Cianchetti *et al.*, "Soft Robotics Technologies to Address Shortcomings in Today's Minimally Invasive Surgery: The STIFF-FLOP Approach," *Soft Robot.*, vol. 1, no. 2, pp. 122–131, Jun. 2014, doi: 10.1089/soro.2014.0001.
- [3] R. Chen *et al.*, "Bio-Inspired Shape-Adaptive Soft Robotic Grippers Augmented with Electroadhesion Functionality," *Soft Robot.*, Jul. 2019, doi: 10.1089/soro.2018.0120.
- [4] W. Hu, G. Z. Lum, M. Mastrangeli, and M. Sitti, "Small-scale soft-bodied robot with multimodal locomotion," *Nature*, vol. 554, no. 7690, pp. 81–85, Feb. 2018, doi: 10.1038/nature25443.
- [5] S. Rosset, P. Gebbers, B. M. O'Brien, and H. R. Shea, "The need for speed," San Diego, California, Apr. 2012, p. 834004. doi: 10.1117/12.914623.
- [6] G. Panaro, G. Rizzello, D. Naso, and S. Seelecke, "Position Control of Dielectric Elastomer Actuators Based on Port-Hamiltonian Framework," in *2018 IEEE Conference on Decision and Control (CDC)*, Dec. 2018, pp. 6888–6893. doi: 10.1109/CDC.2018.8619077.
- [7] S. Michel, X. Q. Zhang, M. Wissler, C. Löwe, and G. Kovacs, "A comparison between silicone and acrylic elastomers as dielectric materials in electroactive polymer actuators," *Polym. Int.*, vol. 59, no. 3, pp. 391–399, Mar. 2010, doi: 10.1002/pi.2751.
- [8] G.-Y. Gu, U. Gupta, J. Zhu, L.-M. Zhu, and X. Zhu, "Modeling of Viscoelastic Electromechanical Behavior in a Soft Dielectric Elastomer Actuator," *IEEE Trans. Robot.*, vol. 33, no. 5, pp. 1263–1271, Oct. 2017, doi: 10.1109/TRO.2017.2706285.
- [9] D. Jin Kang, S. An, A. L. Yarin, and S. Anand, "Programmable soft robotics based on nano-textured thermo-responsive actuators," *Nanoscale*, vol. 11, no. 4, pp. 2065–2070, 2019, doi: 10.1039/C8NR08215D.
- [10] B. Shin *et al.*, "Hygrobot: A self-locomotive ratcheted actuator powered by environmental humidity," *Sci. Robot.*, vol. 3, no. 14, p. eaar2629, Jan. 2018, doi: 10.1126/scirobotics.aar2629.
- [11] P. Rothmund *et al.*, "A soft, bistable valve for autonomous control of soft actuators," *Sci. Robot.*, vol. 3, no. 16, p. eaar7986, Mar. 2018, doi: 10.1126/scirobotics.aar7986.
- [12] A. H. Gelebart *et al.*, "Making waves in a photoactive polymer film," *Nature*, vol. 546, no. 7660, pp. 632–636, Jun. 2017, doi: 10.1038/nature22987.
- [13] J.-S. Plante and S. Dubowsky, "Large-scale failure modes of dielectric elastomer actuators," *Int. J. Solids Struct.*, vol. 43, no. 25, pp. 7727–7751, Dec. 2006, doi: 10.1016/j.ijsolstr.2006.03.026.
- [14] M. Duduta, E. Hajiesmaili, H. Zhao, R. J. Wood, and D. R. Clarke, "Realizing the potential of dielectric elastomer artificial muscles," *Proc. Natl. Acad. Sci.*, vol. 116, no. 7, pp. 2476–2481, Feb. 2019, doi: 10.1073/pnas.1815053116.
- [15] Y. Zhang *et al.*, "Electrical and Mechanical Self-Healing in High-Performance Dielectric Elastomer Actuator Materials," *Adv. Funct. Mater.*, vol. 29, no. 15, p. 1808431, 2019, doi: <https://doi.org/10.1002/adfm.201808431>.
- [16] X. Ji *et al.*, "An autonomous untethered fast soft robotic insect driven by low-voltage dielectric elastomer actuators," *Sci. Robot.*, vol. 4, no. 37, Dec. 2019, doi: 10.1126/scirobotics.aaz6451.
- [17] P. Chouinard and J.-S. Plante, "Bistable Antagonistic Dielectric Elastomer Actuators for Binary Robotics and Mechatronics," *IEEEASME Trans. Mechatron.*, vol. 17, no. 5, pp. 857–865, Oct. 2012, doi: 10.1109/TMECH.2011.2135862.

- [18] T. Chen and K. Shea, “An Autonomous Programmable Actuator and Shape Reconfigurable Structures Using Bistability and Shape Memory Polymers,” *3D Print. Addit. Manuf.*, vol. 5, no. 2, pp. 91–101, May 2018, doi: 10.1089/3dp.2017.0118.
- [19] T. Chen, O. R. Bilal, K. Shea, and C. Daraio, “Harnessing bistability for directional propulsion of soft, untethered robots,” *Proc. Natl. Acad. Sci.*, vol. 115, no. 22, pp. 5698–5702, May 2018, doi: 10.1073/pnas.1800386115.
- [20] Y. Qiu, Z. Lu, and Q. Pei, “Refreshable Tactile Display Based on a Bistable Electroactive Polymer and a Stretchable Serpentine Joule Heating Electrode,” *ACS Appl. Mater. Interfaces*, vol. 10, no. 29, pp. 24807–24815, Jul. 2018, doi: 10.1021/acsami.8b07020.
- [21] B. Wagner, H. J. Quenzer, S. Hoerschelmann, T. Lisec, and M. Jueress, “Bistable microvalve with pneumatically coupled membranes,” in *Proceedings of Ninth International Workshop on Micro Electromechanical Systems*, Feb. 1996, pp. 384–388. doi: 10.1109/MEMSYS.1996.494012.
- [22] Y. Forterre, J. M. Skotheim, J. Dumais, and L. Mahadevan, “How the Venus flytrap snaps,” *Nature*, vol. 433, no. 7024, pp. 421–425, Jan. 2005, doi: 10.1038/nature03185.
- [23] S. N. Patek, W. L. Korff, and R. L. Caldwell, “Biomechanics: Deadly strike mechanism of a mantis shrimp,” *Nature*, vol. 428, no. 6985, p. 819, Apr. 2004, doi: 10.1038/428819a.
- [24] H. Shao, S. Wei, X. Jiang, D. P. Holmes, and T. K. Ghosh, “Bioinspired Electrically Activated Soft Bistable Actuators,” *Adv. Funct. Mater.*, vol. 28, no. 35, p. 1802999, Aug. 2018, doi: 10.1002/adfm.201802999.
- [25] S. Wei, H. Shao, and T. K. Ghosh, “Bioinspired bistable soft actuators,” in *Electroactive Polymer Actuators and Devices (EAPAD) XXI*, Mar. 2019, vol. 10966, p. 1096629. doi: 10.1117/12.2522123.
- [26] M. Hitzbleck, L. Avrain, V. Smekens, R. D. Lovchik, P. Mertens, and E. Delamarche, “Capillary soft valves for microfluidics,” *Lab. Chip*, vol. 12, no. 11, pp. 1972–1978, 2012, doi: 10.1039/C2LC00015F.
- [27] Q. Yu, J. M. Bauer, J. S. Moore, and D. J. Beebe, “Responsive biomimetic hydrogel valve for microfluidics,” *Appl. Phys. Lett.*, vol. 78, no. 17, pp. 2589–2591, Apr. 2001, doi: 10.1063/1.1367010.
- [28] D. McCoul and Q. Pei, “Tubular dielectric elastomer actuator for active fluidic control,” *Smart Mater. Struct.*, vol. 24, no. 10, p. 105016, Sep. 2015, doi: 10.1088/0964-1726/24/10/105016.
- [29] “Soft-seal valves for industrial uses.” <https://www.pinch-valve.com/soft-seal-valves.html> (accessed Apr. 14, 2020).
- [30] X. Jiang, M. Pezulla, H. Shao, T. K. Ghosh, and D. P. Holmes, “Snapping of Bistable, Prestressed Cylindrical Shells,” *ArXiv180403072 Cond-Mat*, Apr. 2018, Accessed: May 17, 2018. [Online]. Available: <http://arxiv.org/abs/1804.03072>
- [31] R. Pelrine, R. Kornbluh, and G. Kofod, “High-Strain Actuator Materials Based on Dielectric Elastomers,” *Adv. Mater.*, vol. 12, no. 16, pp. 1223–1225, Aug. 2000, doi: 10.1002/1521-4095(200008)12:16<1223::AID-ADMA1223>3.0.CO;2-2.
- [32] R. Shankar, T. K. Ghosh, and R. J. Spontak, “Electroactive Nanostructured Polymers as Tunable Actuators,” *Adv. Mater.*, vol. 19, no. 17, pp. 2218–2223, Sep. 2007, doi: 10.1002/adma.200602644.
- [33] F. W. Strong, J. L. Skinner, and N. C. Tien, “Electrical discharge across micrometer-scale gaps for planar MEMS structures in air at atmospheric pressure,” *J. Micromechanics Microengineering*, vol. 18, no. 7, p. 075025, Jun. 2008, doi: 10.1088/0960-1317/18/7/075025.

- [34] Z. Chen, Q. Guo, C. Majidi, W. Chen, D. J. Srolovitz, and M. P. Haataja, “Nonlinear Geometric Effects in Mechanical Bistable Morphing Structures,” *Phys. Rev. Lett.*, vol. 109, no. 11, p. 114302, Sep. 2012, doi: 10.1103/PhysRevLett.109.114302.

Chapter 6 Moisture-Driven Cellulose Actuators with directional motion and programmable shapes

Abstract

The hygroscopic motion of plants has inspired the development of soft actuators driven by the abundant moisture sources in the environment. The autonomous and untethered moisture-driven actuators driven by environmental moisture and their fluctuation are of great research interest. However, the slow response and the monotonous bending deformation restrict their further application. Here, we present fast-morphing, locomotion direction-controllable, and motion-programmable soft actuators using low-cost and commercially available cellulose films (cellophane). The cellophane films reported here bend almost instantaneously under changing humidity, with maximum curvature of 4 cm^{-1} when the relative humidity (RH) decreases from 55 (ambient) to 15%. The cellophane actuators show high repeatability and negligible hysteresis upon cyclic variation of RH from 20 to 80%. We used both coated and uncoated cellophane films for different actuation modes. The uncoated cellophane is used as a self-walking actuator that can continuously move on a moist substrate through autonomous bending-rolling-flipping cycles. The flipping frequency and direction are controlled by increasing the angular momentum and shifting the center of weight through attaching appropriate weights to the leading ends of the cellophane. The coated cellophane film was used to fabricate motion-programmable actuators through heat-laminating. We design and fabricate several actuator structures and demonstrate their diverse moisture-induced motions.

1. Introduction

In nature, moisture is the primary driving force for the passive actuation in plants. Examples include the opening of pea pods [1] and pinecone [2] for seed disposal, as well as the locomotion

of wheat awns [3], all due to the change in environmental humidity. The passive motion relies on the moisture absorption and desorption-induced volume change of hygroscopic constituent materials, mainly cellulose. Different movement such as bending, twisting, and coiling is achieved at the microscopic level through the response of moisture active and inactive materials present in the structures; for example, the opening of pinecone under decreasing humidity results from the differential deswelling of the bi-layered scale [2]. The various motions of plants have given insight into the design of soft artificial actuators [4], which play a crucial role in emerging technologies such as human-machine interfaces [5] and smart textiles [6].

Soft actuators produce mechanical work under a variety of energy inputs. The active materials used for soft actuators include dielectric elastomers (DE) [7], photo-responsive polymers [8], thermoplastic polymers [9], hygroscopic materials [10], carbon nanotubes [11], etc. The actuation performance such as the large actuation strain of DEs over 200% [12], the high output stress of twisted and coiled polymer (TCP) over 22 MPa [13], the high energy density of CNT actuators of 160 J/kg [14], and the wide range of mechanical flexibility and multi-stimuli responsiveness [15] point to the potential of soft actuators to overcome the limits of conventional actuators (e.g., motors) and possibly surpass the performance of natural muscles.

Among various stimuli used to power the soft actuators, moisture can be rated as the greenest energy that is abundantly available in the environment. The variety of sources include the sweat and breath of humans, day-night rhythm of environmental humidity, and that near and away from the water source, etc. Soft actuators based on the principle of moisture absorption and desorption-induced reversible volume change of the hygroscopic materials designed to convert the moisture gradient into mechanical work have been reported [16]–[19]. However, the slow response speed is a common issue in moisture actuation due to the time needed for moisture diffusion, absorption, and desorption [20], [21]. Therefore, efforts are underway to increase the

actuation speed by creating porous structures to facilitate diffusion [19], [22], accelerating desorption rate by heating [16], and adjusting the absorption and desorption rate of the material [23]. Another limitation of moisture actuation is the limited motion types due to the global moisture variation and less-explored structural design. Typically, the actuator takes the shape of a film that bends or twists upon exposure to a moisture source as a result of differential swelling [23]–[25] [6], [18]. Moreover, the moisture-driven soft actuators are restricted by the lumbering change of the relative humidity (RH) that lack speed and precision. Photo- or electro-thermal [16], [17] and other stimuli-responsive elements [15], [23] have been employed to assist in the quick response of moisture-driven actuators.

Here we report fast, motion-programmable, and locomotion direction-controllable moisture-driven soft actuators using commercially available cellulose films (cellophane). Cellophane is a thin sheet, highly sensitive to moisture with a large swelling ratio (fractional increase in the weight due to water absorption) and the ability to absorb and desorb (fast response) moisture at high speed [26]. It is biodegradable (environmental-friendly) and commonly used in packaging and filtration industries [27]. Two types of cellophane, i.e., uncoated and one side-coated, were characterized for their material properties and moisture-induced bending behavior. The uncoated cellophane deforms continuously in an environment with varying moisture gradients (e.g., the palm of a hand, near water surface) through a series of bending, rotating, and flipping motions. We increased the speed of such movement and achieved directional motion by simply increasing the angular momentum and shifting the center of gravity by attaching appropriate weights to the leading ends of the actuator. For the coated cellophane, a thin coating of moisture-blocking polyvinyl dichloride (PVdC) on the film's surface enhances the bending motion through the differential swelling of the bilayer. The additional heat-laminating capability of PVdC enables the convenient hot press method to fabricate structured actuators with other movements. We

demonstrated several programmable movements of the cellophane actuators, including rotation, snake-like motion, and lifting motions.

2. Materials and methods

Materials: Commercially available uncoated cellophane films with three different thicknesses (21, 28, 42 μm) and one-side, PVdC-coated cellophane (24 μm), were used (Futamura, Atlanta, GA).

Fabrication of motion-programmable actuator: Coated films were used to construct the programmable actuators through heat-lamination. The films were cut into designed shapes, and then laminated with the coated sides in contact with each other at 120°C for 2 minutes using a heat press machine.

Characterization: The degree of crystallinity and preferential crystal alignment direction were measured using a wide-angle X-ray diffractometer (WXR) (Rigaku SmartLab X-ray diffractometer). The water-induced swelling ratios of the uncoated cellophane in three dimensions, i.e., machine direction (MD), cross direction (CD), thickness direction (TD), were measured at ambient temperature, with the in-plane dimensions measured with a ruler, and the thickness measured with a digital thickness gauge (Digital thickness gauge, Mitutoyo). The mechanical properties of the uncoated cellophane in the ambient environment and the wet condition were measured using a tensile tester (MTS, 30-G) with appropriate load cells. The coating thickness was measured on the microscopic images under scanning electron microscopy (SEM TM4000, Hitachi).

Moisture-induced bending analysis: The moisture-induced bending behavior of the cellophane was characterized in both natural moisture-rich environments and a humidity-controlled chamber. The palm of hand and water were used as natural humidity sources. Actuation measurements were performed in a glove box to avoid air movement while the bending motion

of the sample was recorded with a video camera. For humidity-controlled actuation, a customized humidity chamber in which the RH is controlled by tuning the wet and dry air influx was used (Figure 6-3a). The bending angle and curvature were then measured frame by frame using Photoshop (Adobe). The relative humidity and temperature near the sample were continuously recorded by a humidity and temperature sensor (SHTC3, Sensirion, Switzerland).

3. Results and Discussion

Moisture-induced bending

Soft actuators with bending motions are usually fabricated from films [23], [28]. At the same time, the extent of their deformation is enhanced by constructing bilayer structures [15], [18] and bending directions is controlled by introducing mechanical anisotropy [29], [30]. In this study, we used cellophane films that are inherently anisotropic and are available with ultrathin hydrophobic coatings.

The anisotropy of the films comes from the extrusion and roll-to-roll fabrication process, where the cellulose molecules are aligned preferentially in-plane along the machine direction forming a semicrystalline structure. The degree of crystallinity of 43% and preferential crystal orientation in $[\bar{1} 1 0]$ plane (in-plane) were determined by the WXR D for our films (

Figure 6-1a). This microstructural characteristics manifests in anisotropic differential swelling and tensile behavior; both are important in the deformation characteristic of the actuator. The measured differential swelling of the films in three principal directions, i.e., MD, CD, and TD, is shown in

Figure 6-1b, c. The swelling was primarily observed in the TD (97%), with minor swelling in the CD (8.7%) and negligible swelling in the MD. The mechanical anisotropy is also illustrated by the tensile behavior of the films (

Figure 6-1e). The measured Young's modulus (E) in the MD ($E_{MD} = 5.76GPa$) is almost twice of that in the CD ($E_{CD} = 3.2GPa$) in the ambient environment (50%RH, 22°C). By submerging the films in water, the anisotropy enhances ($E_{MD} = 0.38GPa, E_{CD} = 0.14GPa$), while E decreases drastically due to the softening effect of water on cellulose [31]. The coated cellophane film is widely used for moisture blocking and heat-sealing purposes. Here we utilize both features to make moisture-sensitive soft actuators with enhanced bending response and programmable motions. The ultrathin PVdC coating of 3.3 μ m (

Figure 6-1d) effectively enables differential swelling of the film and thereby enhances the bending deformation.

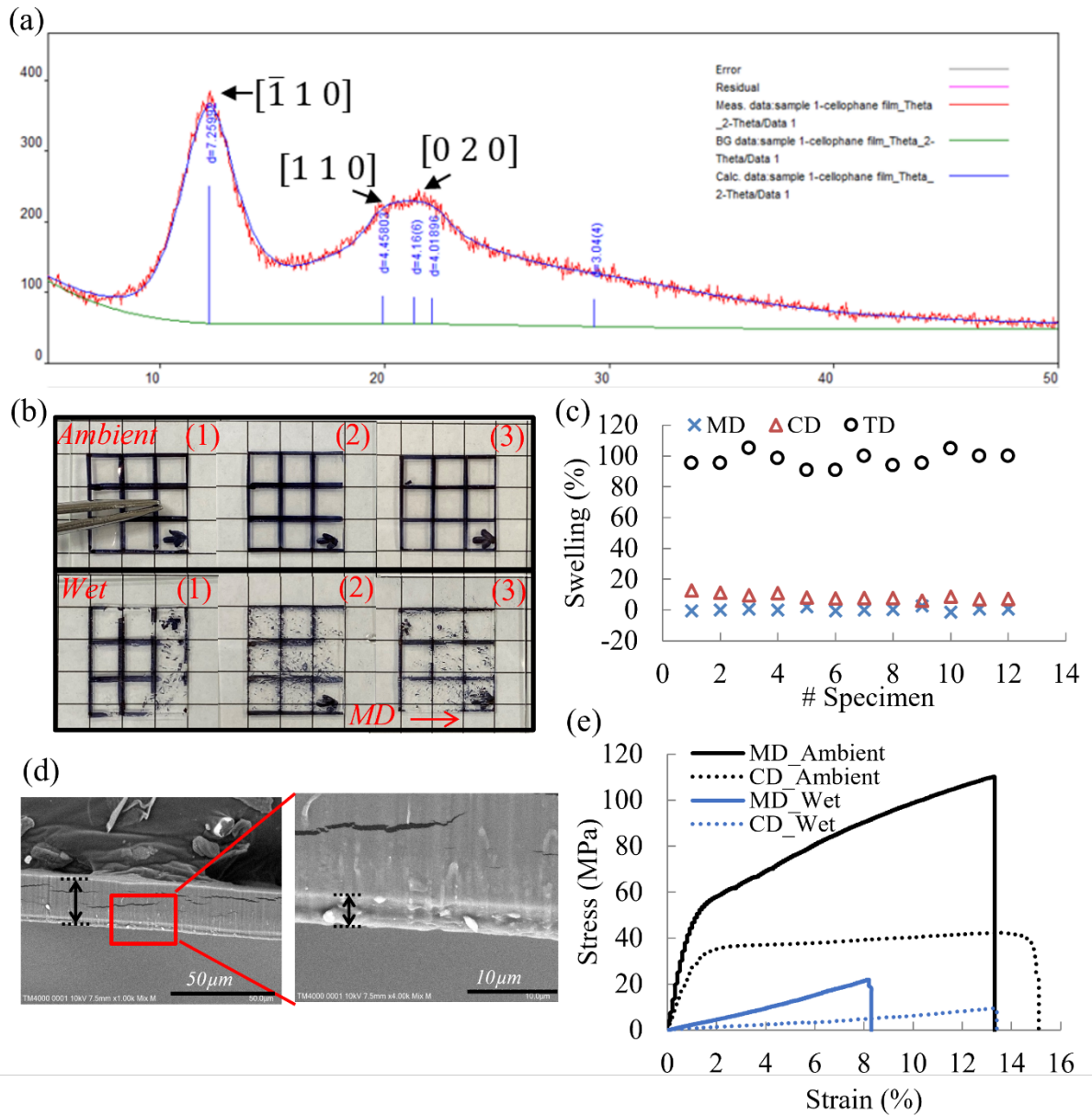


Figure 6-1. Material properties of cellophane films. (a) Semicrystalline information by WAXRD. (b) Water-induced dimensional swelling of uncoated cellophane, and (c) anisotropic swelling in three dimensions. (d) SEM images of the cross-section of the one-side coated cellophane. (e) Anisotropic tensile properties at ambient and wet conditions.

To study the effect of film thickness and coating on the hygroscopic bending performance, we compared the uncoated cellophane films of three thicknesses (21, 28, 42µm) and a 24µm-thick one side-coated cellophane. Unless otherwise specified, all samples for moisture-induced bending actuation were cut along CD in 20mm length and 5mm width. Samples were placed on a

polyester screen mesh that neither blocks nor absorbs the moisture, and then housed in a glove box to avoid air movement.

The films instantaneously bend upward when a water bath was abruptly brought beneath the film and then recover when the moisture source was removed (**Video S2**). The curvature (κ) of different samples and RH as well as temperature near the surface of the film as a function of time are shown in **Figure 6-2c**. In general, thicker films show lower curvature and longer response time because of the higher bending stiffness and prolonged diffusion of water molecules into the film [26]. The coated cellophane generates almost twice the curvature of the uncoated cellophane under similar exposure to moisture, suggesting that the bilayer structure with differential swelling can effectively improve the response. Similar response has been observed upon placing the film on the palm of hand. However, it is important to note that larger κ and faster bending speed are observed on top of the palm of a hand, due to higher and faster increase of RH (**Figure 6-2d**, **Video S3**).

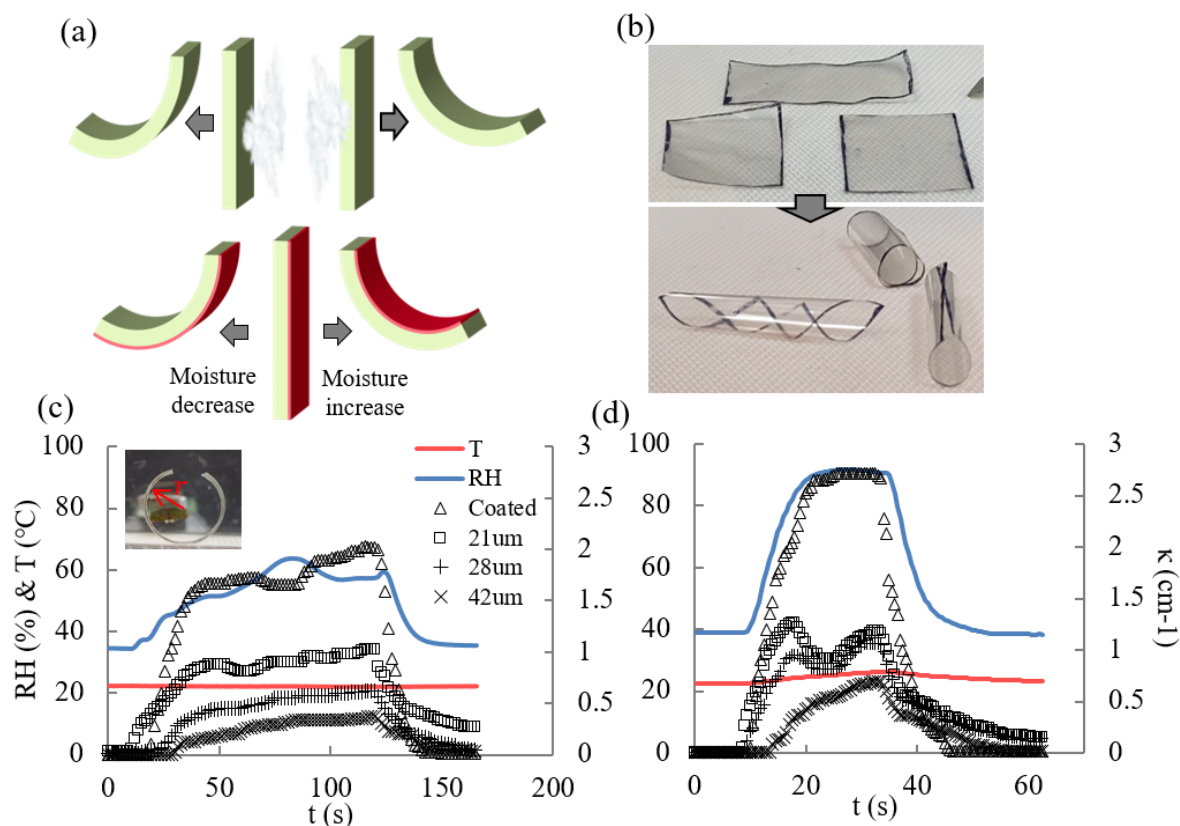


Figure 6-2. Actuation of cellophane under natural moisture gradient. (a) Schematic of moisture-induced bending of the pure and coated cellophane. (b) Photographs of moisture-induced bending of cellophane films cut along MD, TD, and 45° to the MD. (c-d) Curvature change of cellophane films and the change of RH and T when (c) water bath and (d) palm of hand approached and removed from beneath.

Based on our observations thus far we focused on a systematic study of the moisture-induced bending behavior of the coated cellophane using a customized humidity chamber, see **Figure 6-3a**. The RH of the chamber is designed to reliably tune the RH from 10% to 90% in around 40 seconds. The coated film is placed on the polyester screen mesh in the chamber, and its bending behavior under the change of RH is measured (Figure 6-3b, c). As the RH increases from that of the ambient environment (55%) to 90%, the film bends toward the coated side to a κ of 2.8 cm⁻¹ in 10 seconds and gradually recovers as the RH passively returns to the ambient condition. When the RH decreases from ambient to 10%, the film bends in the opposite direction

with an equilibrium κ of 4 cm^{-1} and flattens as RH recovers (Figure 6-3d). The change in curvature follows the RH change closely, which is determined by the RH chamber (e.g., chamber size) and is the primary restriction of actuation speed in this experiment.

The response of the film was further evaluated by subjecting it to cyclic change in RH between 20% and 80%. This range was selected for faster actuation speed due to the nature of the experimental set up that allowed for faster change in RH in that range. In the cyclic actuation of 30s/cycle, the curvature changes repetitively between -3cm^{-1} and 2cm^{-1} (Figure 6-3f, **video S4**). Interestingly, the curvature changes almost linearly with RH during the absorption as well as desorption during one of the cycles, see Figure 6-3g. The result of five actuation cycles demonstrates good repeatability of actuation with small hysteresis (Figure 6-3h). The film recovers to nearly zero curvature in each cycle when RH returns to the ambient level.

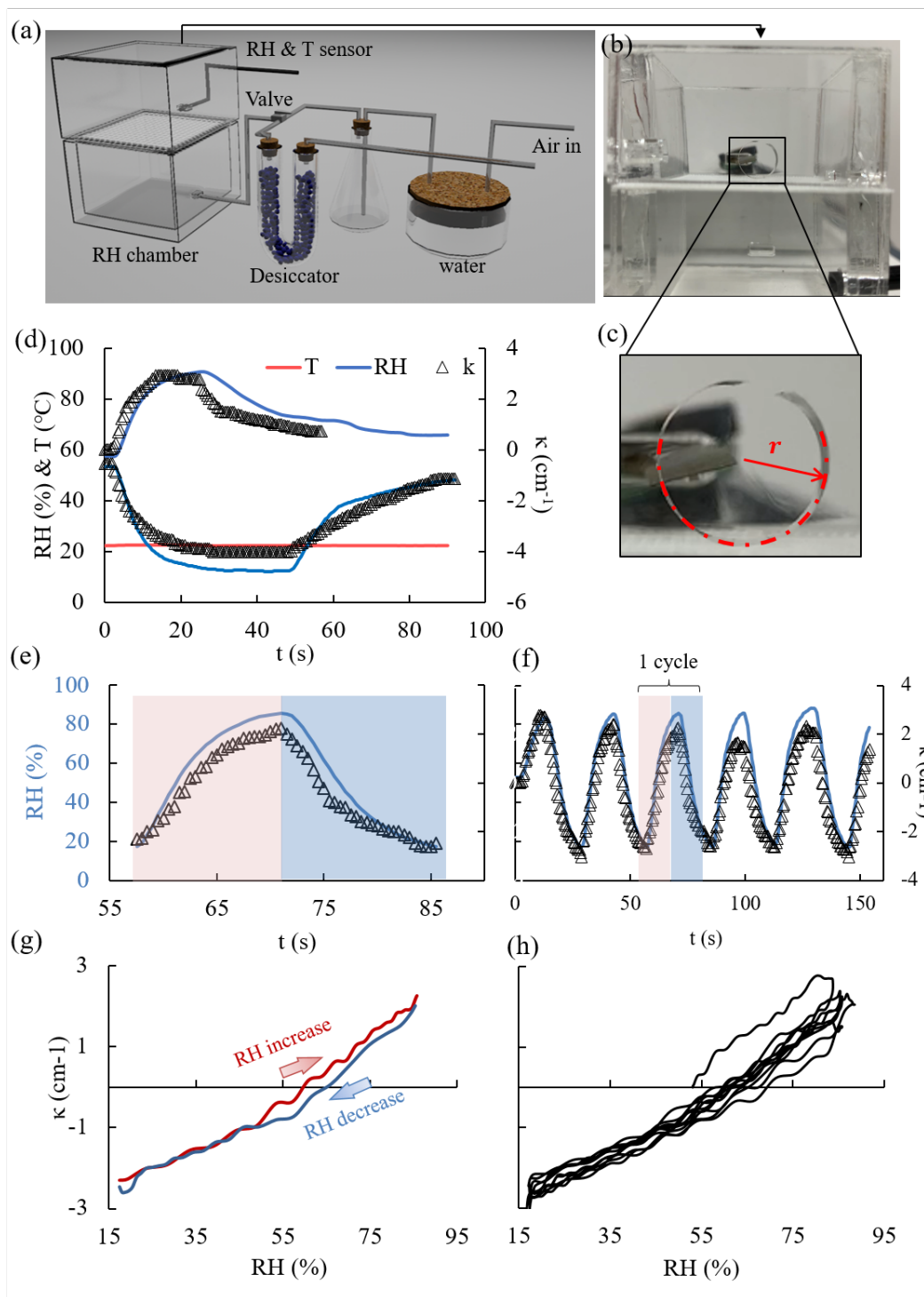


Figure 6-3. Actuation of the one-side coated cellophane in an RH-controlled chamber. (a) Schematic of the customized RH control unit. (b) A photograph of the chamber. (c) Curvature measurement of a bent film. (d) Actuation results under maximum RH capacity of the chamber. (e) One actuation cycle from (f) cyclic actuation within the selected RH range. (g) One actuation cycle from (h) cyclic actuation plotted as a function of RH.

Self-walking Actuators

The published work on the moisture-driven self-walking actuators are primarily designed based on two working principles; (1) oscillatory bending motion with asymmetric frictional legs/substrate for directional motion under changing RH [18], [32], and (2) continuous rolling and flipping locomotion on a moist surface [23], [33]–[35]. Constructing self-walking actuators using the second mechanism is promising; first, there is no need for tedious RH tuning, and second, the rotation is much faster than bending and can be used to enhance locomotion speed.

Here we also observed the continuous bending and flipping motion of uncoated cellophane films on moist surfaces. The mechanism of such locomotion are described in other reports [33], [36] and is shown in **Figure 6-4a**. In brief, when a film is (1) placed on a surface with moisture gradient (e.g., water surface, palm of a hand, wet paper, etc.), (2) it bends upward due to the differential moisture absorption to a certain curvature that leads to instability and (3) the bent film rotates. At this point it can either (4) flip or (4') oscillate back depending on the angular momentum (L) of the bent film as the rolling begins. (4) If the bent film flips, (5) it then flattens, the flat film (6) quickly bends upward due to higher moisture at the bottom side and continues the aforementioned steps. However, such locomotion motion is arbitrary, without control of the flipping and flipping direction.

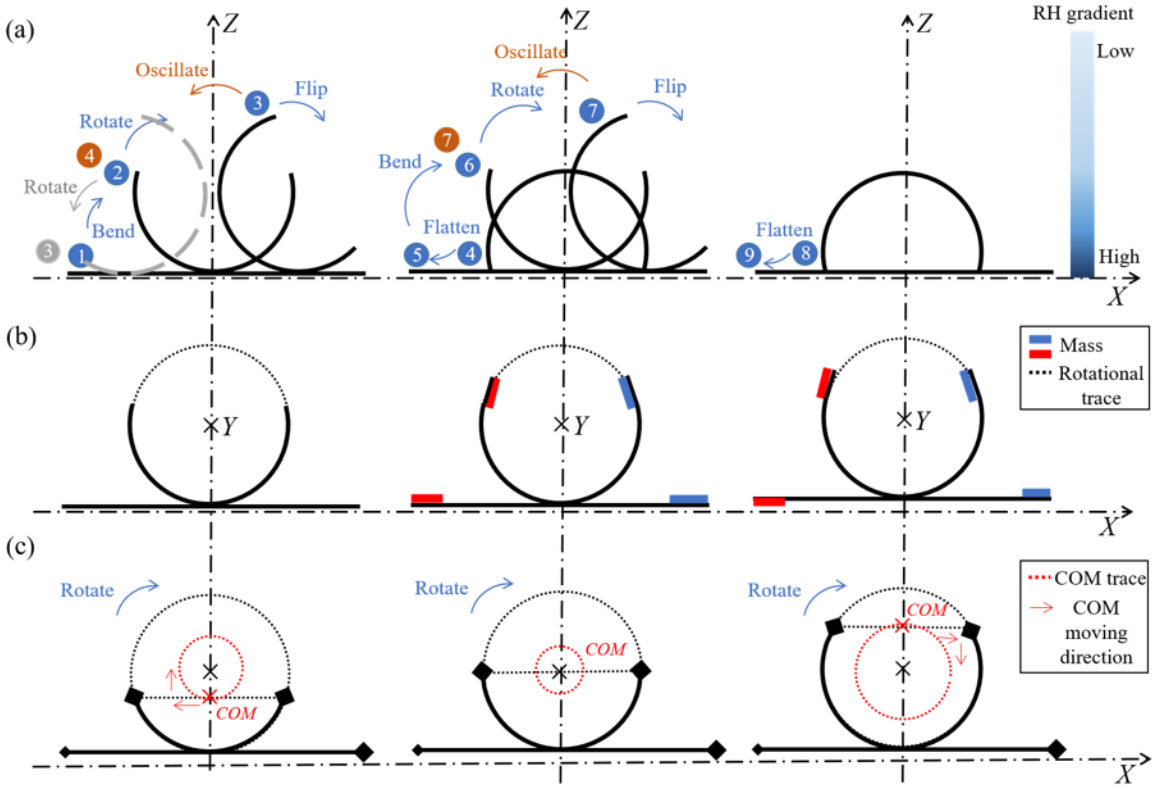


Figure 6-4. Schematic of self-walking actuator design. (a) Locomotion steps of pure cellophane on a moist surface. (b) Modifying locomotion by attaching masses. From left to right: pure cellophane, identical masses attached to top ends to decrease the chance of oscillation (symmetric), identical masses attached to top and bottom ends for directional locomotion (asymmetric). (c) Effect of bending angle on the chance of flipping of the symmetric sample. From left to right: $\theta < 180^\circ$, $\theta = 180^\circ$, $\theta > 180^\circ$.

Here we increased the flipping frequency and controlled the locomotion direction using a simple method of attaching appropriate weights at the two ends of the films, with the schematics shown in Figure 6-4b. Compared to the uncoated cellophane that tends to oscillate after bending to a certain curvature, that with weights added at two ends on the top of the film tends to flip due to the increased angular momentum (**Video S5**). The angular momentum can be written as,

$$L = I\omega = 2\omega m_{ms}r^2$$

where I is the moment of inertia, W_{ms} , L_{ms} , h_{ms} , ρ_{ms} are the width, length, thickness, and density of the mass, and ω is the rotational speed of the actuator. Assumptions are made

including the negligible weight of cellophane (1mg) compared to the attached masses ($m_{ms} = 10mg$), symmetric bending, uniform bending curvature, and constant radius of curvature (r) during rotating and flipping. The initial ω is hard to determine, since the rotation is triggered by any instability due to the air turbulence, surface roughness of the substrate, etc. Increasing the weight increases the L and thus facilitates the flipping motion, but too large weight can restrict the bending deformation and thus inhibit flipping. Therefore, we choose 10mg weight for the cellophane actuators.

The bending angle (θ) is another important factor for the flipping of the film. The schematics of symmetric actuators (masses attached on top of the film at two ends) with three bending angles ($\theta < 180^\circ$, $\theta = 180^\circ$, $\theta > 180^\circ$) are shown in Figure 6-4c. If we assume the energy conservation (energy conversion between potential energy and kinetic energy, and no energy dissipation) during the rolling of the actuators, the potential change due to the height change of the center of mass (COM) can be used to infer the chance of flipping of the bent film (Figure 6-4c). Specifically, when $\theta < 180^\circ$, the kinetic energy converts into potential energy due to the increase of the height of COM (Figure 6-4c, left), leading to a decrease of the rotational speed. When $\theta = 180^\circ$, the kinetic energy remains constant as the COM remains in the center of curvature (Figure 6-4c, middle), and thus the actuator rotates with a constant speed. When $\theta > 180^\circ$, the potential energy converts into kinetic energy due to the decreasing of the height of COM (Figure 6-4c, right), and therefore, the actuator rotates with an increasing speed. The experimental results of the effect of θ on the chance of flipping are shown in **Video S6-8**, where the θ is tuned simply by changing the length of the film. By increasing the length of the film from 10mm to 25mm, while keep the width constant at 10mm, the film bends with higher θ under the same actuation condition, and thus have higher chance of flipping.

To control the flipping direction, the weights are attached to the top of one end of the film and bottom of the other end (Figure 6-4b, right) to off-center the COM to one side of the Z-axis. In the schematic shown in the right of Figure 6-4b, the COM is shifted to the left side where the weight is further away from the rotating center. After flipping and bending, the COM is still on the left side. Therefore, it is expected to always rotate counterclockwise and move to the left (Figure 6-5a). To demonstrate this hypothesis, the uncoated cellophane film ($L=20\text{mm}$, $W=10\text{mm}$) was attached at the top and bottom of the two ends with two identical masses ($m_{ms}=10\text{mg}$) and then placed on a substrate on top of water bath (water $T=34\pm 0.5^\circ\text{C}$) (Figure 6-5b). As a result, the cellophane actuator bends and flips at a frequency of 7 rotation/min, flips to the expected direction with 78% confidence, with a minimum oscillation ratio of 7% (Figure 6-5c, **Video S9**). Ideally, the asymmetric cellophane actuator flips to the direction where the mass is away from the center and achieves directional motion, but there are still chances of opposite flipping direction. Possible issues can be: (1) instability due to air turbulence and surface roughness of the substrate, (2) minor human errors due to the hand-trimming and attaching of masses.

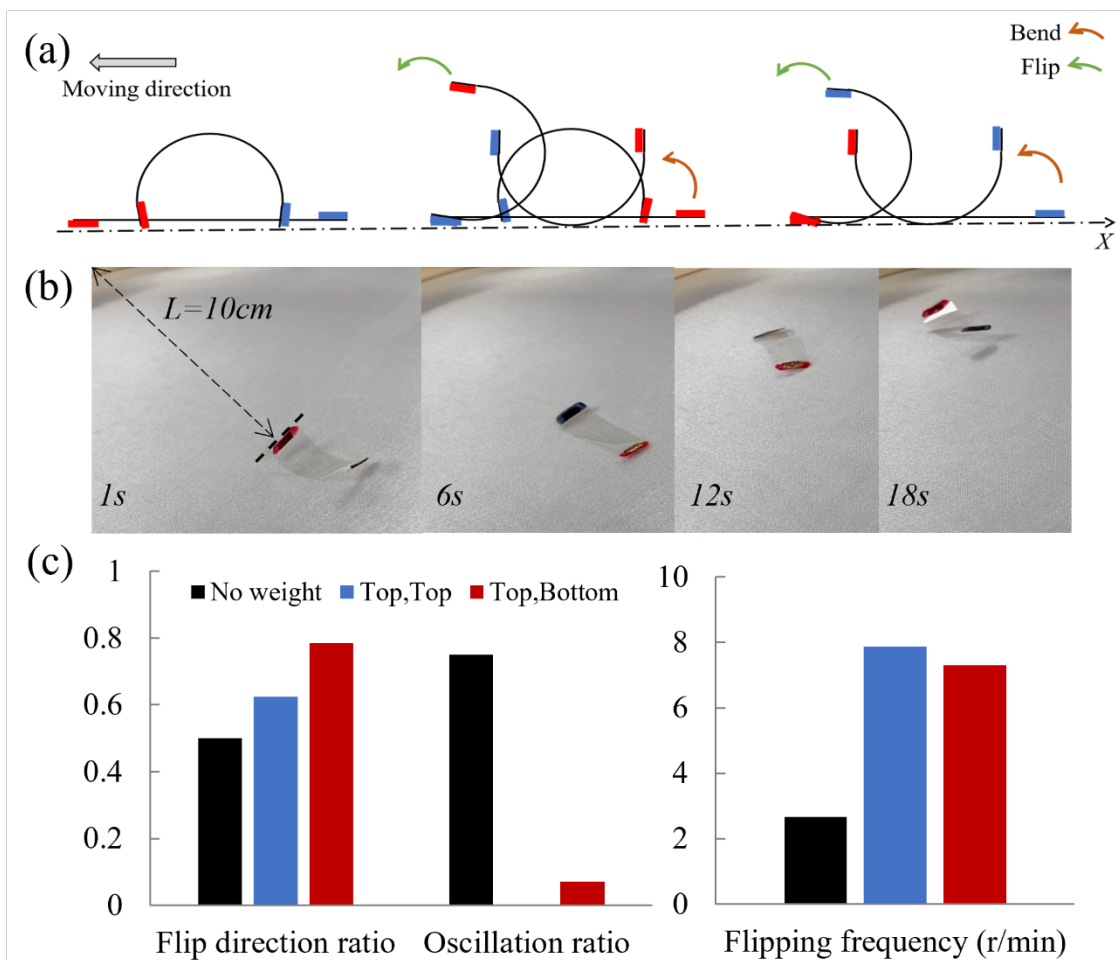


Figure 6-5. Directional self-walking actuators. (a) Schematic and (b) experimental photographs of the directional motion of asymmetric design. (c) Actuation results of the three self-walking designs.

Programmable actuators by heat laminating

The coated cellophane film was used to fabricate programmable actuators with different motions. As mentioned above, it bends instantaneously with a large bending curvature due to differential moisture absorption (or desorption) under RH change. The thin thermoplastic coating enhances the bending deformation and enables a convenient heat-sealing method for programmable actuator fabrication. Here we designed several structures to convert the bending

motion of the film into various motion types for potential applications in robotic locomotion and shape-changing textiles.

A rotational actuator is shown in **Figure 6-6b**, **Video S10**, fabricated by heat-laminating three coated cellophane strips (each trimmed at 45° to TD). As the strips deform into helical shapes under changing RH, they exert rotational forces to the laminate that lead to its rotational locomotion. Another designed actuator generates bidirectional bending with lifting motion (Figure 6-6c, **Video S11**). In particular, two cellophane strips were trimmed along TD and then cross-laminated with the coating side facing each other. Changing the RH results in the strips' bending in opposite directions, leading to the lifting motion of the actuator at both increasing and decreasing RH. Another design utilized the bidirectional bending of the coated cellophane to generate snake-like motion by alternatively laminating cellophane strips in a linear manner (Figure 6-6d). The adjacent strips bend in opposite directions as RH changes, leading to an overall wavy deformation. Cycling the RH between low and high levels leads to repetitive bending directions change of the individual strips (Figure 6-6d, **Video S12**).

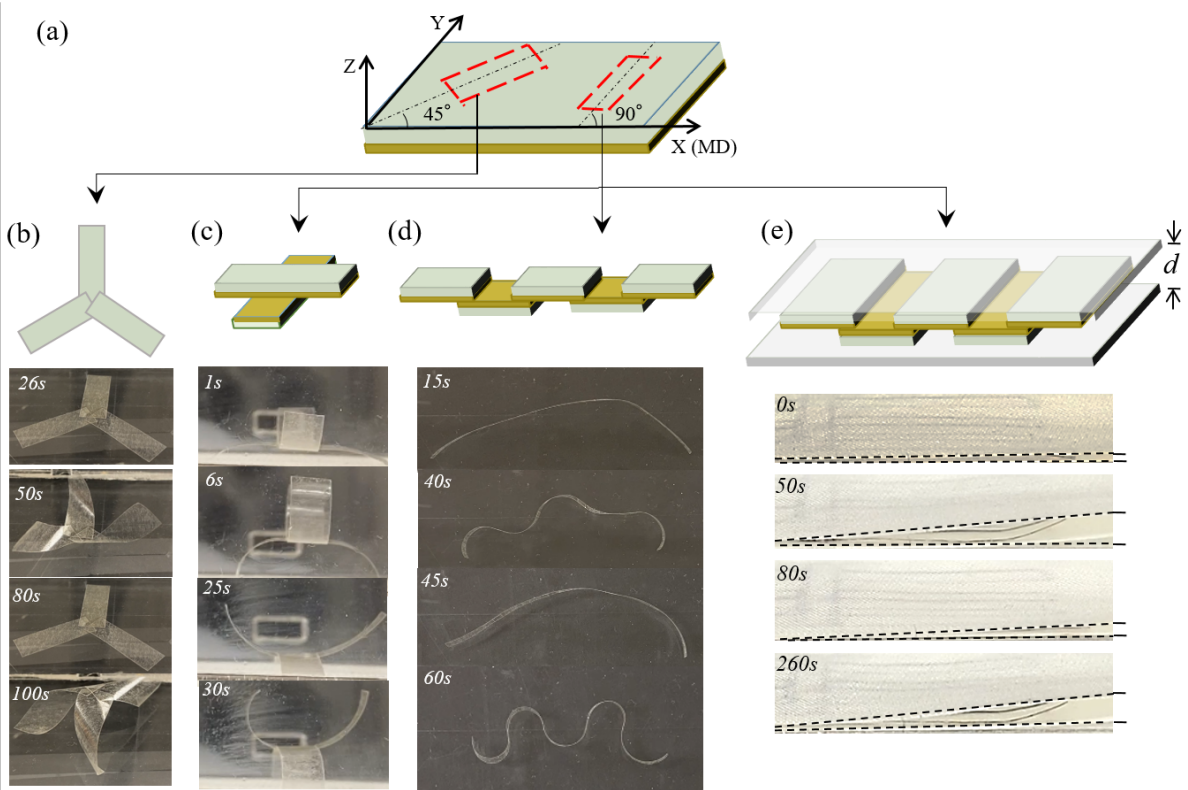


Figure 6-6. Design and actuation of programmable actuators. (a) Strip trimming angles. (b) The rotational actuator. (c) The lifting actuator. (d) The snake-like actuator. (e) The thickness-changing fabric.

The transformation between flat to wavy shapes of the laminated cellophane was further utilized to induce the thickness change of a fabric. As shown in Figure 6-6e, several laminated actuators with wavy motions were sandwiched in a two-layer fabric that were sewed together along three boundaries. The length of the laminated actuators was similar to the fabric length for overall thickness change, and the width was kept low (5mm) to allow efficient moisture diffusion in the fabric. As a result, the bending of the cellophane increases the distance of the two layers of the fabric (Figure 6-6e). However, due to the small bending force, the thickness change of the fabric is almost negligible.

4. Conclusion

Low-cost and commercially available cellophane films were studied for hygroscopic bending motion and demonstrated the potential use as self-walking and motion-programmable actuators. The large and anisotropic swelling behavior, as well as the decent moisture absorption and desorption speed, makes it a good candidate as hygroscopic bending actuators. Remarkably, the pure cellophane can move continuously on a moist substrate, converting the chemical potential (moisture gradient) into the mechanical energy that powers its motion. We enhanced such self-walking motion by increasing angular momentum for flipping and shifting the center of mass for directional locomotion. Moreover, the one side-coated cellophane films were studied and showed larger bending curvature than the uncoated ones due to the differential swelling of the two layers. The coating promotes the bending motion and also enable the heat-laminating ability, which was used as a convenient method to build different actuator structures for diversified motions. We demonstrated several motion-programmable actuators through structural design, including the rotational, lifting, and snake-like actuators and thickness-changing fabric.

References

- [1] S. Armon, E. Efrati, R. Kupferman, and E. Sharon, “Geometry and Mechanics in the Opening of Chiral Seed Pods,” *Science*, vol. 333, no. 6050, pp. 1726–1730, Sep. 2011, doi: 10.1126/science.1203874.
- [2] C. Dawson, J. F. V. Vincent, and A.-M. Rocca, “How pine cones open,” *Nature*, vol. 390, no. 6661, p. 668, Dec. 1997, doi: 10.1038/37745.
- [3] R. Elbaum, L. Zaltzman, I. Burgert, and P. Fratzl, “The Role of Wheat Awns in the Seed Dispersal Unit,” *Science*, vol. 316, no. 5826, pp. 884–886, May 2007, doi: 10.1126/science.1140097.
- [4] K. Oliver, A. Seddon, and R. S. Trask, “Morphing in nature and beyond: a review of natural and synthetic shape-changing materials and mechanisms,” *J. Mater. Sci.*, vol. 51, no. 24, pp. 10663–10689, Dec. 2016, doi: 10.1007/s10853-016-0295-8.
- [5] J. Yin, R. Hinchet, H. Shea, and C. Majidi, “Wearable Soft Technologies for Haptic Sensing and Feedback,” *Adv. Funct. Mater.*, vol. n/a, no. n/a, p. 2007428, doi: <https://doi.org/10.1002/adfm.202007428>.
- [6] W. Wang *et al.*, “Harnessing the hygroscopic and biofluorescent behaviors of genetically tractable microbial cells to design biohybrid wearables,” *Sci. Adv.*, vol. 3, no. 5, p. e1601984, May 2017, doi: 10.1126/sciadv.1601984.
- [7] H. Shao, S. Wei, X. Jiang, D. P. Holmes, and T. K. Ghosh, “Bioinspired Electrically Activated Soft Bistable Actuators,” *Adv. Funct. Mater.*, vol. 28, no. 35, p. 1802999, Aug. 2018, doi: 10.1002/adfm.201802999.
- [8] K. Kumar *et al.*, “A chaotic self-oscillating sunlight-driven polymer actuator,” *Nat. Commun.*, vol. 7, p. 11975, Jul. 2016, doi: 10.1038/ncomms11975.
- [9] S. M. Mirvakili and I. W. Hunter, “Multidirectional Artificial Muscles from Nylon,” *Adv. Mater.*, vol. 29, no. 4, p. 1604734, 2017, doi: 10.1002/adma.201604734.
- [10] D. Liu *et al.*, “Spider dragline silk as torsional actuator driven by humidity,” *Sci. Adv.*, vol. 5, no. 3, p. eaau9183, Mar. 2019, doi: 10.1126/sciadv.aau9183.
- [11] A. E. Aliev *et al.*, “Giant-Stroke, Superelastic Carbon Nanotube Aerogel Muscles,” *Science*, vol. 323, no. 5921, pp. 1575–1578, Mar. 2009, doi: 10.1126/science.1168312.
- [12] R. Shankar, T. K. Ghosh, and R. J. Spontak, “Electroactive Nanostructured Polymers as Tunable Actuators,” *Adv. Mater.*, vol. 19, no. 17, pp. 2218–2223, Sep. 2007, doi: 10.1002/adma.200602644.
- [13] C. S. Haines *et al.*, “Artificial Muscles from Fishing Line and Sewing Thread,” *Science*, vol. 343, no. 6173, pp. 868–872, Feb. 2014, doi: 10.1126/science.1246906.
- [14] M. D. Lima *et al.*, “Electrically, Chemically, and Photonically Powered Torsional and Tensile Actuation of Hybrid Carbon Nanotube Yarn Muscles,” *Science*, vol. 338, no. 6109, pp. 928–932, Nov. 2012, doi: 10.1126/science.1226762.
- [15] Y. Dong *et al.*, “Multi-stimuli-responsive programmable biomimetic actuator,” *Nat. Commun.*, vol. 10, no. 1, Art. no. 1, Sep. 2019, doi: 10.1038/s41467-019-12044-5.
- [16] H. Arazoe *et al.*, “An autonomous actuator driven by fluctuations in ambient humidity,” *Nat. Mater.*, vol. 15, no. 10, Art. no. 10, Oct. 2016, doi: 10.1038/nmat4693.
- [17] A. L. Duigou, G. Chabaud, F. Scarpa, and M. Castro, “Bioinspired Electro-Thermo-Hygro Reversible Shape-Changing Materials by 4D Printing,” *Adv. Funct. Mater.*, vol. 29, no. 40, p. 1903280, 2019, doi: 10.1002/adfm.201903280.
- [18] B. Shin *et al.*, “Hygrobot: A self-locomotive ratcheted actuator powered by environmental humidity,” *Sci. Robot.*, vol. 3, no. 14, p. eaar2629, Jan. 2018, doi: 10.1126/scirobotics.aar2629.

- [19] Q. Zhao *et al.*, “An instant multi-responsive porous polymer actuator driven by solvent molecule sorption,” *Nat. Commun.*, vol. 5, p. 4293, Jul. 2014, doi: 10.1038/ncomms5293.
- [20] J. F. Fuzek, “Absorption and desorption of water by some common fibers,” *Ind. Eng. Chem. Prod. Res. Dev.*, vol. 24, no. 1, pp. 140–144, Mar. 1985, doi: 10.1021/i300017a026.
- [21] S. Shrestha, J. A. Diaz, S. Ghanbari, and J. P. Youngblood, “Hygroscopic Swelling Determination of Cellulose Nanocrystal (CNC) Films by Polarized Light Microscopy Digital Image Correlation,” *Biomacromolecules*, vol. 18, no. 5, pp. 1482–1490, May 2017, doi: 10.1021/acs.biomac.7b00026.
- [22] J. Mu *et al.*, “Molecular-channel driven actuator with considerations for multiple configurations and color switching,” *Nat. Commun.*, vol. 9, no. 1, p. 590, Feb. 2018, doi: 10.1038/s41467-018-03032-2.
- [23] L. Zhang, H. Liang, J. Jacob, and P. Naumov, “Photogated humidity-driven motility,” *Nat. Commun.*, vol. 6, no. 1, Art. no. 1, Jun. 2015, doi: 10.1038/ncomms8429.
- [24] M. Wang, X. Tian, R. H. A. Ras, and O. Ikkala, “Sensitive Humidity-Driven Reversible and Bidirectional Bending of Nanocellulose Thin Films as Bio-Inspired Actuation,” *Adv. Mater. Interfaces*, vol. 2, no. 7, p. 1500080, May 2015, doi: 10.1002/admi.201500080.
- [25] M. Ma, L. Guo, D. G. Anderson, and R. Langer, “Bio-Inspired Polymer Composite Actuator and Generator Driven by Water Gradients,” *Science*, vol. 339, no. 6116, pp. 186–189, Jan. 2013, doi: 10.1126/science.1230262.
- [26] A. J. Stamm, “Diffusion of Water into Uncoated Cellophane. I. From Rates of Water Vapor Adsorption, and Liquid Water Absorption,” *J. Phys. Chem.*, vol. 60, no. 1, pp. 76–82, Jan. 1956, doi: 10.1021/j150535a019.
- [27] G. C. Inskeep, “Cellophane,” *Ind. Eng. Chem.*, p. 14.
- [28] H. Okuzaki, T. Kuwabara, K. Funasaka, and T. Saido, “Humidity-Sensitive Polypyrrole Films for Electro-Active Polymer Actuators,” *Adv. Funct. Mater.*, vol. 23, no. 36, pp. 4400–4407, 2013, doi: 10.1002/adfm.201203883.
- [29] A. Sydney Gladman, E. A. Matsumoto, R. G. Nuzzo, L. Mahadevan, and J. A. Lewis, “Biomimetic 4D printing,” *Nat. Mater.*, vol. 15, no. 4, pp. 413–418, Apr. 2016, doi: 10.1038/nmat4544.
- [30] L. T. de Haan, J. M. N. Verjans, D. J. Broer, C. W. M. Bastiaansen, and A. P. H. J. Schenning, “Humidity-Responsive Liquid Crystalline Polymer Actuators with an Asymmetry in the Molecular Trigger That Bend, Fold, and Curl,” *J. Am. Chem. Soc.*, vol. 136, no. 30, pp. 10585–10588, Jul. 2014, doi: 10.1021/ja505475x.
- [31] Zhou, K. Tashiro, T. Hongo, H. Shirataki, C. Yamane, and T. Ii, “Influence of Water on Structure and Mechanical Properties of Regenerated Cellulose Studied by an Organized Combination of Infrared Spectra, X-ray Diffraction, and Dynamic Viscoelastic Data Measured as Functions of Temperature and Humidity,” *Macromolecules*, vol. 34, no. 5, pp. 1274–1280, Feb. 2001, doi: 10.1021/ma001507x.
- [32] C. Lv *et al.*, “Sensitively Humidity-Driven Actuator Based on Photopolymerizable PEG-DA Films,” *Adv. Mater. Interfaces*, vol. 4, no. 9, p. 1601002, 2017, doi: <https://doi.org/10.1002/admi.201601002>.
- [33] T. Yang *et al.*, “Tough biomimetic films for harnessing natural evaporation for various self-powered devices,” *J. Mater. Chem. A*, vol. 8, no. 37, pp. 19269–19277, Sep. 2020, doi: 10.1039/D0TA04221H.
- [34] J. Mu, C. Hou, B. Zhu, H. Wang, Y. Li, and Q. Zhang, “A multi-responsive water-driven actuator with instant and powerful performance for versatile applications,” *Sci. Rep.*, vol. 5, no. 1, Art. no. 1, Mar. 2015, doi: 10.1038/srep09503.

- [35] Z. Zhao *et al.*, “Actuation and locomotion driven by moisture in paper made with natural pollen,” *Proc. Natl. Acad. Sci.*, vol. 117, no. 16, pp. 8711–8718, Apr. 2020, doi: 10.1073/pnas.1922560117.
- [36] F. Gao, N. Zhang, X. Fang, and M. Ma, “Magnetically directed soft actuators driven by moisture,” *J. Mater. Chem. C*, vol. 5, no. 17, pp. 4129–4133, May 2017, doi: 10.1039/C7TC01062A.

Chapter 7 Multi-Stimuli-Driven Viscose Rayon TCPAs

Abstract

Twisted and coiled structures have transformed the conventionally passive textile fibers and yarns into soft actuators that can be potentially used for soft robotics and smart textiles. For wearable applications, moisture is an abundant source of stimuli for soft actuators in the near-body environment but is limited by the slow response speed and lack of active control. Here we demonstrate rapid and multi-stimuli-activation of highly twisted and coiled polymer actuators (TCPAs) fabricated from a conventional textile material – viscose rayon. After inserting a high level of twist, the large and rapid radial expansion of viscose rayon fiber upon exposure to moisture is converted to torsional (maximum stroke of 288 degree/cm and speed of 60 rad/s) and linear motions (maximum strain of 12% and blocking force of 4.2mN/fiber). We designed hierarchical twisted structures of TCPAs and investigated the effect of key structural parameters on the actuation performance. Self-plyed yarns formed by a number of twisted single fibers generate optimal torsional performance, while the self-coiled yarns fabricated by overtwisting a minimal number of fibers produce highest linear performance. We also report accelerated desorption of moisture through resistive heating by plying conductive CNT yarns with the highly twisted viscose rayon for active, reversible, and fast torsional actuation of rayon TCPAs.

7.1 Introduction

Twisted yarns, in singles and plies, are used in everyday and specialty textiles ranging from apparels to fishing nets and parachutes. These textiles may serve as passive covers (apparel) or perform one or more specific functions (parachute). The recent discovery of the actuation behavior of highly twisted and coiled polymer actuators (TCPAs) and developments since then have been opened up new avenues to incorporate smart and responsive behavior in these textile products. These TCPAs are capable of producing mechanical motion upon exposure

to moisture and other stimuli and have been explored as powerful yet simple soft actuators [1], [2] with potential applications in robotics [3], [4] and smart textiles [1], [5]. The compact and easily processable TCPAs are capable of producing large deformation and force and can be assembled into textiles. After Foroughi et al [2] reported the first highly twisted fiber-based torsional actuator with carbon nanotube (CNT) and demonstrated its large torsional stroke ($250^\circ/\text{mm}$) at fast speed (590rpm), there have been intensive investigations on TCPAs in terms of material and structure development [6], actuation control and optimization [7], modeling [8], and assembly for potential applications [4]. Powered by electrical potential, current, heat, solvent, vapor, and more, a variety of fiber forming materials including metallic fibers [9], carbon-based fibers [2], [10], synthetic fibers [11] and natural fibers [5] have been investigated. Stimuli-induced radial expansion of constituting fibers or yarns and their highly twisted and coiled structure are recognized as the origins of their outstanding actuation performance [1]. Most reported works on TCPAs are focused on the monofilament yarn [11], while a few reported core-sheath yarn [6], staple yarn [12], and multifilament yarn [13]. Additionally, while most of the reported research focus on influence of material behavior on TCPA performance, structural aspects of the TCPAs have not received deserved attention.

Soft actuators that are responsive to vapor or solvent through absorption and desorption, are designed to have slender structures for larger surface area and fast transportation. Fibers and yarns (fiber assembly) are ideal structures from this perspective. Spider silk [14] and collagen fibers [15] have shown interesting deformation performance under moisture or solvent. TCPAs provides an opportunity for more fibers with otherwise overlooked sorptive response, such as worm silk [5], cellulose fibers [16], alginate fibers [17], and chitosan fibers [18] to use for actuators.

Here, we investigate the actuation performance of hierarchically structured TCPAs made from commercially available viscose rayon fibers. Viscose rayon is a regenerated cellulosic fiber with large radial swelling and relatively fast swelling rate [19], [20]. The fibers were twisted, plied, and coiled into yarn structures to produce torsional and linear actuation under moisture (vapor and liquid) application. The effect of fiber and yarn structure on the actuation performance was studied. Key structural parameters, including the fiber diameter, number of fibers in the twisted yarn, and twist density in the single and plied yarns were investigated. Moreover, active moisture desorption was investigated by incorporating resistive heating elements in the TCPA by plying the twisted viscose rayon with carbon nanotube (CNT) yarns.

7.2 Results and discussion

7.2.1 Fiber properties

The viscose rayon fibers used in this research (Century Rayon, India) are continuous filaments with typical irregular cross-sectional shapes (**Figure 7-1c**). Due to the non-circular shape, representative fiber diameter (d_f) is calculated from the linear density of the fiber (given by the manufacturer) and mass density ($1.5\text{g}/\text{cm}^3$, from the published literature [21]). The calculated fiber diameters of different fiber samples range from 14 to $30.7\mu\text{m}$, similar to that measured under the microscope (Figure S7- 1a, b).

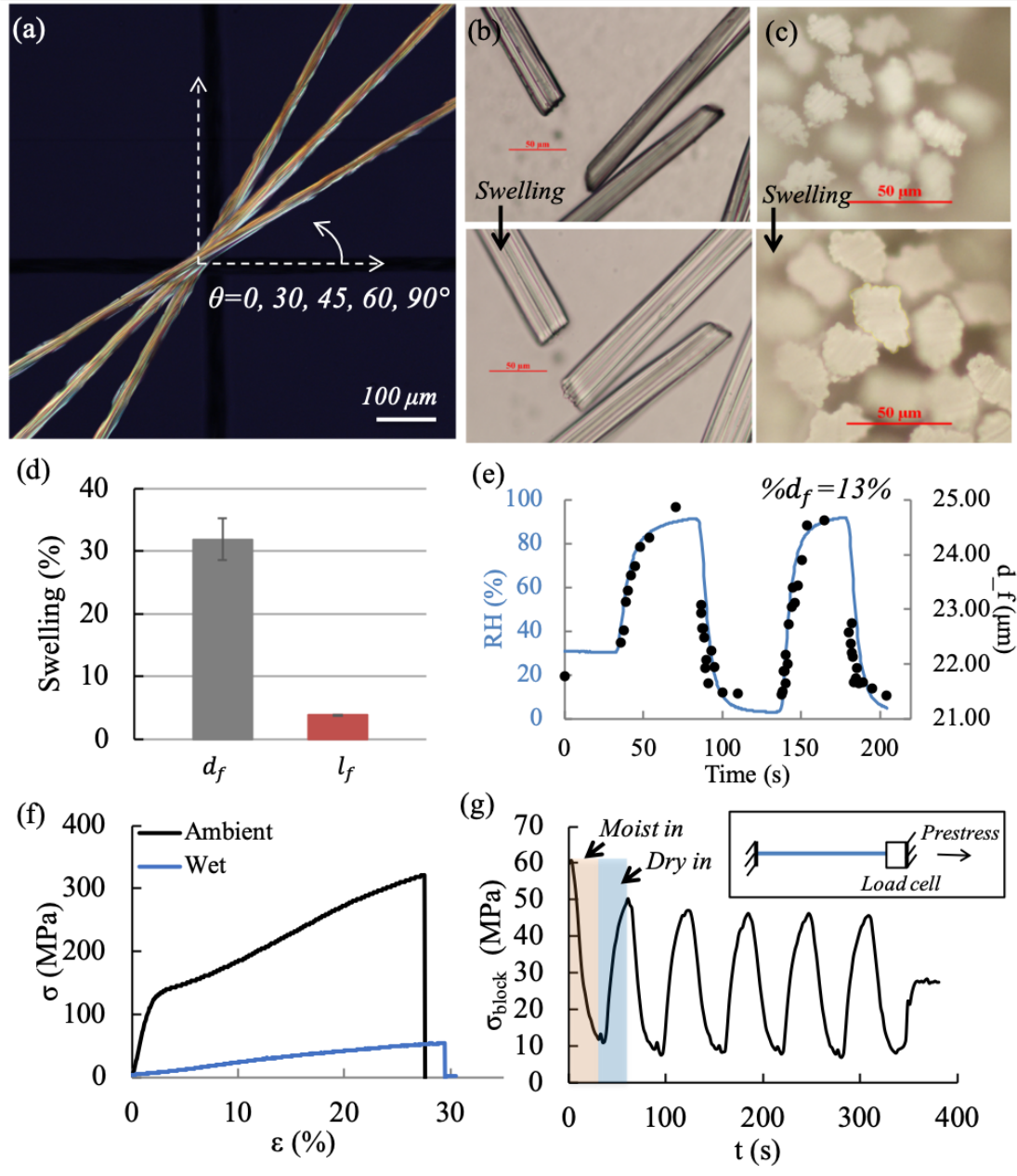


Figure 7-1. Fiber properties. (a) Anisotropy of the fiber under polarized light microscope. (b, c) Water-induced radial expansion of the fiber at the cross-sectional and projected length view under the microscope. (d) Anisotropic swelling of diameter and length of the fiber under water exposure. (e) Moisture-induced fiber diameter change. (f) Tensile property of the fiber under ambient and wet conditions. (g) Reversible stress relief of the prestressed fiber under cyclic moisture change.

Viscose rayon fibers are anisotropic due to the preferential molecular alignment along fiber direction during fiber manufacturing process. The anisotropy is common in textile fibers

and can be visualized under polarized light microscope. When the fibers are oriented neither parallel nor perpendicular to the polarizer, they can be illuminated (Figure 7-1a).

The anisotropy of the viscose rayon fiber leads to differential swelling when exposed to water or moisture. The increase in its diameter (diameter strain of 34%) is much more significant than the increase in length (length strain of 4%) when in contact with water droplets (Figure 7-1d). Both dimensions recovered as the water evaporated from the sample. When exposed to a cyclic RH change between 10% and 90% (around 80 seconds/cycle), a reversible diameter strain of 13% is produced (Figure 7-1e) with a minimal change in length of 1%. The curves of d_f and RH change nearly overlap, indicating the high sensitivity and fast moisture response of the viscose rayon fibers. Such significant and preferential radial expansion, high moisture sensitivity, and fast response speed make the viscose rayon a promising material for moisture-driven TCPA.

The mechanical behavior of fiber materials for use in TCPA fabrication is very important. Accordingly, the viscose rayon fiber (of 21.7 μm diameter) was evaluated for its tensile properties in ambient and wet conditions, see Figure 7-1f. The fiber is mechanically strong and extensible in ambient conditions, with Young's modulus of 7GPa, breaking strength of 300MPa, and breaking strain of 25% to 30%. The wet fiber is much weaker, with Young's modulus of 0.17GPa, breaking strength of 54MPa, and a slightly higher breaking strain (30% to 40%). The significant softening effect of viscose rayon in water is due to the breakage of cross-links (hydrogen-bonds between cellulose molecules) in the amorphous regions [22].

Interestingly, such water-absorption-induced softening effect can relax the prestress in the fiber, which is restored upon subsequent water desorption. The phenomenon can be illustrated by the variation of stress during the absorption and desorption cycles of a prestressed, two end-tethered viscose rayon fiber as shown in Figure 7-1g. In this instance, the relative

humidity was cycled between 5 to 85%, resulting in a reversible and consistent blocking stress of around 40MPa after initial two cycles.

7.2.2 TCPA properties

The viscose rayon fibers are twisted into hierarchical TCPA structures (see Methods cf. section 7.6.1.2), shown in Figure 7-2. In brief, the fibers are straightened with a small tensile load attached at one end while twists are inserted from the other end with a hand twister. Twisted yarns are plied or coiled to form higher level yarns. Fibers are wet with water during fabrication process to apply larger number of twist (**Figure 7-3a**).

The 1st-level structure is the precursor fiber (Figure 7-2b, c), characterized by its diameter (d_f) and length (l_f). The 2nd-level structures, dubbed as HT (Figure 7-2d), are obtained by inserting a high level of twist into the fiber(s). Another type of 2nd-level structures, named HTCo (Figure 7-2e), is fabricated by overtwisting the HTn to form uniform coils. The 3rd-level structures are plied yarns, fabricated by self-plying or manual-plying a number of twisted yarns, named as HTsPly and HTmPly, respectively (Figure 7-2f, g). The 4th-level structures are cable yarns obtained by plying the plied yarns (Figure 7-2h).

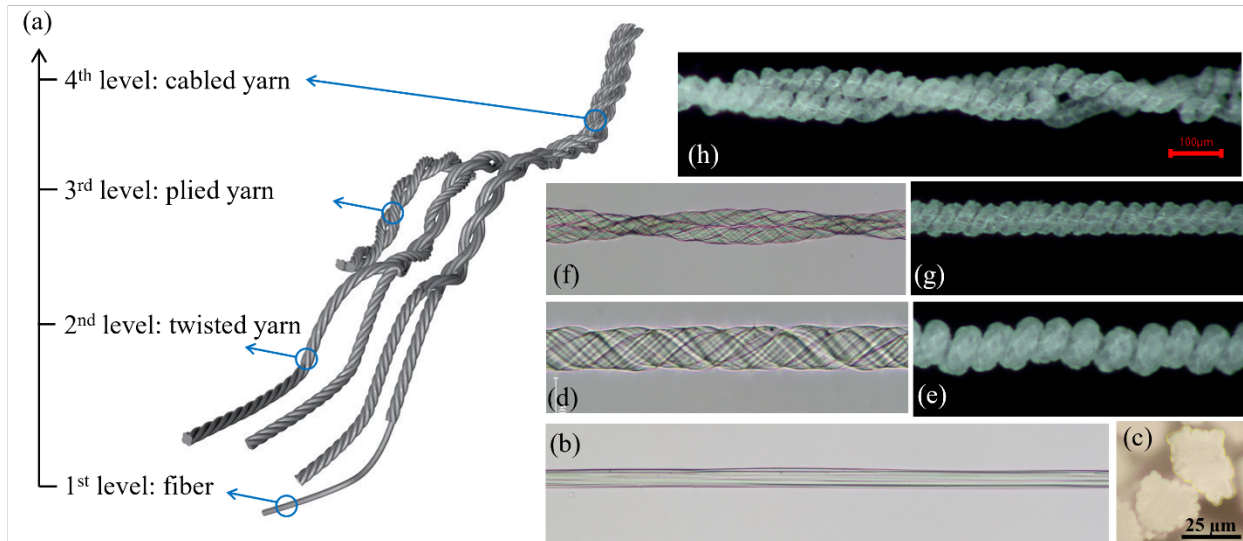


Figure 7-2. Hierarchical structures of the TCPAs. (a) Schematic of a hierarchical yarn structures constructed from a fiber. Microscope images of (b) a precursor viscose rayon fiber, and (c) its cross-sectional shape, (d) highly twisted monofilament yarn, (e) self-plied yarn, (f) self-plied yarn, (g) manually-plied yarn, (h) cabled yarn (twisting a number of plied yarns).

For a twisted yarn, the twisting conditions and fiber geometries are critical to the maximum twist density (T_t) which in turn affects the actuation performance. With an increase of applied tensile stress (3 to 20MPa), the maximum T_t of a single fiber twisted in water increases from 90 to 140 turn/cm, which is higher than twisted in air (**Figure 7-3a**). In addition, water effectively stabilizes the twisted shape of the fibers, resulting in a free-standing, highly twisted yarn, while that twisted in air rapidly untwists when released from constraints. Thus an appropriate level of tensile stress of 6MPa is used to insert twist into wet fibers to form free-standing, highly twisted yarn. Moreover, larger fiber diameter and higher number of fibers in the yarn decreases the maximum T_t . While the maximum T_t decreases with larger fiber diameter, the helical angles (α_t) of the monofilament yarns of different diameter at their maximum twist remain relatively constant (from 30° to 35°). Theoretical α_t derived from the single helix model matches well with the experiment, while there is an increasing deviation at both low and high twist (Figure S7- 7c). In terms of mechanical properties, higher twist density lowers the overall

mechanical properties of the yarn (Figure S7- 7d). In particular, the Young's modulus of the HT yarn decreases from 8 to 4GPa with an increase of T_t from 0 to 100 turn/cm (Figure 7-3b)

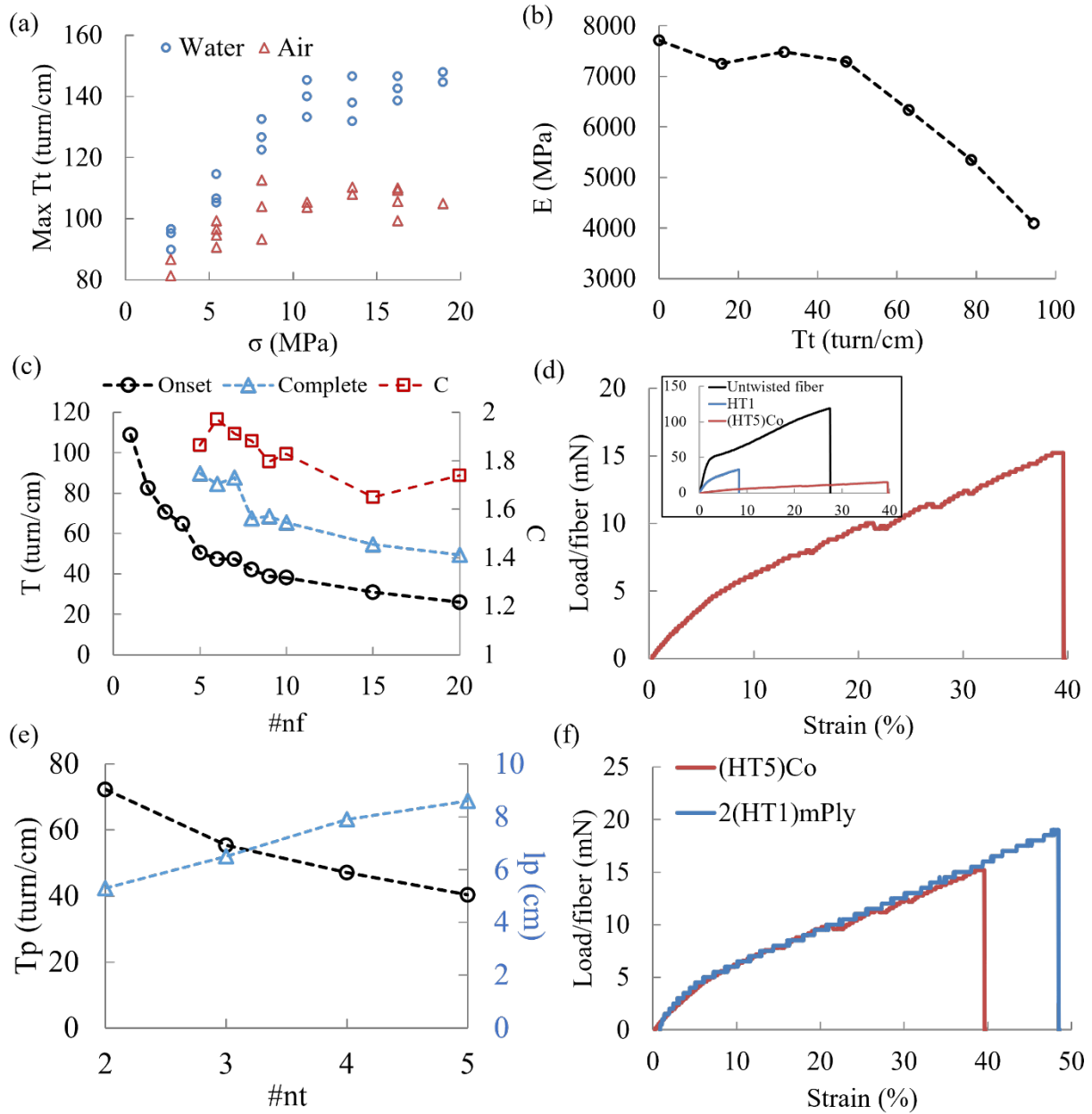


Figure 7-3. Fabrication and properties of TCPAs. (a) Maximum twist density of HT1 inserted in air and water, as a function of applied tensile stress. (b) Young's modulus of HT1 varying twist density (turns/cm). (c) Twist density (onset and complete of self-coiling) and spring index of $(HTn)Co$ as a function of $\#n_f$. (d) Tensile property of the $(HT5)Co$. The inset is a comparison of tensile property of the precursor fiber, HT1, and $(HT5)Co$. (e) Ply density and length of the n (HT1)mPly as a function of $\#n_t$. (f) A comparison of the tensile property of the self-coiled yarn and the manually plied yarn.

By overtwisting the HT yarn beyond the critical level, coils start to develop [1]. Empirically, when the number of fibers ($\#n_f$) is less than 5, overtwisting causes the yarn breakage or snarl at a range of tensile stress, but when $\#n_f \geq 5$, overtwist leads to continuous self-coiling. The self-coiled yarn is fabricated by overtwisting the HT yarn in water at an appropriate tensile stress (Figure S7- 7h). The critical T_t (onset of self-coiling), total T_t (fully coiled), and spring index (C , ratio of the diameters of the coil and the twisted yarn) as a function of number of fibers ($\#n_f$) are shown in Figure 7-3c. Generally, as the $\#n_f$ increases, the twist density at onset and the complete of coiling decrease. The spring index of the HTCo is in the range of 1.6 to 2, varying slightly with the change of $\#n_f$. The coiled yarns have low modulus and strength but high strain due to the spring-like structure. In particular, HTCo (fabricated by overtwisting five fibers) has the breaking strength of 15mN/fiber and breaking strain of 40%, that differ significantly to the precursor fiber and the highly twisted yarn (Figure 7-3d).

The 3rd-level structure are plied yarns, including the HTsPly and HTmPly. The primary advantages of the HTsPlys are their shape stability and reversible torsional actuation as a result of its torque-balanced structure. HTsPly with different number of fibers ($\#n_f$) and different number of twisted single yarns ($\#n_t$) are shown in Figure S7- 7e, f. HTmPly are initially intended to hold the maximum level of twist in the structure, as more twists are inserted into a bundle of twisted yarns. As the number of single yarn ($\#n_t$) increases, the maximum ply density (T_p) decreases, accompanied with a significant length contraction (Figure 7-3e). Interestingly, the structural and mechanical properties of HTmPly are similar to the HTCo, see Figure S7-8g, h and Figure 7-3f.

7.2.3 Torsional actuation of HT

The torsional actuation performance of the highly twisted monofilament yarn under a repetitive RH change between 10 and 85% is shown in Figure 7-4. As RH increases, the yarn untwists rapidly with the number of rotations (ΔN) of around 100 turns (1/15 of the applied twist in the yarn) and a maximum rotational speed (ω) of 27 radians/s (or 286 rpm) in the first actuation cycle. As RH decreases, the yarn retwists with a higher maximum rotational speed of 37 radians/s (Figure 7-4c). In the cyclic actuation, only a fraction of the untwisting rotation is recovered in each cycle of retwisting, leading to a continuous reduction in yarn twist (Figure 7-4c, d). With the gradual decrease of yarn twist in the cyclic actuation, the extent of untwisting decreased from 100 to 70 turns in 6 cycles before being stable, while the extent of retwisting remained almost constant at 65 turns (Figure 7-4b)

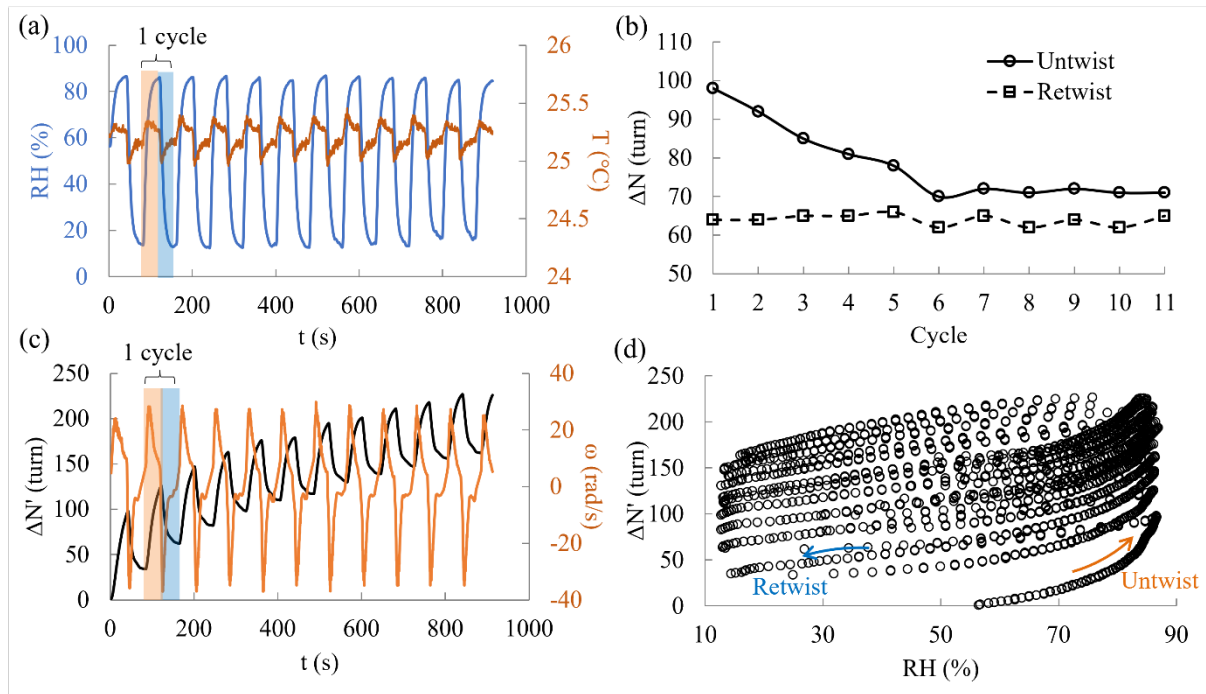


Figure 7-4. Torsional actuation of HT. (a) Cyclic change of RH (with minor variation of temperature, T) in the chamber for actuation. (b) Number of rotation ($\Delta N'$, reset) during untwisting and retwisting in each cycle. (c) Number of rotation ($\Delta N'$, accumulated) and rotational speed (ω) as a function of time. (d) $\Delta N'$ as a function of RH showing the actuation

hysteresis and gradual untwist. The parameters of HT in this experiment is: $d_f = 21.7\mu\text{m}$, $T_t = 100\text{turn/cm}$, $\#n_f = 1$, $l_t = 10\text{cm}$.

Assuming negligible change of lengths of fibers (l_f) and twisted yarns (l_t) during actuation [23], the theoretical number of rotations can be calculated by,

$$\Delta N = n_{t,0} \left(\frac{d_{t,0}}{d_{t,1}} - 1 \right) = l_f T_t \frac{l_t}{l'_t} \left(\frac{d_{t,0}}{d_{t,1}} - 1 \right) \quad \text{Eq. 27}$$

where $d_{t,0}$ and $d_{t,1}$ represent the diameters of the highly twisted yarns at ambient and swelled state, $n_{t,0}$ is the number of inserted twists in the yarn ($n_{t,0} = T_t l_f \frac{l_t}{l'_t}$), l'_t and l_t are the length of the twisted yarn after twist insertion and length of the yarn for actuation, respectively. In this example, $l_f = 15\text{cm}$, $l_t = 11\text{cm}$, $l'_t = 13\text{cm}$. This equation suggests that the torsional stroke is dependent on the inserted twist density and the radial expansion of the twisted yarn. Here we further approximate the radial expansion of the twisted yarn as a function of that of the precursor fiber using the trigonometric relation,

$$\frac{d_{t,0}}{d_{t,1}} = \frac{d_{f,0}}{d_{f,1}} \cos \alpha_{t,0} \quad \text{Eq. 28}$$

By using the experimentally measured $\alpha_{t,0}$ (Figure S7-8c) and the d_f at different RH (Figure 7-1e), we calculated the ΔN of 119 turns for the HT, which is higher than the experimental ΔN of 100 turns and 65 turn/cm (number of untwist and retwist of the first actuation cycle) shown in Figure 7-4b. Such difference between the calculated and experimental values of ΔN can be explained by several factors: (1) non-circular cross-sectional shape of the yarn, (2) the slight increase in length of the yarn due to moisture absorption (Figure 7-1d), and (3) reduced swelling capacity of the highly twisted [12] and strained yarn [19]. Others also reported [23] similar observations, with nylon TCPAs having relatively low twist density (around 1.7 turn/cm) and the calculated ΔN being higher than the experimental ΔN with increasing twist density. However,

some reported opposite phenomenon. For example, Li et al [12] and Jia et al [5] reported underestimation of ΔN at increasing twist density.

Given that the HT yarn is too fragile to measure the torque, the principle of torsional pendulum is used here to characterize the torsional mechanical output of the yarn. In brief, the motion of the paddle attached at the bottom of the yarn during actuation is recorded to interpret the initial torque (τ) and peak power output (P) of the yarn. They are $10.5nN * m$ and $0.97\mu W$, calculated by,

$$\tau = I_{pad}\alpha_{initial} = \frac{m_{pad}W_{pad}^2}{12}\alpha_{initial} \quad Eq. 29$$

and,

$$P = \frac{I_{pad}\omega_{peak}^2}{2} \quad Eq. 30$$

where I_{pad} is the moment of inertia of a rectangular ($1.41 * 10^{-9} \text{ kg}\cdot\text{m}^2$), m_{pad} and W_{pad} are the mass and width of the paddle, and $\alpha_{initial}$ and ω_{peak} are the peak rotational speed and initial acceleration. The torque density and peak power density, normalized by the mass of the yarn ($6.11\mu\text{g}$), are $173 \text{ mN}\cdot\text{m}/\text{kg}$ and $16 \text{ W}/\text{kg}$, respectively.

7.2.4 Torsional actuation of HTsPly

The torsional performance of the self-plyed yarn is better than the twisted yarn. During torsional actuation, the torque generated in the constituting HTs in the untwisting direction induces plying of the HTsPly. Upon subsequent retwisting of the HTs, the number of twist in the plyed yarn recovers almost completely due to the torque-balanced structure of the HTsPly (**Figure 7-5a-c**). Compared to the actuation performance of HT, the HTsPly has higher maximum ω ($45\text{rad}/\text{s}$), τ ($19nN * m$) and peak P ($1.2\mu W$), and similar ΔN . However, when normalized, the torque density and peak power density ($155 \text{ mN}\cdot\text{m}/\text{kg}$ and $9.7 \text{ W}/\text{kg}$) are both

lower than the HT. The results indicate that self-plying not only enhances the actuation reversibility but also increases the torque and power output.

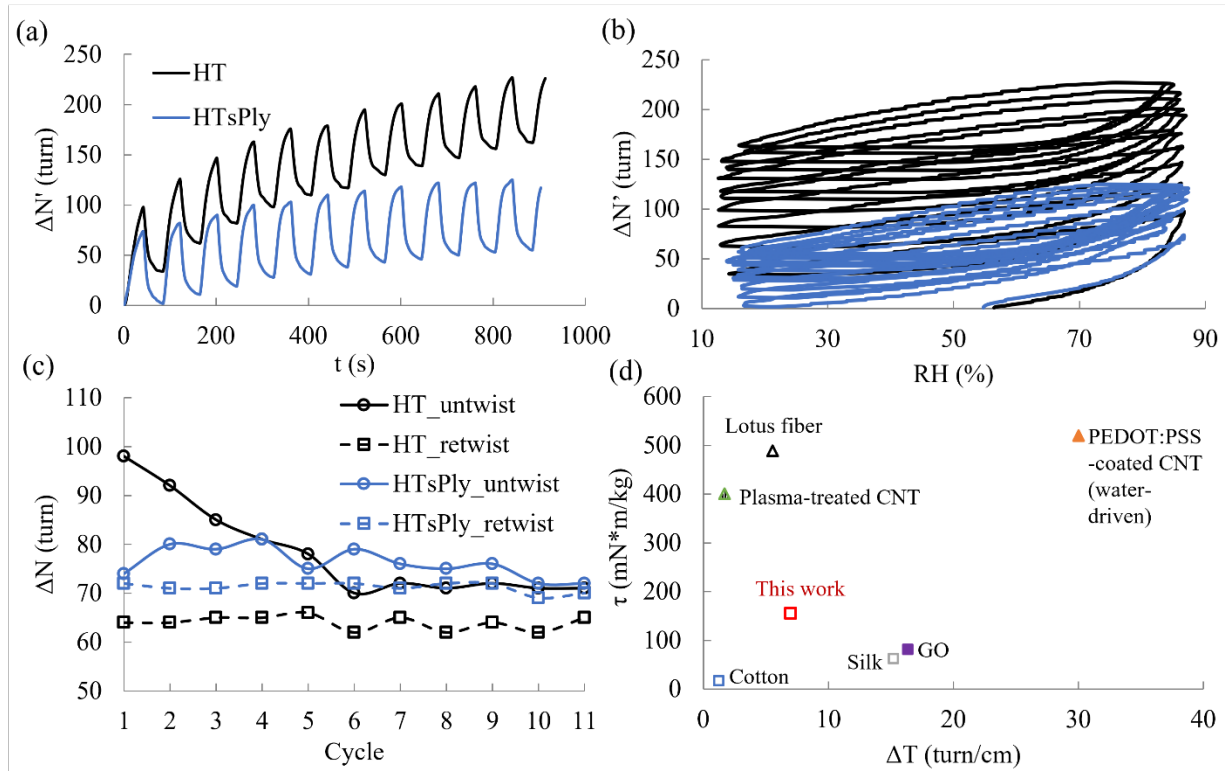


Figure 7-5. Torsional actuation of HT and HTsPly. (a, b) $\Delta N'$ of HT and HTsPly in a cyclic moisture actuation as a function of (a) time and (b) RH. (c) ΔN of untwist and retwist. (d) Comparison of torsional actuation performance with other moisture/water driven TCPAs. Triangle symbol (\blacktriangle) represents water actuation, and rectangle symbol (\blacksquare) represents moisture actuation. Unfilled symbol (\square) represents 2-ply yarn, solid-filled symbol (\blacksquare) represents single yarn, and pattern-filled symbol represents 10-ply yarn. The parameters of HT in this experiment is: $d_f = 21.7\mu\text{m}$, $T_t = 100\text{turn/cm}$, $\#n_f = 1$, $l_t = 10\text{cm}$. Two of such HTs are self-plyed to form the HTsPly studied here.

Figure 7-5g compares the torsional actuation stroke ($\Delta T = \frac{\Delta N}{l_t}$) and peak torque density of the above HTsPly to other reported moisture (or water)-driven TCPAs [5], [10], [12], [13], [24], [25]. The measurement of torsional stroke and calculation of torque are the similar in all reports, while the former counts the number of rotations of a yarn with a paddle attached at the bottom, and the latter is based on the rotational dynamics of the paddle. As a result, the viscose rayon-

based TCPA in our experiment produces relatively higher torque density and moderate torsional stroke.

The self-plyed yarn have been often reported for reversible torsional actuation of TCPAs[5], [11]. However, we noticed that there is a lack of study on the effect of structures on the actuation performance of HTsPly. Therefore, in the following sections, the key structural parameters of HTsPlys (d_f , T_t , $\#n_f$, $\#n_t$) are evaluated on their torsional performance, with the purpose of optimizing the actuation performance through the structural design.

7.2.4.1 Effect of fiber diameter and twist density

Viscose rayon fibers with diameter of 14, 21.7, and 25.4 μm (**Figure 7-6a**) were used to study the effect of d_f on the torsional actuation of HTsPly. A constant T_t of 100turn/cm was inserted into HT, and two of them were then self-plyed into HT1sPly. With increasing fiber diameter, there is a slight increase and then decrease of ΔN (average of three specimens and five actuation cycles for each specimen) (Figure 7-6b). The change of ΔN with d_f is subtle, considering the variation of ΔN due to the slight difference in (1) RH in different cycles, (2) and the structural difference of different specimen due to fiber non-uniformity. The maximum rotational speed, peak torque and power output, however, increase obviously with the increase of fiber diameter (Figure 7-6c, d). In particular, the ω of untwist and retwist increases from 18 to 34 rad/s and -23 to -48 rad/s, respectively, τ increases from 5 to 21 nN*m, and peak P increases from 0.3 to 1.4 μW .

The effect of T_t on the torsional performance of HTsPly is studied insert different twist into the viscose rayon fibers of a constant d_f of 21.7 μm , see Figure 7-6e-h. As expected, the actuation performance enhances with the increase of T_t . In particular, when T_t increases from 50 to 100 turn/cm, the ΔN increases from 40 to 70 turns (Figure 7-6f), ω of untwist and retwist

increases from 20 to 32 rad/s and -22 to -40 rad/s (Figure 7-6g), respectively, peak τ increases from 7 to 19 nN*m, and peak P increases from 0.4 to 1.2 μ W (Figure 7-6h).

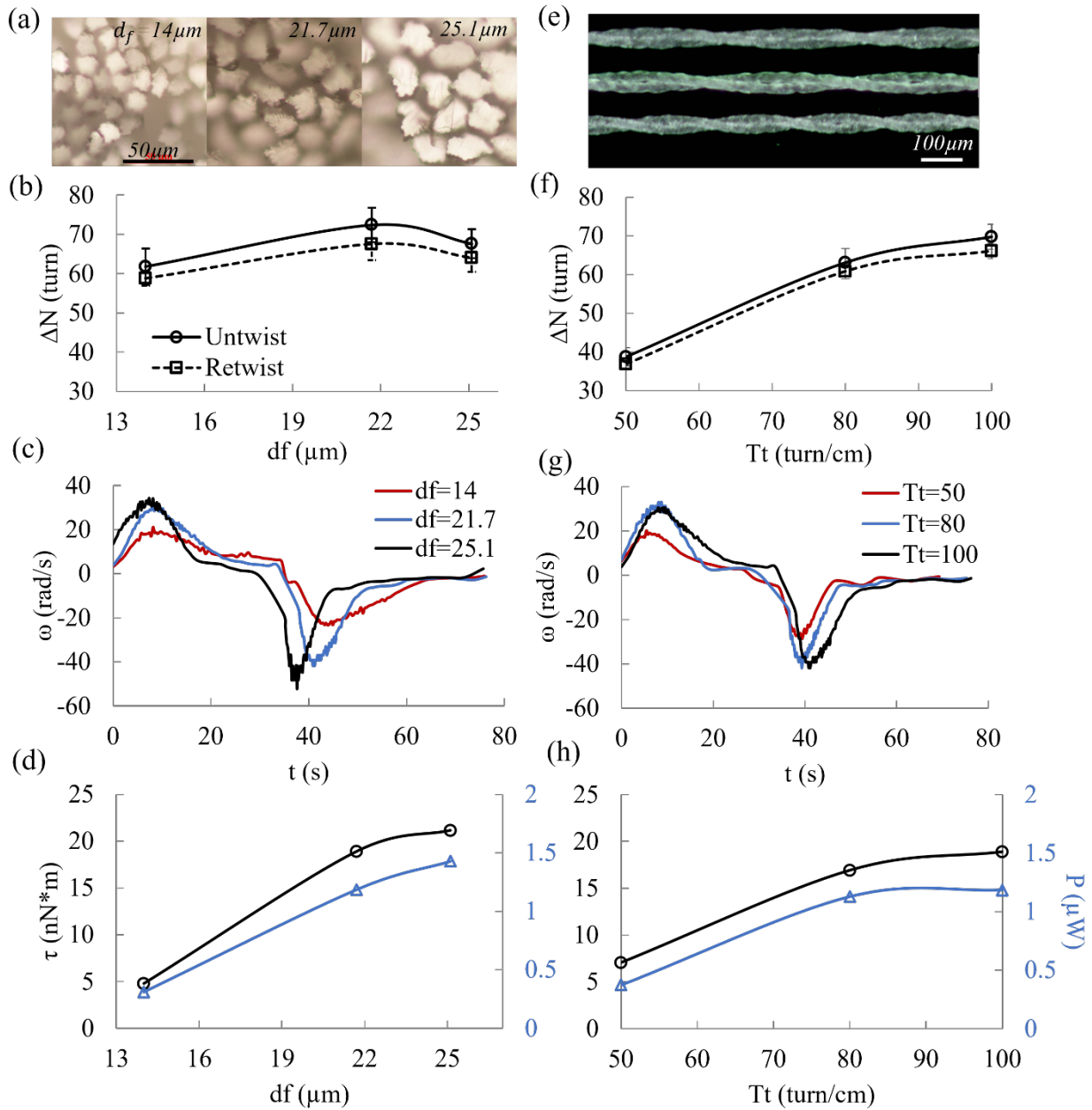


Figure 7-6. Effect of fiber diameter and twist density on the torsional results of HTsPly. (a) Cross-sectional images of fibers with diameters of 14, 21.7, 25.1 μ m. (b-d) Torsional actuation results of the HTsPly fabricated from fibers of three diameters with same twist density of 100 turn/cm. (e) Microscope images of HTsPlys fabricated from 21.7 μ m fiber with different twist density, and (f-h) their torsional actuation results.

7.2.4.2 Effect of the number of fiber and single yarns

Monofilament yarns with diameters of 10 to 30 μ m are mechanically weak. A common method to enhance the strength of the yarn is to twist more fibers into the yarn. Here we increase the number of fibers in the self-plied yarn by two approaches: (1) increase $\#n_f$ in the single yarn, (2) increase $\#n_t$ in the plied yarn.

The effect of $\#n_f$ on the actuation performance of HTsPly is shown in **Figure 7-7a-d**. Since the maximum T_t decreases with increasing $\#n_f$, and low T_t reduces the actuation performance, we limit the maximum $\#n_f$ to 5 and insert a constant T_t of 50 turn/cm. As a result, there is an overall reduction in the actuation performance when $\#n_f$ increases (Figure 7-7b-d). In particular, the number of rotation decreases from 42 to 27 turns, the maximum rotational speed decreases from -26 to -6 rad/s, the initial τ and peak P decreases from 7 nN*m and 0.37 μ W to 2.3 nN*m and 0.03 μ W, respectively. The results suggest that to achieve better actuation performance, the $\#n_f$ should be minimized.

Then, the effect of $\#n_t$ on the torsional performance of HTsPly is studied. A constant T_t of 100 turn/cm was inserted into a single fiber, followed by self-plying a number of them (Figure 7-7e). As a result, with an increasing $\#n_t$, the torsional actuation performance enhances (Figure 7-7f-h), with a slight increase of ΔN from 70 to 80 turns, higher rotational speed increased from 40 to 60 rad/s, as well as an increase of the initial τ and peak P from 19 to 30 nN*m, and 1.2 to 2.3 μ W, respectively. The results suggest that the torsional actuation of HTsPly can be enhanced by plying more twisted yarns.

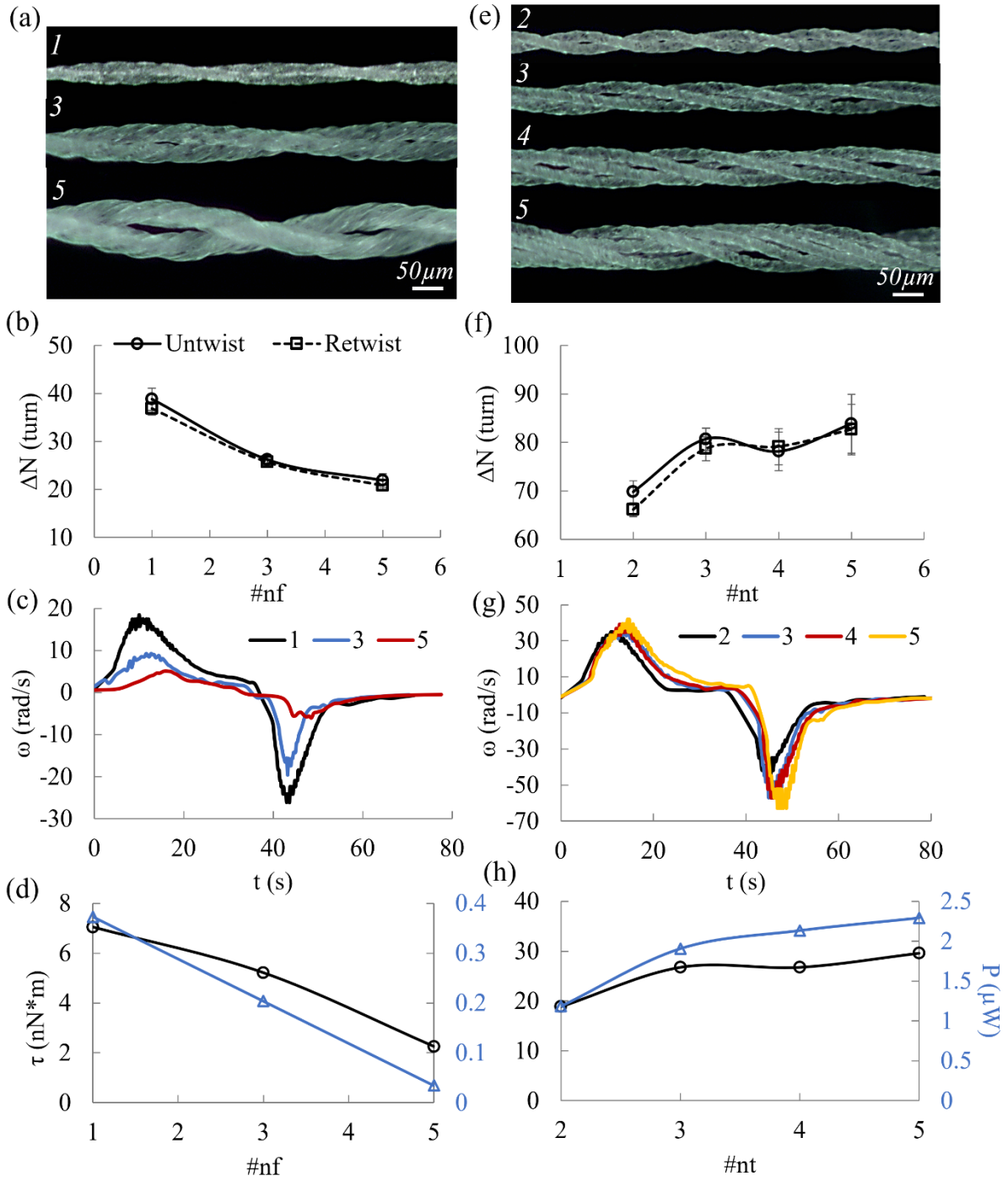


Figure 7-7. Effect of the number fibers ($\#n_f$) and single yarns ($\#n_t$) on the torsional results of HTsPly. (a) Microscope images of HTsPly, and (b-d) their torsional actuation results. (e) Microscope images of HTsPly, and (f-h) their torsional actuation results.

7.2.5 Linear actuation of HTCo

The coiled yarns fabricated by overtwisting contract immediately when exposed to moisture (vapor or water) and recover after moisture desorption. The microscopic structures of HTCo and their actuation results are shown in **Figure 7-8a-d**. The linear strain of the HTCo due to water absorption is around 10% (**Video S1**), which remains relatively constant with increasing $\#n_f$. However, the linear strain is lower when actuated with RH change and decreases from 8% to 2% with increasing $\#n_f$ (Figure 7-8b, **Video S2**). This might be due to the restricted transportation of water molecules in the vapor form into the inner fibers of the highly packed yarn. A constant stress of 6MPa is applied during actuation, giving a work output of $3 * 10^{-5} J$ and work capacity of 100 *J/kg* of HTCo.

The blocking force HTCo, shown in Figure 7-8c, d, was measured isometrically (constant length) by exposing the two end-tethered yarn to water mists. The blocking force was triggered by continuous spray and cyclic spray of water mist. The former method saturates the yarn with water and thus induces the yarn contraction of its full capacity, while the latter method is used to demonstrate the cyclic actuation of HTCo. As a result, with increasing $\#n_f$, the overall blocking force increases, but the force density (normalized by $\#n_f$) decreases from 4.2 to 3 *mN/fiber* under continuous spray of water (Figure 7-8c). The cyclic spray of water generates lower but relatively steady blocking force as the water quickly evaporates and dissipates in the ambient (Figure 7-8d).

The manual-plied yarn, HTmPly, also generate large linear contraction during moisture absorption, see Figure 7-8e, f,. The linear strain decreases almost linearly with increasing $\#n_t$ under both water and moisture actuation (Figure 7-8f).

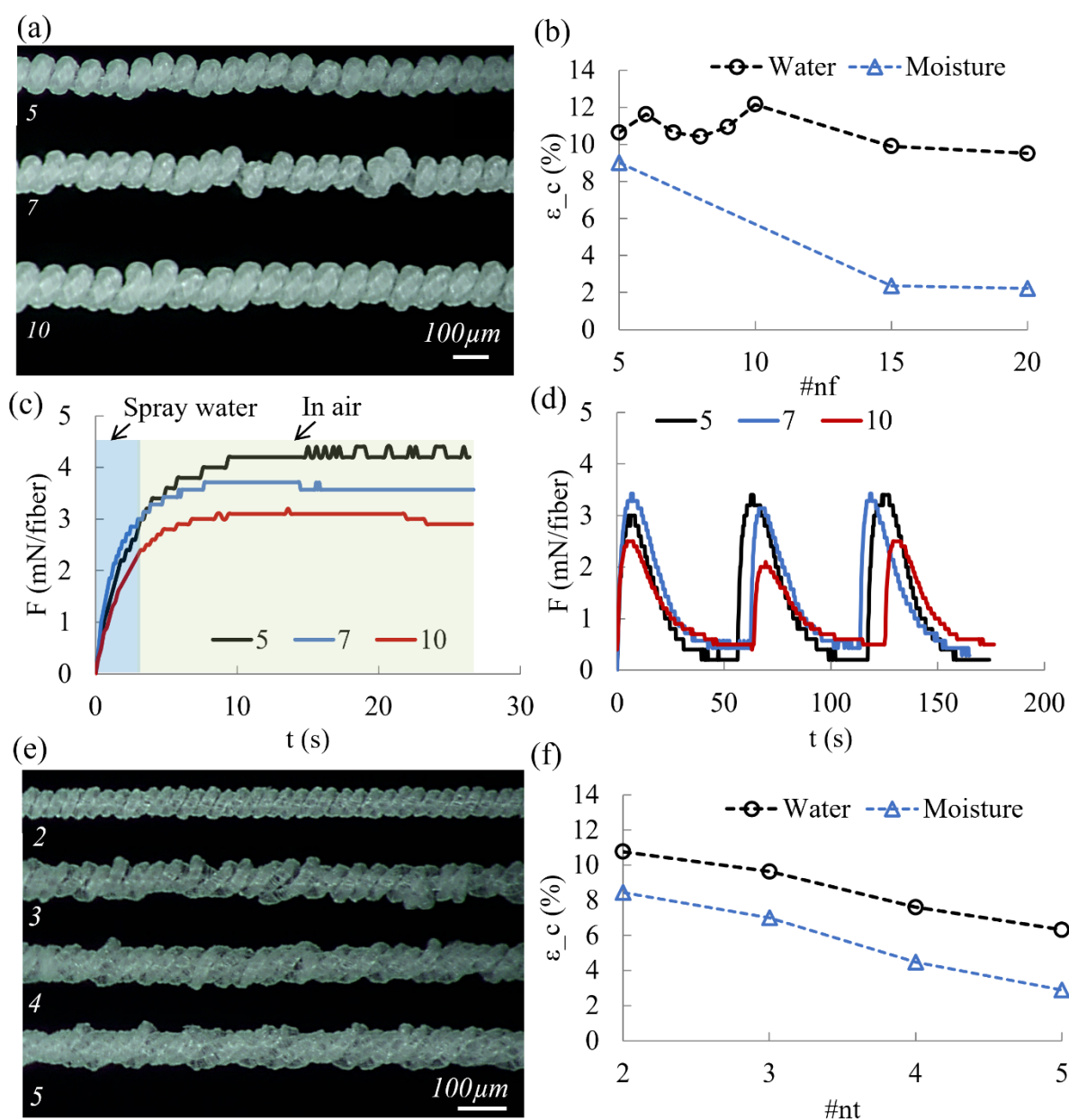


Figure 7-8. Linear actuation results of (HTn)Co. (a) Microscope images of the (HTn)Co. (b) Linear strains of (HTn)Co made with different number of precursor fibers as a result of water and moisture. (c) Full (equilibrated) blocking force of selected (HTn)Co by continuous spray of water mist. (d) Blocking force of selected (HTn)Co by one-time spray of water mist.

7.2.6 Electrical actuation of torsional TCPAs

We observed that the HTsPly rotates in one direction when hand approaches but rotates in the opposite direction when the approaching hand is covered by a moisture-barring glove (Video S3). The former phenomenon is due to the high RH near the hand (85%) that induces the

radial expansion of the viscose rayon. The latter phenomenon is possibly due to the slightly higher temperature near the hand (+4°C) that induces the moisture desorption from the yarn. We hypothesized that the yarn can be actuated by elevating temperature. Therefore, electrothermal actuation is studied by plying a CNT yarn (resistive heating) with the viscose rayon yarns (**Figure 7-9b**). Two of such plied yarns are brought together in order to connect electrical wires from one end for voltage application (**Figure 7-9c**).

The CNT yarns were fabricated by drawing a CNT sheet from the forest and inserting twists in the meantime (**Figure 7-9a**). The obtained CNT yarn has a diameter of $50\pm 5\mu m$, and a resistance of around $280\Omega/cm$ for voltage between 5 to 15V (**Figure 7-9d**). The self-plied CNT-viscose rayon yarns are shown in **Figure 7-9b**. Upon application of 15V, the yarn rotate immediately for 20 turns (with the direction same as the RH decrease-induced rotation) with maximum speed of 25 rad/s, and recovers partially with a much slower speed (**Figure 7-9g**, **Video S4**). The numbers of untwist and retwist in a cyclic actuation are relatively stable at around 12 and 18 turns, respectively (**Figure 7-9g-h**). Compared to the electrothermal actuation, the moisture actuation of the same yarn of the same yarn have generates higher torsional stroke, speed, and reversibility (**Figure 7-9e**, **Video S5**).

Under the electrothermal actuation, the two strands of the yarn plies, leading to an increase of contact region of CNT yarns and an increase in electrical current under same applied voltage. While the contact area between CNT yarns is too large, the heat generated by the instantaneous current surge can burn the viscose rayon (**Figure 7-9i**). Since the large current passes only through the upper region of the yarns that are not plied, the rest region remains visually intact. Interestingly, such “damaged” yarn can still work under electrothermal actuation, with slightly decreased torsional stroke **Figure 7-9j**). This suggest that the properties of the unburned region of the yarn are not altered.

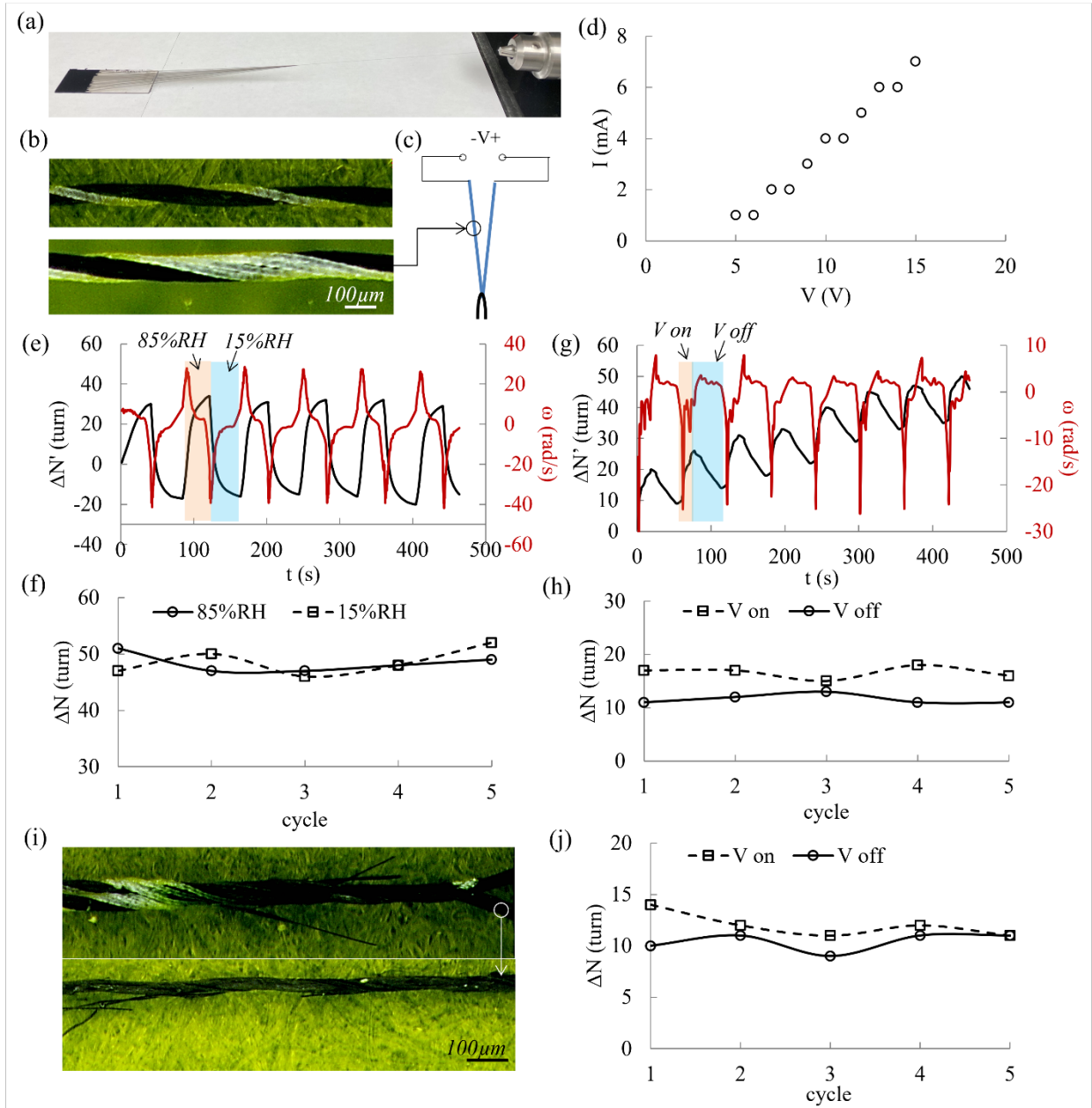


Figure 7-9. (a) Drawing and twisting of CNT yarn from forest. (b) Microscope images of a CNT yarn plied with one and four HTI. (c) Schematic of electrothermal actuation setup. (d) IV curve of the CNT yarn. (e-f) Moisture actuation and (g-h) electrothermal actuation results of the CNT-plied yarn. (i) Microscope images of burned region of the yarn due to overheating. (j) Electrothermal actuation results of the burned yarn shown in (i).

7.3 Conclusion

In conclusion, we demonstrated the moisture-driven torsional and linear actuation capability of viscose rayon by constructing highly twisted structures and studied the structural parameters on the actuation results. As expected, self-plyed yarns show higher actuation reversibility compared to the single yarns, due to the torque-balanced structures. Increasing twist density is an effective method to enhance the torsional actuation results. However, the maximum twist density in a yarn decreases with increasing fiber diameter and increasing number of fibers in a yarn. With same twist density, yarns with larger diameter generate similar torsional stroke but have higher speed, torque and peak power output. With same twist density, yarns with more precursor fibers have an overall decreasing actuation result. Therefore, the optimal torsional actuation can be obtained by inserting largest twist density into one fiber of an appropriate diameter. Self-plying more numbers of HT enhances the mechanical strength and the overall actuation performance of the yarn. For linear actuation, the self-coiled yarns generate a contractile strain of around 10%, with blocking force of 3 to 4.2 mN/fiber, by applying water mist to the yarn. For the water actuation, increasing the number of fibers has small effect on the linear strain but longer recovering time and decreasing blocking force density. For moisture actuation, the overall actuation results decrease with increasing number of fibers. We also demonstrated electrothermal actuation of the torsional yarns, by plying a conductive CNT yarn with the highly twisted viscose rayon. By applying a cyclic voltage of 0 to 15V, the plied yarn generates reversible rotation with a decent torsional stroke and speed.

References

- [1] C. S. Haines, N. Li, G. M. Spinks, A. E. Aliev, J. Di, and R. H. Baughman, “New twist on artificial muscles,” *Proc. Natl. Acad. Sci.*, vol. 113, no. 42, pp. 11709–11716, Oct. 2016, doi: 10.1073/pnas.1605273113.
- [2] J. Foroughi *et al.*, “Torsional Carbon Nanotube Artificial Muscles,” *Science*, p. 1211220, Oct. 2011, doi: 10.1126/science.1211220.
- [3] L. Saharan, M. J. de Andrade, W. Saleem, R. H. Baughman, and Y. Tadesse, “iGrab: hand orthosis powered by twisted and coiled polymer muscles,” *Smart Mater. Struct.*, vol. 26, no. 10, p. 105048, Sep. 2017, doi: 10.1088/1361-665X/aa8929.
- [4] L. Wu and X. Wang, “A modular twisted and coiled polymer actuator unit for robotic tentacles,” in *Electroactive Polymer Actuators and Devices (EAPAD) XXI*, Mar. 2019, vol. 10966, pp. 59–67. doi: 10.1117/12.2514400.
- [5] T. Jia *et al.*, “Moisture Sensitive Smart Yarns and Textiles from Self-Balanced Silk Fiber Muscles,” *Adv. Funct. Mater.*, vol. 29, no. 18, p. 1808241, 2019, doi: 10.1002/adfm.201808241.
- [6] J. Mu *et al.*, “Sheath-run artificial muscles,” p. 7, 2019.
- [7] H. Song and Y. Hori, “Force control of twisted and coiled polymer actuators via active control of electrical heating and forced convective liquid cooling,” *Adv. Robot.*, vol. 32, no. 14, pp. 736–749, Jul. 2018, doi: 10.1080/01691864.2018.1494629.
- [8] C. Wu and W. Zheng, “A Modeling of Twisted and Coiled Polymer Artificial Muscles Based on Elastic Rod Theory,” *Actuators*, vol. 9, no. 2, Art. no. 2, Jun. 2020, doi: 10.3390/act9020025.
- [9] S. M. Mirvakili *et al.*, “Niobium Nanowire Yarns and their Application as Artificial Muscles,” *Adv. Funct. Mater.*, vol. 23, no. 35, pp. 4311–4316, 2013, doi: 10.1002/adfm.201203808.
- [10] H. Cheng *et al.*, “Moisture-Activated Torsional Graphene-Fiber Motor,” *Adv. Mater.*, vol. 26, no. 18, pp. 2909–2913, May 2014, doi: 10.1002/adma.201305708.
- [11] C. S. Haines *et al.*, “Artificial Muscles from Fishing Line and Sewing Thread,” *Science*, vol. 343, no. 6173, pp. 868–872, Feb. 2014, doi: 10.1126/science.1246906.
- [12] Y. Li *et al.*, “Moisture-Sensitive Torsional Cotton Artificial Muscle and Textile,” *Chin. Phys. B*, 2020, doi: 10.1088/1674-1056/ab7745.
- [13] Y. Wang *et al.*, “Humidity- and Water-Responsive Torsional and Contractile Lotus Fiber Yarn Artificial Muscles,” *ACS Appl. Mater. Interfaces*, Jan. 2021, doi: 10.1021/acsami.0c20456.
- [14] D. Liu *et al.*, “Spider dragline silk as torsional actuator driven by humidity,” *Sci. Adv.*, vol. 5, no. 3, p. eaau9183, Mar. 2019, doi: 10.1126/sciadv.aau9183.
- [15] I. Z. Steinberg, A. Oplatka, and A. Katchalsky, “Mechanochemical Engines,” *Nature*, vol. 210, no. 5036, pp. 568–571, May 1966, doi: 10.1038/210568a0.
- [16] X. Yang, W. Wang, and M. Miao, “Moisture-Responsive Natural Fiber Coil-Structured Artificial Muscles,” *ACS Appl. Mater. Interfaces*, vol. 10, no. 38, pp. 32256–32264, Sep. 2018, doi: 10.1021/acsami.8b12144.
- [17] W. Wang *et al.*, “Natural alginate fiber-based actuator driven by water or moisture for energy harvesting and smart controller applications,” *J. Mater. Chem. A*, vol. 6, no. 45, pp. 22599–22608, Nov. 2018, doi: 10.1039/C8TA08064J.
- [18] A. Mirabedini, S. Aziz, G. M. Spinks, and J. Foroughi, “Wet-Spun Biofiber for Torsional Artificial Muscles,” *Soft Robot.*, vol. 4, no. 4, pp. 421–430, Jun. 2017, doi: 10.1089/soro.2016.0057.

- [19] J. M. Preston and M. V. Nimkar, "MEASURING THE SWELLING OF FIBRES IN WATER," *J. Text. Inst. Proc.*, vol. 40, no. 7, pp. P674–P688, Jul. 1949, doi: 10.1080/19447014908664692.
- [20] A. J. Stamm, "Diffusion of Water into Uncoated Cellophane. I. From Rates of Water Vapor Adsorption, and Liquid Water Absorption," *J. Phys. Chem.*, vol. 60, no. 1, pp. 76–82, Jan. 1956, doi: 10.1021/j150535a019.
- [21] M. L. Staples, "The Saturation Regain of Viscose Rayon Deduced from Density and Swelling Data," *Text. Res. J.*, vol. 28, no. 11, pp. 950–955, Nov. 1958, doi: 10.1177/004051755802801107.
- [22] T. Hatakeyama, Y. Ikeda, and H. Hatakeyama, "Effect of bound water on structural change of regenerated cellulose," *Makromol. Chem.*, vol. 188, no. 8, pp. 1875–1884, 1987, doi: 10.1002/macp.1987.021880811.
- [23] S. Aziz, S. Naficy, J. Foroughi, H. R. Brown, and G. M. Spinks, "Controlled and scalable torsional actuation of twisted nylon 6 fiber," *J. Polym. Sci. Part B Polym. Phys.*, vol. 54, no. 13, pp. 1278–1286, 2016, doi: 10.1002/polb.24035.
- [24] S. He *et al.*, "A Mechanically Actuating Carbon-Nanotube Fiber in Response to Water and Moisture," *Angew. Chem.*, vol. 127, no. 49, pp. 15093–15097, 2015, doi: <https://doi.org/10.1002/ange.201507108>.
- [25] X. Gu *et al.*, "Hydro-actuation of hybrid carbon nanotube yarn muscles," *Nanoscale*, vol. 8, no. 41, pp. 17881–17886, 2016, doi: 10.1039/C6NR06185K.
- [26] D. E. Henshaw, *Self-twist yarn*. Watford (276 Hempstead Rd, Watford, Herts.) : Merrow Publishing Co., 1971., 1971. [Online]. Available: <https://catalog.lib.ncsu.edu/catalog/NCSU161725>

7.6 Supplementary information

7.6.1 Experimental method

7.6.1.1 Fiber characterization

The as-received viscose rayon filament yarns are slightly twisted filament bundles composed of tens to hundreds of filaments of certain denier (grams per 9000 meter), shown in **Figure S7-1a**.

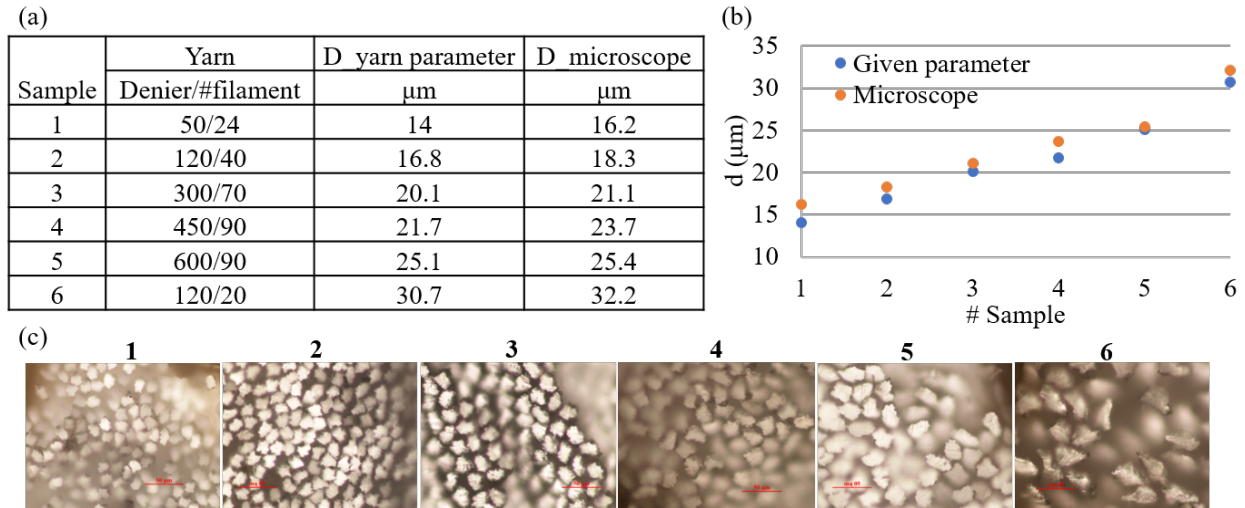


Figure S7- 1. Fiber diameter of the viscose rayon samples. (a) The table of yarn parameter, and diameters calculated from given yarn parameters and microscope images. (b) A plot of d_f calculated from two methods. (c) Cross-sectional microscope image of the fiber samples.

Structural, mechanical, and swelling properties of viscose rayon fibers were characterized. The cross-sectional view of fiber bundles was captured under optical microscope, and the fiber diameter was measured by calculating the cross-sectional area of the fiber. The cross-section of the fiber bundle was prepared by fixing the bundle in a rubber cork and then slice a flat thin layer. The anisotropic property of the fiber was visualized under the polarized light microscope, as the fiber is only visible when the fiber length direction is neither parallel nor perpendicular to the incident light direction.

The swelling behavior of the fiber was recorded under microscope, and the change in cross-sectional area or the diameter was measured on the video frame by frame. For water-

induced swelling, the cross-sectional view of the fiber bundle for microscopy was prepared as above, then a droplet of water was brought in contact with the bundle and left evaporating naturally in air. Microscope images of the fiber cross-section before swelling, just after swelling, and after deswelling were taken and the diameter change was measured. The water-induced swelling of the fiber was also measured at its projected length on single fiber (not bundled). The moisture sorption-induced swelling was also measured, by enclosing the fiber in a RH chamber that can change from 5% to 90%RH within a minute. A stereomicroscope (AmScope, SM-3 series) with large space between the lens and sample stage (165mm) was used to place the customized RH chamber (30*30*100mm). The projected diameter change of the fiber under cycles of RH from 5 to 90% was recorded by microscope video, and in the meantime, the RH was recorded with a RH sensor. The length change due to water and RH was measured by a video camera, as the fiber elongates and recovers with by hanging a light weight (0.1g, 5.4MPa) at the fiber end.

The mechanical properties of the fiber were measured by a universal tensile tester (MTS, 30G). The stress-strain behavior was recorded by stretching a 3-cm long fiber to break at a speed of 1cm/min. A 1N load sensor was used to measure such tiny force generated by a single fiber. The ambient mechanical test was conducted under 55%RH and 23°C. The wet mechanical test was conducted by immerse the fiber in a water bath (room temperature), while the fiber was connected to the load sensor at one end, and at the other end connected to a heavy weight seated at the bottom of the water bath (Figure S7-2). The stress of the fiber was calculated by normalizing the force by the cross-sectional area of the fiber, which was calculated by taking the areal strain of 65%. The stress relaxation of the fiber conducted by prestretching the fiber to 0.03N (86.7MPa) and then measuring the force change with time at the ambient condition.

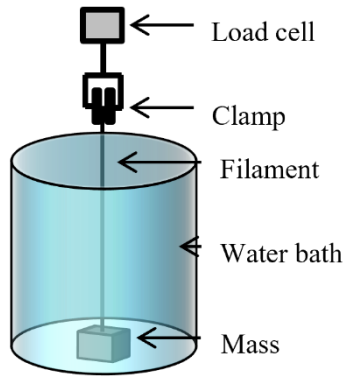


Figure S7- 2. Mechanical test of the wet fiber.

7.6.1.2 Fabrication of hierarchical TCPAs

A large number of twist (50~180 turn/cm) was inserted into the viscose rayon fibers to make TCPAs. A twist tester was modified and used to insert twist into fibers. As shown in Figure S7-3, a fiber with given length was clamped at one end to the twister head to insert twist in Z-direction, and at the other end tied to a lightweight paddle to; 1) straighten the fiber for twisting, 2) keep the fiber end from rotating (untwisting), 3) allow twist contraction, 4) prevent early snarling. The fiber can be twist in air (Figure S7-3b) or in water Figure S7-3c), while the latter method can insert more twist and at the same time stabilize the twisted shape. In addition to that, the fiber twisted in air tends to break at a certain amount of twist, while that twisted in water is prone to snarl (Figure S7-4). Both higher twist density and self-coiling (due to the onset of local snarling) are desirable for TCPAs. Therefore, unless specified, all the TCPAs used in this experiment was twisted (and coiled) in water.

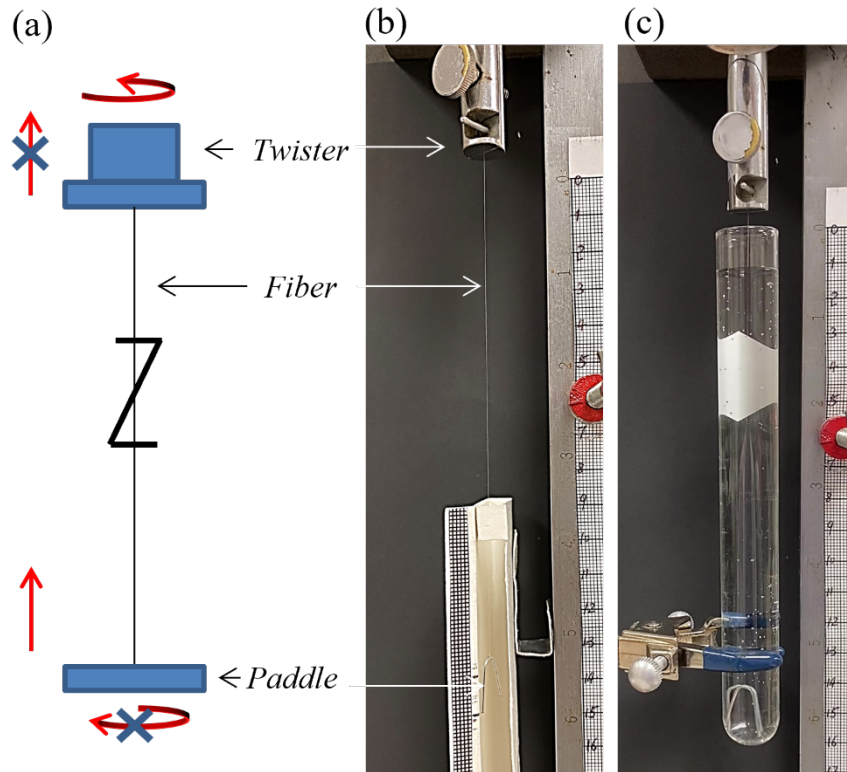


Figure S7- 3. Fiber (or yarn) twisting setup. (a) Schematic of fiber twisting. A fiber is Z-twisted by rotating the twisting head counter-clockwise, while restricting the rotation of the other end of the fiber with a lightweight paddle. Twist contraction is allowed. (b) Setup of fiber twisting in air. (c) Setup of fiber twisting in water.

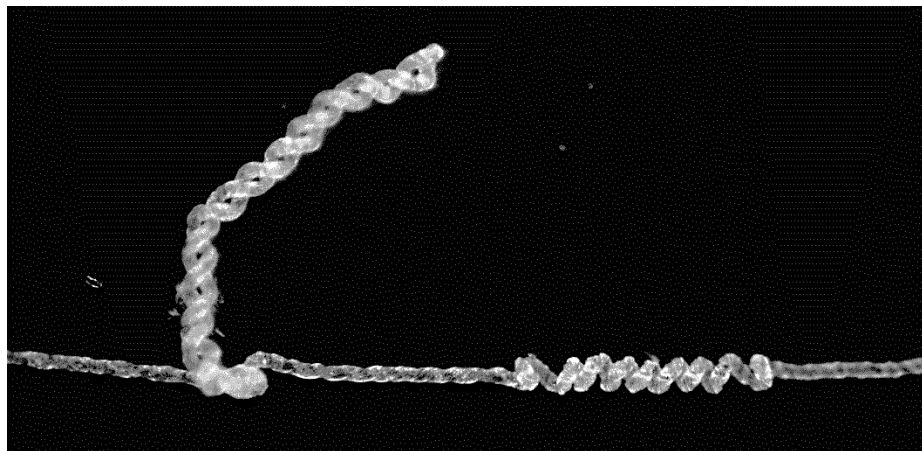


Figure S7- 4. Snarling and self-coiling of the highly twisted fiber.

The tensile stress exerted by the paddle is critical in the twisting process. If too large, the fiber breaks at low twist; if too small, the fiber snarls at low twist (Figure S7-4). To increase the twist density and being able to make coils by overtwisting, the appropriate tensile stress (or the

weight of the paddle normalized by the cross-sectional area of the fibers) need to be determined. Paper clips were used as the paddle for the easy shaping, tying to the fiber, and changing the weight. Figure S7-5 shows the paper clips with weight from 0.1g to 1g.

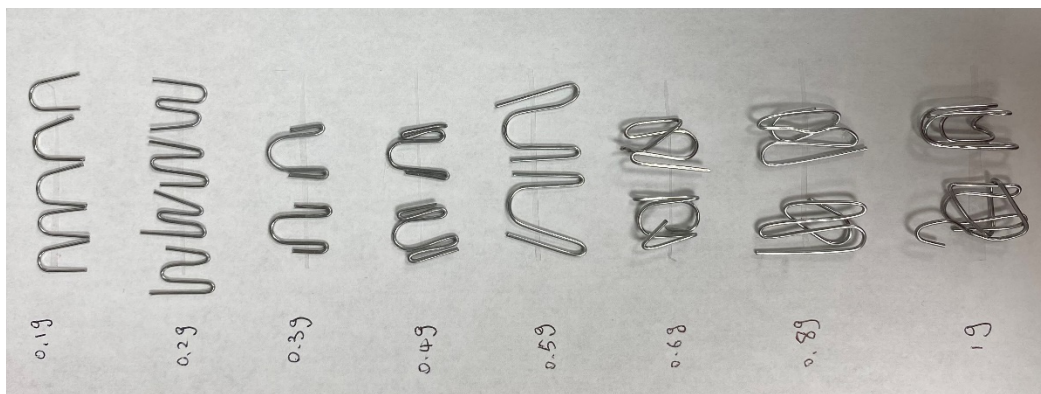


Figure S7- 5. Weights used for the tensile stress during TCPA fabrication.

The highly twisted single yarn, named as HT n , with $n \geq 1$, was fabricated in water with a selected tensile stress of 6MPa (unless specified otherwise). By overtwisting the HT n at an appropriate tensile stress in water, uniform coils can be formed throughout the yarn. The self-coiled yarn, (HT n)Co, is fabricated with this process.

The self-plyed yarns were fabricated by bringing a number of HT n s together at two leading ends, applying water, and letting them freely rotate to self-ply. We named the self-plyed yarns as the n (HT n)sPly, with the n in the parentheses refers to the number of fibers in the single yarn ($\#n_f$), and n outside the parenthesis represents the number of single yarns ($\#n_t$). To prevent the local snarling of the yarn due to slacking, individual single yarns were straightened by the tensile load generated by the paper clips, which can prevent the rotation of individual yarn in the ply while maintaining the tension on each yarn (Figure S7-6a, d). Water droplet was applied to the bundle to initiate rapid self-plying in the S-direction, opposite to the twisting direction of single yarns. By applying water to the yarn and let it evaporate naturally in air for several times, the self-plyed yarn with visually uniform ply was obtained (Figure S7-6e, f). A black CNT yarn

was used here to show the uniformity of the ply that can be easily seen with bare eyes. A rectangular reflector was then attached to the yarn for later torsional actuation.

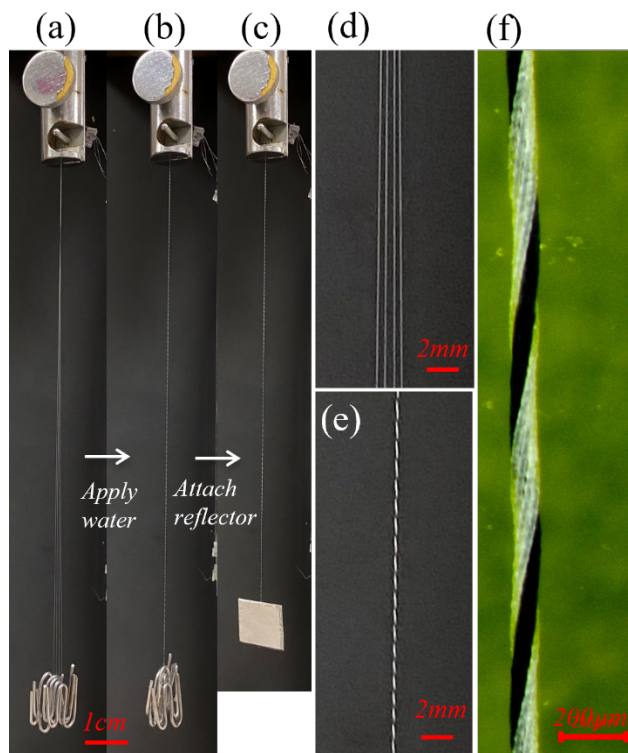


Figure S7- 6. Self-plying process. (a) A bundle of HTNs was clamped on the twister. (b) The bundle self-plies after applying water and let dry in air. (c) A reflector was attached to the ply for later torsional actuation. (d, e) Zoomed-in views of the bundle before and after self-plying. (f) Microscope image of the self-plied yarn. In this example, four HTIs (white) and a CNT yarn (black) were plied.

The manually plied yarns, named $n(\text{HTn})\text{mPly}$ were fabricated similar to $n(\text{HTn})\text{sPly}$, but the twists were manually inserted into the bundle in the same direction as the single yarns. The initial purpose of making $n(\text{HTn})\text{mPly}$ is twofold; 1) having higher twist to the yarn for better actuation performance, and 2) increase the mechanical strength of the yarn. However, in the fabrication process, we noticed a phenomenon similar to the $(\text{HTn})\text{Co}$, i.e., the yarn length shortens significantly after a critical twist level, upon which local knots start to develop and propagate. If not broken during the twisting process, a visually uniform $n(\text{HTn})\text{mPly}$ can be obtained with a significant length contraction (around half the original length of the single yarn HTn).

The cabled yarns were fabricated by plying the plied yarns, similar to the process of making plied yarns.

7.6.1.3 TCPA characterization

The TCPAs were characterized by their structural and mechanical properties, similar to the characterization of viscose rayon fibers. The swelling-induced torsional and linear motion detection are described the actuation sections. The structural features of TCPAs were primarily identified by the optical or the stereo microscopy, with key structural parameters measured from the microscope images. These structural parameters include the twist angle of single yarn (α_t), ply angle of the plied yarn (α_p), spring index of the self-coiled yarn ($C = \frac{d_c}{d_t}$), and their lengths (l_t, l_p, l_c) (Figure S7-7). The mechanical properties were obtained by stretching the yarn to break at 10mm/min with the tensile tester and the force was measured with the 1N load cell.

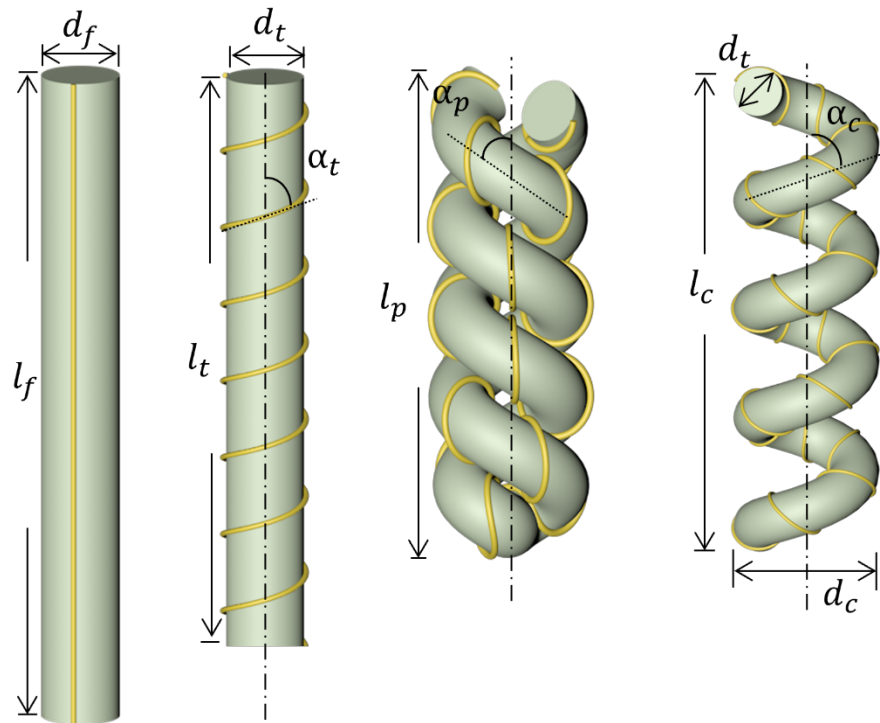


Figure S7- 7. Structural parameters of TCPAs. From left to right are, precursor fiber, highly twisted yarn, self-plied yarn, and self-coiled yarn. The yellow line on the fiber surface is used to guide your eyes.

The structural and mechanical properties of highly twisted monofilament yarn, HT1, is shown in Figure S7-8a-d. Due to the irregular cross-sectional shapes of the fiber, the diameter and helical angle of the twisted yarn varies along the length of the yarn. An averaged helical angle as a function of twist density is shown in Figure S7-8c, which is close to the theoretical value. The tensile properties (stress-strain curve) of HT1 as a function of twist density is shown in Figure S7-8d. The microscopic structures of other hierarchical TCPAs fabricated with different structural parameters are shown in Figure S7-8e-h.

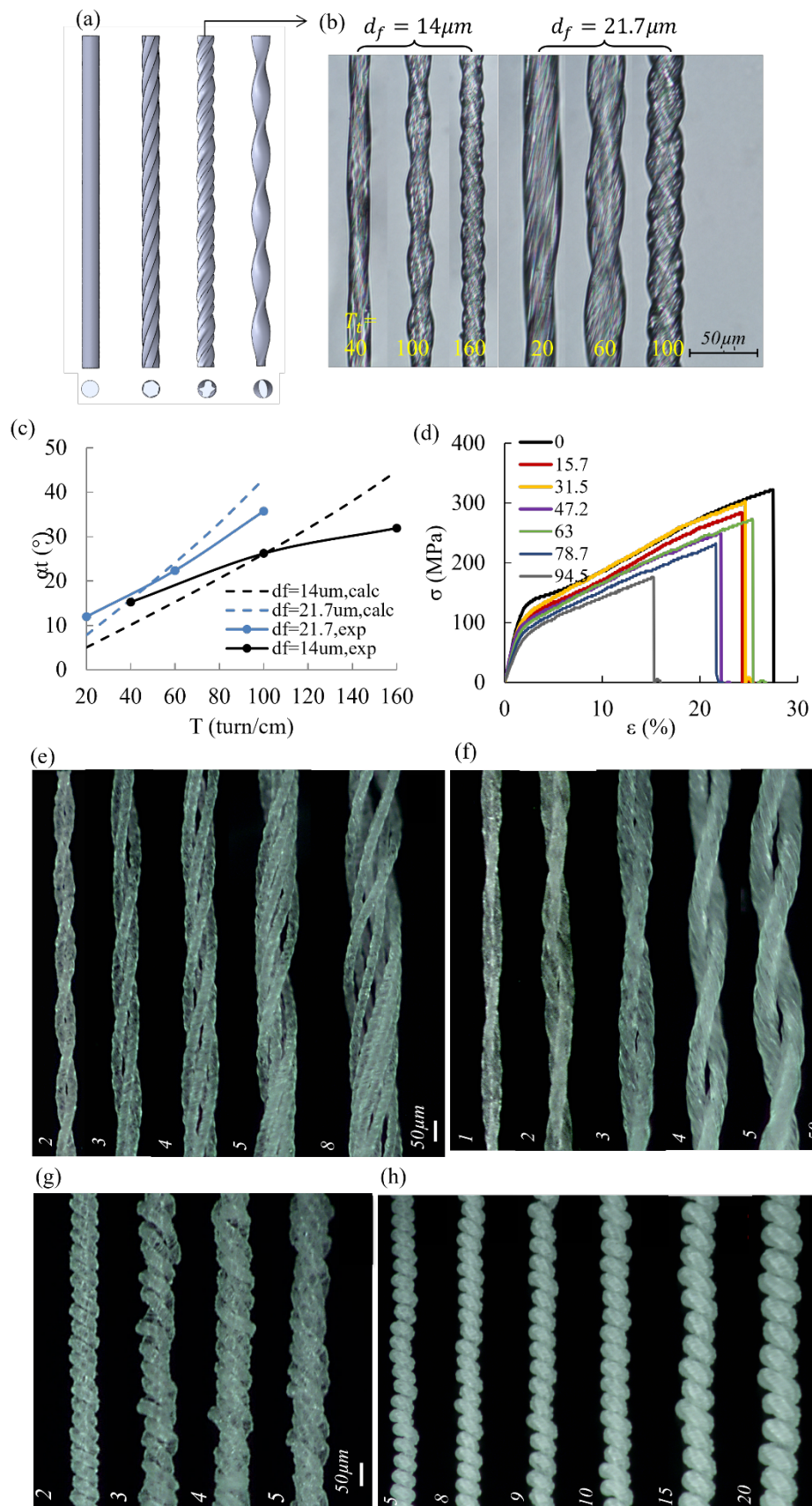


Figure S7- 8. Structural features of the TCPAs. (a-c) Structural features of highly twisted monofilament. (a) Schematics of twisted fibers with different cross-sectional shapes. (b) Microscope images of highly twisted viscose rayon fiber. (c) Experimental and theoretical helical angle of HT1 as a function of twist density. The HT1s are fabricated from fibers with diameters of 14 and 21.7 μ m. (d) Stress-strain curves of HT1 with different twist density. (e-f) Microscopic images of self-plied yarns, including (d) the n(HT1)sPly and (e) the 2(HTn)sPly. (g) Microscope images of manually plied yarns, n(HT1)mPly. (h) Microscope images of self-coiled yarns, (HTn)Co.

7.6.1.4 Torsional actuation test

When exposed to moisture or water, the highly twisted (and plied) yarns rotate rapidly due to the swelling-induced untwisting of single yarns. They rotate back upon subsequent moisture decrease or drying. The torsional actuation and measurement setup is shown in Figure S7-9a, b. The highly twisted (and plied) yarns were hung on the twister and enclosed by a customized humidity chamber. The chamber (Figure S7-9c) is capable of reliably change RH from 10% \pm 5 to 85% \pm 5 in 40 seconds (Figure S7-9d), by controlling the input of humid and dry air which was created by pumping water through water tank and desiccating tube, respectively (Figure S7-9b). The rapid rotation of yarns was recorded with an infrared sensor (Gikfun, China) that counts the number of rotations by the reflection of the aluminum reflector attached at the free end of the yarn. The tachometer was wired on the Arduino Uno and then interfaced with Matlab to record the rotation data. The Matlab (code in the Appendix) recorded the rotation data as the number of rotations as a function of time, and processed it into the forward and backward rotation (or untwisting and retwisting of the yarn), as well as the rotational speed. At the same time, the real-time RH and T were recorded by the RH sensor (SHTC3, Sensirion AG, Switzerland).

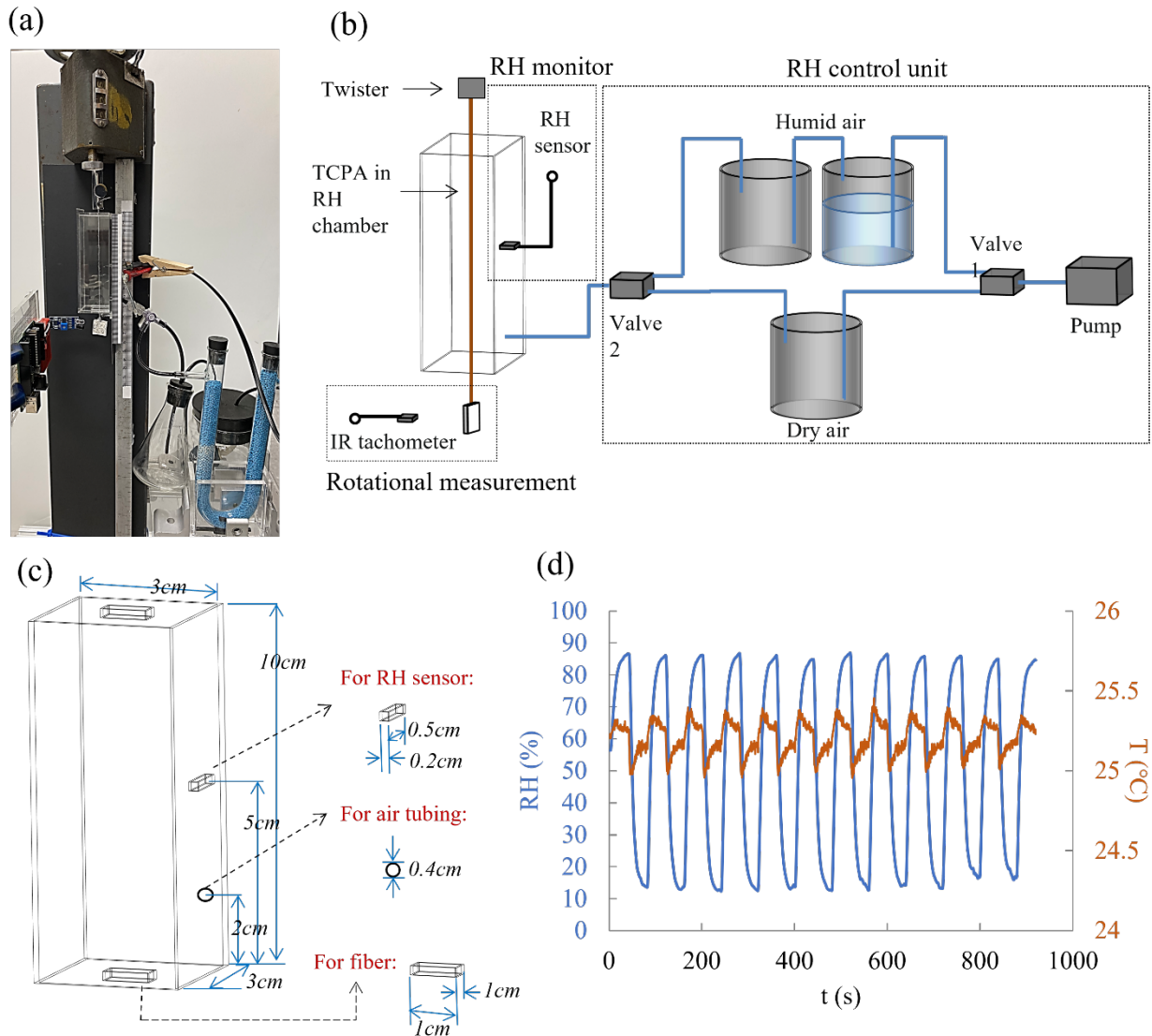


Figure S7- 9. Torsional actuation and measurement setup. (a) Photograph of the experimental setup. (b) Schematic of the setup. (c) RH chamber design. (d) Cyclic RH change in the chamber.

The maximum rotational speed and initial acceleration used to calculate the initial torque and peak power output were obtained by analyzing the data measured by the tachometer. As shown in Figure S7-10a, b, the maximum ω of HTsPly of around 38 rad/s is observed in the retwisting (RH decrease) process during cyclic actuation. The initial acceleration is obtained at the nearly linear acceleration region during retwisting within 5 seconds (Figure S7-10c).

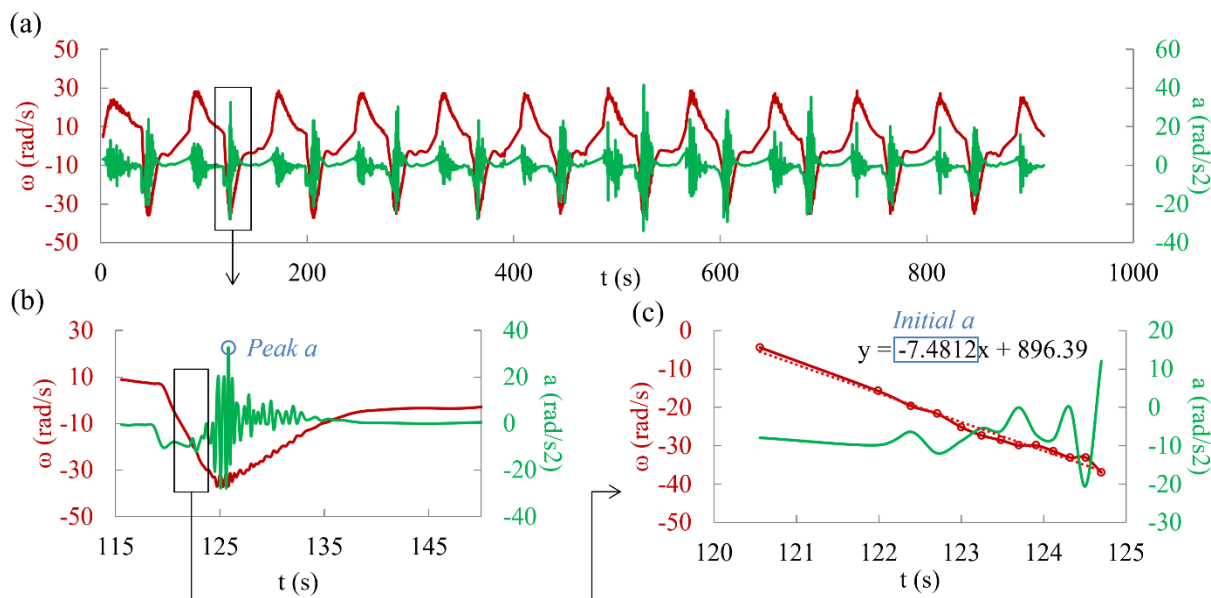


Figure S7- 10. Obtaining the torsional acceleration for initial torque calculation. (a) Torsional speed and acceleration of HT under cyclic actuation. (b) Zoomed-in view of half of a cycle during RH reduction. (c) Zoom-in view of initial near-linear acceleration region, and linear curve fitting to obtain the initial acceleration.

7.6.1.5 Linear actuation test

The linear actuation of the TCPAs was driven by water and RH change. In both cases, the yarns were hanging vertically on a wall with one end fixed and the other end tied to a paper clip with known mass. The paper clip exerted tensile stress on the yarn to prevent it from untwisting, and also prevent over-contraction and snarling when actuated. Since the linear actuation is relatively slow (seconds) and easy to track, a video camera was used to record the actuation behavior. For water-induced linear actuation, a water droplet was rapidly swipec through the yarn (about a second), which contracted in five to ten seconds and then extended back as the water evaporates (Figure S7-11a). For RH-induced linear actuation, the RH of the chamber was cycled between 10% to 85% in 80 seconds (Figure S7-11b). The length change of the yarn was measured by analyzing the video frames.

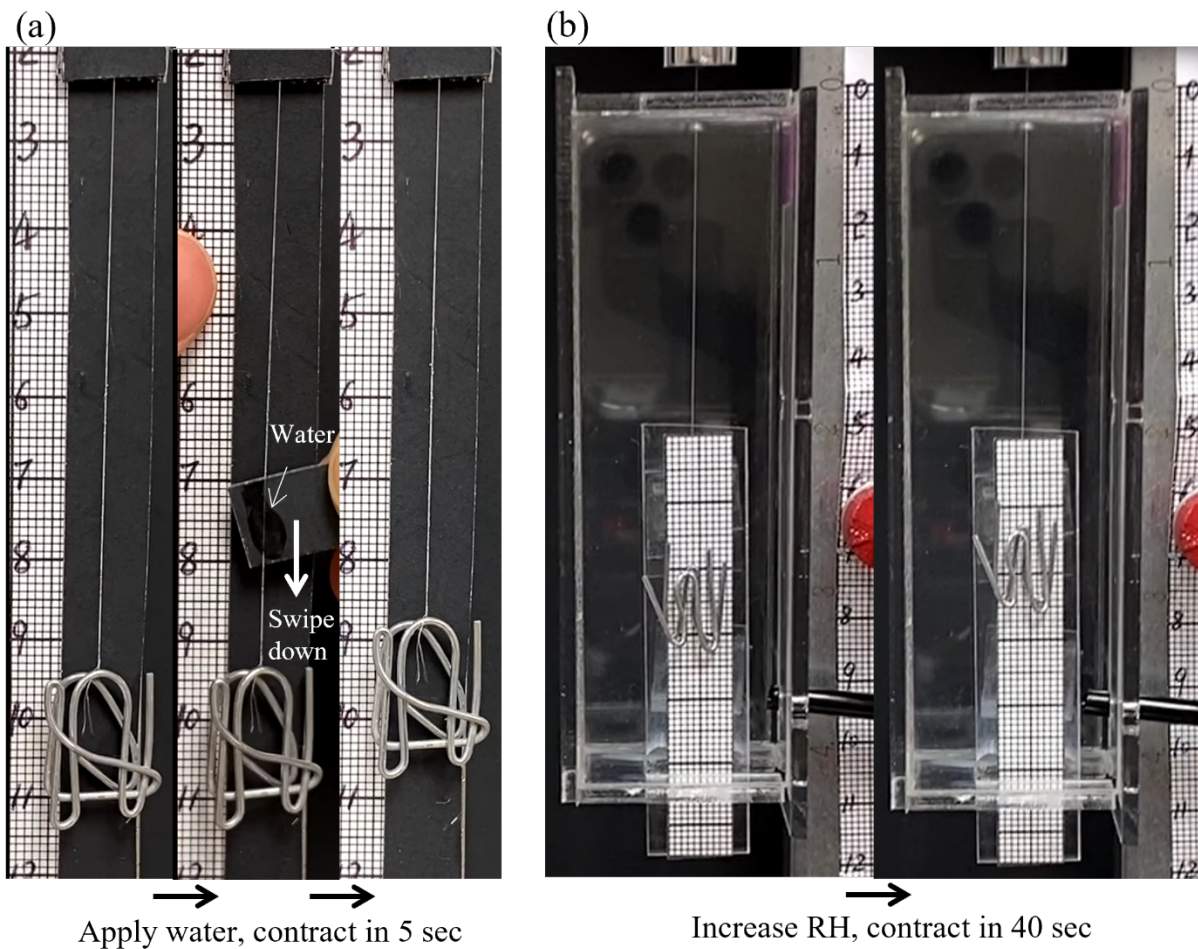


Figure S7- 11. Linear actuation and measurement setup. (a) Linear actuation by applying water. (b) Linear actuation by changing RH.

Chapter 8 Conclusion

Lightweight, compact, and reliable soft actuators are needed for many emerging applications such as wearable and biomedical devices, but such practical devices remain elusive. Better material choice together with appropriate structural design provide a potential approach to develop soft actuators capable of producing diverse motions. This dissertation aims to examine appropriate structures of soft actuators for wearable applications. Three types of structures covering different stimuli-responsive materials and actuation methods have been investigated. First, we discuss a bistable laminated DEA inspired by the fast closure of the Venus Flytrap, that is capable of rapid and self-sustainable shape transformation. Due to the high voltage required for actuation and its potential safety concerns, we then examine moisture as a more suitable source of stimuli for soft actuators. Commercial films (cellophane) and fibers (viscose rayon) made from regenerated cellulose were selected as the base materials for the following investigations. Cellophane actuators were designed into self-walking robots and motion-programmable actuators based on the moisture-induced bending deformation of the film. Similarly, highly twisted and coiled polymer actuators (TCPAs) made from viscose rayon were designed into hierarchically twisted structures that generated rapid torsional and linear motion under moisture and electrical actuation.

The studies on bistable DEA demonstrate a facile design that can be switched between two stable states using a sufficiently high electric field. The bistable DEA fabricated using the stretch-attach-release process offer many advantages, including control of the DE layer thickness that can reduce the actuation voltage, compact and lightweight without the need of rigid frames to maintain the stretch, and self-sustainable shape at no energetic cost. We demonstrated the use of bistable DEA as a binary valve or shutter that can operate on curved surfaces. Bistable DEAs offer promising potential for applications in wearables and other soft robotics due to the facile

fabrication, lightweight, and low cost. However, many issues need to be addressed for their future application, including the high actuation voltage and related material failure, long-term shape stability due to stress relaxation, and complex electronics that provide multiple high voltage channels.

The second study presented a rapid, large, and reversible bending of cellophane under moisture change. The films were designed into self-walking robots that can autonomously and directionally move on a moist surface. Diverse actuation motions of the films were designed and fabricated with a facile trim-laminate method. Cellophane actuators can be potentially used in soft robotics or for smart textiles due to their commercial availability materials, fast and reliable response, and facile structural design for diversity of motions. However, the application of the cellophane can be restricted by the shape distortion by water and low force output through bending actuation.

The third study reported torsional and linear motion of TCPAs fabricated from hierarchically twisted viscose rayon fibers. Key structural features of the TCPAs were identified, and their effects on the actuation results were evaluated. While self-plying multiple twisted yarns enhanced the reversibility of the torsional actuation, plying more twisted yarns made from a few fibers improved the overall performance. For linear actuation, the self-coiled yarn generated a maximum contractile strain of 12% and blocking stress of 4 mN/fiber, while the mandrel-coiled yarn generated a remarkable strain of around 500% with negligible force output. Electro-thermal actuation at a low voltage was achieved by plying a conductive yarn (CNT) with the twisted viscose rayon. Multistimuli-driven, viscose rayon-based TCPAs provide promising potential in the application of wearables and smart textiles due to their remarkable performance (i.e., high speed, strain, force, output power, and energy density), lightweight and compact structures, facile fabrication, compatible integration into textiles, and low cost. Further efforts are needed to

bridge the gap between the benchtop study and the real-world applications, including the fabrication of longer length TCPAs at a larger scale, assembly for higher mechanical strength and larger mechanical output, integration into higher-level systems (i.e., fabrics) with reliable actuation performance.